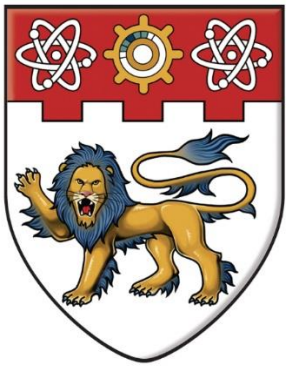

NANYANG TECHNOLOGICAL UNIVERSITY

OPTICAL-SPIN DYNAMICS IN ORGANIC-INORGANIC HYBRID LEAD HALIDE PEROVSKITES

DAVID GIOVANNI

INTERDISCIPLINARY GRADUATE SCHOOL

ENERGY RESEARCH INSTITUTE @ NTU (ERI@N)

2017

OPTICAL-SPIN DYNAMICS IN ORGANIC-INORGANIC HYBRID LEAD HALIDE PEROVSKITES

DAVID GIOVANNI

Interdisciplinary Graduate School
Energy Research Institute @ NTU (ERI@N)

A thesis submitted to Nanyang Technological University in partial fulfillment of the requirement for the degree of
Doctor of Philosophy

2017

ABSTRACT

Low temperature (< 150°C) solution-processed organic-inorganic hybrid lead halide perovskites are an emergent class of material which has attracted the full attention of the academic community. Apart from its striking optoelectronic properties and economical production cost, the chemical versatility for facile properties-tuning is its primary appeal. Recent works have demonstrated the potential of this material system for light-harvesting (*i.e.* solar cell) and light-emitting (*e.g.* LEDs, lasers, *etc.*) devices with ground-breaking efficiencies. Moreover, this perovskite system also exists in with various dimension of connectivity from 0D to 3D, which provides an additional platform for tunability. Researchers in the field, especially optical spectroscopists, have focused their study on understanding why lead halide perovskites work so well.

Despite from the worldwide efforts to elucidate the fundamental physics behind lead halide perovskite system, it still has untapped potential. Owing to its heavy-element components, the spin-orbit coupling (SOC) in this material system is known to be huge. Since in normal condition light does not interact with electron's spin, SOC becomes a prerequisite to optically access the spin degree of freedom in a material. Ability to optically manipulate the spin degree of freedom via SOC will enable us to realize novel *opto-spintronics* technology using lead halide perovskites. Herein, the spin photophysics in lead halide perovskites has not been fully explored and understood, which therefore forms the focus of the thesis. Here, time-resolved transient absorption spectroscopy was used as the main technique to explicate the transient dynamics of photoexcited carriers and spin polarization in lead halide perovskite system. Our study spans across the multi-dimensional structural phase of lead halide perovskites from 2D, Ruddlesden-Popper (RP) phase, and 3D systems.

To understand the optical-spin dynamics, the first half of the thesis focused on elucidating the dynamics of the photoexcited species in the conventional lead halide perovskites. In the 3D system (*i.e.* $CH_3NH_3PbI_3$) where the main photoexcited species are free carriers, we determined the branching ratio of multiple relaxation pathways of these photoexcited free carriers. On the other hand, in the 2D and RP phase (up to $n = 4$) system, we discovered that the

photoexcited species is dominated by excitons. We determined the origin of their transient spectral features and investigated the relaxation mechanism of these photoexcited excitons.

The second half of the study then proceeded to elucidate the optical-spin dynamics in these multi-dimensional lead halide perovskites. Our results show that the *J*- (or spin-) polarized carriers/excitons can be photoexcited in this multi-dimensional perovskites by using circularly polarized light. This photoexcited spin-polarization decays within the first 10 ps of the dynamics, which to some extent can be tuned by the film morphology or its dimensional phase. In the 3D system, we observed that the spin-polarized carriers relax via Elliot-Yafet mechanism, but with a weak spin-phonon coupling; and ultra-large Faraday rotation up to 10°/μm. On the other hand, in the 2D system, we observed a strong coupling between the photons and exciton spin states, which manifested in spin-selective optical Stark effect. This coupling strength can be tuned by simply varying the dielectric contrast between the organic and inorganic layers in the 2D perovskites. We also noted the peculiar behavior of the spin relaxation in the RP phase (up to $n = 4$), which is in contrast to the current understanding of exciton spin relaxation mechanism in conventional III-V or II-VI semiconductor system; implying that another mechanism or higher order process might be dominant in lead halide RP perovskites. Importantly, our study does not only lay down the fundamentals of spin photophysics in lead halide perovskites but also demonstrates its potential for opto-spintronic applications.

ACKNOWLEDGEMENTS

My two years and eight months of Ph.D. in NTU were the most challenging and breathtaking time for me. Despite having been introduced to research since undergraduate time, it was my first experience to be fully responsible for my own research project. It was a time full of blessings, hope, and growth. Now it will be closed by this thesis which I am content and grateful for. Regardless of how excellent or disappointing people might see this thesis is, I may not boast of my own self for this achievement. It is not by me, but by God, Jesus Christ who has strengthened me. For in Him all things were created: things in heaven and on earth, visible and invisible, whether thrones or powers or rulers or authorities; all things have been created through Him and for Him. He is before all things, and in Him, all things hold together. To Him be all the praise and glory forever.

I would like to also thank *Interdisciplinary Graduate School* (IGS*), Energy Research Institute @ NTU* (ERI@N) and *Johnson-Matthey* (JM) for the opportunity given to me via the Ph.D. programme and the scholarship offered, which have brought me up to this point. This opportunity has enabled me not only to get a degree and to achieve a better career in the future but also to a chance to explore what I love in science and experience the life as a real cutting-edge scientist.

In order for this project to reach this point, there is a long list of names should my thanks be dedicated to. First of all, I would like to thank my dearly academic supervisor *Asst. Prof. Nripan Mathews*, for his cheerful mentorship which made my life as a Ph.D. student so vibrant; my co-supervisor *Assoc. Prof. Sum Tze Chien*, who has been wisely and meticulously helping and guiding me in academia; my mentor *Prof. Subodh Gautam Mhaisalkar*, who has also been a great mentor to me; and my JM supervisor Dr. *Robert Potter* for all his advice which helped me through the Ph.D. process. It was because of their patience, ideas, inspirations, and advice which made my research life felt so interesting and vibrant. Under their supervision, I was given free, yet guided, to challenge myself asking and solving the right important scientific questions for research.

The next person I would like to express my thanks to is my beloved wife *Devina Wongso*, who has fervently and faithfully cheered, supported and loved me during hard times, and shared the joy with me during good times. Thanks also for my beloved parents, who have supported me and restlessly prayed for me regardless of my weakness and limitations. My gratitude is also addressed to my friends, mentors, and collaborators: *Dr. Julianto Chua* and *Dr. Herlina Arianita Dewi*, who have been tirelessly listened and granted my unceasing request for samples. Thanks to them I can finish this thesis in a relatively short time. Last but not least, I would like to address my gratitude to the rest of my co-workers in *Femtosecond Dynamics Laboratory*, the lab in which I have grown for almost seven years: *Assoc. Prof. Ma Hong, Dr. Wu Bo, Dr. Wei Qiang, Dr. Ming Jie, Lim Swee Sien, Chong Wee Kiang, Goh Teck Wee, Eugene Tay, etc.* whom I did not mention all in name, for the fun and vibrant research environment which has carved a great impression on me. It always strengthens me to know that no matter how difficult your own research might be, there will always be some fellows who are available to support you.

Lastly, I would like to thank all of my friends and mentors who have cared about me, prayed for me, cheered me, supported me and listened to my sharing during my difficult days of my Ph.D. years. Thanks to *Lisman Komaladi, Victor Wibowo, Darryl Putra, Chatharin Yap, Pearlyn Tan, Dora Chiang, Fernaldo Richtia Winnerdy, Hendra Kwee etc.* which I could not mention all of them by name here. I am grateful for having such good friends like them, and without them, I would not be who I am now.

TABLE OF CONTENTS

ABSTRACT i

ACKNOWLEDGEMENTS iii

TABLE OF CONTENTS v

FIGURE CAPTIONS xi

TABLE CAPTIONS xxi

ABBREVIATIONS xxiii

CHAPTER 1: INTRODUCTION 1

1.1 Motivation for research beyond conventional electronics 2

1.2 Organic-inorganic hybrid perovskites 5

1.2.1 What is perovskite? 5

1.2.2 What is OIHP? 7

1.2.3 OIHP for electronics 9

1.2.4 OIHP for optoelectronics 9

1.2.5 Potential of OIHP for opto-spintronics 11

1.3 Ph.D. in the context of literature 15

1.4 Objectives and Scope of Work 16

1.5 Thesis Overview 17

1.6 Findings and Originality 18

1.7 Bibliography 18

CHAPTER 2: EXPERIMENTAL METHODS 25

2.1 Laser system 26

2.1.1 Pulsed laser 26

2.1.2 Ultrafast laser spectroscopy system 27

2.2 Ultrafast time-resolved optical spectroscopy 31

2.2.1 Transient absorption spectroscopy 31

2.2.2 Time-resolved photoluminescence (TRPL) spectroscopy 40
2.3 Steady-state optical spectroscopy.....41
2.3.1 Linear absorption spectroscopy.....41
2.3.2 Steady-state photoluminescence spectroscopy.....42
2.3.3 X-ray diffraction (XRD).....43
2.4 Miscellaneous measurement techniques 44
2.4.1 Spot-size measurement.....44
2.4.1 Pump fluence calculation 46
2.4.2 Sample thickness measurement.....46
2.5 Fabrication of OIHP thin films.....47
2.5.1 Standard spin-coating technique. 48
2.5.2 Toluene treatment.....49
2.5.3 Hot-casting technique.....49
2.6 Bibliography.....49
CHAPTER 3: OPTICAL-SPIN DYNAMICS IN 3D ORGANIC-INORGANIC HYBRID LEAD HALIDE PEROVSKITES 51
3.1 Linear properties 52
3.1.1 Structural properties 52
3.1.2 Optical properties 53
3.1.3 Section Summary 54
3.2 Non-equilibrium carrier dynamics 54
3.2.1 Assignment of TA spectra origin 55
3.2.2 Assignment of carrier relaxation dynamics.....58
3.2.3 Section Summary 62
3.3 Optical-spin dynamics.....62
3.3.1 Modelling of spin dynamics.....63
3.3.2 Preliminary measurement.....66

3.3.3 Temperature and power dependent TA 67
3.3.4 Assignment of spin relaxation mechanism 73
3.3.5 Effect of morphology 75
3.3.6 Effect of organic and halide substitution 79
3.3.7 Summary 80
3.4 Conclusions 81
3.5 Bibliography 81
CHAPTER 4: OPTICAL-SPIN DYNAMICS IN 2D ORGANIC-INORGANIC HYBRID LEAD HALIDE PEROVSKITES 87
4.1 Linear properties 88
4.1.1 Structural properties 88
4.1.2 Optical properties 89
4.1.3 Optical selection rules 90
4.1.4 Section Summary 91
4.2 Non-equilibrium exciton dynamics 91
4.2.1 Assignment of TA spectrum 92
4.2.2 Assignment of exciton relaxation dynamics 98
4.2.3 Coherent exciton-phonon coupling 100
4.2.4 Section Summary 102
4.3 Spin-selective optical Stark effect (OSE) 103
4.3.1 Theory of photon-dressed state 103
4.3.2 Spectral signature of OSE 107
4.3.3 Spin-selectivity of OSE 108
4.3.4 Estimation of the energy shift 111
4.3.5 Tunability of OSE 114
4.3.6 Comparison with conventional semiconductor system 117
4.3.7 Section Summary 118

4.4 Conclusion....118
4.5 Bibliography....119
CHAPTER 5: OPTICAL-SPIN DYNAMICS IN MULTI DIMENSIONAL RUDDLESDEN-POPPER ORGANIC-INORGANIC HYBRID LEAD HALIDE PEROVSKITES....125
5.1 Linear properties....126
5.1.1 Structural properties....126
5.1.2 Linear optical properties....129
5.1.3 Section summary....131
5.2 Transient photoexcited dynamics....131
5.2.1 Transient spectral features....132
5.2.2 Relaxation kinetics....142
5.2.3 Section summary....149
5.3 Optical spin dynamics....150
5.3.1 Exciton angular momentum states....150
5.3.2 Preliminary results....152
5.3.3 Exciton spin relaxation pathway....155
5.3.4 Exciton spin relaxation model....156
5.3.5 Effect of dimensionality....158
5.3.6 Section summary....162
5.4 Conclusion....163
5.5 Bibliography....163
CHAPTER 6: SUMMARY, CONCLUSION AND FUTURE WORK....167
6.1 Summary of the study....168
6.2 Outstanding questions....169
6.3 Proposed future works....171
6.3.1 Perovskite single crystals....171
6.3.2 Magnetic doping in perovskites....172

6.3.3 Theory on the spin dynamics in Ruddlesden-Popper perovskites.....174

6.4 Implication, conclusion, and outlook 175

6.5 Bibliography.....176

APPENDIX 179

FIGURE CAPTIONS

Figure 1.1 | Microprocessor transistors counts and Moore's law. The transistor counts over the years from 1971 up to 2011 and its comparison with Moore's law. This figure is adapted from ref. [4]. 2

Figure 1.2 | New branches of technology and their respective DOF. New branches of technology and their respective Degree of Freedom (DOF) provided in nature and utilized in the technology. 3

Figure 1.3 | Perovskite generic crystal structure. The cubic crystal structure of 3D perovskite system with generic formula of AMX_3. The blue-shaded region shows the $[MX_6]^{4-}$ octahedron. 6

Figure 1.4 | Multi-dimension perovskite structures. The general crystal structures of perovskite for (**A**) 3D, (**B**) 2D, (**C**) 1D and (**D**) 0D system. The blue octahedron represents the $[MX_6]^{4-}$ structure with X anions represented as orange spheres. This figure is adapted from ref. [28].....6

Figure 1.5 | <100> Perovskite system in between 2D and 3D. The dimensionality is determined by the number of octahedron layer connected before the separation by the long organic group. This figure is adapted from ref. [29]. 7

Figure 1.6 | Potential applications of lead-based OIHP $CH_3NH_3PbX_3$. (**A**) Solar cell architecture using $CH_3NH_3PbI_3$ as the active medium. This figure is adapted from ref. [42]. (**B**) Tunable amplified spontaneous emission (ASE) from $CH_3NH_3PbX_3$ thin film for laser applications. This figure is adapted from ref. [45]. (**C**) Light emitting diode (LED) made from $CH_3NH_3PbX_3$. This figure is adapted from ref. [48]. (D) Sensitive and fast photodetector based on $CH_3NH_3PbX_3$. This figure is adapted from ref. [49].....10

Figure 1.7 | Illustration of switchable Rashba effect in 3D lead halide perovskites. Application of external electric field can control the polarization of the non-centrosymmetric perovskites crystal which therefore switch the spin band momentum splitting. This figure is adapted from ref. [67]. 12

Figure 1.8 | Perovskite-based spin FET design. Suggested spin FET design by using $CH_3NH_3PbI_3$ utilizing its strong spin-orbit coupling and Rashba effect. This figure is adapted from ref. [66]. 13

Figure 1.9 | Strong coupling in 2D $(C_6H_5C_2H_4NH_3)_2PbI_4$ microcavity. The lower and upper exciton-polariton branch position obtained from angle-resolved reflectivity

measurement. The anti-crossing behavior between these two branches is the proof for the strong coupling regime. This figure is adapted from ref. [75]. 15
Figure 2.1 | Superposition of many CW modes. The ultrashort pulsed laser comes from the superposition of many CW modes. Here, *f* is the repetition rate of the pulse laser, while Δ*t* is the pulse duration. 27
Figure 2.2 | Ultrafast laser system. The *Coherent*© *LIBRA*™ ultrafast laser system used in this study. The output is ~50 fs 800 nm laser pulses with pulse energy of 4 mJ and repetition rate of 1 kHz. 28
Figure 2.3 | Kerr Lens Modelocking in *VITESSE*. The self-focusing of high-intensity pulsed laser, which can be used to eliminate the residual CW component. This figure is adapted from *Coherent*©. 29
Figure 2.4 | Schematic of the regenerative amplifier. The regenerative amplifier takes energy from the pump laser to amplify the ultrashort pulses from the seed laser. This figure is provided by *Coherent*©. 30
Figure 2.5 | The working principle of pump-probe. (A) By moving the delay stage, the time delay between the pump pulse and the probe pulse can be controlled. (B) Both pump and probe beam are spatially overlapped on the sample. In transmission geometry, by detecting the change of the probe transmission as a function of time delay between the pump and probe, the time-resolved information of the photoexcited species can be obtained. 33
Figure 2.6 | Degenerate transient-absorption setup. Here, BS is beam splitter, LP is linear polarizer and WP is Wollaston prism. By using a quarter wave-plates and Wollaston prism, the left circular and right circular component from linearly polarized probe can be deconvolved and detected by the two probes of balanced photodetector. 34
Figure 2.7 | Origin of Faraday rotation. Illustration of (A) photoinduced and (B) magnetic field induced asymmetric changes of absorbance, which by Kramers-Kronig relation, they result in asymmetric changes of refractive index. This results in the rotation of the polarization plane. The spectral behaviors of Faraday rotation with different origins are shown. This figure is adapted from ref. [3]. 36
Figure 2.8 | Photoinduced Faraday rotation. (A) Illustration of circular-polarized pump-induced Faraday rotation and (B) detection setup of the Faraday rotation. 37
Figure 2.9 | WLTA experimental setup. The probe beam is focused into a Sapphire crystal to generate white light probe. 750 nm short-pass filter is introduced to eliminate

the 800 nm residual. The transmitted white light probe from the sample is directed into a monochromator and photomultiplier tube (PMT) system, coupled with pre-amplifier and lock-in amplifier for signal detection. 39

Figure 2.10 | Steady-state PL experimental setup. The emission from the sample is collected into an optical fiber by using two lenses before directed into a monochromator coupled with CCD camera for detection. 42

Figure 2.11 | XRD working principle. Based on the interference of the diffracted x-ray at a particular angle 2θ, the inter-plane distance in the crystal can be deduced. 43

Figure 2.12 | TEM_{00} Gaussian beam profile. (A) Spatial profile of the TEM_{00} mode around the focal point, and (B) temporal profile of the Gaussian pulse. 45

Figure 2.13 | Spin-coating technique. The spin-coating technique involves (A) dropping the precursor solution into the treated substrate, (B) wetting the substrate with the solution and (C) spinning the substrate with the predetermined rotation speed and duration to form a uniform film. 48

Figure 3.1 | Structure and XRD spectrum of MAPI. (A) Generic 3D perovskites structure. (B) XRD spectrum of our solution processed spin-coated MAPI thin film on amorphous quartz. (C) Crystal cutting of MAPI at (110) planes, with an inter-plane spacing of 0.63 nm. 52

Figure 3.2 | Linear optical properties of MAPI thin film. (A) The absorption coefficient α (red) and the PL emission (blue) of MAPI thin film. (B) Estimation of MAPI bandgap (~1.595 eV) from the Tauc plot. 53

Figure 3.3 | TA spectrum of MAPI thin films. (A) The experimental TA spectra of MAPI thin film at various probe delay positions. The sample is photoexcited by 760 nm pump (10 $\mu J/cm^2$) at room temperature. (B) TA spectrum based on parabolic band model. 55

Figure 3.4 | Carrier relaxation channels in MAPI. (A) Schematic of the relaxation channels of band edge carriers in MAPI, where (1) trap-assisted recombination (2) geminate recombination (3) non-geminate/bimolecular recombination and (4) Auger recombination. (B) Pump fluence dependent TA kinetics of MAPI thin films pumped and probed 760 nm, with fluence ranging from 2.5 $\mu J/cm^2$ to 20 $\mu J/cm^2$. The relaxation dynamics is global-fitted by rate eq. (3.6). 59

Figure 3.5 | Branching ratio of relaxation pathways in MAPI. (A) Density-dependent contribution of each relaxation channel of the photoexcited carriers in MAPI thin film. Three relaxation pathways are shown: mono- (red square, trap-assisted recombination),

bi- (blue circle, radiative recombination) and tri-molecular (magenta diamond, Auger recombination). (B) Density-dependent PL quantum yield of MAPI.....61
Figure 3.6 | Selection rule at band-edge of MAPI. The conservation of angular momentum in absorption process results in the selection rule for σ^+ (red) and σ^- (blue) circularly polarized light. 63
Figure 3.7 | Model for spin dynamics in MAPI. Excitation by σ^+ pump (red thick arrow) will populate the $|1/2,+1/2\rangle$ CBM state and depopulate the $|1/2,-1/2\rangle$ VBM state. The dynamics are followed by electrons and holes *J*-flip which populates the respective counterpart *J*-states. The populations of each spin-state can be monitored by σ^+ (red thin arrow) and σ^- (blue thin arrow) probe. 64
Figure 3.8 | Degenerate pump-polarization dependent TA on MAPI thin film. The kinetics of spin-states in MAPI thin film monitored by σ^+ (red square) and σ^- (blue circle) probe, photoexcited by (A) σ^+, (B) linear and (C) σ^- polarized pump. The data is globally fitted with eq. (3.16).....66
Figure 3.9 | Degenerate TA of MAPI thin film at different temperatures. The polarization dependent degenerate TA photoexcited with λ = 750 nm σ^+ pump with a fluence of ~19 μJ/cm^2 at (A) 77 K and (B) 293 K. The σ^+ probe, σ^- probe and their total are shown in red square, blue circle, and magenta diamond, respectively. 68
Figure 3.10 | Spin lifetime of MAPI thin film. (A) Temperature T dependent spin lifetime at fluence of 19 μJ/cm^2. The solid lines are for comparison with $T^{-0.5}$ trend. (B) Power dependent spin lifetime at 293 K. All measurements were performed using λ = 750 nm. The short and long lifetime components are shown in red and blue, respectively. 69
Figure 3.11 | Non-degenerate TA on MAPI thin film. (A) Momentum and relaxation of non-resonantly photoexcited carriers involving phonons in MAPI. (B) TA spectra of co- (bottom) and counter-circular (top) pump and probe polarization of MAPI photoexcited with 700 nm pump and fluence of 16 μJ/cm^2. The fast and slow rise of the co- and counter-circular band-edge photobleaching signal respectively, indicate the presence of spin dynamics. (C) Kinetics probed at 760 nm (band-edge) and pumped at 700 nm of the co-circular (blue) and counter-circular (red) signal.....70
Figure 3.12 | TRFR measurement on MAPI. (A) Comparison between TRFR (red) and spin-population dynamics obtained by TA (blue) in MAPI. (B) TRFR signal on MAPI thin film photoexcited with σ^+ (blue), s-polarized (magenta), and σ^- (red) pump

polarization. All measurements were performed in 293 K with λ = 750 nm (19 μJ/cm^2). 71

Figure 3.13 | Temperature and fluence dependent TRFR in MAPI thin film. (A) Maximum rotation and (B) lifetimes' dependence on temperature. (C) Maximum rotation and (D) lifetimes' dependence on pump fluence. All measurements were performed with λ = 760 nm. 72

Figure 3.14 | SEM images of MAPI with different treatments. The morphologies of different MAPI thin films with different fabrication treatment. Std and washed refer to standard (*i.e.* without extra treatment) and toluene treated sample, respectively. The weight percent concentrations of the precursor solutions are also indicated. 75

Figure 3.15 | TRFR of standard and toluene treated MAPI samples. The TRFR kinetics of standard (red squares) and toluene treated (blue circles) samples, fitted with bi-exponential and single exponential decay function, respectively, at (A) 294 K and (B) 77 K. All measurements were performed by λ = 760 nm and fluence 19 μJ/cm^2. 76

Figure 3.16 | Magnetization lifetimes of toluene treated MAPI thin films. (A) Fluence and (B) temperature dependent magnetization lifetime obtained by TRFR measurements. All measurements were performed at λ = 760 nm. The lifetimes of standard samples are re-plotted in the overlay for comparison. 77

Figure 3.17 | Comparative study of MAPI film thickness. (A) Normalized magnetization kinetics and (B) maximum Faraday rotation for MAPI films with two different thicknesses of 70 ± 10 nm and 200 ± 50 nm. 78

Figure 3.18 | Comparison of spin dynamics among the few 3D perovskite systems. (A) Normalized band-edge $|\sigma^+ - \sigma^-|$ signals from degenerate TA of MAPI (red square), FAPI (blue circle), MAPB (magenta diamond) and PbI_2 (green hexagon). (B) Faraday rotation per unit length of these materials at 293 K. 79

Figure 4.1 | PEPI crystal structure. (A) XRD spectrum of PEPI, obtained by Cu K-α source with λ = 1.5418 Å. (B) Illustration of PEPI crystal structure with alternating organic-inorganic layers.....89

Figure 4.2 | Linear optical properties of PEPI thin film. (A) The absorption coefficient α (red) and the PL emission (blue) of PEPI thin film. (B) Measurement of PEPI bandgap from the Tauc plot. The bandgap is estimated to be 2.554 eV, which gives exciton binding energy of 150 meV.....90

Figure 4.3 | Optical selection rules for circularly polarized photon. The selection rules are presented in bands (left) and exciton (right) representations. Different photon helicity will excite exciton spin states. 91
Figure 4.4 | White light TA study on PEPI thin film. (A) TA spectra at several delay positions and (B) their kinetics at 495 nm (red square), 516 nm (blue circle) and 528 nm (magenta diamond). The sample was excited by 400 nm (8 μJ/cm^2) pump. 92
Figure 4.5 | Post thermalization evolution of TA spectra in PEPI. (A) TA spectrum of PEPI photoexcited by 400 nm (8 μJ/cm^2) pump at 5 ps probe delay, well-fitted by 3 Lorentzian peaks, named PA1, PB, and PA2. (B) Thermalization process causes ratio change between spectral overlaps of the transition probabilities of PA1, PB, and PA2 with the exciton distribution, which results in different A_1 between these 3 peaks. (C) Time evolution of the fitted Lorentzian peaks at different delay positions. Inset: height ratios of PB/PA1 and PA2/PA1. (D) The time evolution of FWHMs and peak positions of the 3 Lorentzian peaks. PA1, PB and PA2 are shown in red, blue and magenta, respectively. 94
Figure 4.6 | TA studies on PEPI with resonant pump excitation. (A) Co-circular and (B) counter-circular TA spectra at various delay positions. (C) The kinetics of co- (red solid) and counter-circular (blue-dashed) polarization, probed at PA1 (500 nm), PB (520 nm) and PA2 (535 nm) regions. All experiments were performed with 515 nm (21 μJ/cm^2). Inset: the net spin population obtained from $|\sigma^+ - \sigma^-|$ probe. (D) Model of the transient optical transitions in PEPI. 96
Figure 4.7 | Relaxation kinetics of PEPI thin film. (A) Fluence dependent TA relaxation kinetics of pumped by 400 nm and probed at 517 nm, fitted by eq. (4.1) with $N = 4$. (B) The contribution of each lifetime component as function of pump fluence. The A_4 component is well-fitted with eq. (4.3). 98
Figure 4.8 | Strong exciton-phonon coupling in PEPI thin film. (A) Comparison of the experimental result (top) and model (bottom) of the first 10 ps kinetics at 5 different probe wavelengths. The kinetics shows strong oscillation only near the PB/PA crossing wavelengths (508 nm and 523 nm). (B) The experimental result (top) and model (bottom) of $\Delta T/T$ TA spectra of PEPI thin film pumped by 400 nm. (c) Low energy Raman study on PEPI thin film, showing a labeled pair of Stokes and anti-Stokes with energies match to the oscillation frequency. 100

Figure 4.9 | Quantum description of the dressed state. (A) Schematic of the new eigenenergies of the photon-dressed states (solid line) in relation to the bare states (dashed line). (B) Illustration of two-level system with by the equilibrium states (solid line) and the pump-induced Floquet quasi-state (dashed line) on the left before OSE, and the resulting photon-dressed states of $|+\rangle$ (solid line) and $|-\rangle$ (dashed line), on the right side after OSE. 106

Figure 4.10 | Optical Stark effect in PEPI. (A) The corresponding linear absorption and TA spectral signatures of. (B) The energy separation Δ = 0.24 eV between the excitonic absorption peak E_0 of PEPI (red) and the excitation pump $\hbar\omega$ (blue). (C) TA spectrum of PEPI following linearly polarized pump-probe at Δt = 0 ps. Inset: ultrafast kinetics of OSE showing a fast process comparable to the pulse duration.....108

Figure 4.11 | Spin-selective OSE in PEPI thin film. (A) Co- and counter-circularly polarized WLTA spectra at various Δt. (B) The kinetics at the negative ΔA peak (2.37 eV). The experiments were performed by using 2.16 eV pump with a fluence of 416 μJ/cm^2. (C) Pump ellipticity (517 μJ/cm^2) dependent OSE spectra at Δt = 0 ps and (D) their kinetics at 2.35 eV, with σ^+ (red), linearly *s*-polarized (σ^0, green) and σ^- (blue) pump polarization and σ^+ probe polarization. (E) Maximum $-\Delta$A signal of σ^+ probe as a function of pump ellipticity, fitted with eq. (4.23).....109

Figure 4.12 | Power dependent OSE study in PEPI thin films. (A) TA spectra for co- (red-solid) and counter-circular (blue-dashed) polarization at Δt = 0 ps. (B) Difference between the co- and counter- circular TA spectra at the same pump fluence at Δt = 0 ps. The vertical dashed line indicates the position of the exciton absorption peak. (C) Estimated Stark shift (green circle, left axis) and two photoexcited exciton population (blue square, right axis) as a function of pump fluence. The former and the latter exhibits linear and quadratic relation, respectively. 113

Figure 4.13 | Comparison of OSE in 3 different 2D perovskites. (A) The Stark shift ΔE and (B) the Rabi energy $\hbar\Omega_R$ as function of pump fluence, together with (D) the absorption spectrum of PEPI (red), PEPB (blue) and FPEPI (green).....115

Figure 4.14 | Correlation between the Rabi-energy and the oscillator strength or dielectric contrast. Measurement of Rabi-energy via OSE on various lead-based 2D perovskite systems, *i.e.* PEPB, PEPI, and FPEPI. There is a clear increasing relation between $\hbar\Omega/\sqrt{I}$ with the dielectric contrast. Meanwhile, no clear correlation is observed between with the oscillator strength and $\hbar\Omega/\sqrt{I}$. 116

Figure 5.1 | RP perovskites crystal structure. The structures of RP lead iodide perovskites with phase n = 1 to 3. The R-NH_3^+ (big circle with tail) and $CH_3NH_3^+$ (big circle) are the bulky and small organic cations, respectively. The generic formula for RP perovskites with phase n is given by $(R\text{-}NH_3)_2(CH_3NH_3)_{n-1}Pb_nI_{3n+1}$.....127
Figure 5.2 | Crystal structures of multi-dimensional RP perovskites. (A) XRD spectra for RP perovskites for phase n = 1 to 4. Illustration for XRD planes for (B) n = 1 and (C) n = 3 phases, showing d_{002} and d_{110} plane spacing. 128
Figure 5.3 | Linear optical properties of RP perovskite thin films. The normalized absorption (red) and integrated PL (blue) spectra of our RP thin films for $\bar{n}$ = 1 to 4 and 3D perovskites. The PL spectra were photoexcited by 400 nm (19 μJ/cm^2) pump.....130
Figure 5.4 | WLTA and TRPL spectra of RP perovskite thin films. (A-D) TA spectra of our RP perovskite thin films with $\bar{n}$ = 1 to 4, photoexcited by 400 nm pump (14 μJ/cm^2) at 5 ps probe delay. PB peaks up to n = 5 can be distinguished. (E-H) The first 40 ps-integrated TRPL spectra of our RP perovskite thin films with $\bar{n}$ = 1 to 4, photoexcited by 400 nm pump (5.7 μJ/cm^2). These emission spectra is well-fitted by multiple Voigt peaks, each corresponds to n = 1 to 5 RP phases. 132
Figure 5.5 | Analysis of γ/σ ratio in RP perovskite thin films. The γ/σ ratio of the Voigt profile for each phase n as function of sample stoichiometric ratio $\bar{n}$. The increase (decrease) in the γ/σ ratio indicates the homogeneous (inhomogeneous) contribution to the peak broadening profile. 134
Figure 5.6 | PL spectra of RP perovskite thin films. (A) Fluence dependent time-integrated PL spectra. The samples were photoexcited by 400 nm pump. (B) Comparison between the time-sliced PL spectra at 10 ps (red), 50 ps (green), 100 ps (blue) and the time-integrated spectra (gray). The samples were photoexcited by 400 nm (1.9 μJ/cm^2) pump.....135
Figure 5.7 | Log-log plot of fluence versus I_{PL0} of RP perovskite thin films. The result for every phase n each in samples is presented. The thin film sample for $\bar{n}$ = 1, 2, 3 and 4 are shown as red square, blue circle, magenta triangle and green diamond, respectively. The γ value for each peak is also shown. The plot are y-offset for clarity. Only first 5 data were used for fitting to avoid saturation effect. 137
Figure 5.8 | WLTA spectra of $\bar{n}$ = 3 RP perovskite thin film. The WLTA spectra taken at (A) 0.5 ps and (B) 5 ps probe delay were photoexcited by 400 nm pump (14 μJ/cm^2). The 5 ps TA spectrum were fitted with 11 Voigt profiles.....139

Figure 5.9 | Comparison of early TA kinetics in $\bar{n}$ = 3 RP perovskites. (A-C) The early (3 ps) TA kinetics of $\bar{n}$ = 3 perovskite thin films photoexcited with 400 nm (14 μJ/cm^2) pump at various probe wavelengths. The kinetics were fitted by eq. (5.5). Dashed lines are eye-guides. (D) The compilation of fitted rise time of the competing process. Filled and hollow symbol represents PB and PA signals, respectively. Red square and blue circle represents fast and slow rising process, respectively. 140
Figure 5.10 | PL Kinetics of RP perovskite thin films at ~525 nm (*n* = 1). The fluence dependent PL kinetics on $\bar{n}$ = 1 to 3 samples were global-fitted over the pump fluence of 0.9 to 19 μJ/cm^2 (400 nm) by using a tri-exponential decay function with lifetimes as shared parameters. Inset: the contribution of each of the lifetime component, shown in red square (A_1), blue circle (A_2) and green triangle (A_3). 142
Figure 5.11 | Illustration of inter-phase band alignment in RP perovskites. The band edge alignment between *n* and *n* + 1 RP perovskites phases in (A) quasi-type I and (B) type-II configurations. For both cases, the band bending creates carrier traps. The Fermi level is assumed to be at the center of the gap. 145
Figure 5.12 | PL Kinetics of RP perovskite thin films at ~575 nm (*n* = 2). The fluence dependent PL kinetics on $\bar{n}$ = 2 to 4 samples were global-fitted across pump fluence of 0.9 to 19 μJ/cm^2 (400 nm) by using tri-exponential decay function with the lifetimes as their shared parameters. 146
Figure 5.13 | PL Kinetics of RP perovskite thin films for *n* = 3 to 5. The fluence dependent PL kinetics on $\bar{n}$ = 2 to 4 samples of the (A) *n* = 3, (B) *n* = 4 and (C) *n* = 5 phases were global-fitted across pump fluence of 0.9 to 19 μJ/cm^2 (400 nm) by using tri-exponential decay function with the lifetimes as their shared parameters. 147
Figure 5.14 | Optical election rule for circular polarization in one-particle picture. Band edge with total angular momentum states $J = 1/2$ and $m_J = \pm 1/2$ across dimensionality in RP perovskite system results in similar spin-selective optical excitation by circularly polarized photon. 150
Figure 5.15 | Band-edge exciton angular momentum states in two-particle picture. The electron (solid arrow) and hole (hollow arrow) which constitute the exciton are presented, for straightforward identification of their original angular momentum state m_J. The resultant exciton states are represented in $|m_J^e, m_J^h\rangle$ notation. 151
Figure 5.16 | Degenerate spin-dependent kinetics of RP perovskite thin films. (A-D) The kinetics captured by co-circular and counter-circular probe for *n* = 1 to 4 or RP

perovskite thin films are shown in red solid and blue dashed line, respectively. Their difference (*i.e.* net spin) and their total (*i.e.* exciton population) are shown in green dotted and magenta dash-dotted line, respectively. 153

Figure 5.17 | Illustration of exciton spin TA kinetics. Without the loss of generality, the TA kinetics assume σ^+ pump excitation and exciton lifetime much longer than the spin lifetime. The figures show the expected TA probe kinetics for the case of (A) direct, (B) indirect and (C) mixed exciton spin relaxation pathway of the σ^+ (red solid), σ^- (blue dashed), net spin (green dotted) and total population (dashed-dotted). 156

Figure 5.18 | Fluence dependent relaxation time of *n* = 1 RP perovskite phase. (A) The kinetics fitted with single exponential transient decay function. (B) The spin relaxation rate shows no dependence on fluence. The average W_x for this $n = 1$ phase is 4.1 ± 0.1 ps^{-1}.....158

Figure 5.19 | Fluence dependent spin relaxation rate of *n* = 2 to 4 RP perovskite. The exciton (W_x), electron (W_e) and hole (W_h) spin relaxation rates are shown as red square, blue circle and green triangle, respectively. 159

Figure 5.20 | Effective spin lifetime vs dimensionality. (A) The kinetics of spin polarization of RP and 3D perovskite thin films. The samples were photoexcited with 10 μJ/cm^2 pump at their respective resonant wavelengths. The kinetics were fitted with transient single exponential decay function (*i.e.* to represent effective lifetime). (B) The effective spin lifetime seems to increase with increasing *n* (decreasing confinement). 161

Figure 6.1 | Magnetism switching in Mn-doped perovskites. The ferromagnetic order of the system can be melted by light illumination and rearranged by external magnetic field. This can hold applications for storage devices. The figure is adapted from ref. [10]. 173

TABLE CAPTIONS

Table 2.1 | List of solution-processed lead-based OIHP with its precursor. All the samples listed here are used in this study together with their stoichiometric molar ratio. 47

Table 3.1 | Global fitting parameters. The a, b and c obtained from the global fitting in the fitting and standard unit. The n refers to the carrier density in fitting unit. 60

Table 3.2 | List of several material systems exhibiting FR. Comparison of our results with several material systems reported in the literature to exhibits large FR. 73

Table 4.1 | Comparison of OSE and Rabi energy in various semiconductors. The information of laser system and intensity/power used to obtain the results are included. CW refers to continuous wave. 117

Table 5.1 | XRD result for d_{020} plane in RP perovskite thin film. The XRD angle 2θ and its corresponding plane spacing d for each phase n are tabulated. 128

Table 5.2 | Exciton peak for each of the n-phase of RP perovskite thin films. The exciton energies are presented in wavelength (nm) and energy (eV) units. 129

Table 5.3 | Fitted lifetimes of the PL kinetics of n = 1 phase. The lifetimes were obtained from global fitting of tri-exponential decay across our excitation fluence. .143

Table 5.4 | Fitted lifetimes of the PL kinetics of n = 2 phase. The lifetimes were obtained from global fitting of tri-exponential decay across our excitation fluence. .146

Table 5.5 | Fitted lifetimes of the PL kinetics of n = 3 to 5 phases. The lifetimes were obtained from global fitting the tri-exponential decay across our excitation fluence. 148

Table 5.6 | Compilation of the estimated properties of each phase in RP perovskite thin films. Here, LX is the localized exciton lifetime; FX is the free exciton lifetime; k_F is the funneling rate from n to n + 1 phase; and η is the funneling efficiency. 148

ABBREVIATIONS

OIHP	Organic-Inorganic Hybrid Perovskites
IC	Integrated Circuits
DOF	Degree of Freedom
FET	Field Effect Transistor
LED	Light Emitting Diode
SOC	Spin-Orbit Coupling
CCD	Charged-Coupled Device
XRD	X-ray Diffraction
SEM	Scanning Electron Microscopy
CW	Continuous Wave
OPA	Optical Parametric Amplifier
Ti:S	Titanium-doped Sapphire
DFG	Different Frequency Generation
SFG	Sum Frequency Generation
TA	Transient Absorption
FR	Faraday Rotation
TRFR	Time-Resolved Faraday Rotation
RP	Ruddlesden-Popper
MQW	Multi Quantum Well

CHAPTER 1:

INTRODUCTION

In this chapter, the rationale and the background literature which motivate this study of the spin dynamics of organic-inorganic hybrid lead halide perovskites are briefly reviewed and presented. While their excellent optoelectronics properties have been intensively studied, these perovskites still hold an untapped potential for novel opto-spintronics technology. Strong spin-orbit coupling in perovskites allows manipulation of the spin degree of freedom in the material by light. Herein, the objectives and scope of the research in the thesis are focused on elucidating the of transient spin dynamics in multidimensional organic-inorganic hybrid lead halide perovskites through ultrafast optical spectroscopy. The overall flow of the thesis is also presented in this chapter.

1.1 Motivation for research beyond conventional electronics

Electronics utilizes the charge degree of freedom of electrons to perform operations. It forms the basis of almost every advance we see around us: cell phones, TV, computers, *etc*. All of these modern electronic devices have one similarity: they are built around one primary building block, *i.e.* transistor. Transistor is basically an electronic device which is used to either amplify or switch electronic signals. They are typically combined to work together in an Integrated Circuits (IC). The more transistors combined into an IC, the stronger the processing power of that IC will be. Nowadays, 1 mm^2 of an IC can contain more than 9 million of transistors.

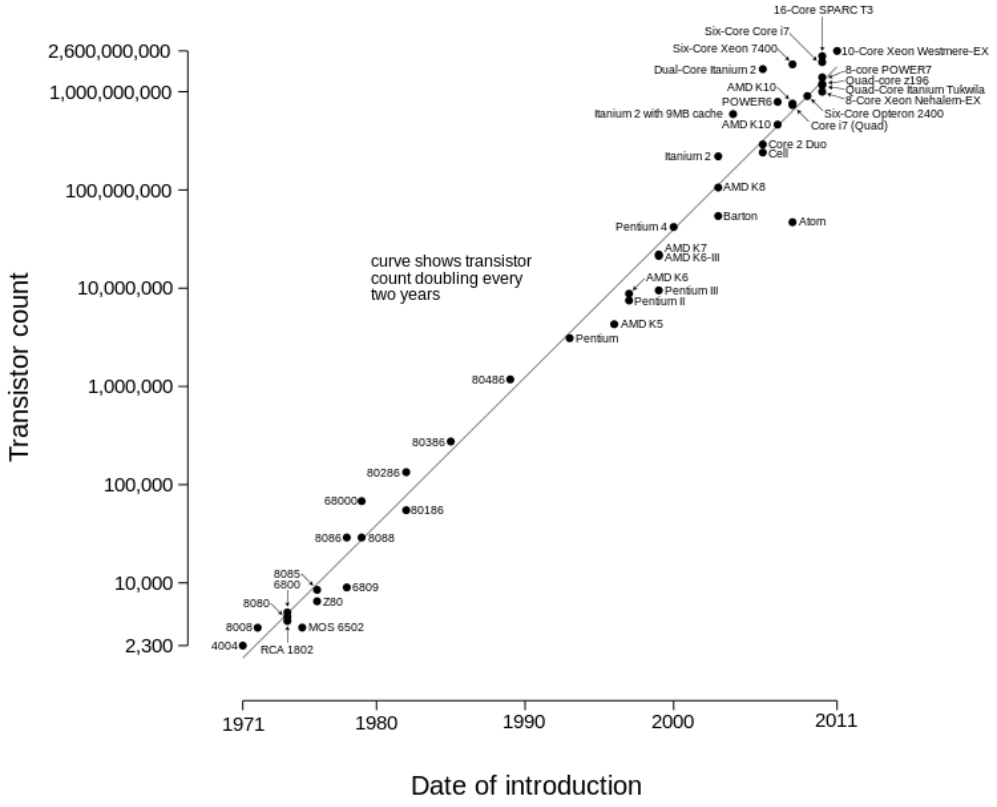

Figure 1.1 | Microprocessor transistors counts and Moore's law. The transistor counts over the years from 1971 up to 2011 and its comparison with Moore's law. This figure is adapted from ref. [4].

In 1965, Gordon E. Moore, one of the co-founders of Intel, wrote a famous prediction based on his observation. He envisaged that the number of components (transistors) in our IC will double every two years [1]. This

prediction is now known as *Moore's law* - **Figure 1.1**. Surprisingly, Moore's law has not only been proven to be accurate for several decades but also used as a long-term guide for setting research and development targets [2]. Nevertheless, the pursuit of Moore's law has seemed to hit a stumbling block due to fundamental limitations of nature. As technology tries to shrink the size of transistors to fit more of them into an IC, transistor sizes have reached a point where quantum effects start to kick in and create challenges, *e.g.* electron tunneling, which leads to source-drain and gate leakage. Currently, these challenges have slowed down the pace of advancement from every ~2 years to ~2.5 years [3].

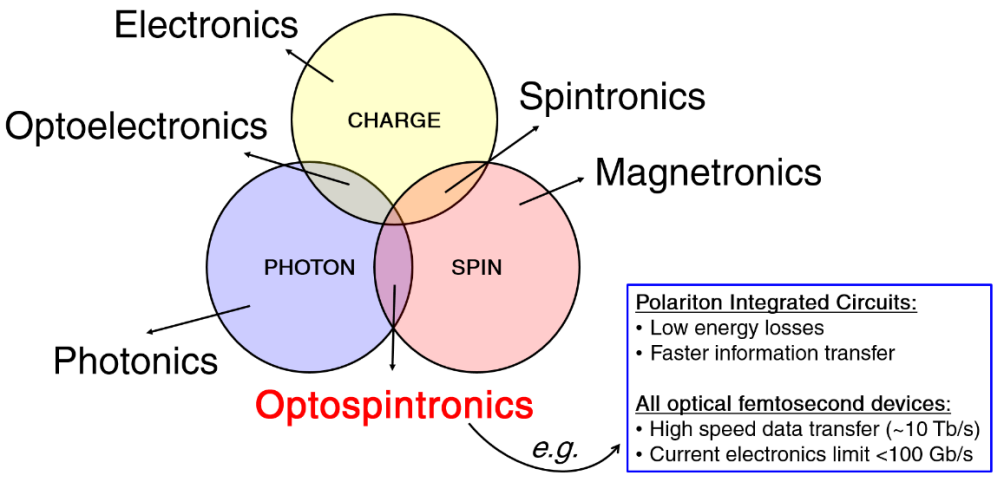

Figure 1.2 | New branches of technology and their respective DOF. New branches of technology and their respective Degree of Freedom (DOF) provided in nature and utilized in the technology.

In the face of such fundamental challenges, research has focused on exploring the alternative *degree of freedom* (DOF) which are available in nature. One of such proposal was put forward by Supriyo Datta and Biswajit Das in 1989, who proposed a theoretical device, which now is known as *spin field effect transistor* (spin-FET) [5]. Spin-FET uses electronic spin-DOF rather than charge-DOF to process information, which has the potential to go beyond the fundamental limitations of silicon electronics. Addition of another DOF on top of charge will allow us to surpass the capability of current electronics. The most prospective candidate for utilization is the spin and photon DOF. Research is

now focused on how to manipulate these DOFs to transfer or extract information in order to use them for applications. Ability to use and manipulate each of this DOF or a hybrid of them will give rise to various exciting new branches of technology - **Figure 1.2**.

One of the most exciting emerging branches of technology is the *opto-spintronics*, where the photon and spin DOF are integrated into a single technology for information transfer and processing - **Figure 1.2**. Due to lower energy losses and much faster propagation speed of photon and polariton as compared to charges, this novel technology is projected to overcome the fundamental electronic speed limit of data transfer (<100 Gb/s) and increase it to the range of 1 – 10 Tb/s, to fulfil our future communication needs [6]. Few examples of opto-spintronic devices which researchers are currently working on are polariton integrated circuits [7, 8], exciton-polariton optical spin switches [9-11], all optical femtosecond switches [12-14], *etc.*

Unfortunately, despite the great potential held by utilizing other DOFs, these new concepts of technologies are far from realization. The major bottleneck comes from the material development side. Research so far is yet to produce an ideal semiconductor material to specifically utilize spin DOF. The main issues revolve around low Curie temperature, short spin transport length, fast spin relaxation and dephasing time [15, 16]. The forerunner material systems which have been extensively studied for decades are mostly inorganic semiconductors, including III-V and II-VI semiconductors [16-19], Dilute Magnetic Semiconductors (DMS) [20, 21], Digital Magnetic Heterostructures (DMH) [22], Silicon [23], *etc*.

Meanwhile, recently organic systems also joins the picture, opening a new branch of research called as '*organic spintronics*' [24-27]. Organic systems are interesting mainly due to its very low spin-orbit coupling (SOC) [25, 26]. Low SOC is a desirable quality to preserve spin polarization in devices (*i.e.* momentum scattering has less effect on spin polarization), which could support an efficient transport of spin-current. This is the reason why most of the studies in organic spintronics are focused on the spin-current injection, transport, and detection of the spin-current through the organic materials [27], *i.e.* spin-valve setup. In this particular experiment geometry, the spin current is passed through the organic material layer, sandwiched between two ferromagnetic electrodes

with prescribed magnetization. By measuring the eletctrical resistance between the two electrodes as a function of their magnetization and utilizing *giant magnetoresistance* (GMR) effect, the efficiency of spin injection and transport inside the organic layer can be studied.

Apart from its low-SOC trait, other advantages such as chemical flexibility and relatively low production costs make organics to be an ideal material system for spintronic applications [26, 27]. Nevertheless, despite their interesting properties, they are not free from issues. Organic materials are typically characterized by a higher degree of morphological disorder, low chemical purity and inferior electronic properties, as compared to inorganics [25]. The charge transport mechanism generally occurs through hopping between localized states, which results in low mobility and uncertainty in carrier density. This can give rise to measurement artifacts for spin-valve measurement, in which spin transport in the organic layer and spin-tunneling between the two ferromagnetic electrodes cannot be distinguished. [25, 27]. The so-called spin-transport proof in organics via *Hanle effect* is also currently still under debate [27]. The studies so far indicate an unexpectedly short spin-transport length not more than few tens of nanometers (nm) in organic systems [27]. Meanwhile, lack of SOC in organic system also limits us from optical means for the study, *i.e.* optical spin injection or detection, which is common for the inorganic system.

1.2 Organic-inorganic hybrid perovskites

In this section, the basics of the material system used for the study: *organic-inorganic hybrid perovskite* (OIHP), together with its realized and potential applications, will be introduced and discussed.

1.2.1 What is perovskite?

The term *perovskite* refers to a generic crystal lattice structure with the $[MX_6]^{4-}$ octahedron cage as the building block. In the cubic-lattice unit-cell representation, this geometry is the following: a metal M cation resides at the cube center, 8 A cations reside at the cube corners and 6 X anions reside at the center of the cube's faces. This cubic crystal structure with formula AMX_3 is shown in **Figure 1.3**.

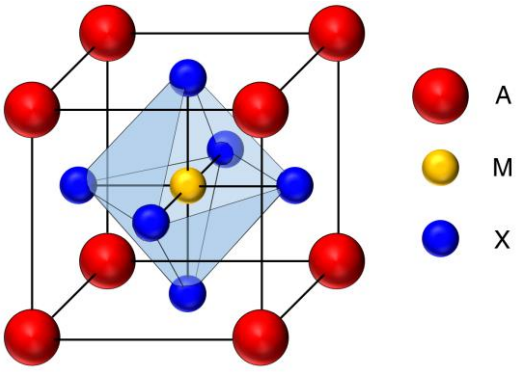

Figure 1.3 | Perovskite generic crystal structure. The cubic crystal structure of 3D perovskite system with generic formula of AMX_3. The blue-shaded region shows the $[MX_6]^{4-}$ octahedron.

This perovskite system comes in multi-dimensional crystal structures system from 3D up to 0D, which is derived from the interconnectivity of their $[MX_6]^{4-}$ octahedron networks [28] - **Figure 1.4**. The multi-dimensionality of the perovskites makes this system to be particularly interesting. Different properties are expected from each dimensionality. For 3D perovskite system, the general chemical formula is AMX_3. Some examples are $CaTiO_3$, $LaAlO_3$, $MgSiO_3$, *etc*. Meanwhile, for 2D perovskites, the general formula is A_2MX_4. One example is $(C_4H_9NH_3)_2PbI_4$.

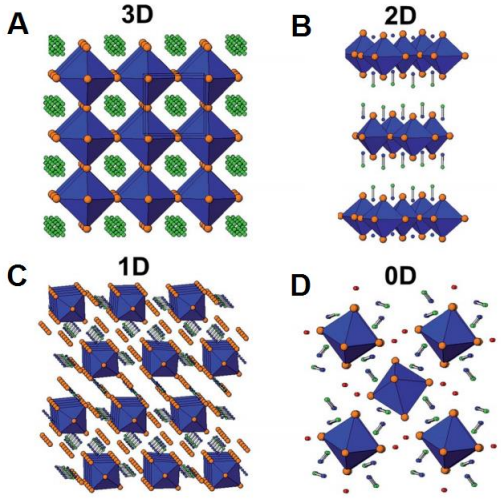

Figure 1.4 | Multi-dimension perovskite structures. The general crystal structures of perovskite for (**A**) 3D, (**B**) 2D, (**C**) 1D and (**D**) 0D system. The blue octahedron represents the $[MX_6]^{4-}$ structure with X anions represented as orange spheres. This figure is adapted from ref. [28].

Between 2D and 3D perovskites, there is also a so-called *pseudo-3D* system, *i.e.* perovskite system with dimensionality in between 2D and 3D, which is determined by the number of the connected inorganic octahedrons in the out-of-plane direction [29] – **Figure 1.5**. This phase is also known as *Ruddlesden-Popper* phase, with general formula $A_{n-1}B_2M_nX_{3n+1}$ where the dimensionality is characterized by a phase number n ($n \geq 1$, where n is the number of perovskite octahedron layer). Here, A^+ and B^+ are the small and long-chain cations which form the 3D and the 2D constituents, respectively. The pure 2D perovskite is formed when $n = 1$, while the pure 3D perovskite is formed when $n = \infty$.

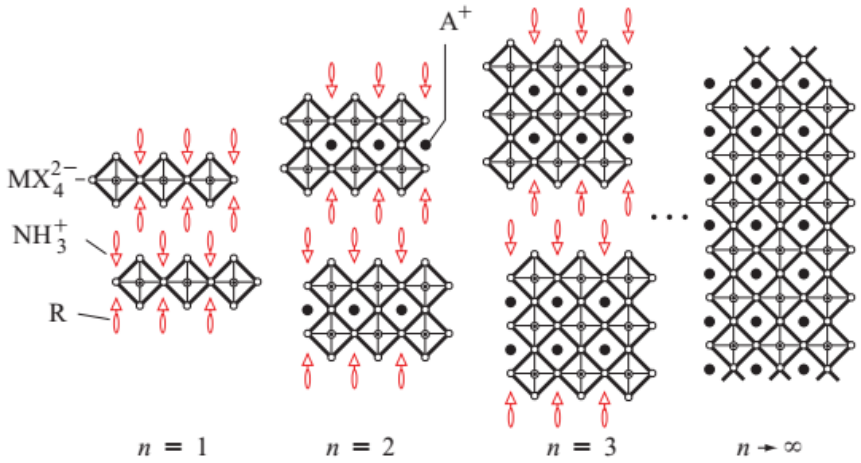

Figure 1.5 | <100> Perovskite system in between 2D and 3D. The dimensionality is determined by the number of octahedron layer connected before the separation by the long organic group. This figure is adapted from ref. [29].

1.2.2 What is OIHP?

Organic-inorganic hybrid, as implied by its name, is a crystalline material made from a combination of the organic and inorganic compounds at the molecular scale. The advantage of such a hybrid is that it combines the best properties of both organic and inorganic semiconductors in one material. The advantages of typical inorganic semiconductors are their robust optical, electric or magnetic properties, which lead to high-performance devices. However, most of the time, relatively advanced and difficult techniques are required for the synthesis, handling, and processing of such material (*e.g.* high vacuum or high

temperature). This incurs costly material fabrication. On the contrary, the organic material acts in opposite behaviors: it is typically relatively easy to produce, economical, chemically flexible and versatile for various applications, yet it suffers from poor performance and properties. Therefore, through being an organic-inorganic hybrid, one would expect to combine the best from both components: to obtain a low-cost, easy to fabricate, versatile, yet with high-quality performance and properties material. Herein, organic-inorganic hybrid perovskites (OIHP), *i.e.* hybrid material in perovskites crystal structure, come into the picture and will be the focus of this thesis.

The term *organic-inorganic hybrid perovskites* (OIHP) refers to the semiconductor material with a perovskite crystal structure, which is formed by the hybridization of organic and inorganic compounds. Generally, in OIHP, the organic material acts as the A^+ cations, while the $[MX_6]^{4-}$ cage is formed by inorganic materials. The M^{2+} cation is a divalent metal cation, while the X^- anions are halide elements. One example is the famous 3D OIHP *methylammonium lead iodide* ($CH_3NH_3PbI_3$), with $CH_3NH_3^+$ as the A^+ cation, Pb^{2+} as the divalent metal cation and I^- as the halide anion. The economic aspect of this material comes about from its low-temperature (~100ºC) solution-processability. This low-temperature solution-processability also makes this material versatile for a wide range of substrates and deposition techniques (*e.g.* spin-coating, drop-casting, dipping, spraying, *etc.*), which allows facile integration with various devices.

In this study, we will focus on the 3D and 2D, and system with dimensionality in between 2D and 3D family (*i.e.* Ruddlesden-Popper phase) of the lead halide OIHP. It is fascinating on how the interconnectivity difference between the 3D and 2D family of OIHP could give rise to totally different photophysics. The 3D lead halide OIHP, *e.g.* $CH_3NH_3PbI_3$ has a bandgap of ~1.6 eV with weak exciton binding energy of a few meV [30] and its photoexcited species being mostly free carriers [28, 31, 32], which therefore makes it excellent for photovoltaic applications. In contrast, its 2D counterparts also with lead (Pb) and idide (I) as the inorganic component, *e.g.* $(C_6H_5C_2H_4NH_3)_2PbI_4$ with alternating organic and inorganic layer structure, forms a natural multi quantum-well system with bandgap ~2.6 eV and strong exciton binding energy of ~200 meV [33, 34]. This results in excitons as its

dominant photoexcited species in 2D systems. Such contrast arises from both confinements from dimensionality and the *dielectric confinement effect* due to high contrast between the dielectric constant of the organic layer ($C_6H_5C_2H_4NH_3^+$ cation, $\epsilon \sim 2$) and the inorganic layer ($[PbI_6]^{4-}$ octahedron, $\epsilon \sim 6$), which enhances the excitonic interaction in the material and the oscillator strength [34]. Such contrasting characteristic results in striking differences between the optical properties of the 3D and 2D OIHP.

1.2.3 OIHP for electronics

For few decades, this economical hybrid material class has attracted communities' attention due to its versatility and excellent electronic properties. The interconnectivity of the $[MX_6]^{4-}$ inorganic octahedron cages in this material system supports high mobility for charge transport, which is desirable for electronic devices. These studies were mainly led by David B. Mitzi, who was the first to introduce 2D tin (Sn) halide OIHP as a thin film field-effect transistor [35-37]. Recently, the lead halide perovskites from the 3D family OIHP with higher carrier mobility has also been used for ambipolar field-effect transistor applications [38, 39].

1.2.4 OIHP for optoelectronics

OIHP, especially lead halide OIHP, has also been known to strongly interact with light. Combined with its excellent electronic properties, it is a great material system for optoelectronic applications - **Figure 1.6**. The archetypal example of this material system is $CH_3NH_3PbI_3$, which has recently gained most of the attention as an excellent active layer in the photovoltaics. Its solar cell efficiency has increased dramatically just in few years, from a value of 3.8% in 2009 [40] to 22.1% [41], which is comparable with the efficiency of commercial Silicon solar cell of ~25% [42, 43]. Such excellent light-harvesting properties stem from the intrinsic properties of $CH_3NH_3PbI_3$: free carrier nature of the photoexcited species [44], high absorption coefficient in visible region [45] and ambipolar long-range carrier diffusion [46], which ensures efficient carrier extraction. Just recently, the Ruddlesden-Popper phase perovskites have also been demonstrated to show promise for photovoltaic application [47]. This work was done on the poly-crystalline $(C_4H_9NH_3)_2(CH_3NH_3)_2Pb_3I_{10}$ ($n = 3$) and

$(C_4H_9NH_3)_2(CH_3NH_3)_3Pb_4I_{13}$ (n = 4) perovskite thin films. These systems show a relatively high efficiency of 12.5% with no hysteresis and greatly improved stability under illumination and the presence of humidity, as compared to the 3D counterparts.

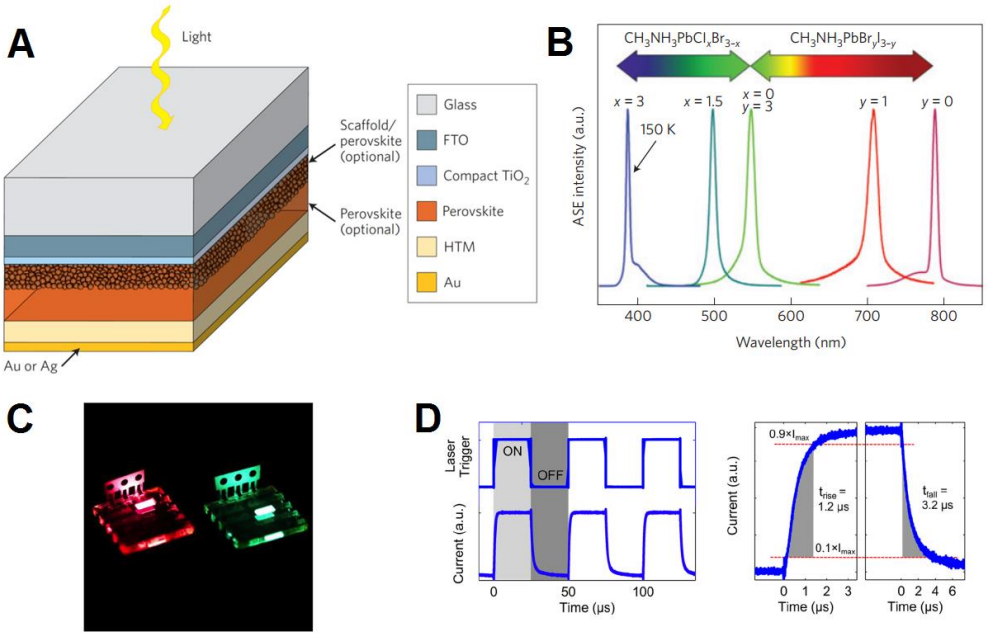

Figure 1.6 | Potential applications of lead-based OIHP $CH_3NH_3PbX_3$. (**A**) Solar cell architecture using $CH_3NH_3PbI_3$ as the active medium. This figure is adapted from ref. [42]. (**B**) Tunable amplified spontaneous emission (ASE) from $CH_3NH_3PbX_3$ thin film for laser applications. This figure is adapted from ref. [45]. (**C**) Light emitting diode (LED) made from $CH_3NH_3PbX_3$. This figure is adapted from ref. [48]. (D) Sensitive and fast photodetector based on $CH_3NH_3PbX_3$. This figure is adapted from ref. [49].

In addition, OIHP, especially lead-based system, has also been known for its excellent light-emitting properties. Studies demonstrated that the three-dimensional (3D) OIHP family $CH_3NH_3PbX_3$ (X = Cl, Br, I) has tunable and low threshold amplified spontaneous emission [45], which is excellent for laser applications. Light emitting diodes (LEDs) have also been made out of CH3NH3PbX$_3$ with relatively excellent efficiency [48]. Meanwhile, the two-dimensional (2D) family of OIHP has also been widely studied and employed as light emitting materials. While there has not been clear evidence of the existence of amplified spontaneous emission in the 2D system [50], several reports of the 2D OIHP family for light emitting diode (LED) [51-53] and white

light emitter [54] have been published. Recently, the Ruddlesden-Popper phase perovskites with mixed phases have also been shown to be an excellent LED, with an enhanced photoluminescence quantum yield as compared to the pure 2D and 3D system [55]. Such observation was assigned to energy and carrier funneling between different phases in the perovskites films. These works exemplify the potential of OIHP for optoelectronic applications. Moreover, another application of 3D lead halide OIHP as photodetectors has also been demonstrated [49, 56-58].

1.2.5 Potential of OIHP for opto-spintronics

Apart from for its potential for optoelectronics, OIHP also has a great prospect for spintronics/opto-spintronic applications. As mentioned, spintronics is an emerging branch of technology which utilizes the electron's spin-DOF, in addition to its charge-DOF as in conventional electronics, to enhance the efficiency or enrich the functionalities of electronic devices [59]. Currently, only metal-based spintronic devices that have been commercialized. Some examples are magnetic random access memory (MRAM) and the read-head of hard disk drive (HDD), which utilizes the giant magnetoresistance (GMR) or the tunnel magnetoresistance (TMR) effect.

While there are numerous designs of semiconductor-based spintronic devices have also been proposed (*e.g.* spin-FET, spin-LED, etc.), their realization for commercial applications remains a problem. Indeed, some semiconductor-spintronic devices have been successfully demonstrated in the laboratory environment (very low temperature/strong magnetic field) [16, 60-62]. Nevertheless, the ultimate challenge is to find a suitable semiconductor system for room temperature and relatively weak magnetic field operation.

There have been some reports which indicate the potential of OIHP as a novel semiconductor system for spin-based applications. One of the important phenomena is Multiferroicity. It is a special property of a material which possesses at least two-coupled ferroic (spontaneous) properties, *e.g.* coupled ferromagneticity and ferroelectricity. This means the ferromagnetic properties of this material can be controlled by electric field, and vice versa. In the literature, several compounds from 2D OIHP family with magnetic metal cation, such as Manganese-based (Pyrrolidinium)$MnBr_3$ [63] and Copper-based

$(C_6H_5CH_2CH_2NH_3)_2CuCl_4$ [64] perovskites have been reported to possess co-existing ferromagnetic and ferroelectric properties, although they have a relatively very low Curie temperature (2.4 K and 219 K respectively for ferromagneticity and ferroelectricity in Mn-based OIHP; 5 K and 340 K respectively for ferromagneticity and ferroelectricity in Cu-based OIHP). Nevertheless, there has not been any study reported regarding the coupling between both of these two coexisting ferroic properties.

Meanwhile, for the 3D OIHP family, to the best of our knowledge, there has been no report so far regarding any multiferroicity nor co-existing ferroicity so far. Nevertheless, some of the spin phenomena have been theoretically predicted for the 3D lead and tin halide OIHP family. The existence of topological phase, which might lead to some exotic spin phenomena, has also been envisaged theoretically in Pb and Sn halide perovskites with Cesium (Cs) as the A^+ cation (instead of an organic cation as typical in OIHPs) when the material is under high pressure of few GPa [65]. DFT calculations have also predicted the existence of Rashba and Dresselhaus effect (*i.e.* spin band splitting in momentum space due to the site and bulk inversion asymmetry, respectively), in $CH_3NH_3PbI_3$ [66, 67] and $NH_2CHNH_2SnI_3$ [68] - **Figure 1.7**.

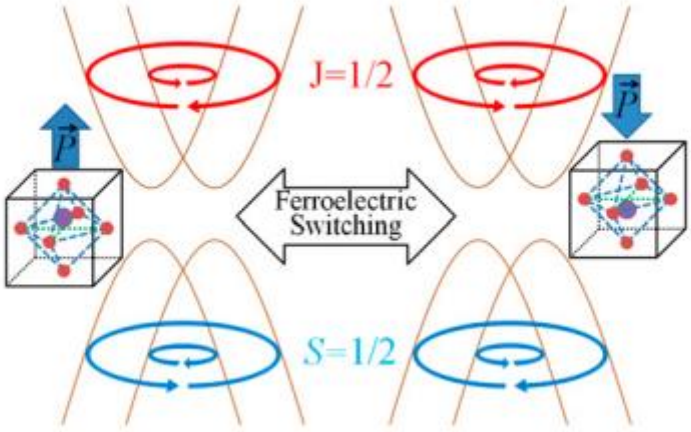

Figure 1.7 | Illustration of switchable Rashba effect in 3D lead halide perovskites. Application of external electric field can control the polarization of the non-centrosymmetric perovskites crystal which therefore switch the spin band momentum splitting. This figure is adapted from ref. [67].

Based on these theoretical studies, Kepenekian *et al.* [66] have suggested a design of a perovskite-based spin-FET – **Figure 1.8**. Coupled with its strong interaction with light, OIHP has become a lucrative option for cheap yet efficient material for opto-spintronic applications. In principle, OIHP offers a flexibility for properties tuning by simply substituting its organic or halide elements, which hence provides easy optimization for various application purposes. This provides an even wider area for exploration.

Unfortunately, up to now, there has not been any experimental confirmations for these predictions due to the limitation of sample preparation techniques. For example, an *angle-resolved photo-emission spectroscopy* (ARPES) is needed for the direct observation of the band splitting due to Rashba and Dresselhaus effects. However, this experiment requires a single crystal OIHP sample with atomically flat surfaces, which still beyond our synthesis capability. On the other side, experiments based on spin-transport electrical measurements have also faced challenges from fast relaxation and dephasing of spin polarization (in the order of few ps, which is part of this thesis), thus prevent them from getting a meaningful spin current signal.

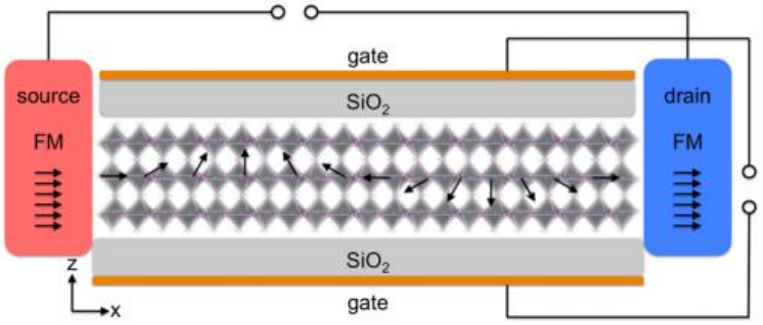

Figure 1.8 | Perovskite-based spin FET design. Suggested spin FET design by using $CH_3NH_3PbI_3$ utilizing its strong spin-orbit coupling and Rashba effect. This figure is adapted from ref. [66].

Other prospective applications for this lead halide OIHP comes from the 2D (layered) family, where the excitonic interaction is greatly enhanced, resulting in strong exciton-photon interaction. One proposal employing this interaction is to utilize a new quasi-particle arising from strong exciton-photon coupling inside a microcavity (optical confinement), known as exciton-

polariton. Exciton-polariton has been appraised by researchers as one of the most potential candidates for future technology because of the exotics physical phenomena arising from the quasi-particle. Exciton-polariton is a boson which typically has an effective mass about four orders of magnitude lower than electron's in semiconductor, enabling it to undergo *Bose-Einstein condensation* (*i.e.* macroscopic occupation of the ground state), at relatively high temperatures, up to room temperature. Bose-Einstein condensed exciton-polariton can emit a coherent monochromatic light, which is a novel type of coherent light source known as *polariton laser* [69, 70]. Other applications by using condensed exciton-polariton include optical-spin switches for transistors and IC [7-11], logic gates [8, 11], *etc.*

Nevertheless, most of the previous architectures utilize inorganic semiconductor nanostructures (e.g. GaAs, InAs, AlGaAs, InP, *etc.*) due to their more robust optical and electrical properties. However, they require cryogenic temperature to maintain the strong coupling regime, due to their weak exciton binding energy (~10 meV) [71]. This limitation could be overcome by moving towards 2D lead halide OIHP, with much stronger exciton binding energy (*i.e.* >100 meV), which guarantees the operation in room temperature. Moreover, 2D lead halide OIHPs have relatively much higher carrier mobility, as compared to the organics. Although typically organics also have a strong exciton binding energy (*i.e.* forming *Frenkel excitons*), it suffer from orders of magnitude lower carrier mobility, which would be an issue for integration with electronics. In contrast, as previously mentioned, several studies have utilized 2D lead OIHP for electronic application as transistors [35-37].

Studies of exciton-polariton system utilizing 2D lead halide OIHP have been pioneered first in 1998 by T. Ishihara's group [72]. The experiment was performed on patterned quartz substrate coated with $(C_6H_5C_2H_4NH_3)_2PbI_4$ 2D perovskite system, forming a *distributed feedback* (DFB) cavity at room temperature. The polaritonic behavior of the system was observed by dips in transmissivity spectra, which marked the sample's absorption. The strong coupling regime in this system was evident from the observed anti-crossing behavior of the position of the dips as a function of the grating periodicities (photon mode detuning). This anti-crossing energy splitting (also known as *Rabi splitting*) was found to be ~100 meV in room temperature, which is much

higher than the ~9 meV splitting of GaAs system. After this first work, follow-up studies were performed mostly by Emmanuelle Deleporte's group in *Fabry-Perot* (FP) cavity geometry - **Figure 1.9** [73-78]. However, those studies are limited only for proving the existence of strong coupling regime in perovskite microcavities through reflectivity and photoluminescence experiments. There have not yet been any fundamental study regarding the exciton-polariton relaxation mechanisms, exciton-polariton interactions, bi-stability, *etc.*, which are important for application purposes, being reported in the literature. Further studies, especially incorporating the spin DOF, are therefore required to advance the agenda.

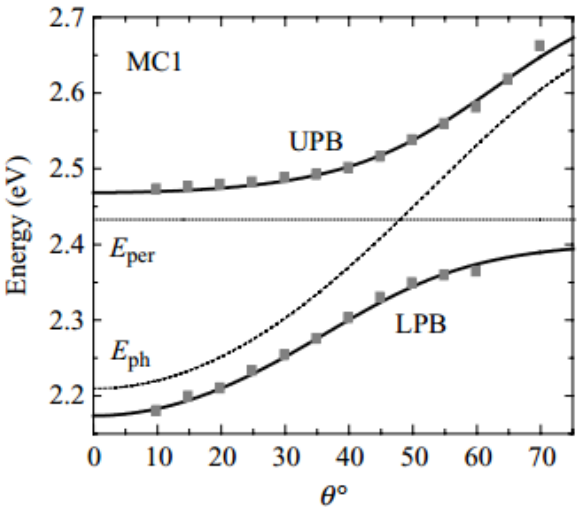

Figure 1.9 | Strong coupling in 2D $(C_6H_5C_2H_4NH_3)_2PbI_4$ microcavity. The lower and upper exciton-polariton branch position obtained from angle-resolved reflectivity measurement. The anti-crossing behavior between these two branches is the proof for the strong coupling regime. This figure is adapted from ref. [75].

1.3 Ph.D. in the context of literature

While OIHP holds such a great prospect, there have been very limited studies which tackle the issue regarding this spin degree of freedom in OIHP, especially in lead (Pb) halide OIHP. Although lead is a non-magnetic metal, lead halide OIHP is known to have one of the strongest SOC (with SOC-induced conduction band splitting up to ~1 eV [30, 79]) and light-matter coupling strength (shown by such excellent optoelectronic devices made out of it) among its peers. In fact, such strong SOC could be responsible for all the exotic spin

phenomena which have been elaborated in the previous section. Furthermore, while fundamentally light/photon could only couple with the orbital angular momentum (*l*) quantum-states of the electrons, in a system with strong SOC such as lead halide OIHP, the orbital and spin quantum-states are coupled via SOC. Hence, such interaction would allow us to access and manipulate the spin DOF in the material by using light.

As mentioned previously, unfortunately, articles discussing the spin dynamics and properties of lead halide OIHP in current literature are not only scarce in numbers but also limited to DFT calculation. Moreover, none of the theoretical report studies the interaction between the spin-DOF with light. Understanding the optical-spin interaction and dynamics, especially from the experimental perspective, is the first step towards not only pursuing the understanding of the exciting fundamental science and phenomena in this exotic material system but also exploring the potential of this material system for novel technological applications.

Motivated by such circumstances, this Ph.D. project addresses one focal question: "*Is lead halide OIHP a suitable material system for application in novel opto-spintronics technology?*" Based on this research problem, this study aims to explore the uncharted science and potential of lead halide OIHP by examining the novel optical-spin phenomena and elucidating their properties and dynamics. Through this study, a better assessment of lead halide OIHP suitability for applications is to be established which could open a pathway towards low-cost semiconductors for the realization of prospective novel opto-spintronics technology.

1.4 Objectives and Scope of Work

Based on the motivation of the research, the objective of this project is to explore and assess the suitability of OIHP material for opto-spintronic applications. The means of achieving such objectives are two-fold:

a. To seek and pursue the fundamental understanding of spin phenomena in 2D and 3D lead-based OIHP. This includes understanding its optical and magneto-optical properties/phenomena, relevant spin relaxation mechanism, etc.

b. To explore, especially 2D and 3D family of OIHP for optimization of its properties. This includes the study of the effect of morphology, sample preparations, the effect of cation/anion substitution, integration into quantum-confined and photon-confined systems, *etc.*

Complete understanding on the system will enable us to design the most suitable material or devices for particular applications.

In this thesis, we limit our interest to the lead (Pb) halide based OIHP system. The choice of lead halide OIHP is due to its well-known robust light-matter interaction and strong SOC. Such traits allow us to optically access and manipulate the spin-DOF in this material system, which is ideal for opto-spintronic applications. The experimental characterization methods of the optical-spin dynamics will be mainly based on optical spectroscopy techniques, especially on ultrafast (femtoseconds) time-resolved optical spectroscopy measurements.

1.5 Thesis Overview

The overview of this thesis is as the following. **Chapter 2** describes the details of the instruments and experimental methodology which is used in this study. The theoretical aspect of these techniques will also be elaborated qualitatively, which is essential for data interpretation. Together with the experimental method, detail of the synthesis techniques for the samples will also be presented.

Chapter 3 presents the optical-spin dynamics observed in 3D lead halide OIHP system. The optical-spin phenomena discovered in this material will be presented and discussed thoroughly. The spin relaxation dynamics will also be studied and examined. Moreover, the effect of sample morphology, as well as the organic and halide components on the spin relaxation, will be presented. Moving from the 3D system, **Chapter 4** presents the optical-spin dynamics observed in 2D lead halide OIHP (layered) system. The optical-spin phenomena discovered in this material will also be presented and discussed in details. The effect of organic and halide components on the spin-phenomena will also be discussed.

In **Chapter 5**, we focus on elucidating the spin-optical dynamics in perovskite systems with dimensionality in between 2D and 3D system, known as *Ruddlesden-Popper* phase lead iodide perovskites. Complete understanding of the effect of dimensionality and confinement on the lead halide OIHP system will provide an additional platform for facile optoelectronics properties tunability. And lastly, **Chapter 6** summarizes and concludes the key findings presented in this thesis. Future works to further advance the work are also suggested.

1.6 Findings and Originality

The originality of the research incorporated in this doctoral thesis lies as the first study to explore the possibility of organic-inorganic hybrid lead halide perovskites for opto-spintronic applications. The novel outcomes/findings from this study can be summarized as the following:

1. Establishing the study of optical-spin injection and the relevant spin relaxation mechanism in 3D lead halide OIHP thin films. It includes the effect of sample morphology on the spin dynamics and also the discovery of ultra-large photoinduced Faraday rotation in $CH_3NH_3PbI_3$ up to $10^o/\mu m$.
2. Establishing the study of carrier dynamics, optical-spin injection and the relevant spin relaxation mechanism in 2D lead halide OIHP thin films. It includes establishing a study of spin-selective optical Stark effect in 2D lead halide OIHP thin films. Another discovery is the straightforward correlation of the Rabi energy and the dielectric contrast between the organic and inorganic layer in 2D lead halide OIHP thin films.
3. Establishing the study of carrier dynamics, optical-spin injection and spin relaxation pathways in RP perovskites. It includes the study of the nature of the photoexcited species, inter-phase interaction and interplay of multiple spin relaxation pathways as a function of different dimensionality.

1.7 Bibliography

1. G. E. Moore, *Understanding Moore's Law: Four Decades of Innovation*. 2006, Philadelphia, USA: Chemical Heritage Foundation.

2. C. Disco and B. van der Meulen, *Getting New Technologies Together*. 1998: Walter de Gruyter.
3. J. Niccolai. *Intel pushes 10 nm chip-making process to 2017, slowing Moore's Law*. 2015 21 April 2016; Available from http://www.infoworld.com/article/2949153/hardware/intel-pushes-10nm-chipmaking-process-to-2017-slowing-moores-law.html.
4. Wikipedia. *Moore's law*. 21 April 2016; Available from https://en.wikipedia.org/wiki/Moore%27s_law.
5. S. Datta and B. Das, *Electronic analog of the electro-optic modulator.* Appl. Phys. Lett., 1990. **56**(7): p. 665-667.
6. W. Osamu, *Femtosecond all-optical devices for ultrafast communication and signal processing.* New J. Phys., 2004. **6**(1): p. 183.
7. T. C. H. Liew, et al., *Exciton-polariton integrated circuits.* Phys. Rev. B, 2010. **82**(3): p. 033302.
8. D. Ballarini, et al., *All-optical polariton transistor.* Nat. Commun., 2013. **4**: p. 1778.
9. G. Li, et al., *Incoherent excitation and switching of spin states in exciton-polariton condensates.* Phys. Rev. B, 2015. **92**(6): p. 064304.
10. A. Amo, et al., *Exciton-polariton spin switches.* Nat. Photon., 2010. **4**(6): p. 361-366.
11. T. Gao, et al., *Polariton condensate transistor switch.* Phys. Rev. B, 2012. **85**(23): p. 235102.
12. D. Hulin, et al., *Ultrafast all-optical gate with subpicosecond ON and OFF response time.* Appl. Phys. Lett., 1986. **49**(13): p. 749-751.
13. T. Volz, et al., *Ultrafast all-optical switching by single photons.* Nat. Photon., 2012. **6**(9): p. 605-609.
14. A. V. Kimel, *All-optical switching: Three rules of design.* Nat. Mater., 2014. **13**(3): p. 225-226.
15. D. D. Awschalom and M. E. Flatte, *Challenges for semiconductor spintronics.* Nat. Phys., 2007. **3**(3): p. 153-159.
16. I. Žutić, J. Fabian, and S. Das Sarma, *Spintronics: Fundamentals and Applications.* Rev. Mod. Phys., 2004. **76**(2): p. 323-410.
17. J. M. Kikkawa and D. D. Awschalom, *Resonant Spin Amplification in n-Type GaAs.* Phys. Rev. Lett., 1998. **80**(19): p. 4313-4316.

18. Y. Q. Li, et al., *Cavity enhanced Faraday rotation of semiconductor quantum dots.* Appl. Phys. Lett., 2006. **88**(19): p. -.
19. P. Nemec, et al., *Spin-dependent electron many-body effects in GaAs.* Phys. Rev. B, 2005. **72**(24): p. 245202.
20. T. Dietl, *A ten-year perspective on dilute magnetic semiconductors and oxides.* Nat. Mater., 2010. **9**(12): p. 965-974.
21. T. Dietl, et al., *Zener Model Description of Ferromagnetism in Zinc-Blende Magnetic Semiconductors.* Science, 2000. **287**(5455): p. 1019-1022.
22. S. A. Crooker, D. D. Awschalom, and N. Samarth, *Time-resolved Faraday rotation spectroscopy of spin dynamics in digital magnetic heterostructures.* Selected Topics in Quantum Electronics, IEEE Journal of, 1995. **1**(4): p. 1082-1092.
23. I. Appelbaum, B. Huang, and D. J. Monsma, *Electronic measurement and control of spin transport in silicon.* Nature, 2007. **447**(7142): p. 295-298.
24. *Why going organic is good.* Nat. Mater., 2009. **8**(9): p. 691-691.
25. C. Boehme and J. M. Lupton, *Challenges for organic spintronics.* Nat. Nanotechnol., 2013. **8**(9): p. 612-615.
26. V. A. Dediu, et al., *Spin routes in organic semiconductors.* Nat. Mater., 2009. **8**(9): p. 707-716.
27. D. Sun, E. Ehrenfreund, and Z. Valy Vardeny, *The first decade of organic spintronics research.* Chem. Commun., 2014. **50**(15): p. 1781-1793.
28. T. C. Sum and N. Mathews, *Advancements in perovskite solar cells: photophysics behind the photovoltaics.* Energy Environ. Sci., 2014. **7**(8): p. 2518-2534.
29. D. B. Mitzi, K. Chondroudis, and C. R. Kagan, *Organic-inorganic electronics.* IBM J. Res. Dev., 2001. **45**(1): p. 29-45.
30. J. Even, L. Pedesseau, and C. Katan, *Analysis of Multivalley and Multibandgap Absorption and Enhancement of Free Carriers Related to Exciton Screening in Hybrid Perovskites.* J. Phys. Chem. C, 2014. **118**(22): p. 11566-11572.
31. C. Sheng, et al., *Exciton versus Free Carrier Photogeneration in Organometal Trihalide Perovskites Probed by Broadband Ultrafast*

Polarization Memory Dynamics. Phys. Rev. Lett., 2015. **114**(11): p. 116601.

32. T. C. Sum, et al., *Spectral Features and Charge Dynamics of Lead Halide Perovskites: Origins and Interpretations.* Acc. Chem. Res., 2016. **49**(2): p. 294-302.
33. X. Hong, T. Ishihara, and A. V. Nurmikko, *Dielectric confinement effect on excitons in PbI_4-based layered semiconductors.* Phys. Rev. B, 1992. **45**(12): p. 6961-6964.
34. T. Ishihara, J. Takahashi, and T. Goto, *Optical properties due to electronic transitions in two-dimensional semiconductors $(C_nH_{2n+1}NH_3)_2PbI_4$.* Phys. Rev. B, 1990. **42**(17): p. 11099-11107.
35. C. R. Kagan, D. B. Mitzi, and C. D. Dimitrakopoulos, *Organic-Inorganic Hybrid Materials as Semiconducting Channels in Thin-Film Field-Effect Transistors.* Science, 1999. **286**(5441): p. 945-947.
36. D. B. Mitzi, C. D. Dimitrakopoulos, and L. L. Kosbar, *Structurally Tailored Organic−Inorganic Perovskites: Optical Properties and Solution-Processed Channel Materials for Thin-Film Transistors.* Chem. Mater., 2001. **13**(10): p. 3728-3740.
37. D. B. Mitzi, et al., *Hybrid Field-Effect Transistor Based on a Low-Temperature Melt-Processed Channel Layer.* Adv. Mater., 2002. **14**(23): p. 1772-1776.
38. Y. Mei, et al., *Electrostatic gating of hybrid halide perovskite field-effect transistors: balanced ambipolar transport at room-temperature.* MRS Commun., 2015. **5**(02): p. 297-301.
39. X. Y. Chin, et al., *Lead iodide perovskite light-emitting field-effect transistor.* Nat. Commun., 2015. **6**.
40. A. Kojima, et al., *Organometal Halide Perovskites as Visible-Light Sensitizers for Photovoltaic Cells.* J. Am. Chem. Soc., 2009. **131**(17): p. 6050-6051.
41. National Center for Photovoltaics. *Research Cell Efficiency Records*. 2016 21 April 2016; Available from http://www.nrel.gov/ncpv/images/efficiency_chart.jpg.
42. M. A. Green, A. Ho-Baillie, and H. J. Snaith, *The emergence of perovskite solar cells.* Nat. Photon., 2014. **8**(7): p. 506-514.

43. M. A. Green, *The path to 25% silicon solar cell efficiency: History of silicon cell evolution.* Prog. Photovolt. Res. Appl., 2009. **17**(3): p. 183-189.
44. M. Saba, et al., *Correlated electron-hole plasma in organometal perovskites.* Nat. Commun., 2014. **5**.
45. G. Xing, et al., *Low-Temperature Solution-Processed Wavelength-Tunable Perovskites for Lasing.* Nat. Mater., 2014. **13**(5): p. 476-480.
46. G. Xing, et al., *Long-Range Balanced Electron- and Hole-Transport Lengths in Organic-Inorganic $CH_3NH_3PbI_3$.* Science, 2013. **342**(6156): p. 344-347.
47. H. Tsai, et al., *High-efficiency two-dimensional Ruddlesden–Popper perovskite solar cells.* Nature, 2016. **536**(7616): p. 312-316.
48. G. Li, et al., *Efficient Light-Emitting Diodes Based on Nanocrystalline Perovskite in a Dielectric Polymer Matrix.* Nano Lett., 2015. **15**(4): p. 2640-2644.
49. B. R. Sutherland, et al., *Sensitive, Fast, and Stable Perovskite Photodetectors Exploiting Interface Engineering.* ACS Photonics, 2015. **2**(8): p. 1117-1123.
50. W. K. Chong, et al., *Dominant factors limiting the optical gain in layered two-dimensional halide perovskite thin films.* Phys. Chem. Chem. Phys., 2016. **18**(21): p. 14701-14708.
51. M. Era, T. Ano, and M. Noto, *Electroluminescent Device Using PbBr-Based Layered Perovskite Having Self-Organized Organic-Inorganic Quantum-Well Structure*, in *Studies in Interface Science*, D. Möbius and R. Miller, Editors. 2001, Elsevier. p. 165-173.
52. K. Chondroudis and D. B. Mitzi, *Electroluminescence from an organic−inorganic perovskite Incorporating a quaterthiophene dye within lead halide perovskite layers.* Chem. Mater., 1999. **11**(11): p. 3028-3030.
53. T. Hattori, et al., *Highly efficient electroluminescence from a heterostructure device combined with emissive layered-perovskite and an electron-transporting organic compound.* Chem. Phys. Lett., 1996. **254**(1–2): p. 103-108.

54. E. R. Dohner, et al., *Intrinsic White-Light Emission from Layered Hybrid Perovskites.* J. Am. Chem. Soc., 2014. **136**(38): p. 13154-13157.
55. M. Yuan, et al., *Perovskite energy funnels for efficient light-emitting diodes.* Nat. Nanotechnol., 2016. **11**: p. 872–877.
56. L. Dou, et al., *Solution-processed hybrid perovskite photodetectors with high detectivity.* Nat. Commun., 2014. **5**.
57. C. Liu, et al., *Ultrasensitive solution-processed perovskite hybrid photodetectors.* J. Mater. Chem. C, 2015. **3**(26): p. 6600-6606.
58. Y. Guo, et al., *Air-Stable and Solution-Processable Perovskite Photodetectors for Solar-Blind UV and Visible Light.* J. Phys. Chem. Lett., 2015. **6**(3): p. 535-539.
59. F. Pulizzi, *Spintronics.* Nat. Mater., 2012. **11**(5): p. 367-367.
60. M. Holub and P. Bhattacharya, *Spin-Polarized Light-Emitting Diodes and Lasers.* Journal of Physics D: Applied Physics, 2007. **40**(11): p. R179.
61. S. D. Bader and S. S. P. Parkin, *Spintronics.* Annu. Rev. Condens. Matter Phys., 2010. **1**(1): p. 71-88.
62. G. Kioseoglou and A. Petrou, *Spin Light Emitting Diodes.* J Low Temp Phys, 2012. **169**(5-6): p. 324-337.
63. Y. Zhang, et al., *The First Organic-Inorganic Hybrid Luminescent Multiferroic: (Pyrrolidinium)MnBr3.* Adv. Mater., 2015. **27**(26): p. 3942-3946.
64. A. O. Polyakov, et al., *Coexisting Ferromagnetic and Ferroelectric Order in a CuCl4-based Organic-Inorganic Hybrid.* Chem. Mater., 2012. **24**(1): p. 133-139.
65. H. Jin, J. Im, and A. J. Freeman, *Topological insulator phase in halide perovskite structures.* Phys. Rev. B, 2012. **86**(12): p. 121102.
66. M. Kepenekian, et al., *Rashba and Dresselhaus Effects in Hybrid Organic-Inorganic Perovskites: From Basics to Devices.* ACS Nano, 2015.
67. M. Kim, et al., *Switchable S = 1/2 and J = 1/2 Rashba bands in ferroelectric halide perovskites.* Proc. Natl. Acad. Sci. U.S.A., 2014. **111**(19): p. 6900-6904.
68. A. Stroppa, et al., *Tunable ferroelectric polarization and its interplay with spin-orbit coupling in tin iodide perovskites.* Nat. Commun., 2014. **5**.

69. S. Kena Cohen and S. R. Forrest, *Room-temperature polariton lasing in an organic single-crystal microcavity.* Nat. Photon., 2010. **4**(6): p. 371-375.
70. C. Schneider, et al., *An electrically pumped polariton laser.* Nature, 2013. **497**(7449): p. 348-352.
71. A. Kavokin and G. Malpuech, *Frequently asked questions*, in *Thin Films and Nanostructures*, K. Alexey and M. Guillaume, Editors. 2003, Academic Press. p. 13-26.
72. T. Fujita, et al., *Tunable polariton absorption of distributed feedback microcavities at room temperature.* Phys. Rev. B, 1998. **57**(19): p. 12428-12434.
73. A. Brehier, et al., *Strong exciton-photon coupling in a microcavity containing layered perovskite semiconductors.* Appl. Phys. Lett., 2006. **89**(17): p. 171110.
74. K. Gauthron, et al., *Optical spectroscopy of two-dimensional layered $(C_6H_5C_2H_4\text{-}NH_3)_2\text{-}PbI_4$ perovskite.* Opt. Express, 2010. **18**(6): p. 5912-5919.
75. G. Lanty, et al., *Strong exciton-photon coupling at room temperature in microcavities containing two-dimensional layered perovskite compounds.* New J. Phys., 2008. **10**(6): p. 065007.
76. Y. Wei, et al., *Strong exciton-photon coupling in microcavities containing new fluorophenethylamine based perovskite compounds.* Opt. Express, 2012. **20**(9): p. 10399-10405.
77. G. Lanty, et al., *UV polaritonic emission from a perovskite-based microcavity.* Applied Physics Letters, 2008. **93**(8): p. 081101.
78. H. S. Nguyen, et al., *Quantum confinement of zero-dimensional hybrid organic-inorganic polaritons at room temperature.* Appl. Phys. Lett., 2014. **104**(8): p. 081103.
79. K. Tanaka, et al., *Comparative Study on the Excitons in Lead-Halide-Based Perovskite-Type Crystals $CH_3NH_3PbBr_3$ $CH_3NH_3PbI_3$.* Solid State Commun., 2003. **127**(9–10): p. 619-623.

CHAPTER 2:

EXPERIMENTAL METHODS

In this chapter, the instruments and methodology for the data acquisition in this study are elaborated. Herein, the experimental methods used are primarily the time-resolved ultrafast optical spectroscopy techniques. The detailed mechanism of ultrashort pulsed laser generation is presented. Both the time-resolved and complementary steady-state experimental techniques, together with the background theories behind them, are discussed in detail. Apart from the experimental method, the detailed procedures for preparation of the solution-processed perovskites samples are also presented.

2.1 Laser system

In the last few decades, lasers have become one of the most important tools for various fields in both industry and research. One example of the major applications is the optical spectroscopy. In this subject, lasers have been an essential device for probing phenomena inside material which are only accessible at higher fluence regime (*e.g.* two-photon absorption, *etc.*), which are unachievable by lamps. It also allows spectroscopists to observe/measure ultra-fast dynamics of electrons inside a material up to femtosecond (10^{-15} s) regime, which is unresolved by electronic devices. In this section, we will discuss the importance especially of ultrafast pulsed laser and the technical aspect of its generation, which is used in this study.

2.1.1 Pulsed laser

A pulsed laser is a laser whose output is modulated in pulses. Utilizing the most advanced technology, the temporal duration of a laser pulse can reach as short as < 100 attoseconds (1 as = 10^{-18} s) [1]. In contrast to continuous wave (CW) laser, pulsed laser system holds two major advantages:

1. Pulsed laser can reach much higher (by several orders of magnitude) peak intensity, as compared to its CW counterparts, which grants us access to much more numerous exotic nonlinear phenomena. Pulsed laser comes from the superposition of many modes/frequencies of continuous waves, which then forms a compressed discrete train of pulses - **Figure 2.1**. Therefore, by conservation of energy, at a given output power, pulsed laser will yield higher peak intensity up to the order of TW/cm^2 (10^{15} W/cm^2).
2. Most of the high-resolution time-resolved spectroscopy techniques employ pulsed laser system, with a high temporal resolution determined by the temporal duration of the ultrashort laser pulse. The temporal resolution by ultrashort pulse techniques is much higher than what can be achieved by electronic devices [2].

With such advantages, pulsed laser has become the cornerstone of our modern high-resolution time-resolved optical spectroscopy.

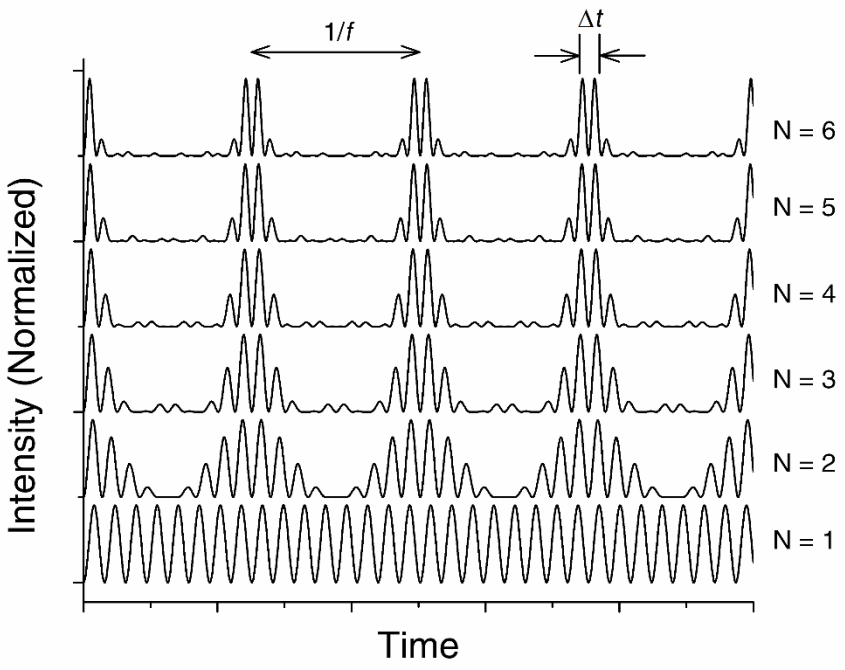

Figure 2.1 | Superposition of many CW modes. The ultrashort pulsed laser comes from the superposition of many CW modes. Here, f is the repetition rate of the pulse laser, while Δt is the pulse duration.

2.1.2 Ultrafast laser spectroscopy system

Bearing such significance, it is essential for ultrafast spectroscopists to understand the general principle of the ultrafast pulsed laser generation. Generally, an ultrafast laser system consists of four main components:

1. *Seed laser*, which generates low power ultrashort pulses.
2. *Pump laser*, which generates high power broad pulses.
3. *Regenerative amplifier*, which received input from both seed and pump lasers to generate high-power ultrashort laser pulses.
4. *Optical parametric amplifier* (OPA), which takes input from the regenerative amplifier and convert it to other wavelengths.

For our system, we use *Coherent© LIBRA*™ which combines the seed laser, pump laser, and regenerative amplifier into one box; and we used *Coherent© OPerA Solo*™ as our OPA - **Figure 2.2**. *LIBRA* outputs 4 mJ pulses with a temporal duration of ~50 fs with a center wavelength of 800 nm and repetition rate of 1 kHz.

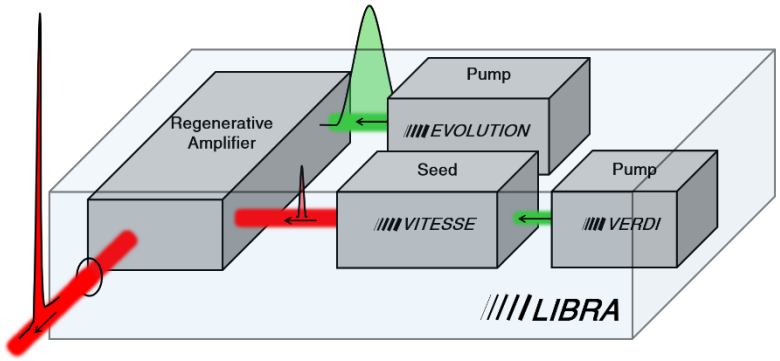

Figure 2.2 | Ultrafast laser system. The *Coherent© LIBRA*™ ultrafast laser system used in this study. The output is ~50 fs 800 nm laser pulses with pulse energy of 4 mJ and repetition rate of 1 kHz.

Seed laser

Seed is a laser which outputs low power ultrashort pulses, which is fed into the regenerative amplifier system. It is also commonly known as an *oscillator*. For this system, there are two main requirements in order to generate ultrashort laser pulses. The first requirement is the superposition of resonant modes inside the laser cavity to build up ultrashort laser pulses – **Figure 2.1**. The second requirement is the fixed phase relation between these resonant modes, called as modelocking. Only when the laser is modelocked, stable ultrashort pulses can be generated with a constant repetition rate.

In our system, the *Coherent© VITESSE*™ is used as the seed laser, which consists of two laser heads. The first head is called as *VERDI*™. *VERDI* is a diode-pumped *Nd-doped Yttrium* laser with *Lithium Triborate* crystal as a second harmonic generator, which gives out green CW output. *VERDI*'s output is then supplied to the next head called as *Coherent© VERDI Pumped UltraFast*™ (*VPUF*), to pump a *Ti:Sapphire* (Ti:S) crystal. The spontaneous emission of this Ti:S crystal will oscillate inside an optical cavity formed by *negative dispersion mirrors*. The optical length of this cavity is perturbed by a vibrating piece of glass to generate various modes of CW, which then start to superpose and form pulses. The intensity of these pulses will build up as they oscillate back and forth inside the cavity, which then after a certain threshold, nonlinear refraction is induced in the Ti:S crystal, *i.e.* the refractive index of the crystal changes as a function of the light intensity (third-order nonlinear

process). This nonlinearity will then induce passive *modelocking* or self-phase modulation to occur, where the phase relationship between each mode is modulated and locked according to their intensity to build shorter pulses. This effect is known as *Kerr lens modelocking*.

The advantage of nonlinear refraction here is twofold. Beside the Kerr lens modelocking, another consequence of this nonlinear refraction is self-focusing (or *Kerr lensing*), where the spatial beam waist/size is tightened or focused by the refraction after passing through the crystal. The tighter beam waist is, the more intense it will be, and hence it will induce more nonlinearity and be focused even tighter. This effect leaves the residual CW component to be left unfocused, which then will be eliminated by a slit – **Figure 2.3**. *VITESSE* outputs 80 MHz pulses, with a central wavelength of 800 nm.

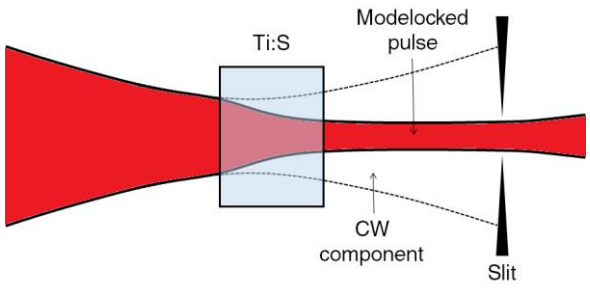

Figure 2.3 | Kerr Lens Modelocking in *VITESSE*. The self-focusing of high-intensity pulsed laser, which can be used to eliminate the residual CW component. This figure is adapted from *Coherent©*.

Pump laser

Pump, which typically is a *Q-switched* laser, is the laser used to pump the gain medium of the regenerative amplifier. Q-switching is the one of technique to generate relatively long pulsed emission (nanosecond pulse). It is done by periodically switching the quality factor (Q-factor) of the optical resonator. In our system, the pump laser used is *Coherent© EVOLUTION-15*, which is a Q-switched pulsed laser that is pumped by diodes and uses *Nd:Yttrium Lithium Fluoride* and *Lithium Triborate* crystal as its gain medium and second harmonic generator, respectively. *EVOLUTION* outputs 527 nm pulsed laser with temporal duration of ~300 ns and repetition rate of 1 kHz.

Regenerative amplifier

Regenerative amplifier is the laser that gains energy from the pump laser, to amplify ultrashort pulses from seed laser. Our regenerative amplifier system uses Ti:S crystal as the gain medium, which is excited by the pump laser - **Figure 2.4**. The working principles of a regenerative amplifier are as follows. In the regenerative amplifier cavity, pulses from seed laser are injected in by the injector. These pulses will build up their intensity as they oscillate inside the cavity and passing through the pumped Ti:S crystal. The result is high-intensity ultrashort laser pulses, which is desired. To prevent optical damage on the Ti:S crystal, stretching of the pulse temporal width is introduced before the seed pulses are injected. This stretching process is done by a grating. After reaching the saturated intensity, the pulses are ejected out from the cavity by the ejector. The ejected pulses are sent into a compressor, which basically is the reverse of the stretcher, to compress the pulse back to their initial temporal width. The final output has a center wavelength of 800 nm and repetition rate of 1 kHz.

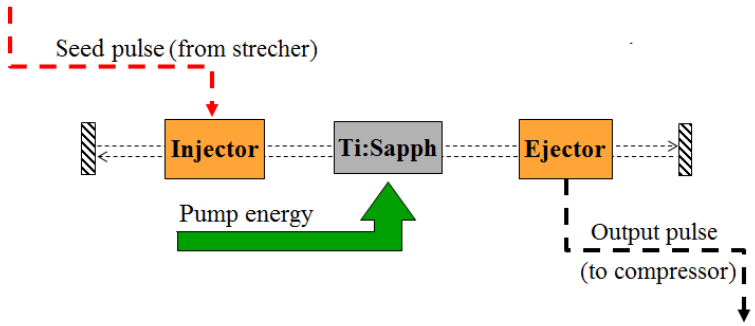

Figure 2.4 | Schematic of the regenerative amplifier. The regenerative amplifier takes energy from the pump laser to amplify the ultrashort pulses from the seed laser. This figure is provided by *Coherent*©.

Optical Parametric Amplifier

Optical parametric amplifier (OPA) is a device which generates laser with variable wavelengths via so-called *parametric amplification* (*i.e.* instantaneous amplification of optical field which does not change the quantum state of the material) by using nonlinear crystal inside the OPA. By changing the incident angle on the nonlinear crystal, different phase matching condition can be achieved and hence different wavelengths can be generated. The basic working

principle of an OPA is by *difference frequency generation* (DFG), which is a second-order nonlinear process, where the frequency of a *pump* photon is converted into two photons with different frequencies, called as *signal* and *idler*. Since it is a parametric process, the energy is conserved ($\hbar\omega_{pump} = \hbar\omega_{signal} + \hbar\omega_{idler}$). This process is an amplification of the signal since the generation rate of the signal is not only proportional to the intensity of the pump, but also on the already present signal. Wavelengths with higher energies than the pump can also be generated by an OPA using *frequency doubling* or *sum frequency generation* (SFG) of the signals. In our system, we use *Coherent© OPerA Solo*™ as our OPA, which takes 800 nm pump input from *LIBRA* and is able to generate output wavelength from 290 nm up to 2600 nm.

2.2 Ultrafast time-resolved optical spectroscopy

Having understood the principles for generation of a pulsed laser, the next crucial step is to understand the ultrafast time-resolved optical spectroscopy techniques, which is used in this study for material characterization. Ultrafast time-resolved spectroscopy can be understood as set spectroscopy techniques which employ ultrashort pulsed laser to study the ultrafast photoexcited dynamics inside a material. Typical temporal resolution of ultrafast techniques lies in the order of hundreds of attoseconds (as) to few nanoseconds (ns). The temporal resolution of such techniques is typically limited by the laser temporal pulse width, which in our case is about ~100 fs.

2.2.1 Transient absorption spectroscopy

Transient absorption (TA) spectroscopy, or also known as *pump-probe* is one of the most powerful techniques in ultrafast optical spectroscopy. This technique allows time-resolved observation with resolution as high as the temporal duration of the laser pulse used. The basic working principle of pump-probe is by splitting one pulsed laser beam into two beams: one beam with much higher intensity called the *pump* whose primary function is to excite the sample, and another beam with much lower intensity called the *probe* whose primary function is to monitor the photoexcited dynamics. The probe beam is then directed into a mechanical delay line, *i.e.* a motorized linear stage system, which

allows manipulation of the probe beam optical path length without changing the output spot position – **Figure 2.5**A. The probe beam is then re-overlapped with the pump beam spatially on the sample before sent for detection – **Figure 2.5**B.

By moving the delay stage, optical path length of the probe beam can be controlled, which consequently allows us to control the time delay between the pump and the probe pulses in reaching the sample. This time delay is equal to the difference in the optical path length of pump and probe beam, divided by the speed of light. The main idea behind this technique is to measure the change in transmission or reflection of the probe beam as a function of the probe pulse at a time delay after the photoexcitation by the pump. Since the changes of probe's transmission/reflection generally indicate the populations of the photoexcited species, hence by varying the time delay between the pump and the probe pulse, the evolution of the transient population of the photoexcited species after 'instantaneous' excitation by ultrashort pump pulse can be mapped in time. The temporal resolution is limited by both movement accuracy of the delay stage and the temporal pulse width of the laser. The delay position when the time delay between the pump and probe pulses equal to zero (*i.e.* both pump and probe pulses overlap spatially and temporally), is called as *time zero*, which is typically marked by the rise of the transient signal.

One basic assumption in pump-probe technique is that the perturbation by probe pulse on the sample should be insignificant as compared to perturbation by the pump pulse. For this reason, the pump intensity is to be set much higher than the probe intensity (at least 10× as a rule of thumb). Another important technical aspect is the detection sensitivity of the pump-induced change of probe transmission/reflection. This change can be as low as only 0.1% of the total probe intensity, which might be smaller than the power fluctuation of the laser. One common procedure used to tackle this issue is by mechanically chopping the pump beam at a fixed frequency together with probe detection coupled with a *lock-in amplifier*, referenced to the chopping frequency. This lock-in detection system allows us to detect only the signal appearing at the predetermined chopping frequency, hence allocating the detection sensitivity only to the pump-induced signal. In our system, a *pre-amplifier* system is introduced to help to filter out unwanted frequencies and to amplify the signal. Chopping frequency

of a prime number 83 Hz is used to prevent any measurement of artifact from any frequency harmonics.

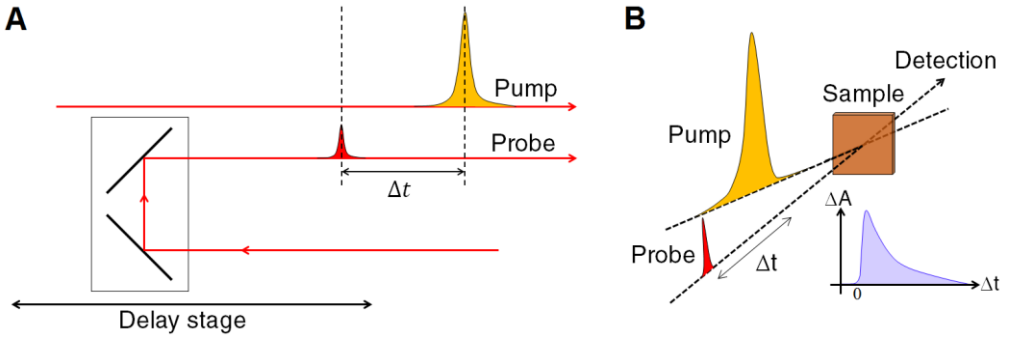

Figure 2.5 | The working principle of pump-probe. (A) By moving the delay stage, the time delay between the pump pulse and the probe pulse can be controlled. (B) Both pump and probe beam are spatially overlapped on the sample. In transmission geometry, by detecting the change of the probe transmission as a function of time delay between the pump and probe, the time-resolved information of the photoexcited species can be obtained.

The typical quantity measured directly by TA technique is the change of probe transmission due to pump pulse, normalized by the total of transmitted probe intensity (*i.e.* $\Delta T/T$). It is related to the pump-induced changed of the material absorption (ΔA, in OD) by the following derivation:

$$T + \Delta T = 10^{-(A+\Delta A)}$$

$$\frac{T + \Delta T}{T} = \frac{10^{-(A+\Delta A)}}{10^{-A}}$$

$$1 + \frac{\Delta T}{T} = 10^{-\Delta A}$$

$$\frac{\Delta T}{T} = 10^{-\Delta A} - 1, \tag{2.1}$$

$$\Delta A = \log\left(1 + \frac{\Delta T}{T}\right). \tag{2.2}$$

Here the transmissivity of the sample is taken as $T = 10^{-A}$. There are several elaborations of the pump-probe technique which are used in this study, which gather different information from the characterized system. These techniques are described here.

Degenerate transient absorption spectroscopy

As suggested by the name, degenerate TA/pump-probe means pump-probe spectroscopy with same pump and probe wavelength/photon energy. This technique is used when we are not interested in the transient spectral information of the material. For our system, it is done by directly splitting the beam output from the OPA using a beam splitter into two: as the pump and the probe. The advantage of using the degenerate pump-probe setup, when combined with a balanced photodetector and two-pairs of pre-amplifier plus lock-in combinations, is its ability to obtain information from two different probe polarization simultaneously. This is important especially for our case of spin relaxation measurement, where each circular polarization of the probe (left circular or right circular) can monitor different spin-state populations (up or down). In contrast to consecutive measurement for each polarization, the benefit of the simultaneous collection of each probe polarization is to eliminate the overtime intensity imbalance of each probe polarization, which might come from laser instability or sample photo-degradation. Hence, it results in a more accurate comparison for dynamics of each probe polarization.

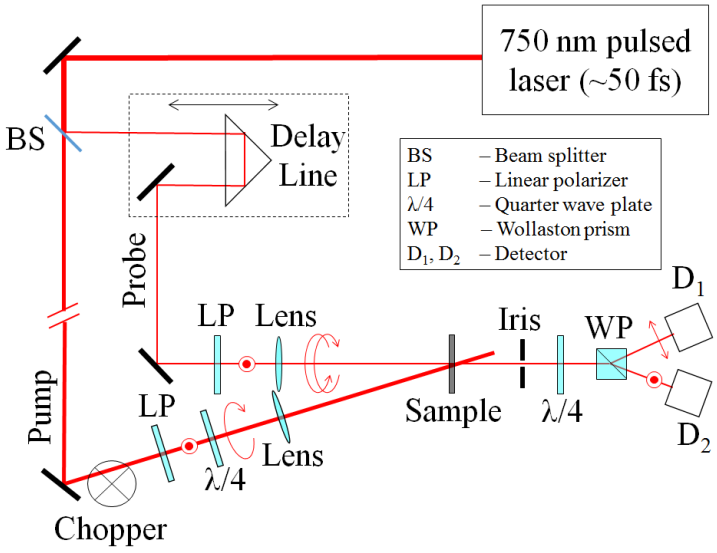

Figure 2.6 | Degenerate transient-absorption setup. Here, BS is beam splitter, LP is linear polarizer and WP is Wollaston prism. By using a quarter wave-plates and Wollaston prism, the left circular and right circular component from linearly polarized probe can be deconvolved and detected by the two probes of balanced photodetector.

The probe used here is linearly polarized photons, which are an equal superposition of left and right circularly polarized photons. Quarter wave-plate ($\lambda/4$) set at 45° from the initial polarization will convert each circular component to either *s*-polarized or *p*-polarized light, which then separated by the Wollaston prism and detected by the balanced photodetector. This conversion can be easily described in *Jones vector* notation (see Appendix A). The experimental setup for our degenerate transient absorption spectroscopy system is illustrated in **Figure 2.6**.

Time-resolved Faraday rotation (TRFR) spectroscopy

Faraday rotation (FR) is the rotation of the light plane of polarization after passing through a medium. It can be induced by external applied magnetic field (static) or by photoexcitation, which creates asymmetric changes of the absorbance of the left (σ^+) and the right (σ^-) circularly polarized component of light in the medium. Since absorption and refractive index of a material are tied together by *Kramers-Kronig relation*, this change of absorbance will also yield to the change of refractive index. Therefore, asymmetric changes in absorbance of σ^+ and σ^- light will create asymmetric changes in refractive index, resulting in a difference in optical path length between them, and hence shifts their relative phase. The end product is the rotation of the resultant plane of polarization of light after passing through the material. The magnitude rotation angle of FR is known to be proportional to the magnetization of the material.

Depending on the origin, the spectral behavior of FR can be very different. **Figure 2.7** shows the spectral behavior of FR originating from photoexcitation and magnetic field. For the case of photoinduced FR, spin-selective pump excitation creates an imbalanced population of spin-up and spin-down, hence resulting imbalanced magnitude of changes of the σ^+ and σ^- probe absorption. This results in an asymmetric behavior of the FR with respect to the absorption peak. Conversely, for the case of the magnetic field induced FR, the field causes opposite symmetric Zeeman shift for the σ^+ and σ^- absorption. This results in the symmetric behavior of the FR with respect to the absorption peak.

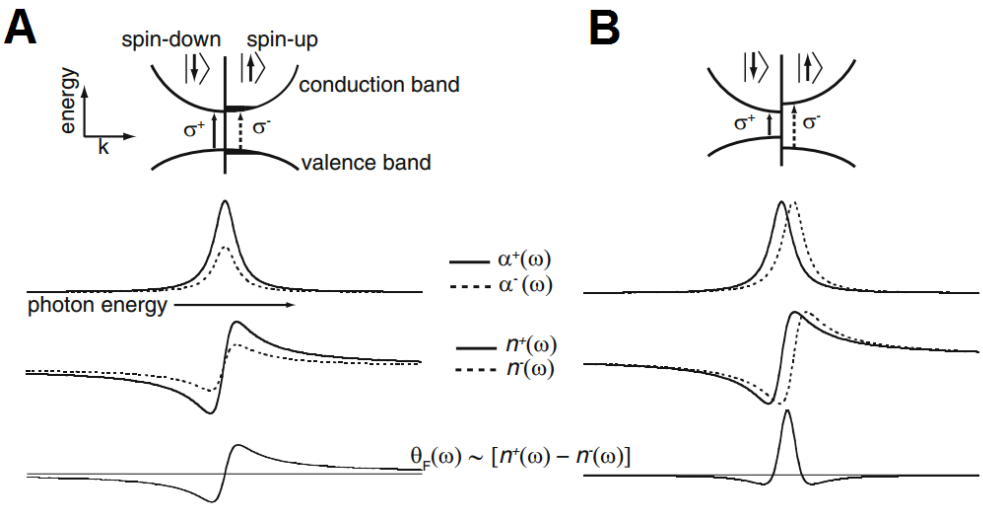

Figure 2.7 | Origin of Faraday rotation. Illustration of (A) photoinduced and (B) magnetic field induced asymmetric changes of absorbance, which by Kramers-Kronig relation, they result in asymmetric changes of refractive index. This results in the rotation of the polarization plane. The spectral behaviors of Faraday rotation with different origins are shown. This figure is adapted from ref. [3].

Study of FR in this thesis is focused on photoinduced FR in lead halide perovskites (**Figure 2.8**A). The experimental setup used in the study is by degenerate TA setup, which uses balanced photodetector for the detection of Faraday rotation. The difference between this setup and the degenerate TA setup in **Figure 2.6** is the use of half-wave plate (λ/2) to replace λ/4 before the Wollaston prism (**Figure 2.8**B). Here, the λ/2 does not alter the component amplitude circular σ^+ and σ^- polarization, but only their phases. It hence results only in angle offset of the main probe polarization plane. This angle offset is used to initially balance the *s*- and *p*-polarized component (*i.e.* $I_s^{\text{off}} = I_p^{\text{off}}$, when there is no pump). These two orthogonal polarizations will then be separated by the Wollaston prism and detected by the balanced detector. In the presence of pump-induced FR, projection length of the *s*- and *p*-components will change, which therefore disturb the initial balance (*i.e.* $I_s^{\text{on}} \neq I_p^{\text{on}}$). Under such case, the photoinduced FR angle θ_F of the probe is given by:

$$\theta_F = \frac{I_p^{\text{on}} - I_s^{\text{on}}}{2(I_p^{\text{off}} + I_s^{\text{off}})} = \frac{\Delta I}{2I_0} \tag{2.3}$$

where $I_0/2 = I_p^{\text{off}} = I_s^{\text{off}}$ and $\Delta I = I_p^{\text{on}} - I_s^{\text{on}}$. The detailed derivation of this equation can be seen in Appendix A.

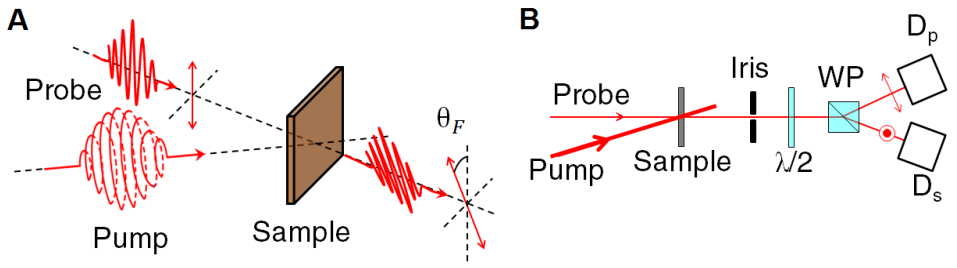

Figure 2.8 | Photoinduced Faraday rotation. (A) Illustration of circular-polarized pump-induced Faraday rotation and (B) detection setup of the Faraday rotation.

TRFR technique can be performed with and without an external magnetic field to probe different magnetization dynamics in the material. For the case with external magnetic field, two typical experimental geometries: Faraday (magnetic field perpendicular to the sample plane), and Voigt (magnetic field in plane with sample plane) geometry, are used to measure *longitudinal spin relaxation time* (T_1) and *spin precession relaxation time* or *spin dephasing time* (T_2), respectively [4]. These two relaxation time are defined in the framework of Bloch-Torrey equations:

$$\frac{\partial M_x}{\partial t} = \gamma\left(\vec{M} \times \vec{B}\right)_x - \frac{M_x}{T_2} + D\nabla^2 M_x \tag{2.4}$$

$$\frac{\partial M_y}{\partial t} = \gamma\left(\vec{M} \times \vec{B}\right)_y - \frac{M_y}{T_2} + D\nabla^2 M_y \tag{2.5}$$

$$\frac{\partial M_z}{\partial t} = \gamma\left(\vec{M} \times \vec{B}\right)_z - \frac{M_z - M_z^0}{T_1} + D\nabla^2 M_z. \tag{2.6}$$

Here, z-axis is defined in the direction of the external magnetic field $\vec{B}$; $\gamma = g\mu_B/\hbar$ is the gyromagnetic ratio with g is the g-factor and μ_B is the Bohr magneton; $\vec{M}$ is the sample magnetization with initial magnetization in z-direction M_z^0; and D is the diffusion coefficient. In this framework, T_1 describes the spin relaxation in the direction of external magnetic field, and T_2 describes the dephasing of spin precession projected into x-y plane.

For our case, we performed TRFR without external magnetic field, *i.e.* $\vec{B} = 0$, $M_z^0 = 0$. The *z*-axis is therefore defined by our excitation pump beam direction, without any spin-precession. Neglecting the effect of diffusion (happens in much longer timescale), the equation can be simplified into:

$$\frac{\partial M_z}{\partial t} = -\frac{M_z}{T_1}. \tag{2.7}$$

Here, M_z is the photoinduced magnetization by our pump beam, and T_1 is the measured spin lifetime by our TRFR system.

White light transient absorption (WLTA) spectroscopy

As implied by its name, white light TA (WLTA) simply means a TA spectroscopy which is performed with white light as the probe. In contrast to degenerate TA, such technique allows simultaneous monitoring of different energy states in the material with pump wavelength as the control variable. Ability to monitor multiple different energy states at similar pump excitation wavelength might help us to reveal many photoexcited dynamics undetected by degenerate TA (*e.g.* energy/charge transfer states, *etc.*).

The WLTA experimental setup in our laboratory is shown in **Figure 2.9**. Beam output from our main laser system (800 nm) is split into two. One beam is directed to the OPA for wavelength conversion, which will then act as the pump. Meanwhile, another beam (800 nm) is directed to the delay stage, before being focused into a *Sapphire* crystal to generate pulsed *white light continuum*, which will then act as the probe. White light continuum generation on the Sapphire crystal is a third order nonlinear process, which is often attributed to either *self-phase modulation* or *four-wave mixing* process [5-7]. In our system, the continuum spans from 450 nm to 1100 nm. Another important technical issue in this technique is to filter out the 800 nm residual component from the white light probe. This residual component might still be strong enough to act as a secondary pump, either via direct excitation or multi-photon excitation. In fact, some novel phenomena reported in the literature have been suspected to be artifacts from this strong 800 nm residual component [8]. In our case, since we

are interested in probing in the visible region, a 750 nm short pass is added to the sapphire crystal to block out the 800 nm residual.

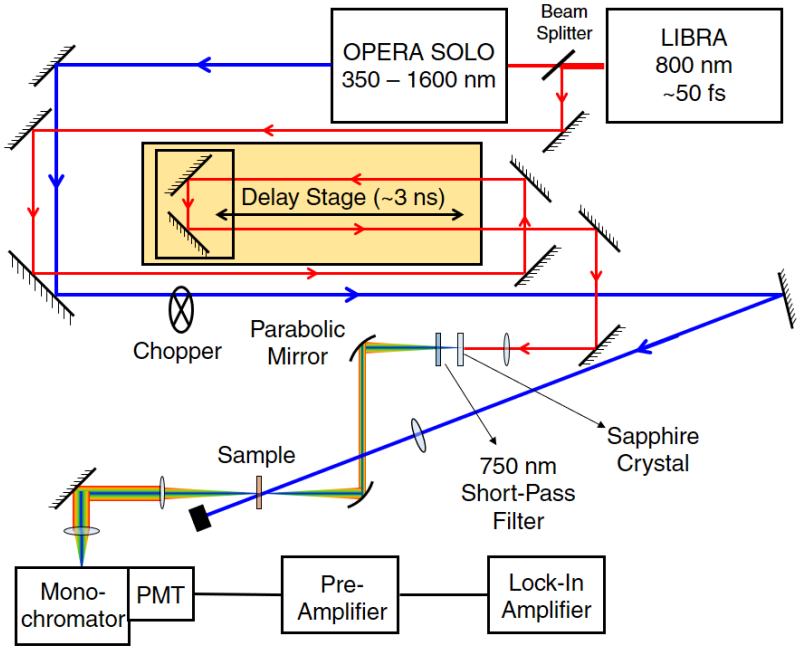

Figure 2.9 | WLTA experimental setup. The probe beam is focused into a Sapphire crystal to generate white light probe. 750 nm short-pass filter is introduced to eliminate the 800 nm residual. The transmitted white light probe from the sample is directed into a monochromator and photomultiplier tube (PMT) system, coupled with pre-amplifier and lock-in amplifier for signal detection.

After the short pass filter, the white light probe is re-collimated and re-focused on the sample by using a pair of parabolic mirrors. Here, a parabolic mirror instead of a lens is used to minimize chirping of the white light pulse. White light chirping occurs due to the intrinsic dispersion of transmissive medium (*i.e.* different refractive index for different wavelength). When the white light travels through a dispersive medium, different refractive index causes one wavelength component to travel slower than the other, which results in different optical path length for different wavelength. White light chirping is an important issue, especially for the interpretation of the early photoexcited dynamics of the system. Failure to include chirp correction might lead to a wrong interpretation of the experimental data.

Chirp correction can be performed pre- or post-experiment. In our system, the chirp correction is performed pre-experimentally by a custom *LABVIEW*

program based on pre-measured white light chirping. To compensate the temporal chirp, motorized delay stage is programmed to perform delay correction for different probe wavelength. The chirp correction can be obtained by measurement of the time zero position for different probe wavelengths on a sample with a broadband transient signal. Generally, the relation between time zero correction as a function of probe wavelength can be approximated by first order *Cauchy relation* of refractive index:

$$\Delta t = C\left[\frac{1}{\lambda} - \frac{1}{\lambda_0}\right]. \tag{2.8}$$

Here, Δt is the time delay correction, C is the coefficient of proportionality and λ_0 is the reference wavelength. The delay time correction typically can range up to few ps. After the sample, the white light probe is then re-collimated by a lens before directed into a *monochromator* to resolve the spectral information. Here, a *photomultiplier tube* (PMT) coupled with a pre-amplifier and lock-in amplifier are used for signal detection. For a particular energy state measurement, the monochromator can be set to output the desired wavelength and to be directed into the PMT.

2.2.2 Time-resolved photoluminescence (TRPL) spectroscopy

Apart from pump-probe technique, another time-resolved spectroscopy technique used in this study is the time-resolved photoluminescence (TRPL). As suggested by its name, this technique is used to acquire the temporal evolution of the luminescence from a material system. In our case, this time-resolved information of the luminescence is extracted by using a *streak camera*. The basic principle behind the streak camera is to rapidly spatially deflect the spot created by incoming photons (*e.g.* from PL). Photons that come at a different time will create different spot positions on the 2D detector. The image forms out of these moving spots will then reflect the temporal evolution of the luminescence, which is known as *streak image*.

In our system, the incoming photons are spectrally resolved by a monochromator, before converted into electrons by using a photocathode. The intensity of the electrons generated by the incoming light is assumed to be linear

to the light intensity. The photogenerated electrons are then accelerated towards a two-dimensional CCD camera as the detector. During the travel, the electrons are deflected by a rapidly varying electric field in the direction perpendicular to the path. The resultant image on the 2D CCD camera is spectrally resolved on one axis and temporally resolved on another. Typically, streak camera needs to be triggered by the pulsed light source, which in our case with the laser system. Temporal resolution up to 6 ps can be achieved by our system. Here, we used *Princeton Instrument* monochromator and *Optronis* SC-10 streak camera.

2.3 Steady-state optical spectroscopy

Steady-state optical spectroscopy is measurement without being concerned about the temporal information of the system response to our perturbations. The data collected in steady-state measurement is the average response over a period of time. Several techniques which are used in this study are elaborated here.

2.3.1 Linear absorption spectroscopy

As implied by its name, this spectroscopy technique is used to acquire the linear absorption spectrum of a material system. Linear absorption spectrum contains invaluable information regarding the optically active energy states inside the system. It sometimes might also reflect the optical coupling strength of the states and the nature of the excited species (*i.e.* excitons or free carriers). The basic principle behind linear absorption spectroscopy is straightforward. White light from a lamp source is collimated and split into two beams: one for the measurement and another for the reference. The sample is then placed in the optical path of the measurement beam. These two beams are then sent to detectors for simultaneous measurement. By simultaneously analyzing the spectrum of the transmitted beam in comparison to the reference, the linear absorption spectrum of the sample can be obtained. Any artifacts arising from intensity fluctuation of the light source has been eliminated by live-normalization with respect to the reference. Typically, prior to sample measurement, similar measurement on the substrate was also performed, to take substrate absorbance into account. It is commonly known as *baseline correction* process.

In our case, the absorption of various thin film samples is measured using the Shimadzu UV-3600 UV-Vis-NIR spectrophotometer (*i.e.* UV = ultraviolet, Vis = visible, and NIR = near infrared). It uses 3 types of detectors: PMT detector for the UV and visible regions, and both InGaAs and PbS detectors for the NIR region. One common assumption in this measurement is negligible scattering and back reflections from the sample. Apart from absorption, such processes might reduce the intensity of the transmitted light, and hence create artifacts of strong absorption. While the assumption is valid for smooth transparent thin film samples (our case), it might not be applicable for rough and reflecting samples. Such issue can be eliminated by incorporating an integrating sphere.

2.3.2 Steady-state photoluminescence spectroscopy

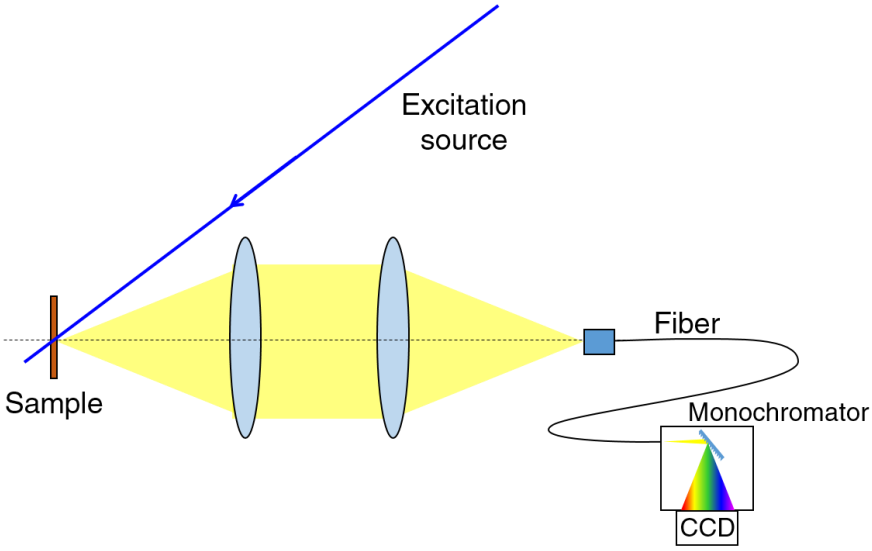

Figure 2.10 | Steady-state PL experimental setup. The emission from the sample is collected into an optical fiber by using two lenses before directed into a monochromator coupled with CCD camera for detection.

Apart from linear absorption spectroscopy, another basic spectroscopy technique is steady-state photoluminescence spectroscopy. This technique is used to study the emission spectrum of the material due to photoexcitation by a light source. In our system, the time-averaged emission from the photoexcited material is collected into an optical fiber by using two positive lenses. The fiber

then directs the collected light into a monochromator to be spectrally deconvolved, before detection by 2D CCD camera. The experimental setup is shown in **Figure 2.10**. In our system, we used Princeton Instrument monochromator and *PIXIS*: 100 (1340 × 100) CCD camera.

2.3.3 X-ray diffraction (XRD)

X-ray diffraction (XRD) is an analytical technique for the identification of the crystalline structure of a solid material, to obtain the information regarding the unit cell dimensions and crystallinity. It is based on the principle of Bragg diffraction of the x-ray, crystal planes in the material provide interference of the diffracted x-ray. The collimated x-ray beam is illuminated on the material at an angle, while the detector is scanned through the polar angle (2θ). Maximum intensity will be obtained at special θ positions where the interference is constructive. This technique is illustrated in **Figure 2.11**.

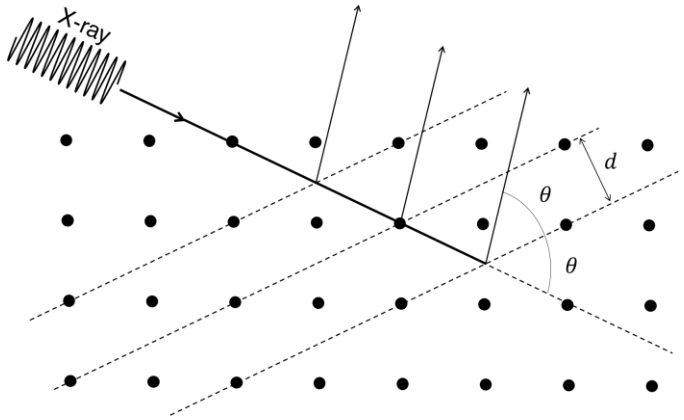

Figure 2.11 | XRD working principle. Based on the interference of the diffracted x-ray at a particular angle 2θ, the inter-plane distance in the crystal can be deduced.

Given the angle of 2θ between the incident beam and the detector position, constructive interference will occur when the X-ray diffracted by crystal planes fulfills the following relation:

$$2d \sin\theta = m\lambda. \tag{2.9}$$

Here, m = 1, 2, 3… is an integer number, λ is the x-ray wavelength, and d is the inter-plane distance in the crystal. For our case, we used *Bruker D8 Advance*

system to performed XRD characterization of our samples, with x-ray source of Cu Kα radiation source (λ = 1.54180 Å). In the case of thin film samples (thickness of ~100 nm), stronger XRD signal from much thicker substrate might engulf the sample's signal. Hence, a modified technique is required. The incident x-ray beam is fixed at a grazing angle (at 2°-5°) to avoid the intense signal from the substrate. This technique is also known as *Grazing Incidence X-ray Diffraction* (GIXRD).

2.4 Miscellaneous measurement techniques

Some supplementary measurements are also required to provide necessary information the data interpretation. The theory and some technical aspect behind these supplementary techniques are presented to help the reader comprehend or reproduce the results of this study.

2.4.1 Spot-size measurement

We approximate the spatial profile of the pulsed laser used in this study to be a Gaussian beam in TEM_{00} mode. The spatial and temporal intensity profile of TEM_{00} Gaussian beam after being focused by a convex lens is shown in **Figure 2.12** and can be expressed by the following equations:

$$I(r,z,t) = I_0 e^{-t^2/\tau^2} \left(\frac{w_0}{w(z)}\right)^2 e^{-2r^2/w^2(z)} \tag{2.10}$$

$$w(z) = w_0 \sqrt{1 + \frac{z^2}{z_0^2}} \tag{2.11}$$

$$z_0 = \frac{\pi w_0^2}{\lambda} \tag{2.12}$$

Here, I is the light intensity in cylindrical coordinate at time t, radius r and position z. The coordinate z is the optical axis of the beam; w_0 is the tightest beam waist which located at position at $z = 0$; $w(z)$ is the beam waist at z; z_0 is the Rayleigh length (depth of focus); λ is the laser wavelength; and τ is the characteristic pulse width of the laser [Full Width Half Maximum (FWHM) = $2\sqrt{\ln 2}\,\tau \approx 1.67\tau$].

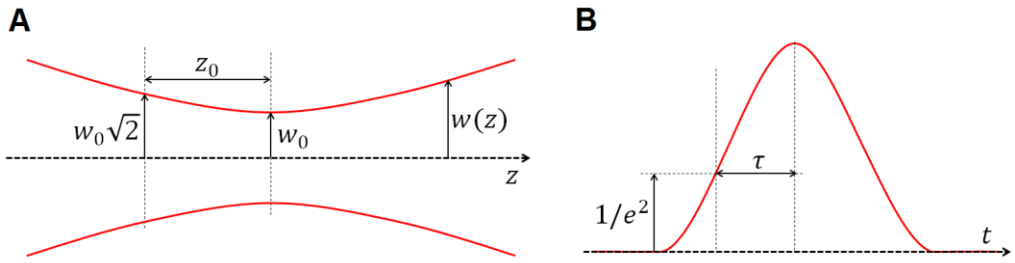

Figure 2.12 | TEM$_{00}$ Gaussian beam profile. (A) Spatial profile of the TEM$_{00}$ mode around the focal point, and (B) temporal profile of the Gaussian pulse.

The energy of a laser pulse E_p contained within radius of R, is given by the integration of the intensity [eq. (2.10)] with respect to the time t and its radius coordinate r:

$$E_p(R) = I_0 \left(\frac{w_0}{w(z)}\right)^2 \int_{-\infty}^{\infty} e^{-t^2/\tau^2} dt \int_0^R 2\pi r e^{-2r^2/w^2(z)} dr \qquad (2.13)$$

$$E_p(R) = \frac{\pi^{3/2}}{2} \tau I_0 w_0^2 \left(1 - \exp\left\{-\frac{2R^2}{w^2(z)}\right\}\right). \qquad (2.14)$$

Herein, we define the beam radius to be $w(z)$, which contains ~87% of the total energy of the beam within the radius. This pulse energy is related to the measured power P by:

$$P = E_p f. \qquad (2.15)$$

Here, f is the repetition rate of the laser system. Since the laser power can be measured straight-forwardly using a power meter, the spot size of the beam can be determined by measuring the laser power after passing a circular pinhole with a well-defined diameter. Given the pinhole diameter to be $2R$, the laser power measured after passing through the pinhole is given by:

$$P = P_0 \left(1 - \exp\left\{-\frac{2R^2}{w^2(z)}\right\}\right), \qquad (2.16)$$

where $P_0 = \tau I_0 w_0^2 f \pi^{3/2}/2$ is the power measurement before the pinhole. The beam diameter d is therefore given by:

$$d = 2w(z) = 2R\sqrt{\frac{-2}{\ln(1 - P/P_0)}}. \quad (2.17)$$

For TA experiment, the typical spot sizes (diameter) for the pump used in this study ranged from ~250 μm to ~1 mm. Meanwhile, the probe spot sizes are kept to be equal or smaller than the pump spot size.

2.4.1 Pump fluence calculation

Typically, in an ultrafast experiment with femtosecond pulsed laser excitation, one is less interested in the peak intensity of the excitation beam, but in the so-called *fluence* of the beam. Fluence is defined as the energy of the pulse per unit area, with a typical unit of μJ/cm^2. In this study, we standardized the fluence (F) calculation by the following equation:

$$F = \frac{1}{f}\frac{P}{\pi w_0^2}. \quad (2.18)$$

Here, f is the laser repetition rate; P is the average laser power obtained by standard power meter; and w_0 is the beam waist obtained from the pinhole measurement.

2.4.2 Sample thickness measurement

For the thin film thickness measurement, we used *Alpha step IQ surface profiler* using a step height analysis. By scanning through the height of the sample on a blank (only substrate) and filled (with sample) area, our sample thickness can be straightforwardly estimated, after a baseline correction. Our typical sample thickness ranged from ~50 nm to ~150 nm.

2.5 Fabrication of OIHP thin films

One of the major advantages of lead halide OIHP over other material systems is its solution processability, which allows for cheaper fabrication, chemical flexibility and versatile material processing for integration with any substrate, without compromising too much on the electronics/optical properties. In this study, the main sample fabrication technique used is by spin-coating the precursor solution onto a desirable substrate (Figure 2.13), which is followed by annealing on a hot plate. The precursor materials and their respective stoichiometric ratio are listed in the table below. All materials are dissolved by using $(CH_3)_2NC(O)H$ (*i.e.* Dimethylformamide, or DMF) as the solvent.

Table 2.1 | List of solution-processed lead-based OIHP with its precursor. All the samples listed here are used in this study together with their stoichiometric molar ratio.

Material	Precursor	Molar Ratio
$CH_3NH_3PbI_3$	PbI_2	1
	CH_3NH_3I	1
$CH_3NH_3PbBr_3$	$PbBr_2$	1
	CH_3NH_3Br	1
$(NH_2CHNH_2)PbI_3$	PbI_2	1
	NH_2CHNH_2I	1
$(C_6H_5C_2H_4NH_3)_2PbI_4$	PbI_2	2
	$C_6H_5C_2H_4NH_3I$	1
$(C_6H_5C_2H_4NH_3)_2PbBr_4$	$PbBr_2$	2
	$C_6H_5C_2H_4NH_3Br$	1
$(C_6H_5FC_2H_4NH_3)_2PbI_4$	PbI_2	2
	$C_6H_4FC_2H_4NH_3I$	1
$(C_6H_5FC_2H_4NH_3)_2(CH_3NH_3)Pb_2I_7$	$C_6H_4FC_2H_4NH_3I$	2
	PbI_2	2
	CH_3NH_3I	1
$(C_6H_5FC_2H_4NH_3)_2(CH_3NH_3)_2Pb_3I_{10}$	$C_6H_4FC_2H_4NH_3I$	2
	PbI_2	3
	CH_3NH_3I	2

$(C_6H_5FC_2H_4NH_3)_2(CH_3NH_3)_3Pb_4I_{13}$	$C_6H_4FC_2H_4NH_3I$	2
	PbI_2	4
	CH_3NH_3I	3

2.5.1 Standard spin-coating technique.

The standard technique used to fabricate our thin film samples is spin-coating. Substrates used for the thin film spin-coating in this study are mainly quartz substrates, which is cut into 0.5-inch × 0.5-inch dimension. The substrates are first treated by using air plasma under medium setting for 2 minutes, for both cleaning and improving the wettability of the substrate surface. The precursor materials in powder form are therefore weighed, mixed and dissolved into DMF solvent according to the stoichiometry ratio with desired weight percent (wt%), i.e. total mass of precursor per total mass of solvent and precursor. The common wt% of the precursor solutions used in this study are typically 10wt%, 12.5wt% or 40wt%. Different wt% precursor solutions used will result in different film thickness.

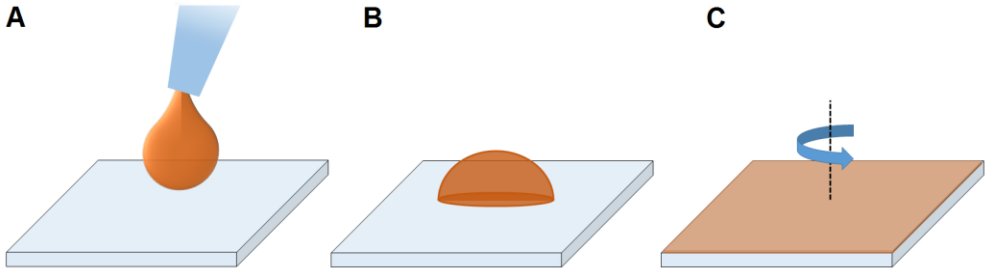

Figure 2.13 | Spin-coating technique. The spin-coating technique involves (A) dropping the precursor solution into the treated substrate, (B) wetting the substrate with the solution and (C) spinning the substrate with the predetermined rotation speed and duration to form a uniform film.

The precursor solution is dropped and spread on the substrate, before being spun with a standardized parameter of 4000 rpm for 30 s or otherwise stated. These spin-coated thin films are then annealed on a hot plate set at 100ºC for 30 minutes to evaporate the remaining solvent and to help the sample crystallization. Note that all of the spin-coating and annealing processes for this study are performed under dry N_2 environment inside a glovebox.

2.5.2 Toluene treatment

A variation of the standard spin-coating technique is to introduce toluene treatment on the thin film. In this case, ~80 μL of toluene is dropped 3 seconds after the perovskites spin-coating started. The rest of sample processing is similar to the standard sample. It has been reported that such treatment will modify the film morphology, where it creates a better film coverage but with smaller grains [8-10].

2.5.3 Hot-casting technique

Another variation of the standard spin-coating technique is the hot-casting technique. In this case, the substrate is pre-heated prior to the spin coating of the sample precursor. It has been reported that such technique results in better morphology and crystallinity of the thin film [11]. For our case, the substrate is pre-heated up to 150°C, before the precursor solution is spin-coated. After the spin-coating, the sample is again annealed at 150°C for 30 s.

2.6 Bibliography

1. Corkum, P., *Laser physics: Attosecond pulses at last.* Nature, 2000. **403**(6772): p. 845-846.
2. Trebino, R., *Frequency-resolved optical gating: the measurement of ultrashort laser pulses*. 2012: Springer Science & Business Media.
3. Crooker, S.A., *Coherent Spin Dynamics of Carriers and Magnetic Ions in Diluted Magnetic Semiconductors*, in *Introduction to the Physics of Dilute Magnetic Semiconductor*, J. Kossut; and J.A. Gaj;, Editors. 2010, Springer. p. 305-334.
4. Žutić, I., J. Fabian, and S. Das Sarma, *Spintronics: Fundamentals and Applications.* Review of Modern Physics, 2004. **76**(2): p. 323-410.
5. Nagura, C., et al., *Generation and characterization of ultrafast white-light continuum in condensed media.* Applied Optics, 2002. **41**(18): p. 3735-3742.

6. Brodeur, A. and S.L. Chin, *Ultrafast white-light continuum generation and self-focusing in transparent condensed media*. Journal of the Optical Society of America B, 1999. **16**(4): p. 637-650.
7. Alfano, R.R. and S.L. Shapiro, *Emission in the Region 4000 to 7000 \AA{} Via Four-Photon Coupling in Glass.* Physical Review Letters, 1970. **24**(11): p. 584-587.
8. Sum, T.C., et al., *Spectral Features and Charge Dynamics of Lead Halide Perovskites: Origins and Interpretations.* Accounts of Chemical Research, 2016. **49**(2): p. 294-302.
9. Jeon, N.J., et al., *Solvent engineering for high-performance inorganic-organic hybrid perovskite solar cells.* Nature Materials, 2014. **13**(9): p. 897-903.
10. Lim, S.S., et al., *Modulating carrier dynamics through perovskite film engineering.* Physical Chemistry Chemical Physics, 2016.
11. Tsai, H., et al., *High-efficiency two-dimensional Ruddlesden–Popper perovskite solar cells.* Nature, 2016. **536**(7616): p. 312-316.

CHAPTER 3:

OPTICAL-SPIN DYNAMICS IN 3D ORGANIC-INORGANIC HYBRID LEAD HALIDE PEROVSKITES

This chapter presents the results of optical studies directed to uncover the fundamental understanding of the ultrafast transient spin photophysics in 3D lead halide perovskites. Here, $CH_3NH_3PbI_3$ was used as the representative of 3D perovskite material system. The first half of this chapter focused on elucidating the origin of transient spectral features and the relaxation dynamics of photoexcited carriers in $CH_3NH_3PbI_3$. The second half of this chapter focused on modeling the dynamics of the photoexcited spin-polarized carriers in $CH_3NH_3PbI_3$. This spin-polarization decays in sub-10 ps timescale via Elliot-Yafet mechanism. Meanwhile, ultra-large photoinduced Faraday rotation up to 10°/μm was observed in $CH_3NH_3PbI_3$. It was also discovered that Pb cation is the main source of the spin-orbit coupling, which then leads to a fast spin relaxation in 3D lead halide perovskites.

3.1 Linear properties

Recently, the 3D lead halide perovskite system has emerged to be the central focus of research due to its excellent optoelectronics properties. While it has not yet reached commercialization, plenty of solution-processed high-performance 3D perovskite-based optoelectronic devices have been proposed and demonstrated in the laboratory level. Examples include solar cells [1-5], LEDs [6-8], photodetectors [9-13], *etc*. In this section, characterizations of the structural and linear optical properties of 3D perovskite thin films are presented and discussed. While they are not the central focus of the study, these linear properties have important implications for the transient dynamics. Herein, this study will be mainly focused on the representative 3D $CH_3NH_3PbI_3$ (hereafter noted as MAPI) low-temperature solution-processed perovskite thin films.

3.1.1 Structural properties

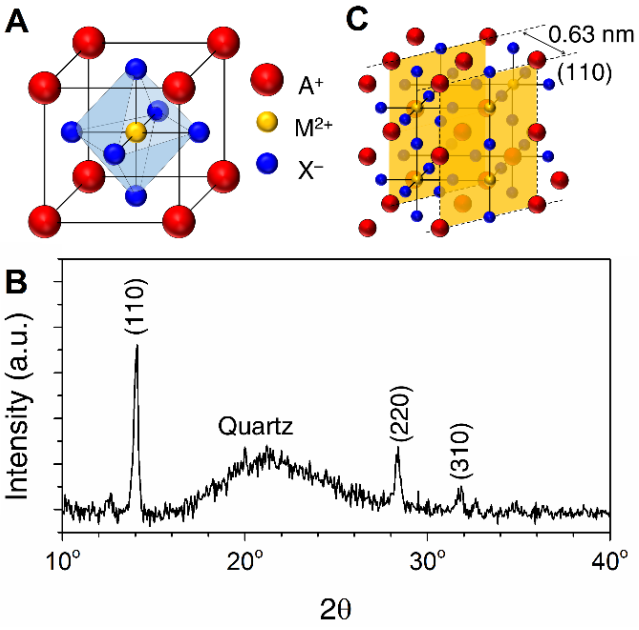

Figure 3.1 | Structure and XRD spectrum of MAPI. (A) Generic 3D perovskites structure. (B) XRD spectrum of our solution processed spin-coated MAPI thin film on amorphous quartz. (C) Crystal cutting of MAPI at (110) planes, with an inter-plane spacing of 0.63 nm.

Structurally, 3D perovskites refer to cubic structures with the generic formula of AMX_3. The A^+ cations reside on the 8 corners of the cube, M^{2+} metal

cation at the center of the cube and X^- anions at the 6 faces of the cube. This structure is illustrated in **Figure 3.1**A. For our case of 3D lead halide OIHP, the A^+ cation corresponds to the organic component $CH_3NH_3^+$, the metal cation of Pb^{2+} and the halide anion I^-. There are 2 known structural phase transitions in MAPI: from orthorhombic to tetragonal at 161 K and from tetragonal to cubic phase at 330 K [14]. The XRD spectrum of our spin-coated MAPI thin film at room temperature (tetragonal) is shown in **Figure 3.1**B. There are 3 apparent sharp peaks at 2θ of 14.1°, 28.4° and 31.8°, which corresponds to (110), (220) and (310) peaks, respectively, which is in good agreement with results reported in the literature for tetragonal phase [15-17]. The broad peak, which spans from 16° to 26°, originates from amorphous quartz from the substrates. The (110) crystal plane is shown in **Figure 3.1**C. From the position of (110) XRD peak, we determined the inter-octahedron spacing to be 0.63 nm.

3.1.2 Optical properties

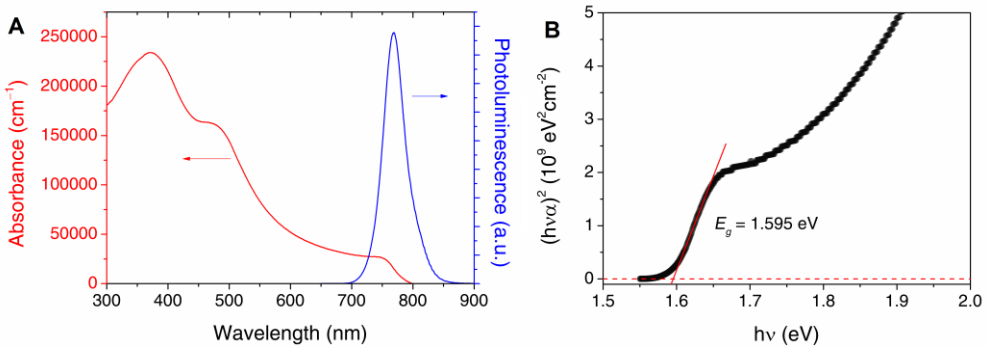

Figure 3.2 | Linear optical properties of MAPI thin film. (A) The absorption coefficient α (red) and the PL emission (blue) of MAPI thin film. (B) Estimation of MAPI bandgap (~1.595 eV) from the Tauc plot.

The absorbance and photoluminescence (PL) spectra of our MAPI thin film at room temperature are shown in **Figure 3.2**A. A band edge absorption is seen at 780nm, which also corresponds to its PL emission. It has been established that MAPI has weak exciton binding energy of few meV [18, 19]. Such weak binding energy implies free carriers as the main photoexcited species in MAPI [20]. The PL emission is expected to originate from bimolecular recombination of the band edge carriers. The Tauc plot of MAPI is shown in **Figure 3.2**B.

Assuming parabolic direct band-edge with $(h\nu\alpha)^2 \propto (E_g - h\nu)$, the bandgap of MAPI is estimated to be 1.595 eV. Our estimation of the bandgap is consistent with values of ~1.6 eV reported in the literature [21-23]. It is noteworthy to mention that the band edge of MAPI is located very close to the ideal bandgap according to Shockley-Queisser limit for maximum solar cell efficiency. This is one of the reasons for the immense interest on MAPI for photovoltaic applications.

3.1.3 Section Summary

In summary, we established a few conclusions on structural and linear optical properties of MAPI based on our experimental results and from the literature. These conclusions are given as such:

1. Our low-temperature solution-processed MAPI thin films samples form tetragonal perovskites structures at room temperature with characteristic spacing between octahedrons of ~0.63 nm.
2. The optical linear characterizations of this PEPI thin film show an absorption edge at ~780 nm, which corresponds to its PL emission. We estimated our MAPI thin film bandgap to be ~1.6 eV, close to the ideal gap according to Shockley-Queisser limit.
3. MAPI possesses weak exciton binding energy of a few meV at room temperature, which makes free carriers as its dominant photoexcited species and bimolecular recombination as its main radiative relaxation pathway.

3.2 Non-equilibrium carrier dynamics

A clear understanding of the dynamics of the non-equilibrium photoinduced carriers in MAPI thin film is crucial for practical applications. While the non-equilibrium carrier dynamics are not the main focus of this thesis, they are still relevant for interpreting the optical-spin dynamics and properties in 3D lead halide perovskites, especially for the carrier dynamics near the band edge. For a more detailed understanding of the carrier dynamics, interested readers are referred to the literature [4, 20, 24-28]. The main experimental technique used to probe the non-equilibrium carrier dynamics in this material system is the white light TA spectroscopy.

3.2.1 Assignment of TA spectra origin

The TA spectra of MAPI thin film, photoexcited resonantly by 760 nm pump, at several probe delay positions are shown in **Figure 3.3**A. Note that although the carriers are photoexcited directly to the band edge, ultrafast thermalization process was still observed to happen within the first ps, where the carriers assembled themselves to follow the Fermi-Dirac distribution. This is evident from the sharp bleaching peak at 0.1 ps probe delay, which broadens and reaches its maximum width before 0.3 ps delay. This observation is different from TA studies with pump excitation further above the band edge (*i.e.* 400 nm or 3.1 eV [29]), which happen in much slower timescale longer 10 ps due to the presence of phonon bottleneck effect [23, 29]. Herein, this observation suggests that for band edge resonant excitation, carrier thermalization is mainly achieved by carrier-carrier scattering processes, which happens in much faster timescale than phonon-assisted processes in MAPI.

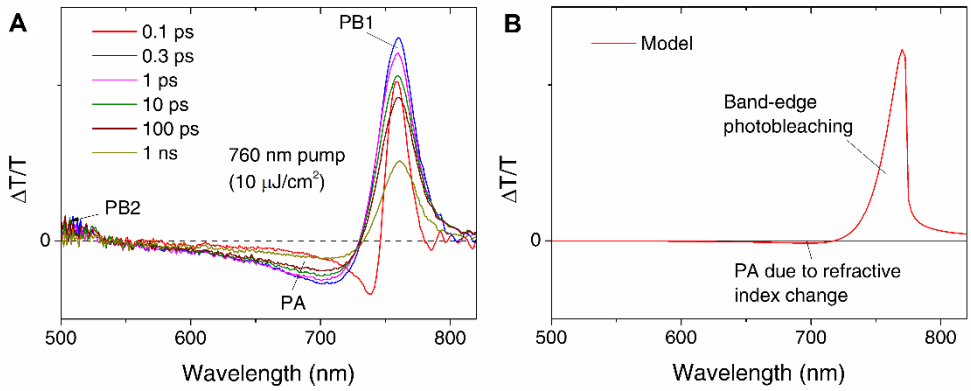

Figure 3.3 | TA spectrum of MAPI thin films. (A) The experimental TA spectra of MAPI thin film at various probe delay positions. The sample is photoexcited by 760 nm pump (10 μJ/cm^2) at room temperature. (B) TA spectrum based on parabolic band model.

The TA spectrum of MAPI can be described by its 3 main features [28]: (i) the strong photobleaching band centered about 760 nm (known as PB1); (ii) broad photoinduced absorption (PA) band; and (iii) weaker photobleaching band centered at 480 nm (known as PB2). Here, in our case (**Figure 3.3**A), only the onset of the PB2 (λ < 530 nm) can be observed due to very weak probe

generation for a wavelength shorter than 500 nm in our system. Note that these 3 features in the MAPI TA spectrum are independent of the pump wavelength. In the literature pump wavelengths of 380-400 nm or 580-600 nm have been commonly used to study these features [26, 28, 30-32], whereas in our case they were also observed by using 760 nm band edge resonant excitation, *i.e.* without photoexciting any higher states. Our observation hence establishes that all these spectral features originate from the band edge population of the carriers.

Given the MAPI band edge at ~1.6 eV [21-23], It is straightforward to assign this PB1 band as the ground state bleaching band, *i.e.* decrease of probe absorption due to state filling of the band edge. While researchers are unanimous in the assignment of PB1, there have been some disputes regarding the assignment of PB2 [28]. Several models which try to explain PB2 are (i) dual valence band model [30], (ii) charge transfer states of iodo-plumbate complexes [31], (iii) PbI_2 impurities [32] and (iv) dual conduction and valence band model [26]. Out of these models, the one that seems to be the most prevalent is the fourth model (dual valence and conduction bands) which were derived from charge transfer study by TA on MAPI/spiro-OMETAD and MAPI/PCBM bilayer structures. This model is also strongly supported by DFT-based band-structure calculation [19].

In the meantime, there has also not been any satisfactory clarification on the origin of the PA band in MAPI. While the most common explanation of the PA band is excited state absorption, there has been no further confirmation or assignment so far of these elusive higher lying states. Another opinion on the origin of this PA band came from Price *et al.* [23], who assigned it to large photoinduced refractive index change (*i.e.* reflectivity change) of the MAPI film. By employing a sophisticated model involving several processes such as bandgap renormalization, phonon bottleneck effect, *etc.*, it was claimed that the spectral behavior of MAPI could be well explained.

In order to confirm this assignment, we assume a simple model of parabolic band semiconductor system. For such system, the linear absorption coefficient $\alpha_0(\omega)$ and the joint density of states $D(\omega)$ can be described as:

$$\alpha_0(\omega) \propto D(\omega) = C\sqrt{\hbar\omega - E_g}. \tag{3.1}$$

Here, C is a constant and E_g is the bandgap of the semiconductor. After the thermalization process, the carriers will follow Fermi-Dirac distribution, which can be approximated as Boltzmann distribution ($E \gg k_B T = 26$ meV). The spectrum of the band edge bleaching due to state filling is given by:

$$\begin{aligned} \Delta\alpha(\omega) &= -\alpha_0(\omega)[f_e(\omega) + f_h(\omega)] \\ &= -xCe^{-\hbar\omega/k_B T}\sqrt{\hbar\omega - E_g}. \end{aligned} \tag{3.2}$$

Here, f_e and f_h are the occupation probabilities of the conduction and valence band respectively, and x is the filled fraction of the band edge. It is also assumed that both valence band and conduction band are symmetrical. The refractive index change and the change of absorption is related to each other via the Kramers-Kronig relation, which is given by:

$$\Delta n(\omega) = \frac{c}{\pi}\wp\int_0^\infty \frac{\Delta\alpha(\omega')}{\omega'^2 - \omega^2}d\omega'. \tag{3.3}$$

Here, $\Delta n(\omega)$ is the change of refractive index due to the change of absorption coefficient $\Delta\alpha(\omega)$; $c = 3.00 \times 10^8$ m/s is the speed of light in vacuum; and the $\wp$ is the *Cauchy principal value* of the improper integral. The change of the measured TA signal ΔT is related to the change of the refractive index via the change of absorption ΔA and reflectivity ΔR:

$$\begin{aligned} R + T + A &= 1 \\ \Delta T &= -(\Delta A + \Delta R). \end{aligned} \tag{3.4}$$

Meanwhile, given the complex refractive index $\tilde{n}(\omega) = n(\omega) + i\kappa(\omega)$ with complex component of $\kappa(\omega) = \alpha(\omega)c/2\omega$, the change or reflectivity due to the change of refractive index is given by:

$$\Delta R = \Delta\left[\frac{(n-1)^2+\kappa^2}{(n+1)^2+\kappa^2}\right] = 4\,\frac{(n^2-1-\kappa^2)\Delta n + 2n\kappa\Delta\kappa}{[(n+1)^2+\kappa^2]^2}. \qquad (3.5)$$

To realistically fit the experimental data, we set $E_g = 1.6$ eV, $C = 5 \times 10^7$ m^{-1} (**Figure 3.2**B), $T = 300$ K, and $n(\omega) = 2.5$ [33, 34]. The simulated TA spectrum obtained by this model is shown in **Figure 3.3**B. The result shows that while the refractive index change due to band edge state filling indeed yields PA band at the correct spectral region, the amplitude of this PA is insignificantly small in proportion to the PB1 band. Experimentally, this is not the case (**Figure 3.3**A), where the amplitude of the PA band is still ~20% of the PB1. Although our model cannot give any further insight on the origin of the PA band, it suggests that the change of refractive index is not the main cause of the PA band observed in MAPI TA spectrum, in contrast to the claim by Price *et al.* [23]. Note that while it is undeniable that the change of refractive index obtained from our model can be considered as huge ($|\Delta n| \approx 0.08$ for $\Delta T/T$ $(\lambda = 760$ nm$) \approx 0.05$), the change of reflectivity is still insignificant to contribute to the whole TA spectrum. Hence, it is still believed that the PA band most likely originates from the still unknown excited state absorption process. Further studies are required to pinpoint the higher lying states which are responsible for this process.

3.2.2 Assignment of carrier relaxation dynamics

Having established the origins and assignment of the TA spectral features of MAPI thin film, it is logical to investigate the relevant relaxation channels of these non-equilibrium carriers. Qualitatively, there are several known relaxation channels in MAPI, which are illustrated in **Figure 3.4**A [4, 5, 28]. At relatively low fluence, the most dominant recombination channels are the monomolecular recombination, which might come from the combination of (1) the non-radiative trap-assisted recombination or (2) the radiative geminate (excitonic) recombination. However, since the exciton population is insignificant in MAPI due to fast dissociation [20, 22, 24], it can be deduced that the trap-assisted recombination is the dominant monomolecular relaxation channel, which is

non-radiative. In such case, the main radiative recombination channel in MAPI are (3) the bimolecular recombination channel [4, 28], which is more dominant in higher fluence regime. At even higher fluence regime, higher-order processes such as (4) the non-radiative Auger recombination (3-particle) or radiative amplified spontaneous emission (ASE) starts to dominate the relaxation pathway.

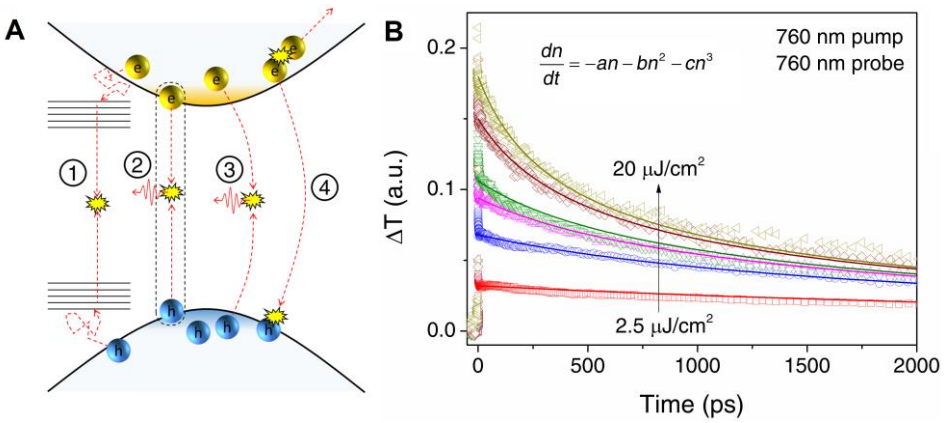

Figure 3.4 | Carrier relaxation channels in MAPI. (A) Schematic of the relaxation channels of band edge carriers in MAPI, where (1) trap-assisted recombination (2) geminate recombination (3) non-geminate/bimolecular recombination and (4) Auger recombination. (B) Pump fluence dependent TA kinetics of MAPI thin films pumped and probed 760 nm, with fluence ranging from 2.5 μJ/cm^2 to 20 μJ/cm^2. The relaxation dynamics is global-fitted by rate eq. (3.6).

For a more quantitative experimental study of the relaxation pathways, we investigated the band edge carrier kinetics of MAPI thin film resonantly pumped and probed at 760 nm. The advantage of resonant excitation, in this case, is to isolate the excited carrier population to be only at the band edge, hence eliminating possible contributions from other processes involving higher states to our probe signal (*e.g.* phonon bottleneck, higher bands/states excitation, *etc.*). Based on the known relaxation channels, the band edge carrier populations $n(t)$ in MAPI can be described by the following differential equation:

$$\frac{dn(t)}{dt} = -an(t) - bn^2(t) - cn^3(t). \qquad (3.6)$$

Here, a, b and c coefficients are the monomolecular (*i.e.* trap-assisted), bimolecular and tri-molecular (Auger) recombination rate constant, respectively. The term mono-, bi- and tri- represents number of carriers involved in the relaxation process, *i.e.* one (1 electron or 1 hole), two (1 electron and 1 hole) and three (2 electrons and 1 hole or 2 holes and 1 electron) carriers for the mono-, bi- and tri- molecular recombination, respectively. This dependence is also reflected on the power of the carrier density in the rate equation.

For our case, we chose the pump fluence to be below the ASE threshold to eliminate complications to the relaxation rate caused by ASE process. The kinetics are then globally fitted by changing only the initial photoexcited carrier density for different pump fluences and with a, b, and c as their shared fitting parameters. The result is shown in **Figure 3.4**B, where the fitting agrees very well with the experimental data, except for the ultrafast relaxation at early time dynamics (< 0.3 ps), which comes from carrier thermalization/redistribution. Given the absorption coefficient of MAPI to be ~2.5×10^4 cm^{-1} at 760 nm (**Figure 3.2**), the derived values of a, b and c were converted from fitting unit into standard unit and are shown in **Table 3.1**. The a, b and c rate constant determined from our global fitting are several times larger than what is reported in ref. [5], yet are still within the large variance of rate constants reported in the literature [5, 24, 25, 27, 30, 35-37].

Table 3.1 | Global fitting parameters. The a, b and c obtained from the global fitting in the fitting and standard unit. The $[n]$ refers to the carrier density in fitting unit.

Parameter	Fitting Unit	Standard Unit*
a	1.52×10^{-4} ps^{-1}	1.52×10^{8} s^{-1}
b	1.37×10^{-3} $[n]^{-1}\mathrm{ps}^{-1}$	1.85×10^{-10} $\mathrm{cm}^3\mathrm{s}^{-1}$
c	6.15×10^{-2} $[n]^{-2}\mathrm{ps}^{-1}$	1.13×10^{-27} $\mathrm{cm}^6\mathrm{s}^{-1}$

*Conversion: $1.00\ [n] = 7.39 \times 10^{18}$ cm^{-3}

From these rate constants, we are able to determine the contribution of each component of the relaxation channels, which is given by:

$$\text{Mono} = \frac{a}{n_0}\int_0^{\infty} n(t)\,dt\,; \tag{3.7}$$

$$\text{Bimolecular} = \frac{a}{n_0}\int_0^{\infty} n^2(t)\,dt \tag{3.8}$$

$$\text{Trimolecular} = \frac{c}{n_0}\int_0^{\infty} n^3(t)\,dt \tag{3.9}$$

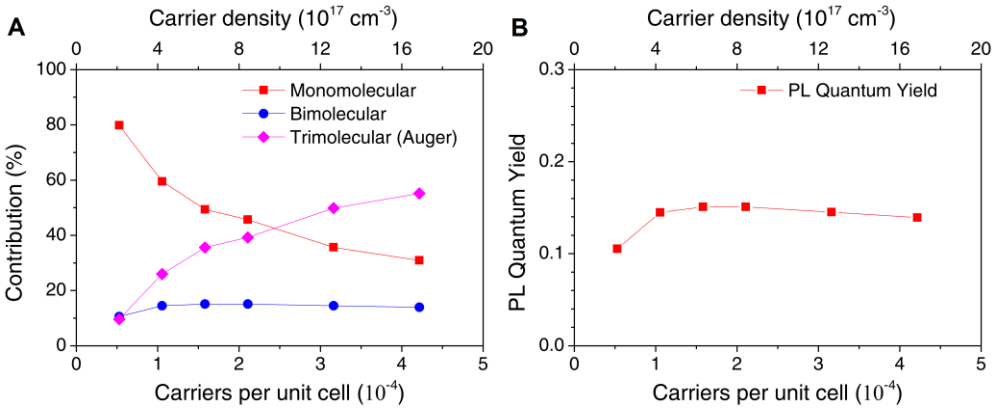

Figure 3.5 | Branching ratio of relaxation pathways in MAPI. (A) Density-dependent contribution of each relaxation channel of the photoexcited carriers in MAPI thin film. Three relaxation pathways are shown: mono- (red square, trap-assisted recombination), bi- (blue circle, radiative recombination) and tri-molecular (magenta diamond, Auger recombination). (B) Density-dependent PL quantum yield of MAPI.

Given the absorption at 760 nm to be 2.2 × 10^4 cm^{-1} and perovskites unit cell size to be ~6.3 Å, the deconvolved contribution for each pathway as a function of no of carrier per unit cell is shown in **Figure 3.5**A. At low carrier density, the monomolecular (trap-assisted) recombination dominates the relaxation process. As the fluence increases, Auger recombination increases and overtakes the monomolecular pathway at fluence >10 μJ/cm^2. Meanwhile, the bimolecular process is also observed to initially increase with increasing carrier density at much slower rate than the Auger recombination; This result is expected as the Auger process in MAPI has been reported to be unusually high (>25 times of GaAs) [5] and is known to be the main competing process for ASE [38]. From this result, assuming radiative bimolecular recombination channel the average PL quantum yield across this range of fluence is estimated to be ~0.15 (**Figure**

3.5B), which is consistent with previous reports [38] and thus further confirms the accuracy of our result. The implication of this findings is that multi-particle scattering (*i.e.* bimolecular scattering and Auger scattering) is an important process in MAPI thin film. This effect might become important for our main the study of optical-spin dynamics in MAPI.

3.2.3 Section Summary

In summary, the study of band-edge photoexcited-carrier relaxation pathways in MAPI thin films has been presented. In particular, the novel results reported in this subsection can be summarized in the following points:

1. Assignment of the spectral feature in the TA spectrum of MAPI. We establish that these observed spectral features originate from the band edge populations.
2. Modelling of the parabolic band edge of MAPI, which suggests that the 'controversial' PA band observed does not only come from the photoinduced refractive index change, in contrary to a recent study.
3. Determination of the relaxation pathways branching ratio of the photoexcited carriers in MAPI thin film. The relaxation channel is dominated by trap-assisted recombination at low fluence and Auger recombination at higher fluence (before ASE threshold).

The comprehension of the non-equilibrium carrier relaxation mechanisms would help us in understanding the optical-spin dynamics in 3D lead halide perovskites.

3.3 Optical-spin dynamics

Regardless of strong SOC in this system which allows strong light-spin coupling, to the best of our knowledge, the study of the spin dynamics in this system has not been explored. The focus of this chapter is to lay down the foundation for understanding the optical-spin dynamics and evaluate the potential of this material system for opto-spin-based applications. The main experimental techniques used to probe the dynamics in this material is the degenerate and white light TA spectroscopy with circular polarization control, and also by using time-resolved Faraday rotation (TRFR) measurement.

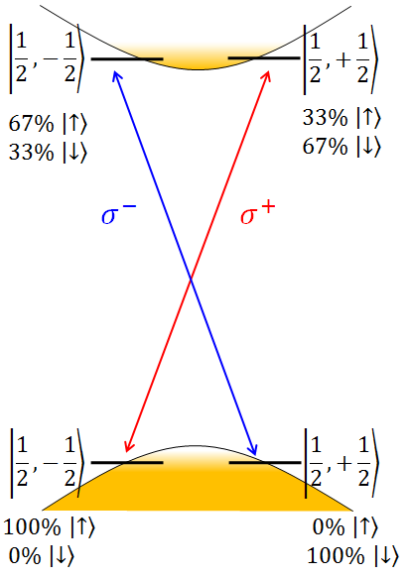

Figure 3.6 | Selection rule at band-edge of MAPI. The conservation of angular momentum in absorption process results in the selection rule for σ^+ (red) and σ^- (blue) circularly polarized light.

The band-edge electronic structure of the 3D lead halide perovskite system is known to be strongly modified by SOC and consists of *s*-like VBM and *p*-like CBM both with $|J, m_J\rangle$ states of $|1/2, \pm 1/2\rangle$ [19, 21]. As the photon carries an angular momentum of ±1, by conservation of angular momentum, the single-photon absorption process will be governed by selection rule of $\Delta m_J = \pm 1$ (**Figure 3.6** |**Figure 3.6**). For circularly polarized light, the σ^+ and σ^- photons carry angular momentum of +1 and –1 respectively, which allow us to selectively excite *J*-polarized (spin-polarized) carriers.

3.3.1 Modelling of spin dynamics

In such system, especially for MAPI where the photoexcited species are dominated by free carriers [20], we are able to model the spin-polarized carrier dynamics photoexcited by using a circularly polarized pump. Without the loss of generality, we assume excitation by σ^+ pump pulse, which populates the $|1/2, +1/2\rangle$ CBM state and depopulates the $|1/2, -1/2\rangle$ VBM state. This 'band-filling' causes the σ^+ probe to experience photobleaching (decrease in absorption) and hence allow us to monitor these *J*-states. The *J*-polarized photoexcited carriers might undergo *J*-flip process, which populates the

$|1/2,-1/2\rangle$ CBM state and $|1/2,+1/2\rangle$ VBM state, which will be monitored by σ⁻ probe. The population dynamics of these *J*-states can be described by the following coupled rate equations:

$$\frac{d}{dt}f_e^{\pm 1/2} = \frac{A}{2}(1 \pm p)e^{-t^2/r^2} - \frac{f_e^{\pm 1/2} - f_e^{\mp 1/2}}{\tau_e} - \frac{f_e^{\pm 1/2}}{\tau_c}, \qquad (3.10)$$

$$\frac{d}{dt}f_h^{\mp 1/2} = \frac{A}{2}(1 \pm p)e^{-t^2/r^2} - \frac{f_h^{\mp 1/2} - f_h^{\pm 1/2}}{\tau_h} - \frac{f_h^{\mp 1/2}}{\tau_c}. \qquad (3.11)$$

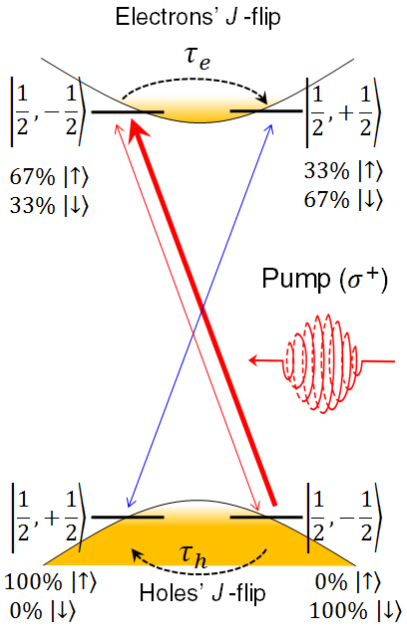

Figure 3.7 | Model for spin dynamics in MAPI. Excitation by σ⁺ pump (red thick arrow) will populate the $|1/2,+1/2\rangle$ CBM state and depopulate the $|1/2,-1/2\rangle$ VBM state. The dynamics are followed by electrons and holes *J*-flip which populates the respective counterpart *J*-states. The populations of each spin-state can be monitored by σ⁺ (red thin arrow) and σ⁻ (blue thin arrow) probe.

The subscript index *e* and *h* refers to electrons' (CBM) or holes' (VBM) states, respectively; $f_{e,h}^{\pm 1/2}$ is the population of the *e* or *h* states with $m_J = \pm 1/2$; $p = (I_+ - I_-)/(I_+ + I_-)$ is the degree of circular polarization of the excitation pump, where I_+ and I_- are the σ⁺ and σ⁻ components intensity of the pump, respectively (*i.e.* $p = +1$, $p = 0$ and $p = -1$ for σ⁺, linear and σ⁻ pump polarization, respectively); *r* is the laser pulse time constant (assuming Gaussian pulse), which is in the order of ~0.1 ps; τ_e and τ_h are the longitudinal

spin relaxation times (*i.e.* T_1 [39], see Chapter 2) of the electrons and holes respectively; and τ_c is the carrier relaxation time. This equation is depicted in **Figure 3.7**. Here, the (+) and (–) signs in the equation are for σ^+ and for σ^- probe polarization, respectively. The absorption coefficient of the σ^+ and σ^- probe as a function of the population of electron and hole states can be described with the following equation:

$$\alpha_{\pm1}\left(f_e^{\pm1/2}, f_h^{\mp1/2}\right) = \alpha_0\left(1 - f_e^{\pm1/2} - f_h^{\mp1/2}\right). \tag{3.12}$$

Here, α_0 is the linear absorption coefficient of the material. The second and third terms in the equation represent decrease in absorption due to stimulated emission from the CBM and depopulation of the VBM, respectively. The +1 and –1 correspond to the σ^+ and σ^- probe, respectively. Assuming an intrinsic semiconductor and very weak probe intensity, when there is no perturbation by pump, the excited state population $f_e^{\pm1/2}\big|_{\text{no pump}} = f_h^{\mp1/2}\big|_{\text{no pump}} \approx 0$. The change of the absorption coefficient due to carrier population by pump excitation ($f_e^{\pm1/2}$ and $f_h^{\mp1/2}$) can therefore be described as:

$$\Delta\alpha_{\pm1}\left(f_e^{\pm1/2}, f_h^{\mp1/2}\right) = -\alpha_0\left(f_e^{\pm1/2} + f_h^{\mp1/2}\right) \tag{3.13}$$

$$\left.\frac{\Delta T}{T}\right|_{\pm1} \propto e^{-\Delta\alpha} - 1 \approx -\Delta\alpha \tag{3.14}$$

$$\left.\frac{\Delta T}{T}\right|_{\pm1} \propto f_e^{\pm1/2} + f_h^{\mp1/2} \tag{3.15}$$

By solving the coupled rate eq. (3.10) and (3.11) analytically, the change of probe transmission due to pump excitation is therefore given by the following equation:

$$\left.\frac{\Delta T}{T}\right|_{\pm1} \propto e^{-t/\tau_c}\left\{\left[1 + \operatorname{erf}\left(\frac{t}{r} - \frac{r}{2\tau_c}\right)\right] \pm \frac{p}{2}\sum_{i=e,h} e^{\frac{r^2}{\tau_i^2}}\left[1 + \operatorname{erf}\left(\frac{t}{r} - \frac{r}{\tau_i}\right)\right] e^{-2t/\tau_i}\right\}. \tag{3.16}$$

As expected from eq. (3.16), by adding the σ^+ and σ^- probe signals together we will lose the information on the individual spin-states, which results in a signal proportional only to the population of the photoexcited carriers and independent of the pump polarization *p*:

$$\left.\frac{\Delta T}{T}\right|_{+1} + \left.\frac{\Delta T}{T}\right|_{-1} \propto e^{-t/\tau_c}\left\{\left[1 + \mathrm{erf}\left(\frac{t}{r} - \frac{r}{2\tau_c}\right)\right]\right\}. \qquad (3.17)$$

3.3.2 Preliminary measurement

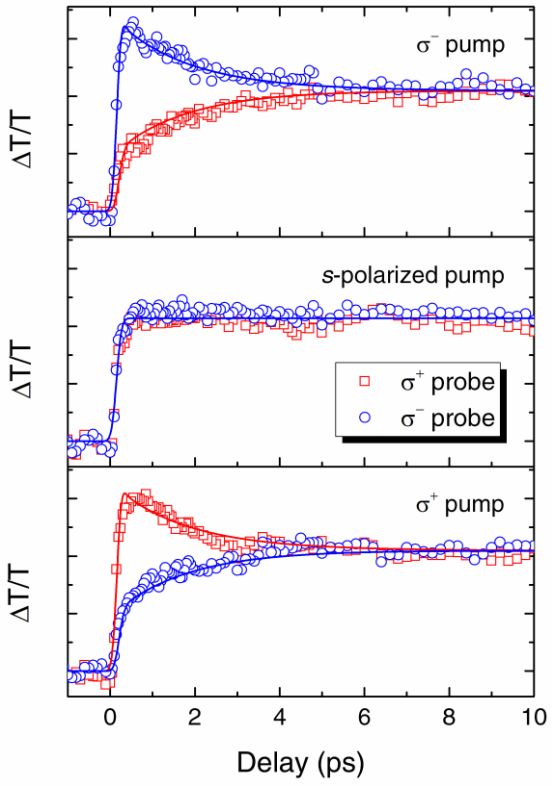

Figure 3.8 | Degenerate pump-polarization dependent TA on MAPI thin film. The kinetics of spin-states in MAPI thin film monitored by σ^+ (red square) and σ^- (blue circle) probe, photoexcited by (A) σ^+, (B) linear and (C) σ^- polarized pump. The data is globally fitted with eq. (3.16).

The experimental results of degenerate TA with σ^+, *s*- (linear) polarized and σ^- pump polarizations on MAPI thin film with band-edge excitation of λ = 750 nm and pump fluence of 19 μJ/cm^2 are shown in **Figure 3.8**. The data is in a good agreement with eq. (3.16), which shows the accuracy of our model. As

predicted by the selection rule and the model, flipping the pump helicity from σ^+ to σ^- will reverse the photoexcited spin populations. Hence this reverses the initial kinetics observed by the σ^+ and σ^- probe signal, which is proportional to the population of the corresponding spin states. This is also shown by the fast rise of the signal when the pump and probe polarizations are co-linear, which indicates 'sudden' specific spin states filling by the pump. Following this fast rise is the few ps decay of co-circular signal concomitantly with the rise of the pump-probe signal with counter-circular polarization until they attain similar signal intensity. This concomitant rise and decay of the co-circular and counter circular signal within 5 ps after pump excitation indicates the fast spin relaxation process in MAPI towards spin-states equilibrium (*i.e.* equal population of spin-up and spin-down).

Meanwhile, for excitation with linearly polarized pump, the spin states are indiscriminately excited by the pump. This results in an equal kinetics of both σ^+ and σ^- probe signals, and hence no observable spin dynamics. From this result, shown by the signal plateau within 10 ps window, it is also concluded that the band-edge photoexcited carrier population dynamics in MAPI happen in much longer timescale than its optical-spin dynamics (T_1 < 5 ps).

3.3.3 Temperature and power dependent TA

Following the preliminary measurement, temperature and power dependent degenerate TA studies were also performed on MAPI thin film to determine the relevant spin relaxation mechanism. **Figure 3.9** shows the experimental data at temperatures of 77 K and 293 K, photoexcited with λ = 750 nm σ^+ pump with a fluence of ~19 μJ/cm^2. The σ^+ and σ^- probe signals are well-fitted with eq. (3.16); and their total is well-fitted with eq. (3.17). Here, the total of the σ^+ and σ^- probe signals signifies the total population of the photoexcited species. The experimental data fitting in **Figure 3.9** yields two spin lifetimes of 1.2 ps and 7 ps at 77 K and slightly shorter lifetimes of 0.35 ps and 4.2 ps at 293 K. Here, the shorter spin lifetime is assigned to the electrons' spin relaxation, which is expected to be short due to the orbital-spin band mixing in the *p*-like CBM; while the longer one is assigned to holes' spin relaxation with pure spin band in *s*-like VBM. Meanwhile, the total photo-excited carrier population is observed to be relatively constant during the 10 ps time window of the experiment, during

which the spin-related dynamics have ended. Such short spin lifetime as compared to the carrier lifetime is expected due to strong SOC, which allows momentum scattering of the carriers to flip their spin.

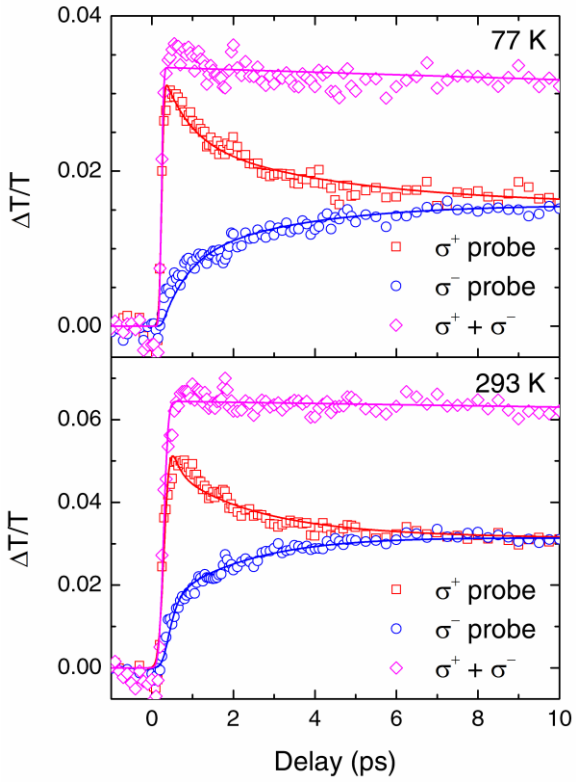

Figure 3.9 | Degenerate TA of MAPI thin film at different temperatures. The polarization dependent degenerate TA photoexcited with λ = 750 nm σ^+ pump with a fluence of ~19 μJ/cm^2 at (A) 77 K and (B) 293 K. The σ^+ probe, σ^- probe and their total are shown in red square, blue circle, and magenta diamond, respectively.

The spin lifetimes obtained from fitting by eq. (3.16) from these temperature- and power-dependent studies are plotted in **Figure 3.10**. From the results, it is observed that the spin lifetime is weakly dependent on temperature. This suggests a weak spin-phonon interaction in MAPI thin films, *i.e.* momentum scattering with phonon does not flip the spin. For comparison, the spin lifetimes are also observed to somewhat follow a temperature dependent trend of $T^{-0.5}$, with correlation factor of R^2 = 0.964 (**Figure 3.10**A). Meanwhile, it is also observed that the spin lifetime is strongly affected by the pump fluence, which suggests an efficient spin-flip process induced by carrier-carrier scattering events (**Figure 3.10**B).

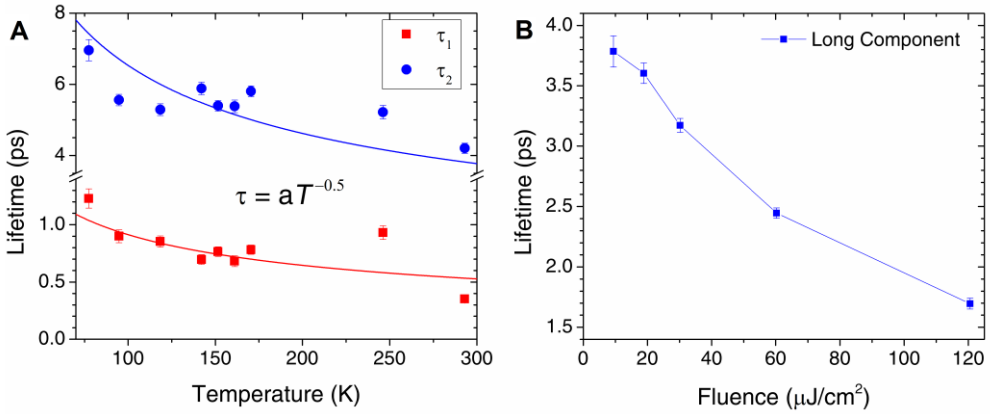

Figure 3.10 | Spin lifetime of MAPI thin film. (A) Temperature *T* dependent spin lifetime at fluence of 19 μJ/cm^2. The solid lines are for comparison with $T^{-0.5}$ trend. (B) Power dependent spin lifetime at 293 K. All measurements were performed using λ = 750 nm. The short and long lifetime components are shown in red and blue, respectively.

Further confirmation on this weak spin-phonon interaction was obtained from white light TA. Here, we used λ = 700 nm (1.77 eV) pump with a fluence of 16 μJ/cm^2, and a broadband white light probe to monitor the band edge spin dynamics. In contrast to the previous measurement where the spin-polarized carriers were directly photoexcited into the band edge, in this case, the spin-polarized carriers were excited to higher excited states. **Figure 3.11**A illustrates how these hot carriers would interact with phonons to undergo energy and momentum relaxation towards the band-edge and tracked by 760 nm probe. **Figure 3.11**B shows the TA spectra of the co- and counter-circular polarized signals at different probe delays. One striking feature is the fast and slow rise of the co- and counter circular band-edge photobleaching signal, respectively.

This observation is further clarified by **Figure 3.11**C, which shows the kinetics of these band-edge TA signals at 760 nm. Note that this difference in band-edge signal rise is similar to the previous case of resonant excitation (degenerate TA, **Figure 3.8**). The implication of this observation is the preservation of the photoexcited spin polarization throughout the phonon-assisted relaxation process to band-edge, which is therefore consistent with our previous hypothesis of weak spin-phonon coupling in MAPI.

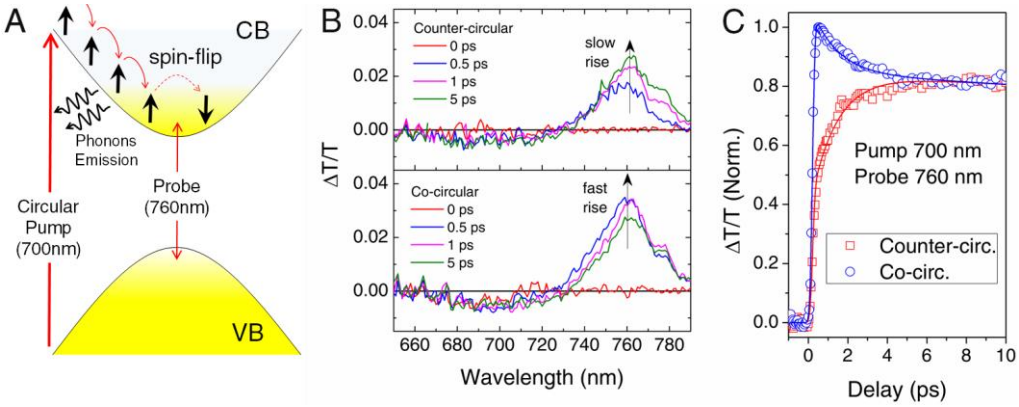

Figure 3.11 | Non-degenerate TA on MAPI thin film. (A) Momentum and relaxation of non-resonantly photoexcited carriers involving phonons in MAPI. (B) TA spectra of co- (bottom) and counter-circular (top) pump and probe polarization of MAPI photoexcited with 700 nm pump and fluence of 16 μJ/cm^2. The fast and slow rise of the co- and counter-circular band-edge photobleaching signal respectively, indicate the presence of spin dynamics. (C) Kinetics probed at 760 nm (band-edge) and pumped at 700 nm of the co-circular (blue) and counter-circular (red) signal.

Time-Resolved Faraday rotation measurement

Another complimentary spin-dynamics measurement using time-resolved Faraday rotation (TRFR) was also performed on the MAPI thin film, without any external magnetic field. As has been discussed in Chapter 2, FR signal, which is proportional to sample magnetization [39-41], is the direct consequence of the imbalanced change of σ^+ and σ^- refractive index of the material due to imbalanced change of its σ^+ and σ^- absorption. These changes of absorption and refractive index are tied together by Kramers-Kronig relation. From the relation, a large material absorption coefficient, which is the case for MAPI, suggests a large refractive index change. Hence, large FR is also expected from MAPI.

Since the photoinduced magnetization in MAPI probed by TRFR comes from the similar origin of imbalance populations between the spin-states (net spin $\neq 0$), it is therefore expected to behave similarly with the spin-population dynamics measured by the TA. This result is confirmed in **Figure 3.12**A, where both the TRFR signal and the net spin from TA signal $|\sigma^+ - \sigma^-|$ show a similar transient dynamic. The pump polarization dependent of the TRFR signal is shown in **Figure 3.12**B. Similar to the case of TA measurement (**Figure 3.8**), the TRFR signal flips when the pump polarization helicity is flipped from σ^+ to

σ^-, indicating a flip in the photoinduced magnetization. Meanwhile, there is no TRFR signal/magnetization observed when the sample is excited with linearly polarized pump. This is expected since there is no net spin of the photoexcited carriers to produce the magnetization. Note that the TRFR lifetime is expected to be 1/2 of the spin lifetime obtained from eq. (3.16).

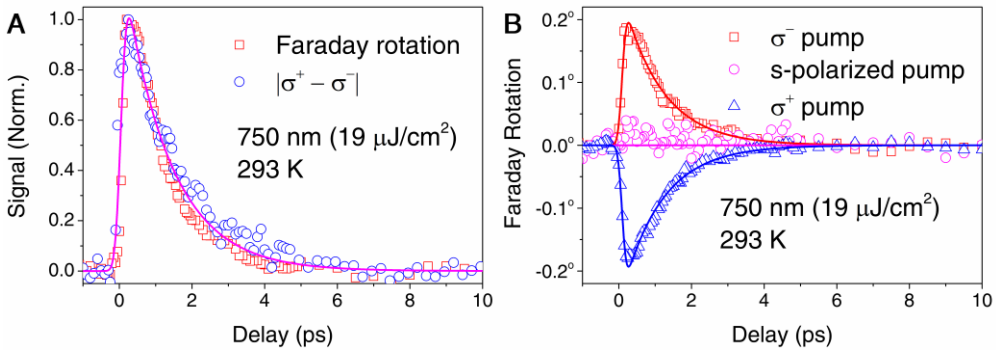

Figure 3.12 | TRFR measurement on MAPI. (A) Comparison between TRFR (red) and spin-population dynamics obtained by TA (blue) in MAPI. (B) TRFR signal on MAPI thin film photoexcited with σ^+ (blue), s-polarized (magenta), and σ^- (red) pump polarization. All measurements were performed in 293 K with λ = 750 nm (19 μJ/cm^2).

From our room temperature result, the photoinduced change of refractive index which results in such FR can be estimated to be:

$$|\Delta n| = \frac{2\lambda\theta_F}{l} \approx 0.075 \tag{3.18}$$

where $\lambda = 750$ nm is the light wavelength; $\theta_F = 0.2° = 0.0035$ rad is the FR; and $l \approx 70$ nm is the sample thickness. This result is consistent with the estimate from our previous model and the Kramers-Kronig relation [c.f. Section 3.2.1 and eq. (3.3)], which yields $|\Delta n| \approx 0.08$ for band edge $\Delta T/T \approx 0.05$ (**Figure 3.9**B). This result also implies the accuracy of our previous model.

Temperature and power dependent studies of the photoinduced FR were also performed to gain further insights into the optical-spin properties of this material system. The compilation of the results is shown in **Figure 3.13**, which shows the maximum rotation and the lifetime of the FR. Here, the lifetime of the FR is fitted with bi-exponential decay with equal contribution from both

components [eq. (3.19)], because of the symmetrical contribution from electron and hole to the dynamics [23].

$$\theta_F = \theta_0 \left\{ \left(1 + \mathrm{erf}\left[\frac{t}{r} - \frac{r}{2\tau_1}\right]\right) e^{-t/\tau_1} + \left(1 + \mathrm{erf}\left[\frac{t}{r} - \frac{r}{2\tau_2}\right]\right) e^{-t/\tau_2} \right\}. \quad (3.19)$$

Here, θ_0 is a proportionality constant; r is the laser time constant/pulse width; and τ is the lifetime. It can be seen from **Figure 3.13**B and D that the lifetimes' trends are weakly dependent on the temperature, while they are strongly affected by pump fluence. This observation is consistent with the previous observation from the TA measurement, which is attributed to the weak spin-phonon coupling in MAPI.

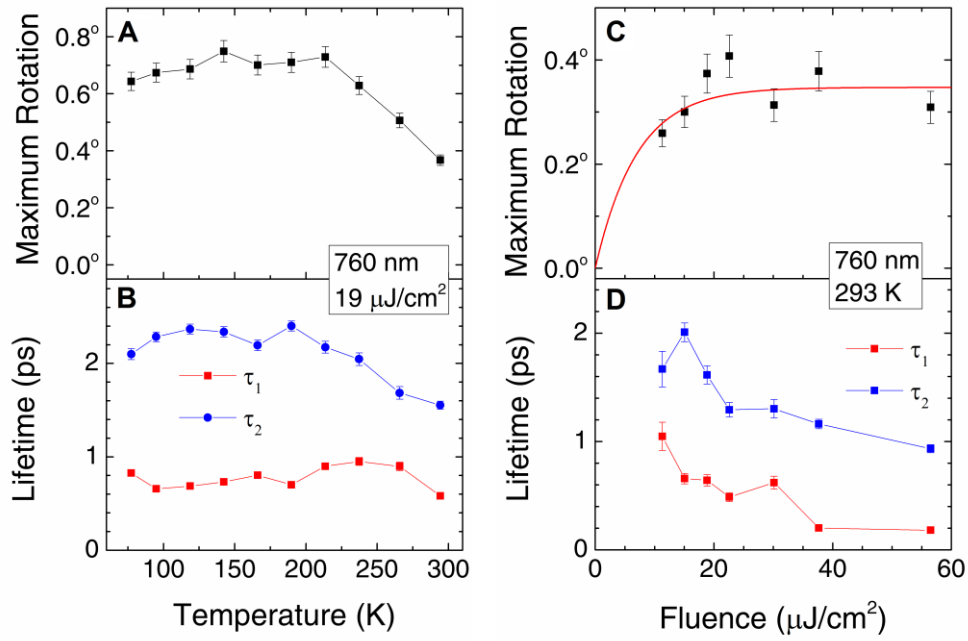

Figure 3.13 | Temperature and fluence dependent TRFR in MAPI thin film. (A) Maximum rotation and (B) lifetimes' dependence on temperature. (C) Maximum rotation and (D) lifetimes' dependence on pump fluence. All measurements were performed with λ = 760 nm.

Meanwhile, for the maximum rotation, **Figure 3.13**C shows a saturation behavior, which is expected due to the ground state bleaching by high fluence

pump excitation. From fitting with state-filling exponential saturation function $\theta(I) = \theta_0(1 - \exp(-I/I_S))$, we obtain saturation fluence $I_S = 8 \pm 2$ μJ/cm^2 and saturation angle of θ_0 = 0.35° ± 0.02°. This implies that our lowest fluence of ~10 μJ/cm^2 had already been in the saturation regime. Unfortunately, measurement at lower fluence would be limited by noise. **Figure 3.13**A shows the peculiar behavior of the maximum Faraday rotation as function of temperature, where the maximum rotation increases as temperature decreases, up to ~200 K, where it forms a plateau. The origin of this behavior is still unclear, but, it is likely related to the known phase transition of MAPI at ~160 K. One striking feature which is also observed in **Figure 3.13**A is the huge FR of 0.70° ± 0.05° at temperature ~200 K from this ~70 nm thick MAPI film. When it is normalized to its thickness (*i.e.* $\theta_F \propto$ thickness), this result corresponds to FR of 10° ± 2°/μm, which to the best of our knowledge is the largest value reported so far for any material system. For comparison, several material systems exhibiting relatively strong FR have been listed in **Table 3.2**.

Table 3.2 | List of several material systems exhibiting FR. Comparison of our results with several material systems reported in the literature to exhibits large FR.

Material System	λ (nm)	T (K)	θ_F (°)	θ_F (°/μm)
$CH_3NH_3PbI_3$	**760**	**200**	**0.7**	**10**
$Bi_3Fe_5O_{12}$ *[42]*	633	300	3	6
MnSE DMH *[41]*	440-510	5	0.6	0.6

This ultra-large FR combined with fast spin relaxation in MAPI highlights the prospect of OIHP systems for ultrafast all-optical spin switch applications since large rotation would be required for the switching contrast (*i.e.* 'on' and 'off' state). This discovery demonstrates the prospect of OIHP for opto-spintronic applications

3.3.4 Assignment of spin relaxation mechanism

In semiconductors, generally, there are four well-known major spin relaxation mechanisms, in which will be discussed briefly here [39, 43, 44]. The first one is the *Elliot-Yafet* (EY) mechanism, which the spin of the carriers relaxes via ordinary collision/momentum scattering. In this case, the rate spin

relaxation will be proportional to the rate of momentum scattering. The second mechanism is *D'yakonov-Perel'* (DP) mechanism, which is the dominant spin relaxation mechanism due to SOC in systems lacking inversion symmetry, due to the crystal effective magnetic field. In contrast to the EY mechanism, the spin relaxes not during, but between the collisions. Hence, in this case, the rate of spin relaxation will be inversely proportional to the rate of momentum scattering. The third mechanism is *Bir-Aronov-Pikus* (BAP) mechanism, which is dominant in heavily p-doped semiconductors due to the exchange interaction between the electron and hole. The last mechanism is relaxation via hyperfine interaction with nuclear spins, in which the spin of the carriers interacts with the spin of the nuclei. This mechanism is important for localized electrons *e.g.* confined in quantum dots (QD) or bound on donors.

To assign a relevant spin relaxation mechanism in MAPI, we summarize the results of the experimental optical-spin dynamics studies. There are two general behaviors of the spin relaxation lifetime which are observed in MAPI thin film:

1. The spin relaxation lifetime is weakly dependent or does not depend on temperature, which has been assigned to weak spin-phonon coupling, *i.e.* spin-preserved scattering with phonon.
2. Strong decreasing of the spin relaxation lifetime as the function of excitation pump fluence. This implies the role of multi-carrier scattering in the spin relaxation process.

From these two behaviors, we assigned the EY mechanism as the main spin relaxation mechanism, with spin relaxation through carriers, impurities and grain boundaries scattering, but weak spin-phonon interaction. This assignment is clear from the spin relaxation rate behavior which is proportional to the scattering rate in the fluence-dependent measurement. Moreover, the correlation of the spin lifetime with temperature $\tau_s \sim T^{-0.5}$ (**Figure 3.10**A) is consistent with theoretical prediction of EY spin relaxation through charged impurities scattering [39]. These charged impurities might come from grain boundaries, bulk defects or ion displacements, which is common in MAPI system [25, 28, 45, 46]. We also eliminate the possibility of other spin relaxation mechanisms; DP mechanism is less likely since the MAPI crystal structure has inversion symmetry, unless the central ion is displaced by external electric field; BAP

mechanism since our system has insignificant p-doping and weak electron-hole exchange interaction (free carrier system); and hyperfine interaction, since our system is a non-localized and unconfined system, with long both electron and hole diffusion length [30].

The implication of this spin relaxation mechanism is that the spin lifetime is not limited by the intrinsic properties of phonon interactions, but with sample imperfections, such as impurities and grain boundaries. This suggests that the improvement of the spin lifetime, possibly up to spin transport applications, can be done by improving the sample qualities to eliminate those imperfections. Elimination of this main spin-relaxation channel, combined with its large carrier mobility [30], may allow the realization of long-range spin transportation in MAPI.

3.3.5 Effect of morphology

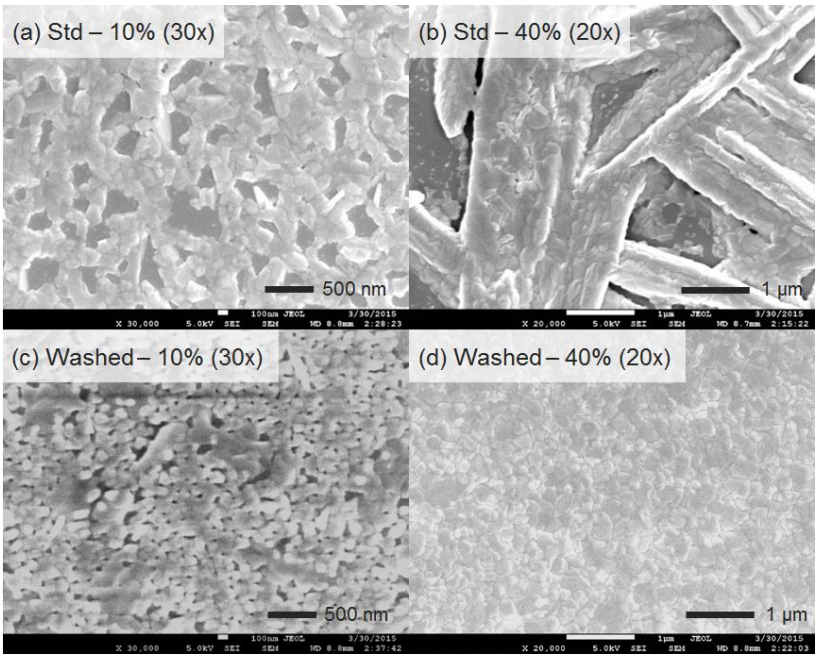

Figure 3.14 | SEM images of MAPI with different treatments. The morphologies of different MAPI thin films with different fabrication treatment. Std and washed refer to standard (i.e. without extra treatment) and toluene treated sample, respectively. The weight percent concentrations of the precursor solutions are also indicated.

In line with the conclusion of Section 3.3.4, further study is performed to understand the effect of morphology on the optical-spin dynamics in MAPI.

Nevertheless, due to the limitation of our current sample fabrication capability, this study is limited only to the modification of sample morphology through solvent engineering technique, *i.e.* by toluene treatment. This toluene treatment on MAPI films has been reported to improve the sample morphology which yields higher efficiency solar cells [47]. In this study, we performed a comparison between standard and toluene treated samples. The detail of the treatment was discussed in **Chapter 2**. The study on the effect of sample thickness was also performed by changing the concentration of the precursor solution. Here, two 10wt% and 40wt% precursor solutions' concentrations are used for the comparison, which yields films with thickness of ~70 nm and ~200 nm, respectively. The comparison of the morphologies from SEM images is shown in **Figure 3.14**. From the SEM images, it is clear that the toluene treatment strongly modifies sample morphologies by greatly reducing pinholes, changing the crystallization structures from dendritic to granular and slightly reduces the grain sizes. Another visually apparent change is the increase in specular reflectivity of the film, which is due to more uniform film coverage on the substrate. While toluene treatment does not improve film crystallinity [47] but undesirably increases the surface traps density [25, 28], the increase in film coverage and uniformity could overcome such adverse effects and yield an overall increase in PV performance as compared to the standard film.

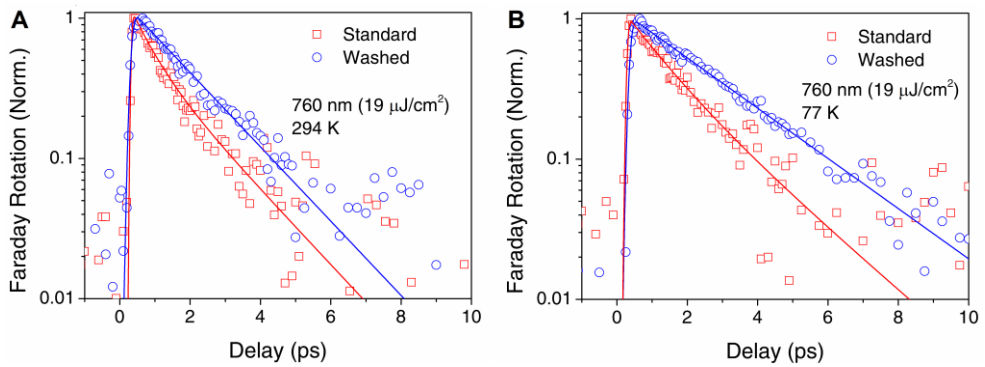

Figure 3.15 | TRFR of standard and toluene treated MAPI samples. The TRFR kinetics of standard (red squares) and toluene treated (blue circles) samples, fitted with bi-exponential and single exponential decay function, respectively, at (A) 294 K and (B) 77 K. All measurements were performed by λ = 760 nm and fluence 19 $\mu J/cm^2$.

TRFR study was performed to compare the magnetization dynamics between the standard and toluene treated samples. The magnetization kinetics photoexcited with λ = 760 nm at 77 K and 293 K are shown in **Figure 3.15**. One striking feature which is clearly observed is their comparison in exponential decay. While the standard sample shows a bi-exponential decay behavior, which previously has been attributed to electrons and holes species, the toluene treated sample shows a single-exponential decay behavior. Since the toluene treatment is expected to only modify the grain surface properties, this indicates that the optical-spin dynamics of the carriers in MAPI does not only occur in the bulk but also at the surface of the material. This result is coherent with recent findings of the importance of surface effects in lead halide perovskites [48, 49].

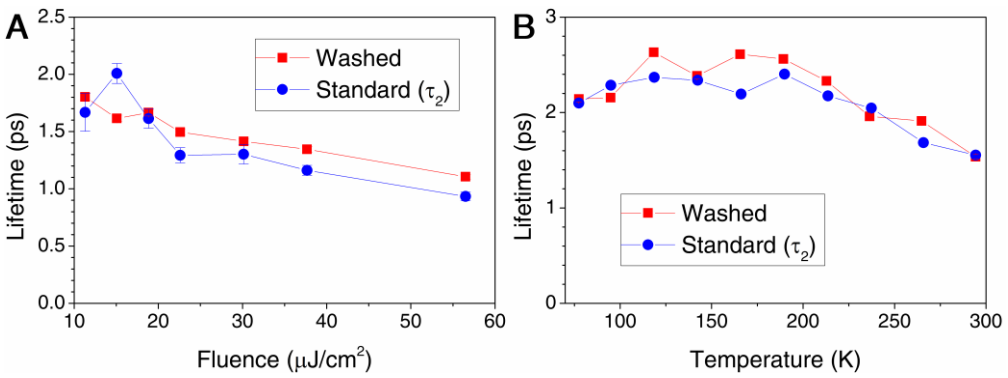

Figure 3.16 | Magnetization lifetimes of toluene treated MAPI thin films. (A) Fluence and (B) temperature dependent magnetization lifetime obtained by TRFR measurements. All measurements were performed at λ = 760 nm. The lifetimes of standard samples are re-plotted in the overlay for comparison.

While the toluene treatment eliminates the short lifetime component of the dynamics, it fails to prolong the magnetization lifetime of MAPI. **Figure 3.16** shows the fluence and temperature dependent study of toluene treated MAPI thin films, which shows similar lifetimes as compared to the long component (τ_2) of the standard samples. Since the toluene treatment is expected to only modify the surface properties, it can be implied from this observation that in standard MAPI thin film, the long lifetime component of the magnetization dynamics (holes) originates from the bulk of the material; while the short lifetime component (electrons) originates from the surface/grain boundaries of the material. In such case, toluene treatment limits the electrons' scattering on

the surface which would flip the spin via EY mechanism (see section 3.3.4), hence prolongs its spin relaxation lifetime up to its intrinsic bulk lifetime. Further studies are required to examine this mechanism in greater detail.

Fluence dependent TRFR studies were also performed to determine the effect of sample thickness on the magnetization dynamics. Here, toluene treated MAPI thin film samples with two different thickness of 70 ± 10 nm (10wt% precursor solution) and 200 ± 50 nm (40wt% precursor solution) were used for the comparative study. The result is shown in **Figure 3.17**. While the film thickness does not affect the magnetization dynamics (**Figure 3.17**A), it strongly modifies the TRFR signal strength. **Figure 3.17**B shows the maximum FR rotation achieved as function of the excitation pump fluence, fitted with state-filling saturation function $\theta(I) = \theta_0(1 - \exp(-I/I_s))$. We obtain maximum FR (θ_0) of 0.53° ± 0.03° and 1.10° ± 0.07°, and saturation fluence (I_s) of 19 ± 2 μJ/cm^2 and 20 ± 2 μJ/cm^2, for ~70 nm- and ~200 nm-thick sample, respectively.

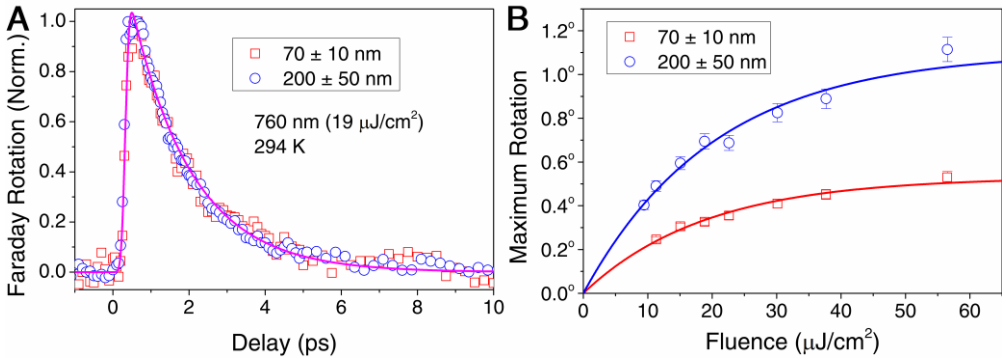

Figure 3.17 | Comparative study of MAPI film thickness. (A) Normalized magnetization kinetics and (B) maximum Faraday rotation for MAPI films with two different thicknesses of 70 ± 10 nm and 200 ± 50 nm.

Here, the higher rotation achieved by the thicker sample is expected, since FR is known to be proportional to sample thickness. Meanwhile, their similar saturation fluences are also to be expected since the photoexcited carrier density (carrier per unit volume) is independent of thickness (given similar absorption coefficient). One notable point is the higher maximum FR and saturation fluence achieved by toluene treated sample (~0.53° and ~19 μJ/cm^2, respectively) as compared to standard sample (~0.35° and ~8 μJ/cm^2,

respectively) with similar thickness (**Figure 3.13**C). This could be due to higher coverage of the toluene treated sample, which allows more material to be excited by similar pump spot size.

3.3.6 Effect of organic and halide substitution

Another major advantage of OIHP system is the tunability of their properties, which can easily be achieved by cation (organic component) or anion (halide component) substitutions of the precursor solutions. It is therefore natural for us to investigate on how each of this component will affect the spin dynamics of the system. Here, the comparative study of the spin dynamics was performed on 3 different 3D perovskite thin films: $CH_3NH_3PbI_3$ (MAPI), $NH_2CHNH_2PbI_3$ (FAPI) and $CH_3NH_3PbBr_3$ (MAPB), together with the PbI_2 thin film.

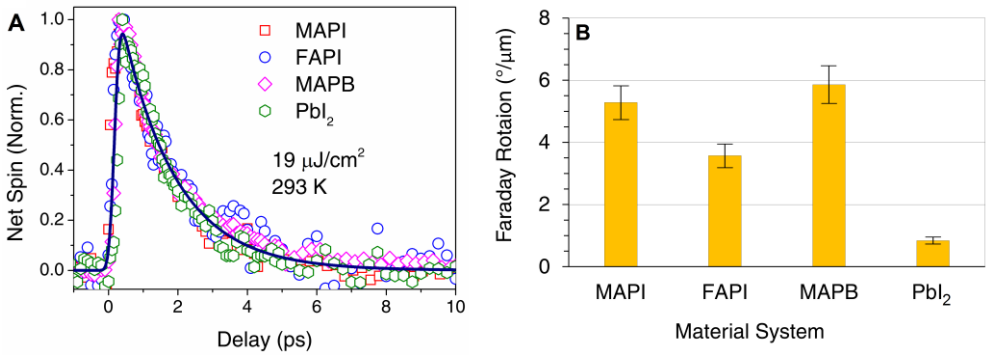

Figure 3.18 | Comparison of spin dynamics among the few 3D perovskite systems. (A) Normalized band-edge $|\sigma^+ - \sigma^-|$ signals from degenerate TA of MAPI (red square), FAPI (blue circle), MAPB (magenta diamond) and PbI_2 (green hexagon). (B) Faraday rotation per unit length of these materials at 293 K.

The comparison is studied by using degenerate TA to obtain the time-resolved band edge net spin population ($|\sigma^+ - \sigma^-|$), whose photobleaching signal is less sensitive to pump and probe wavelength (relatively broad bleaching spectrum). Here, our perovskite thin film samples MAPI ($E_g \approx 1.6$ eV [21]), FAPI ($E_g \approx 1.5$ eV [50]) and MAPB ($E_g \approx 2.3$ eV [21]) were spin-coated from 0.25 M of the respective precursor solutions (for MAPI it corresponds to 10wt%). Meanwhile, the PbI_2 thin film ($E_g \approx 2.4$ eV [51]) was spin-coated from

1 M solution. Since it has been well-established that these material systems have similar band-edge electronic structures of $|m_J = \pm 1/2\rangle$ [21, 49], the selection rule for circularly polarized excitation is expected to be similar as in for MAPI (Section 3.3.1). The comparison of their band-edge net spin dynamics is shown in **Figure 3.18**.

Figure 3.18A shows that the spin states relaxation from $|m_J = \pm 1/2\rangle$ to $|m_J = \mp 1/2\rangle$ in 3D perovskites families: MAPI, FAPI, and MAPB to possess similar dynamics. From this observation, it can be concluded that the spin relaxation channels in 3D lead halide OIHP originate significantly from the SOC by the Pb^{2+} cation; while the organic and halide components give insignificant contributions. This is further confirmed by measurement on the layered semiconductor PbI_2 thin film, which was discovered also to share similar spin-state dynamics. However, while they share similar optical-spin relaxation dynamics, the advantages of 3D OIHP system as compared to PbI_2 is the strength of light-matter coupling. This is shown in **Figure 3.18**B, where under similar pump excitation, the amplitude of the photoinduced FR is magnified by several folds. This result therefore highlights the advantage of the 3D OIHP to its purely inorganic PbI_2 counterpart, especially for optical spin-switching applications.

3.3.7 Summary

In summary, the study on the non-equilibrium photoexcited spin dynamics has been presented and discussed in this section. The novel key results can be summarized in these following few points:

1. Demonstration of optical excitation of perfectly *J*- (spin) polarized carriers at band edge, which decays in the order of few ps in MAPI, whose dynamics is well-explained by our simple two-level *J*-states model.
2. Assignment of Elliott-Yafet mechanism through carriers, impurities, and grain boundary scattering as the main spin relaxation mechanism, with weak spin-phonon interaction. This result implies that spin lifetime can be improved through better sample quality.

3. Demonstration of ultra-large photoinduced Faraday rotation in MAPI thin films, with photoinduced FR up to 10°/μm. To the best of our knowledge, this is the largest value that has been reported so far.
4. Understanding the effect of sample morphology on the spin dynamics, demonstrated by more symmetrical electrons and holes spin dynamics in toluene treated films, yet without improvement in the spin lifetime.
5. Assignment of Pb^{2+} cation as the major contributor of SOC in 3D lead halide OIHP, which results in spin relaxation.

3.4 Conclusions

In conclusion, through the study of optical-carrier-spin dynamics in 3D lead halide perovskites presented in this chapter, the prospect of 3D lead halide OIHP for opto-spintronic applications has been demonstrated and evaluated. In particular, MAPI holds great prospects for applications as ultrafast spin switches, due to its ultra-large photoinduced Faraday rotation. Further applications including spin-transporters or spin-injectors could also be made possible by improving the material fabrication techniques. While the basic understanding of the physics and mechanism behind the observed spin dynamics in this material system has been established through this study, further studies, especially for devices architectures and integration with other systems, are still required for the realization of OIHP-based opto-spintronics technology.

3.5 Bibliography

1. D. Bi, et al., *Efficient luminescent solar cells based on tailored mixed-cation perovskites.* Sci. Adv., 2016. **2**(1).
2. M. A. Green, A. Ho-Baillie, and H. J. Snaith, *The emergence of perovskite solar cells.* Nat. Photon., 2014. **8**(7): p. 506-514.
3. H. S. Jung and N.-G. Park, *Perovskite Solar Cells: From Materials to Devices.* Small, 2015. **11**(1): p. 10-25.
4. T. C. Sum and N. Mathews, *Advancements in perovskite solar cells: photophysics behind the photovoltaics.* Energy Environ. Sci., 2014. **7**(8): p. 2518-2534.

5. M. B. Johnston and L. M. Herz, *Hybrid Perovskites for Photovoltaics: Charge-Carrier Recombination, Diffusion, and Radiative Efficiencies.* Acc. Chem. Res., 2016. **49**(1): p. 146-154.
6. Z.-K. Tan, et al., *Bright light-emitting diodes based on organometal halide perovskite.* Nat. Nanotechnol., 2014. **9**(9): p. 687-692.
7. S. A. Veldhuis, et al., *Perovskite Materials for Light-Emitting Diodes and Lasers.* Adv. Mater., 2016. **28**(32): p. 6804-6834.
8. J. Xing, et al., *High-Efficiency Light-Emitting Diodes of Organometal Halide Perovskite Amorphous Nanoparticles.* ACS Nano, 2016. **10**(7): p. 6623-6630.
9. L. Dou, et al., *Solution-processed hybrid perovskite photodetectors with high detectivity.* Nat. Commun., 2014. **5**.
10. Y. Fang, et al., *Highly narrowband perovskite single-crystal photodetectors enabled by surface-charge recombination.* Nat. Photon., 2015. **9**(10): p. 679-686.
11. Y. Guo, et al., *Air-Stable and Solution-Processable Perovskite Photodetectors for Solar-Blind UV and Visible Light.* J. Phys. Chem. Lett., 2015. **6**(3): p. 535-539.
12. C. Liu, et al., *Ultrasensitive solution-processed perovskite hybrid photodetectors.* J. Mater. Chem. C, 2015. **3**(26): p. 6600-6606.
13. B. R. Sutherland, et al., *Sensitive, Fast, and Stable Perovskite Photodetectors Exploiting Interface Engineering.* ACS Photonics, 2015. **2**(8): p. 1117-1123.
14. N. Onoda-Yamamuro, T. Matsuo, and H. Suga, *Dielectric study of CH3NH3PbX3 (X = Cl, Br, I).* Journal of Physics and Chemistry of Solids, 1992. **53**(7): p. 935-939.
15. J. Qiu, et al., *All-solid-state hybrid solar cells based on a new organometal halide perovskite sensitizer and one-dimensional TiO2 nanowire arrays.* Nanoscale, 2013. **5**(8): p. 3245-3248.
16. S. Luo and W. Daoud, *Crystal Structure Formation of $CH_3NH_3PbI_{3-x}Cl_x$ Perovskite.* Materials, 2016. **9**(3): p. 123.
17. Q. Wang, et al., *Transition from the Tetragonal to Cubic Phase of Organohalide Perovskite: The Role of Chlorine in Crystal Formation of*

$CH_3NH_3PbI_3$ on TiO2 Substrates. J. Phys. Chem. Lett., 2015. **6**(21): p. 4379-4384.

18. A. Miyata, et al., *Direct measurement of the exciton binding energy and effective masses for charge carriers in organic-inorganic tri-halide perovskites.* Nat. Phys., 2015. **11**(7): p. 582-587.
19. J. Even, L. Pedesseau, and C. Katan, *Analysis of Multivalley and Multibandgap Absorption and Enhancement of Free Carriers Related to Exciton Screening in Hybrid Perovskites.* J. Phys. Chem. C, 2014. **118**(22): p. 11566-11572.
20. C. Sheng, et al., *Exciton versus Free Carrier Photogeneration in Organometal Trihalide Perovskites Probed by Broadband Ultrafast Polarization Memory Dynamics.* Phys. Rev. Lett., 2015. **114**(11): p. 116601.
21. K. Tanaka, et al., *Comparative Study on the Excitons in Lead-Halide-Based Perovskite-Type Crystals $CH_3NH_3PbBr_3$ $CH_3NH_3PbI_3$.* Solid State Commun., 2003. **127**(9–10): p. 619-623.
22. M. Saba, et al., *Correlated electron-hole plasma in organometal perovskites.* Nat. Commun., 2014. **5**.
23. M. B. Price, et al., *Hot-carrier cooling and photoinduced refractive index changes in organic-inorganic lead halide perovskites.* Nat. Commun., 2015. **6**.
24. L. M. Herz, *Charge-Carrier Dynamics in Organic-Inorganic Metal Halide Perovskites.* Annu. Rev. Phys. Chem., 2016. **67**(1): p. 65-89.
25. S. S. Lim, et al., *Modulating carrier dynamics through perovskite film engineering.* Phys. Chem. Chem. Phys., 2016.
26. A. Marchioro, *Interfacial Charge Transfer Dynamics in Solid-State Hybrid Organic-Inorganic Solar Cells*. 2014, EPFL.
27. R. L. Milot, et al., *Temperature-Dependent Charge-Carrier Dynamics in $CH_3NH_3PbI_3$ Perovskite Thin Films.* Adv. Funct. Mater., 2015. **25**(39): p. 6218-6227.
28. T. C. Sum, et al., *Spectral Features and Charge Dynamics of Lead Halide Perovskites: Origins and Interpretations.* Acc. Chem. Res., 2016. **49**(2): p. 294-302.
29. Y. Yang, et al., *Observation of a hot-phonon bottleneck in lead-iodide perovskites.* Nat. Photon., 2016. **10**(1): p. 53-59.

30. G. Xing, et al., *Long-Range Balanced Electron- and Hole-Transport Lengths in Organic-Inorganic $CH_3NH_3PbI_3$.* Science, 2013. **342**(6156): p. 344-347.
31. K. G. Stamplecoskie, J. S. Manser, and P. V. Kamat, *Dual nature of the excited state in organic-inorganic lead halide perovskites.* Energy Environ. Sci., 2015. **8**(1): p. 208-215.
32. L. Wang, et al., *Femtosecond Time-Resolved Transient Absorption Spectroscopy of $CH_3NH_3PbI_3$ Perovskite Films: Evidence for Passivation Effect of PbI2.* J. Am. Chem. Soc., 2014. **136**(35): p. 12205-12208.
33. P. Löper, et al., *Complex Refractive Index Spectra of $CH_3NH_3PbI_3$ Perovskite Thin Films Determined by Spectroscopic Ellipsometry and Spectrophotometry.* J. Phys. Chem. Lett., 2015. **6**(1): p. 66-71.
34. C.-W. Chen, et al., *Optical properties of organometal halide perovskite thin films and general device structure design rules for perovskite single and tandem solar cells.* J. Mater. Chem. A, 2015. **3**(17): p. 9152-9159.
35. C. Wehrenfennig, et al., *High Charge Carrier Mobilities and Lifetimes in Organolead Trihalide Perovskites.* Adv. Mater., 2014. **26**(10): p. 1584-1589.
36. H. Oga, et al., *Improved Understanding of the Electronic and Energetic Landscapes of Perovskite Solar Cells: High Local Charge Carrier Mobility, Reduced Recombination, and Extremely Shallow Traps.* J. Am. Chem. Soc., 2014. **136**(39): p. 13818-13825.
37. C. Zhang, et al., *Magnetic field effects in hybrid perovskite devices.* Nat. Phys., 2015. **11**(5): p. 427-434.
38. G. Xing, et al., *Low-Temperature Solution-Processed Wavelength-Tunable Perovskites for Lasing.* Nat. Mater., 2014. **13**(5): p. 476-480.
39. I. Žutić, J. Fabian, and S. Das Sarma, *Spintronics: Fundamentals and Applications.* Rev. Mod. Phys., 2004. **76**(2): p. 323-410.
40. S. A. Crooker, *Coherent Spin Dynamics of Carriers and Magnetic Ions in Diluted Magnetic Semiconductors,* in *Introduction to the Physics of Dilute Magnetic Semiconductor*, J. Kossut; and J.A. Gaj;, Editors. 2010, Springer. p. 305-334.
41. S. A. Crooker, D. D. Awschalom, and N. Samarth, *Time-resolved Faraday rotation spectroscopy of spin dynamics in digital magnetic heterostructures.*

Selected Topics in Quantum Electronics, IEEE Journal of, 1995. **1**(4): p. 1082-1092.

42. S. Kahl, V. Popov, and A. M. Grishin, *Optical transmission and Faraday rotation spectra of a bismuth iron garnet film.* J. Appl. Phys., 2003. **94**(9): p. 5688-5694.
43. M. I. Dyakonov, *Basics of Semiconductor and Spin Physics*, in *Spin Physics in Semiconductors*, M.I. Dyakonov, Editor. 2008, Springer Berlin Heidelberg. p. 1-28.
44. M. W. Wu, J. H. Jiang, and M. Q. Weng, *Spin dynamics in semiconductors.* Physics Reports, 2010. **493**(2–4): p. 61-236.
45. Y. Deng, Z. Xiao, and J. Huang, *Light-Induced Self-Poling Effect on Organometal Trihalide Perovskite Solar Cells for Increased Device Efficiency and Stability.* Adv. Energy Mater., 2015. **5**(20): p. 1500721-n/a.
46. Z. Xiao, et al., *Giant switchable photovoltaic effect in organometal trihalide perovskite devices.* Nat. Mater., 2015. **14**(2): p. 193-198.
47. N. J. Jeon, et al., *Solvent engineering for high-performance inorganic-organic hybrid perovskite solar cells.* Nat. Mater., 2014. **13**(9): p. 897-903.
48. R. J. Stewart, et al., *Approaching Bulk Carrier Dynamics in Organo-Halide Perovskite Nanocrystalline Films by Surface Passivation*. J. Phys. Chem. Lett., 2016, **7**(7): p. 1148-1153.
49. E. Mosconi, T. Etienne and F. D. Angelis, *Rashba Band Splitting in Organohalide Lead Perovskites: Bulk and Surface Effects*. J. Phys. Chem. Lett., 2017, **8**(10): p. 2247-2252.
50. G. E. Eperon, et al., *Formamidinium lead trihalide: a broadly tunable perovskite for efficient planar heterojunction solar cells.* Energy Environ. Sci., 2014. **7**(3): p. 982-988.
51. E. Doni, G. Grosso, and G. Spavieri, *Band structure and absorption edge of PbI2.* Solid State Commun., 1972. **11**(4): p. 493-497.

CHAPTER 4:

OPTICAL-SPIN DYNAMICS IN 2D ORGANIC-INORGANIC HYBRID LEAD HALIDE PEROVSKITES

This chapter presents the results of our optical studies directed to uncover the fundamental understanding of the transient photoexcited optical-spin dynamics in the 2D lead halide perovskite. Here, $(C_6H_5C_2H_4NH_3)_2PbI_4$ was used as the representative of 2D perovskite material system. This perovskite is known to be strongly excitonic with binding energy up to a few hundred of meV. The first half of this chapter focused on elucidating the origin of transient spectral features and the relaxation dynamics of photoexcited excitons in $(C_6H_5C_2H_4NH_3)_2PbI_4$. Strong exciton-phonon coupling was observed in the system, manifested in oscillation of the transient absorption signal. The second half of this chapter focused on the study of spin-selective optical Stark effect in $(C_6H_5C_2H_4NH_3)_2PbI_4$, where the exciton spin-state can be selectively blue shifted by a red-detuned circularly polarized photon. It was also discovered that this interaction could be tuned by simply modifying the dielectric contrast between the organic and inorganic layer in 2D perovskites.

4.1 Linear properties

While the 3D lead halide OIHP system has been the central focus for research due to its outstanding optoelectronic properties, recently much emphasis has also been directed to the 2D family of excitonic perovskites as a contender for solar cells [1] and LED applications [2,3]. Unlike the 3D system where the organic and inorganic constituents are uniformly distributed, the 2D analog (*e.g.*, $(C_6H_5C_2H_4NH_3)_2PbI_4$ – hereafter called as PEPI) comprises of alternating organic ($C_6H_5C_2H_4NH_3^+$) and inorganic ($[PbI_6]^{4-}$ octahedron) layers forming naturally self-assembled multi-quantum-well (MQW) structures. Such unique crystal structure gives rise to remarkable optical properties, distinct from its 3D counterpart. In this section, characterizations of the structural and linear optical properties are presented and discussed. These linear properties have important implications for the nonlinear dynamics, which are of interest for this study. The large dielectric contrast between the barrier and the well gives rise to *dielectric confinement effect* which enhances its exciton binding energy (*i.e.* hundreds of meV) [4-6] and oscillator strength [6-8]. These unique properties of 2D perovskites point to a highly promising system for realizing perovskites based opto-spintronic technological applications. Herein, we focus on PEPI as the representative material system for 2D lead halide OIHP.

4.1.1 Structural properties

As mentioned, the uniqueness of the 2D lead halide OIHP lies in its self-assembled MQW structures constituted of alternating organic and inorganic layer. These layers are bound together by *van der Waals* force. For the case of PEPI the organic and inorganic layer thicknesses (energy gap) are given by ~1 nm (~4.2 eV) and ~0.6 nm (2.39 eV), which acts as a barrier and well in MQW structure, respectively [9,10]. **Figure 4.1**A shows the XRD spectrum of the PEPI thin film. Only a single peak is apparent at $2\theta = 5.4^{o}$, which corresponds to the (002) diffraction plane. This (002) plane refers to the planar layer of the inorganic $[PbI_4]^{-4}$ octahedrons (*i.e.* single unit cell contains 2 inorganic layers) [6]. The single well-defined peak in the XRD spectrum of this polycrystalline thin film also implies that the 2D perovskite planes are parallel to the substrate plane. The structure of 2D perovskites is illustrated in **Figure 4.1**B. From the

(002) XRD peak, the interlayer distance between these two inorganic slabs is deduced to be d = 1.64 nm, while the width of the $[PbI_4]^{-4}$ octahedron is known to be ~0.63 nm [6,9].

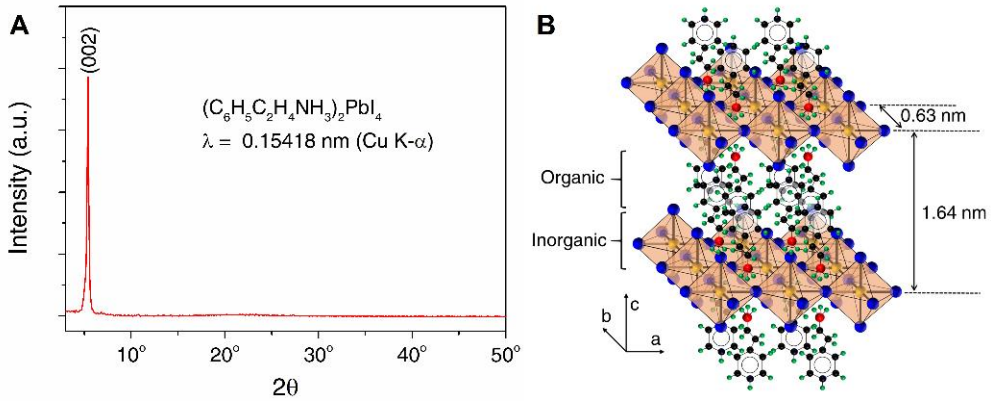

Figure 4.1 | PEPI crystal structure. (A) XRD spectrum of PEPI, obtained by Cu K-α source with λ = 1.5418 Å. (B) Illustration of PEPI crystal structure with alternating organic-inorganic layers.

4.1.2 Optical properties

To understand the basic linear optical properties of PEPI, we performed measurements of absorption coefficient α and photoluminescence (PL) spectra on PEPI thin film. The result is shown in **Figure 4.2**A. We observed a strong peak in the absorption coefficient spectrum before the band onset, which verifies that this system is strongly excitonic. Large Stokes shift of ~9 nm from the absorption peak at 516 nm to the PL peak at 525 nm was also observed, owing to dense vibrational states of the system [11]. For materials with parabolic direct band-edge, it is known from the Tauc relation that $(h\nu\alpha)^2 \propto (E_g - h\nu)$. From this relation, we can deduce the bandgap E_g of the PEPI. The Tauc plot of PEPI thin film is shown in **Figure 4.2**B. From the plot, we deduced the bandgap of PEPI in room temperature to be ~2.55 eV, which corresponds to an exciton binding energy of 150 meV >> k_BT = 26 meV. Such strong binding energy arises from the dielectric confinement effect. The implication is that excitons are the primary photoexcited species (~99%) in PEPI, in contrast to the primarily free carrier species in the 3D perovskite MAPI system.

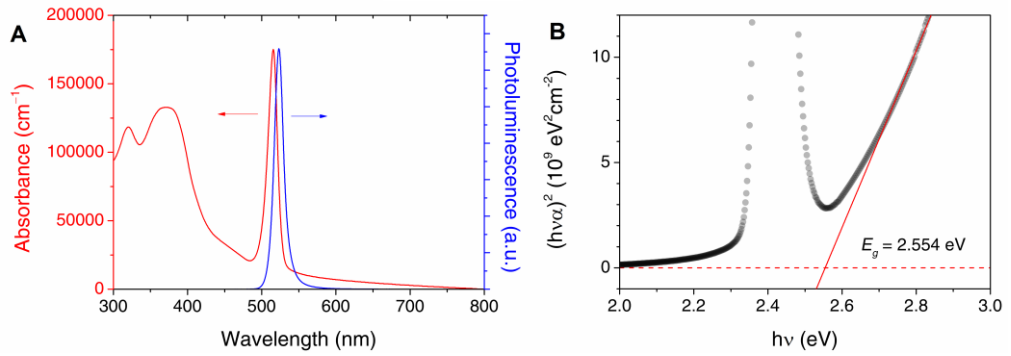

Figure 4.2 | Linear optical properties of PEPI thin film. (A) The absorption coefficient α (red) and the PL emission (blue) of PEPI thin film. (B) Measurement of PEPI bandgap from the Tauc plot. The bandgap is estimated to be 2.554 eV, which gives exciton binding energy of 150 meV.

4.1.3 Optical selection rules

In this 2D lead halide perovskite system, this lowest exciton state originates from strongly modified conduction band (CB) and valence band (VB). The presence of strong crystal field and SOC strongly affects the CB, which arises mainly from the Pb-6p orbital forming a *p*-like band; while leaving the VB, which arises mainly from the Pb-6s and I-5p orbital forming an *s*-like band, to be relatively intact [4-6,12]. The organic component does not play a significant role in determining the electronic structure [6].

Taking account of the crystal field and SOC, the electronic structures of both the VB maximum and CB minimum are described by the angular momentum quantum number J = 1/2, and magnetic quantum number $m_J = \pm 1/2$; which is also applicable for exciton; forming the doubly degenerate $|m_J = \pm 1\rangle$ states [4]. By conservation of angular momentum, the optical selection rule in 2D lead halide perovskites is given by $\Delta m_j = \pm 1$, as a single photon may carry angular momentum of $\pm\hbar$. This selection rule is illustrated in **Figure 4.3**. Note that this requirement for magnetic quantum number holds for the case of photon polarization $\boldsymbol{E}$ parallel to the *c*-axis (*i.e.*, $\boldsymbol{E} \perp \boldsymbol{c}$ or light direction perpendicular to the substrate plane). For the case of photon polarization parallel to the *c*-axis (*i.e.* $\boldsymbol{E} // \boldsymbol{c}$, or light direction parallel to the substrate plane) weak triplet optical transition with $\Delta m_j = 0$ may also be observed [4,6]. In this study, we were concerned only with the $\boldsymbol{E} // \boldsymbol{c}$ case, as we restricted our beams to be perpendicular to the sample plane.

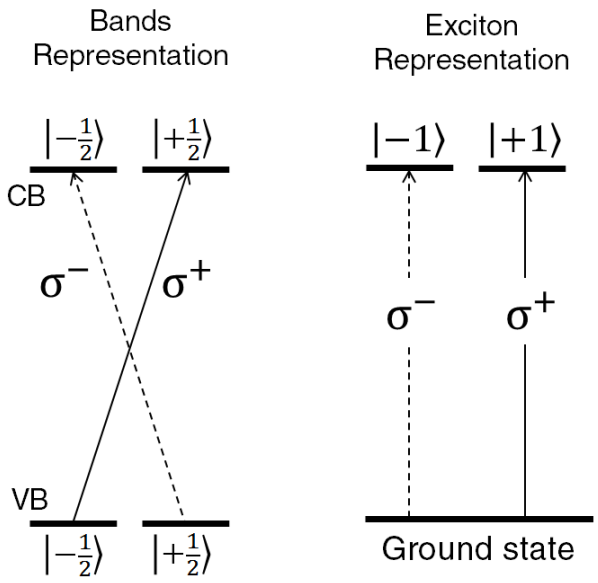

Figure 4.3 | Optical selection rules for circularly polarized photon. The selection rules are presented in bands (left) and exciton (right) representations. Different photon helicity will excite exciton spin states.

4.1.4 Section Summary

In summary, we establish few conclusions on based on our experimental results and prior literature. Our solution processed PEPI thin films forms a layered structure with alternating organic and inorganic slabs, mainly aligned parallel to the quartz substrate, with an inter-plane distance of ~1.64 nm. The linear optical characterizations of this PEPI thin film show a strong excitonic absorption with large PL Stokes' shift. We determined the band edge of our PEPI thin film to be ~2.55 eV with exciton binding energy of 150 meV. Such large exciton binding energy results in excitons as its primary photoexcited species. The electronic structure of PEPI is strongly modified by crystal field and SOC, which results in lowest exciton states with $m_J = \pm 1$. This allows selective photoexcitation of exciton spin states using circularly polarized light.

4.2 Non-equilibrium exciton dynamics

While the 2D OIHP material system has been known and studied for more than two decades, most of those studies focused on either the linear optical properties [4,6,9,13-17] or devices such as LED [2,3] and thin film transistors

[18-21]. To the best of our knowledge, there were very limited studies that focus on the ultrafast nonlinear/non-equilibrium dynamics in this excitonic material system, where strong exciton-photon from oscillator strength enhancement would give rise to numerous exotic optical phenomena. This section is therefore dedicated to develop a fundamental understanding of the photophysics of non-equilibrium photoexcited excitons in the 2D lead halide perovskite system. The study was carried out with the white light TA spectroscopy as the main characterization technique, and with PEPI as the main representative material system.

4.2.1 Assignment of TA spectrum

To uncover the ultrafast nonlinear dynamics of this material system, we must first understand the existing transient optical transitions due to strong optical excitation, which in our case was probed by the commercial *HELIOS*^{TM} white light TA spectroscopy system. The TA spectra of PEPI thin film at various probe delay positions, photoexcited by 400 nm pump with a fluence of 8 μJ/cm^2, are shown in **Figure 4.4**A. There are 3 prominent features which can be observed from these spectra: photoinduced absorption (PA) peak at 495 nm (called as PA1), a strong photobleaching peak at 516 nm (called as PB) and another PA peak at 528 nm (called as PA2). The kinetics of each of this peak is shown in **Figure 4.4**B.

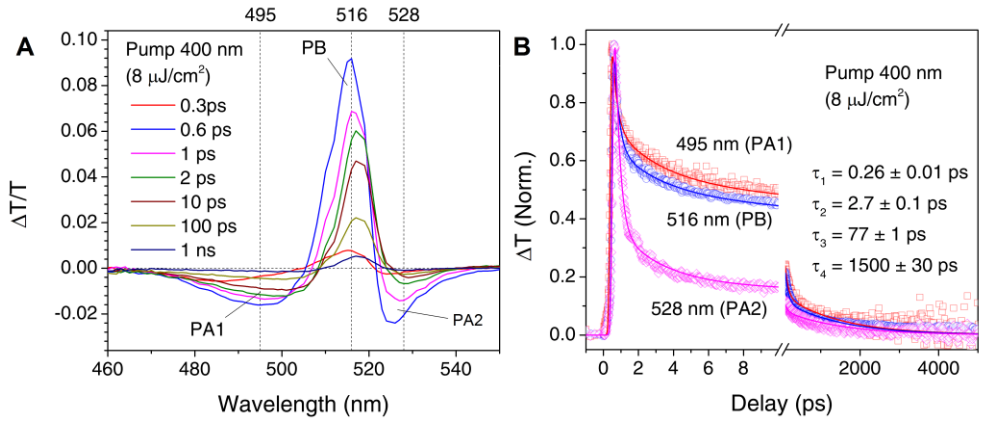

Figure 4.4 | White light TA study on PEPI thin film. (A) TA spectra at several delay positions and (B) their kinetics at 495 nm (red square), 516 nm (blue circle) and 528 nm (magenta diamond). The sample was excited by 400 nm (8 μJ/cm^2) pump.

For the assignment of the origins of these spectral features, it is straightforward to assign the PB peak as the ground state bleaching (*i.e.* due to the state-filling of the ground state), as it spectrally coincides very well with the excitonic absorption peak at 516 nm (**Figure 4.2**A). However, it is nontrivial to assign the origins of the PA1 and PA2. To gain more insight on the issue, we performed fitting on the kinetics at these three spectral positions (**Figure 4.4**B) using a multi-exponential decay function:

$$\frac{\Delta T}{T}(t) = \frac{1}{2}\sum_{i=1}^{N} A_i \left[1 + \mathrm{erf}\left(\frac{t}{r} - \frac{r}{2\tau_i}\right)\right] e^{-t/\tau_i}. \qquad (4.1)$$

Here, t is the time delay of the probe; r is the laser pulse width; A_i is the amplitude of each lifetime component; and τ_i is the exponential decay lifetime. The number of components N was chosen to be a minimum such that they can satisfactorily fit the experimental data, which in our case $N = 4$. From the fitting, we discovered that the kinetics at these 3 wavelengths could be fitted with 4 similar lifetimes: $\tau_1 = 0.26 \pm 0.01$ ps; $\tau_2 = 2.7 \pm 0.1$ ps; $\tau_3 = 77 \pm 1$ ps; and $\tau_4 = 1500 \pm 30$ ps. The origins of these 4 relaxation lifetimes will be discussed below. One important implication of these shared lifetimes is that these 3 features likely originate from optical transition involving a similar excited state. In such case, we posited that the amplitudes of these 3 features would reflect the population of the shared excited state, *i.e.* the first excitonic state at ~2.4 eV.

Figure 4.5A shows the TA spectrum of PEPI at 5 ps delay. The TA spectrum can be deconvolved into 3 Lorentzian peaks; each of the peaks corresponds to PA1, PB and PA2 transitions. The Lorentzian nature of these peaks signifies the excitonic nature of these 3 transient optical transitions. Assuming our hypothesis of transitions from the shared excited state, these 3 peaks should share the same dynamics. Meanwhile, different amplitudes of the first decay component A_1 originates from the thermalization process, where the photoexcited excitons redistribute themselves to follow the Bose-Einstein distribution. The existence of such thermalization process is evident from

Figure 4.4A, where the PB peak narrows and is slightly red shifted after the first ps.

During the thermalization process, the evolving photoexcited non-thermalized exciton population distribution creates ratio changes of the spectral overlap between the exciton distribution and each of the transition probability of these 3 TA spectral features. This ratio changes, therefore, result in different A_1 components, as the overlap of each feature evolves differently. This process is illustrated in **Figure 4.5**B. Such fast lifetime component arising from the exciton thermalization process is also commonly observed in excitonic inorganic MQW [22].

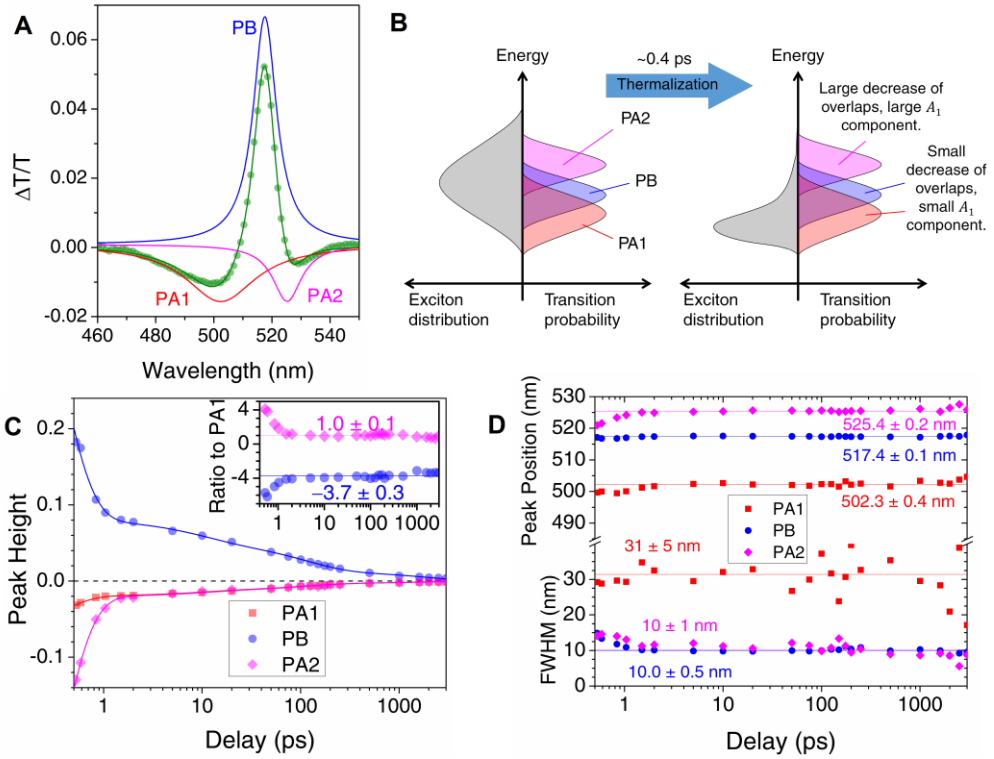

Figure 4.5 | Post thermalization evolution of TA spectra in PEPI. (A) TA spectrum of PEPI photoexcited by 400 nm (8 μJ/cm^2) pump at 5 ps probe delay, well-fitted by 3 Lorentzian peaks, named PA1, PB, and PA2. (B) Thermalization process causes ratio change between spectral overlaps of the transition probabilities of PA1, PB, and PA2 with the exciton distribution, which results in different A_1 between these 3 peaks. (C) Time evolution of the fitted Lorentzian peaks at different delay positions. Inset: height ratios of PB/PA1 and PA2/PA1. (D) The time evolution of FWHMs and peak positions of the 3 Lorentzian peaks. PA1, PB and PA2 are shown in red, blue and magenta, respectively.

The hypothesis of the shared transient states is also evident from **Figure 4.5**C which shows the dynamics of these fitted peaks. After the thermalization (t > 2 ps), the photoexcited exciton distribution is expected to become more or less static, where there is no longer change in the ratio of overlaps between these features. In this phase, the amplitudes of these 3 peaks are expected to be proportional to the population of the shared excited state. The inset of **Figure 4.5**C shows constant height ratios of PB/PA1 and PA2/PA1 for t > 2 ps, which clearly indicates that these 3 spectral peaks evolve with similar dynamics. These dynamics in **Figure 4.5**C can be well-fitted by eq. (4.1) with $N = 4$. The fitting yields 4 shared lifetimes of 0.25 ± 0.01 ps, 9 ± 3 ps, 110 ± 20 ps and 2000 ± 600 ps. The first fitted lifetime is consistent with the thermalization timescale, while different A_1 component for each peak. The other 3 post-thermalization lifetimes are consistent with the lifetimes obtained from fitting in **Figure 4.4**B, with similar $A_2 : A_3 : A_4$ ratio, which further supports our hypothesis. **Figure 4.5**D shows analysis of the FWHMs and peak positions of these 3 optical transition peaks. There is no notable change of the peak positions and FWHMs of these peaks post-thermalization, which implies a static exciton distribution as the excitons relaxes.

To further pinpoint the optical transitions responsible for these 3 peaks, we performed white light TA measurement with resonant excitation and circular polarization control, performed by our home built setup. By using circularly polarized light we were able to selectively excite the desired exciton J- (spin-) states, and hence deduced the spin structure of the existing transient optical transition. Such photoinduced spin polarization is analogous to our work for MAPI [23] reported in Chapter 3, where the absorption of σ^+/σ^- generates J-polarized (or spin-polarized) carriers. In the case of PEPI, it generates spin-polarized excitons. The TA spectra of co- and counter-circular pump-probe polarization pumped by 515 nm (21 μJ/cm^2) at various delay positions are shown in **Figure 4.6**A and B, respectively. At early time dynamics ($t = 0.5$ ps), asymmetrical differential-like shape signals were observed in the co-circular (**Figure 4.6**A), but not on the counter-circular case. This is due to the contribution of the spin-selective optical Stark effect (OSE). OSE is an energy-

shift of exciton absorption due to strong interaction with photon near the resonant frequency. This phenomenon will be discussed in greater detail in Section 4.3. Here, 3 similar spectral features by resonant excitation were observed at later time delay ($t > 2$ ps), as in the case of 400 nm excitation. Since the 515 nm pump only excites the lowest exciton state, it validates our assignment of transient optical transitions PA1, PB and PA2 to involve the lowest exciton state as the shared transient state. Note that no notable red shift of the exciton peak is observed in the case of resonant excitation.

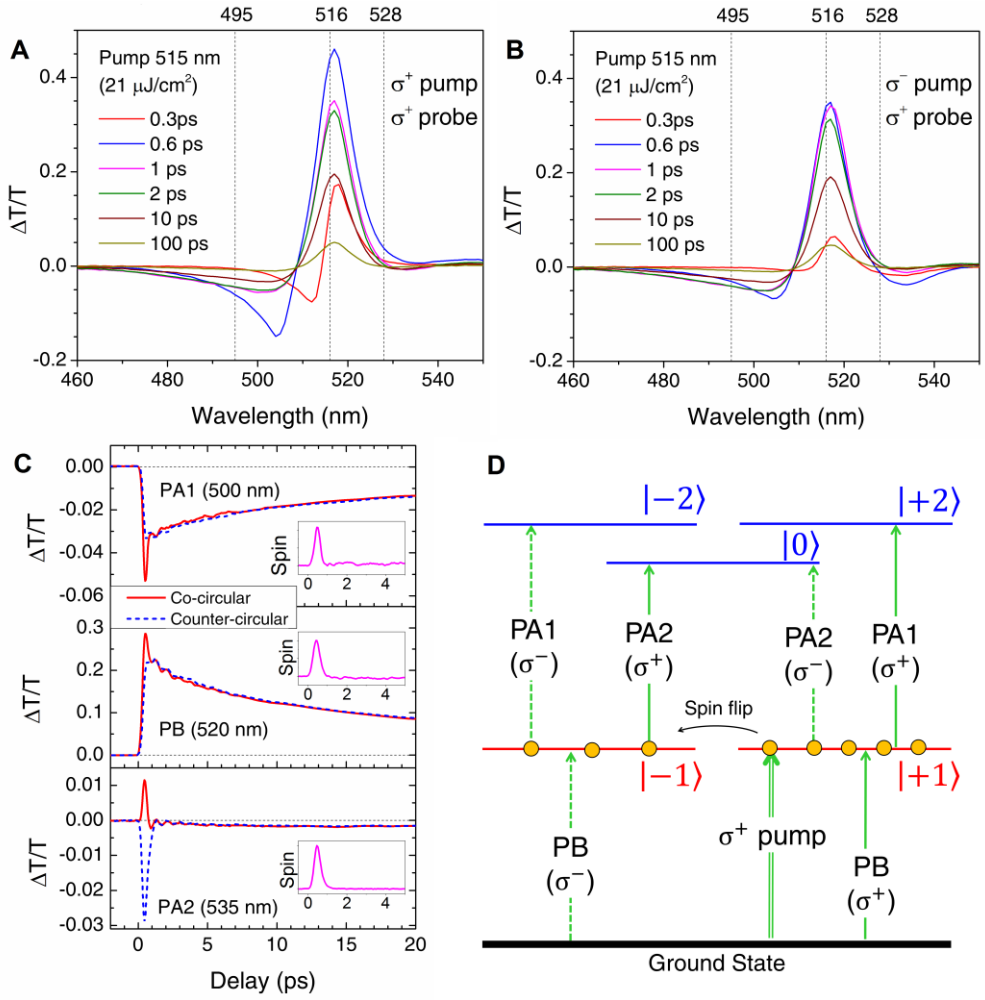

Figure 4.6 | TA studies on PEPI with resonant pump excitation. (A) Co-circular and (B) counter-circular TA spectra at various delay positions. (C) The kinetics of co- (red solid) and counter-circular (blue-dashed) polarization, probed at PA1 (500 nm), PB (520 nm) and PA2 (535 nm) regions. All experiments were performed with 515 nm (21 μJ/cm^2). Inset: the net spin population obtained from $|\sigma^+ - \sigma^-|$ probe. (D) Model of the transient optical transitions in PEPI.

Figure 4.6C shows the kinetics of excitons probed at the PA1 (500 nm), PB (520 nm) and PA2 (535 nm) regions. The most notable differences between the two polarizations happen at early time dynamics ($t < 1$ ps), where PA1 peak displays 'fast rise' while PA2 peak displays 'slow rise' for co-circular case; and vice versa where PA1 peak displays 'slow rise' while PA2 peak displays 'fast rise' for counter-circular case. On the PB peak, such 'fast rise' for co-circular and 'slow rise' for counter-circular at $t < 1$ ps can also be observed. The responsible phenomenon is the photoexcitation of the spin-polarized excitons, which is similar to the observation in 3D perovskite system. The co- and counter-circular signals then merge together in timescale of < 0.5 ps, which implies ultrafast exciton spin relaxation in PEPI. Similar signal merging is also observed on PA1 and PA2 peaks. The insets in **Figure 4.6**C shows the net exciton spin population obtained by subtracting the co- and counter-circular signal, which yield fitted exciton spin lifetime of 0.11 ± 0.1 ps. Also, note that the oscillatory signal observed originates from the strong exciton-phonon coupling, which will be discussed in greater detail later. Note that there is no dependence of pump-probe polarization observed for excitation with 400 nm pump.

From these peculiar behaviors of peaks 'fast rise' and 'slow rise' at different spectral regions, we were able to identify the states which are responsible for the observed transient optical transitions. The proposed model for the involved states $|m_J\rangle$ is shown in **Figure 4.6**D. Without any loss of generality, we assume photoexcitation by σ^+ pump, which populates only the $|+1\rangle$ state. The populated $|+1\rangle$ yields a fast-rise of σ^+ PB probe due to state filling effect together with slower rise of σ^- PB probe. This 'fast rise' is quickly followed by fast decay for co-circular PB signal and merging with the counter-circular PB signal due to exciton spin relaxation. The co- and counter-circular PA1 probes shows similar behaviors.

Having established that these transitions come from the first exciton state, conservation of angular momentum will only allow photoinduced absorption of σ^+ probe with $\Delta m_J = +1$, which implies σ^+ PA1 transition occurs from the populated $|+1\rangle$ to $|+2\rangle$ state. The spin relaxation which depopulates the $|+1\rangle$ state and populates $|-1\rangle$ state, which then allows the $|-1\rangle$ to $|-2\rangle$ transition to

occur and be detected by σ^- PA1 probe. For the case of PA2 the fast rise of σ^- probe (or counter-circular) implies that the transition occurs from $|+1\rangle$ to $|0\rangle$ state. The weak photobleaching for co-circular signal comes from the tail of PB peak. The population of $|-1\rangle$ state due to spin relaxation then allows the $|-1\rangle$ to $|0\rangle$ transition by σ^+ probe to occur, which give rise to σ^+ PA2 probe signal. A schematic of these processes is depicted in **Figure 4.6**D. Note that these states are optically inaccessible from ground state via linear absorption study ($i.e. \Delta m_J = 0, \pm 2$).

4.2.2 Assignment of exciton relaxation dynamics

Having established the assignments of the existing optical transition, we proceed with the study of exciton relaxation dynamics. The fluence dependent kinetics of PEPI thin film pumped at 400 nm and probed at 517 nm is shown in **Figure 4.7**A. The experiments were performed by using our home-built white light TA setup. The kinetics are global-fitted by eq. (4.1) (with $N = 4$), with the 4 lifetimes as the shared parameter. The fitting yields lifetime of $\tau_1 = 0.43 \pm 0.02$ ps; $\tau_2 = 8.5 \pm 0.2$ ps; $\tau_3 = 90 \pm 2$ ps; and $\tau_4 = 1500 \pm 30$ ps, which is consistent with our fitting in **Figure 4.4**B and **Figure 4.5**C, which reaffirms the reproducibility of results.

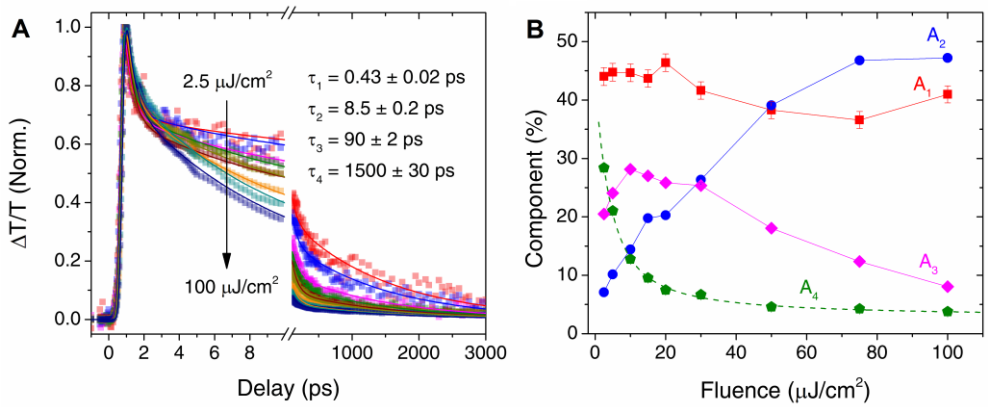

Figure 4.7 | Relaxation kinetics of PEPI thin film. (A) Fluence dependent TA relaxation kinetics of pumped by 400 nm and probed at 517 nm, fitted by eq. (4.1) with $N = 4$. (B) The contribution of each lifetime component as function of pump fluence. The A_4 component is well-fitted with eq. (4.3).

The contribution of each lifetime component to the relaxation process is plotted in **Figure 4.7**B. In the previous section, it has been established that the first lifetime-component can be assigned to ultrafast thermalization process of the photoexcited excitons, with relaxation time constant within < 0.5 ps. Since the fraction of excitons that undergo thermalization/redistribution will not change with exciton density, this is consistent with the observed A_1 behavior, which shows independency to pump fluence. Meanwhile, the contribution from A_2 component is observed to increase with fluence, followed by concomitant drop of contribution from A_3 component, which signifies weight transfer from A_3 to A_2 with increasing fluence. It can therefore be concluded that A_2 originates from a higher order density-dependent process than A_3. Here, since the lifetime τ_3 matches very well with the monomolecular lifetime elucidated by time-resolved PL measurement of PEPI (~100 ps) [24], we assign A_3 process as the monomolecular recombination (*i.e.* density independent process). The A_2 process can hence be assigned to exciton-exciton annihilation process (*i.e.* density dependent process), which happens in faster timescale of ≤ 10 ps.

Figure 4.7B also shows a decrease in the contribution from A_4 as a function of pump fluence, which is similar to the characteristics of a trap filling process. This is also consistent with its observed long lifetime expected for a process involving trap states. To further affirm this assignment, we utilized a simple phenomenological model to simulate the behavior of the trap states contribution as a function of pump fluence. Consider a system with total trap density of n_T^0, the rate of excitons trapping $dn_T(t)/dt$ is expected to be proportional to the trapping rate k_T and the number of un-trapped excitons $n(t)$:

$$\frac{dn_T(t)}{dt} = k_T\big(n_T^0 - n_T(t)\big)n(t). \tag{4.2}$$

Given the total number of photoexcited excitons n_0, we can straightforwardly solve the differential equation to obtain the fraction of trapped excitons:

$$x_{\mathrm{Trap}}(n_0) = \frac{n_T(\infty)}{n_0} = x_0 + 100\% \times \frac{n_T^0}{n_0}(1 - e^{-\gamma n_0}). \tag{4.3}$$

Here, x_0 is an additional offset and γ is a constant, with $\int_0^\infty n(t)dt \propto n_0$. **Figure 4.7**B shows that A_4 component contribution is well fitted by eq. (4.3), which affirms our assignment of A_4 to originate from trapped exciton. Given the absorption coefficient of PEPI at 400 nm to be ~9×10^4 cm^{-1} (**Figure 4.2**A), the fitting yields trap density of $(1.7 \pm 0.1) \times 10^{17}$ cm^{-3}. This trap state density is in the same order of magnitude as in its MAPI thin films [25-27]. Additional small fluence independent ($x_0 = 2.7\% \pm 0.2\%$) offset is also elucidated by the fitting. This offset might come from the contribution of triplet states ($J_z = 0$) weak transition known in 2D lead perovskites [4] to A_4.

4.2.3 Coherent exciton-phonon coupling

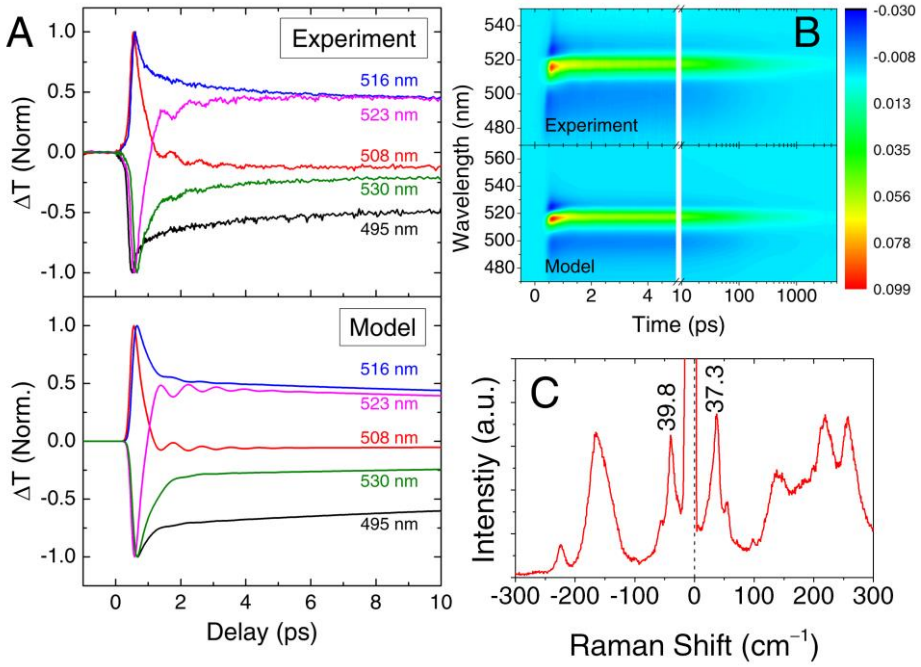

Figure 4.8 | Strong exciton-phonon coupling in PEPI thin film. (A) Comparison of the experimental result (top) and model (bottom) of the first 10 ps kinetics at 5 different probe wavelengths. The kinetics shows strong oscillation only near the PB/PA crossing wavelengths (508 nm and 523 nm). (B) The experimental result (top) and model (bottom) of $\Delta T/T$ TA spectra of PEPI thin film pumped by 400 nm. (c) Low energy Raman study on PEPI thin film, showing a labeled pair of Stokes and anti-Stokes with energies match to the oscillation frequency.

Another fascinating phenomenon uncovered by our study is the observation of oscillatory signals in the TA kinetics of PEPI. **Figure 4.8**B (top) shows the contour plot of TA spectrum of PEPI thin film photoexcited at 400 nm (8 μJ/cm^2) up to 5 ns probe delay. Based on our model of transient optical transition in **Figure 4.6**D, we created a phenomenological model to simulate the experimental result. The simulation result is shown in **Figure 4.8**B (bottom), which satisfactorily reproduces the general spectral features and kinetics obtained from the experiments with R^2 = 0.97. The details of this phenomenological model can be found in the Appendix B. This model affirms our previous assignment of the spectral features and is also crucial for understanding the origin of the observed oscillatory behavior. The experimental early first 10 ps TA kinetics of PEPI thin film at 5 different probe wavelengths is shown in **Figure 4.8**A (top). Peculiarly, the oscillatory signals are observed the strongest at the PA1/PB (508 nm) and the PB/PA2 (516 nm) crossing points. Away from these crossing points, the oscillatory signals diminish. The fitting of the oscillatory component yields a frequency of 1.15 ± 0.05 THz (corresponds to the energy of 4.8 ± 0.2 meV) and a decay lifetime of 1.2 ± 0.2 ps.

The observation of strong oscillatory component only near the crossing points can be explained by assigning the origin from the oscillation of the lowest exciton energy level. This hypothesis is proven by incorporating an additional small energy oscillation (~2 meV amplitude) of the lowest excited state into our model. The result is shown in **Figure 4.8**A (bottom). It is clear that incorporation of small oscillation of the exciton energy in our model satisfactorily reproduce the experimental result, where notable oscillations are only observed around the crossing points (*i.e.* at ~508 nm and ~523 nm). The phase and frequency of the oscillation are independent of the pump fluence.

More insights were obtained from low energy Raman measurement on drop-casted PEPI sample. The result is shown in **Figure 4.8**C, where a pair of Stokes peak (37.3 cm^{-1} = 4.6 meV) and anti-Stokes peak (39.8 cm^{-1} = 4.9 meV) is observed. The energy of these peaks corresponds very well with the energy of the TA oscillatory component, implying that the oscillation is related to the vibrational/phonon states. Hence, it can be concluded that the ultrafast pump excitation induces the formation of coherent phonons, which then strongly interact with the photoexcited excitons. It is noteworthy to mention that similar

but much stronger oscillatory behavior is also observed for resonant pumping (**Figure 4.6**C). In this case, the oscillation can still be observed at probe wavelengths away from the crossing points. This is because the excitation by resonant pump creates much higher exciton population and hence results in much stronger interaction. Nonetheless, similar oscillation frequencies and decay times are obtained from 400 and 515 nm pumping. This is consistent with our assignment of the oscillation to originate from the interaction between these coherent phonons and lowest energy excitons.

These findings uncover new insights and understanding transient dynamics and coherent interactions in 2D perovskite system. To the best of our knowledge, this is the first report on the interplay of photoexcited excitons and coherent phonons and their relaxation mechanisms in 2D perovskite system. Nevertheless, further studies are still required for the assignment of the phonon modes and their generation mechanisms.

4.2.4 Section Summary

In summary, we reported a study of photoexcited non-equilibrium exciton dynamics established in 2D lead halide perovskites PEPI. The novel key findings of the study can be summarized in the following points.

1. Assignment of TA spectrum in PEPI thin film. We determined the origin of the spectral features and the electronic states which responsible for the transient optical transition.
2. Understanding of the non-equilibrium exciton relaxation dynamics. The exciton relaxation mechanisms involve exciton-exciton annihilation, radiative recombination, and trap-assisted recombination, depending on the excitation pump fluence. We estimated the trap state density in PEPI thin film to be $(1.7 \pm 0.1) \times 10^{17}$ cm^{-3}, which is in the same order of magnitude as in its 3D counterparts.
3. Observation of strong exciton-coherent phonon interaction. By using our phenomenological model to reproduce the TA spectra, we established that oscillation of TA kinetics around the PA1/PB and the PB/PA2 crossing points originates from the coherent oscillation of the lowest exciton energy level as result of interaction with phonons.

4.3 Spin-selective optical Stark effect (OSE)

Apart from the strong coherent exciton-phonon interaction observed, another interesting strong interaction phenomenon involving excitonic systems with enhanced oscillator strength such as 2D perovskites, is the strong coupling between the photons and exciton states. This strong interaction is manifested in the *Optical Stark Effect* (OSE), which is a transient blue shift of the exciton energy state due to exciton states hybridization with red-detuned incident light (photon-energy below the absorption level). OSE is a coherent, third-order nonlinear light-matter interaction arising from the hybridization between photons and electronic states (known as the *photon-dressed state*). Here, we will start by first discussing the fundamental physics concept of photon-dressed state.

4.3.1 Theory of photon-dressed state

We start by applying the Jaynes-Cummings model of interaction in a system with two optically coupled eigenstates $|1\rangle$ and $|2\rangle$ with energy E_1 and E_2, respectively, *i.e.*, $E_2 - E_1 = \hbar\omega_0 > 0$, in the presence of electromagnetic radiation with photon energy $\hbar\omega$. The total Hamiltonian of the system comprises of three distinct components:

$$H_S = E_1|1\rangle\langle 1| + E_2|2\rangle\langle 2| \tag{4.4}$$

$$H_L = \hbar\omega\left(\hat{a}^\dagger\hat{a} + \frac{1}{2}\right) \tag{4.5}$$

$$H_I = \hbar\omega_R\left(|1\rangle\langle 2|\hat{a}^\dagger + |2\rangle\langle 1|\hat{a}\right) \tag{4.6}$$

where H_S, H_L, and H_I are the Hamiltonian of the two-level system, the electromagnetic (EM) radiation, and the interaction between them, respectively. The *Rabi frequency* is given by $\Omega_R = 2\omega_R\sqrt{n+1}$, where ω_R is the *vacuum Rabi frequency* and n is the number of photons in the system. The vacuum Rabi frequency ω_R is given by:

$$\hbar\omega_R = |p_{12}|\sqrt{\frac{\hbar\omega}{2\epsilon V_m}}. \tag{4.7}$$

The $|p_{12}| = \langle 1|\hat{p}|2\rangle$ is the transition dipole moment which contains the optical selection rule for transition, where $\hat{p}$ is the electric dipole operator, ϵ is the dielectric constant and V_m is the photon confinement (cavity mode) volume [28,29]. The inverse relation between the Rabi frequency to the square root of the photon confinement volume allows for additional degree of freedom to tune Ω_R using different cavities. In our case, there is no external photonic cavity was used. Our sample was PEPI thin films thin films spin-coated on quartz.

Here, $\hbar\Omega_R$ is also known as *Rabi energy*, which parameterizes the coupling strength of the light-matter interaction. The operators $\hat{a}^\dagger$ and $\hat{a}$ are the creation and annihilation operators of the photon, respectively, which act on the Fock states $|n\rangle$ (*i.e*. photon number eigenstates) under the following relations:

$$\hat{a}^\dagger|n\rangle = \sqrt{n+1}|n+1\rangle \tag{4.8}$$

$$\hat{a}|n\rangle = \sqrt{n}|n-1\rangle. \tag{4.9}$$

The total Hamiltonian is given by $H = H_S + H_L + H_I$. Based on energy conservation, we are interested in the two out of the four states resultant from Hilbert space multiplication of the atomic and Fock states: $|1, n+1\rangle$ and $|2, n\rangle$. These two states can be understood as $(n+1)$ photons with the system is in state $|1\rangle$ and n photons with the system in state $|2\rangle$, respectively. Using these two states as the basis $\{|1, n+1\rangle, |2, n\rangle\}$, the total Hamiltonian can be written in matrix representation as:

$$H = \begin{pmatrix} E_1 + \hbar\omega\left(n + \frac{3}{2}\right) & \frac{1}{2}\hbar\Omega_R \\ \frac{1}{2}\hbar\Omega_R & E_2 + \hbar\omega\left(n + \frac{1}{2}\right) \end{pmatrix}. \tag{4.10}$$

Without the loss of generality, we can set the energy level reference such that $E_1 = -\hbar\omega_0/2$ and $E_2 = \hbar\omega_0/2$. The Hamiltonian can be rewritten as:

$$H = \begin{pmatrix} -\frac{\hbar\omega_0}{2} + \hbar\omega\left(n+\frac{3}{2}\right) & \frac{1}{2}\hbar\Omega_R \\ \frac{1}{2}\hbar\Omega_R & \frac{\hbar\omega_0}{2} + \hbar\omega\left(n+\frac{1}{2}\right) \end{pmatrix} = \begin{pmatrix} -\frac{\Delta}{2} + \hbar\omega(n+1) & \frac{1}{2}\hbar\Omega_R \\ \frac{1}{2}\hbar\Omega_R & \frac{\Delta}{2} + \hbar\omega(n+1) \end{pmatrix} \quad (4.11)$$

where $\Delta = \hbar\omega_0 - \hbar\omega$ is the detuning energy between the equilibrium state and the photon energy of the laser.

For the case where there is no coupling between the system and the photon, *i.e.*, $\hbar\Omega_R = 0$, the Hamiltonian will reduce to:

$$H = \hbar\omega(n+1) + \begin{pmatrix} -\frac{\Delta}{2} & 0 \\ 0 & \frac{\Delta}{2} \end{pmatrix}. \quad (4.12)$$

Here, the eigenstates of this Hamiltonian is our initial basis of $|1, n+1\rangle$ and $|2, n\rangle$, which are known as *bare states*. In the presence of light-matter interaction (*i.e.* $\hbar\Omega_R > 0$), the Hamiltonian is not a diagonal matrix [eq. (4.11)]. In this case, the states $|1, n+1\rangle$ and $|2, n\rangle$ are no longer the eigenstates of the system. The new eigenstates can be obtained by re-diagonalizing the Hamiltonian:

$$H = \hbar\omega(n+1) + \frac{1}{2}\begin{pmatrix} -\sqrt{(\hbar\Omega_R)^2 + \Delta^2} & 0 \\ 0 & \sqrt{(\hbar\Omega_R)^2 + \Delta^2} \end{pmatrix}. \quad (4.13)$$

Here, the two diagonal matrix elements are the new eigenenergies of the system, which is given by:

$$E_{\pm} = \hbar\omega(n+1) \pm \frac{1}{2}\sqrt{(\hbar\Omega_R)^2 + \Delta^2}\,. \quad (4.14)$$

Two new eigenstates $|-\rangle$ and $|+\rangle$ are defined as the basis/eigenstates of the diagonalized Hamiltonian. The non-zero static energy of $\hbar\omega(n+1)$ in the eigenenergies is due to the presence of other photons in the system. Here, $\sqrt{(\hbar\Omega_R)^2+\Delta^2}$ is also known as *generalized Rabi energy*. These two new eigenstates can be expressed in the term of the bare states as:

$$|-\rangle = -\sin\theta_n\,|1,n+1\rangle + \cos\theta_n\,|2,n\rangle \tag{4.15}$$

$$|+\rangle = \cos\theta_n\,|1,n+1\rangle + \sin\theta_n\,|2,n\rangle \tag{4.16}$$

$$\tan\theta_n = \frac{\hbar_{\Omega_R}}{\sqrt{(\hbar\Omega_R)^2+\Delta^2}-\Delta}. \tag{4.17}$$

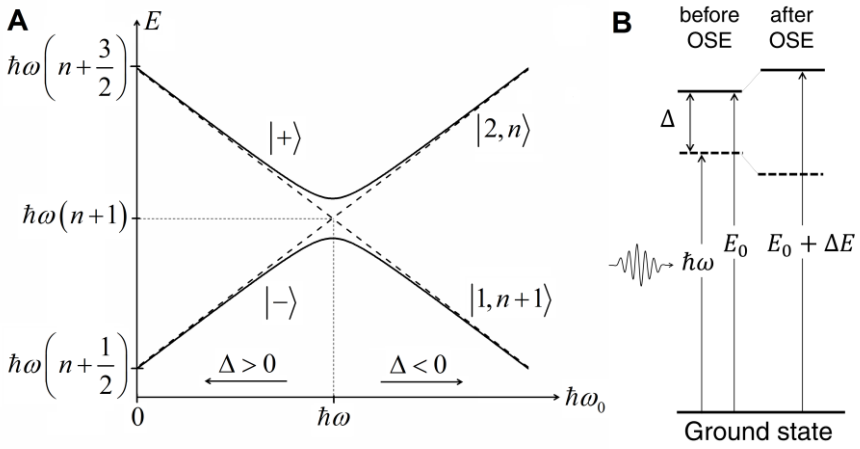

Figure 4.9 | Quantum description of the dressed state. (A) Schematic of the new eigenenergies of the photon-dressed states (solid line) in relation to the bare states (dashed line). (B) Illustration of two-level system with by the equilibrium states (solid line) and the pump-induced Floquet quasi-state (dashed line) on the left before OSE, and the resulting photon-dressed states of $|+\rangle$ (solid line) and $|-\rangle$ (dashed line), on the right side after OSE.

These two new eigenstates are also known as the *Floquet states* or *photon-dressed states*, which are the mixture of both photon state and exciton state. For the case of a semiconductor, photon-dressed states are also known as *exciton-polariton* states. A plot of the eigenenergies as function of $\hbar\omega_0$ with (solid lines) and without light-matter interaction (dashed lines) is given in **Figure 4.9**A. For $\Delta = 0$, the two bare states are degenerate. The energy of *n* photon with the system in $|2\rangle$ is equal to energy of (n + 1) photon with the system in state $|1\rangle$.

A crossing behavior is also observed for the bare states as we tune the exciton enregy $\hbar\omega_0$ across the photon energy $\hbar\omega$; in contrast with the anti-crossing behavior from the photon-dressed state. Here, the energy gap between $|-\rangle$ and $|+\rangle$ at $\Delta = 0$ is the Rabi energy $\hbar\Omega_R$. An important phenomenon which can be seen in **Figure 4.9**A is the occurrence of energy gap between the two new eigenstates and the bare states. This gap is observable as an absorption energy shift in experiments, which is known as the *Optical Stark Effect* (OSE).

Here, our case where $\Delta > 0$ is depicted in **Figure 4.9**B. the hybridized states are observable in experiments as a blue-shift of the exciton energy ΔE. The resultant is exciton-like $|+\rangle$ state (solid line, after OSE) and photon-like $|-\rangle$ state (dashed line, after OSE). In another representation, this phenomenon could also be understood from Floquet picture as a repulsion between equilibrium states (solid line, before OSE) and Floquet quasi-states (dashed line, before OSE), resulting in a blue-shift of exciton energy [30]. The energy shift ΔE is given by the energy difference of $|+\rangle$ state [eq. (4.14)] and the bare exciton $|2, n\rangle$ state [eq. (4.12)]:

$$\Delta E = \frac{1}{2}\left(\sqrt{(\hbar\Omega_R)^2 + \Delta^2} - \Delta\right) \approx \frac{(\hbar\Omega_R)^2}{4\Delta} \propto \text{Intensity.} \qquad (4.18)$$

The approximation is valid for the case of $\Delta >> \hbar\Omega_R$. Since Ω_R is proportional to the electric field induced by light, the Stark shift is therefore expected to be linear to the pump fluence.

4.3.2 Spectral signature of OSE

This energy shift due to OSE causes a change in the absorption spectrum and can be observed via TA spectroscopy. **Figure 4.10**A illustrates the key spectral signatures of OSE. A derivative-like feature in the TA spectrum is to be expected from such coherent process [31]. **Figure 4.10**B shows the comparison of the excitonic absorption peak of PEPI at E_0 ~2.39 eV and the pump pulse of ~2.16 eV (*i.e.*, detuned by $\Delta \approx 0.24$ eV) used for our study. Here, there is no spectral overlap between the pump and the absorption peak, which ensures no single photon excitation process can happen.

The TA spectrum at probe delay Δt = 0 ps photoexcited by this detuned pump with a fluence of 416 μJ/cm^2 is shown in **Figure 4.10**C. Here, an asymmetrical derivative-like feature in the experimental TA spectrum is observed, which comprises of the OSE signal, superimposed on a photobleaching (PB) peak (*i.e.*, negative ΔA peak) arising from the state-filling of excitons by two-photon excitation (see later discussion). The kinetic trace at 2.37 eV probe (inset) shows that the ultrafast OSE process is comparable to the pulse duration. The timescale of this process corresponds to the pump and probe pulse cross-correlation, which in our case is given by FWHM ~290 fs. The much weaker oscillatory PB signal arises from excitons photoexcited via two-photon-excitation. These excitons strongly interact with coherent with optical phonon (see Section 4.2.3).

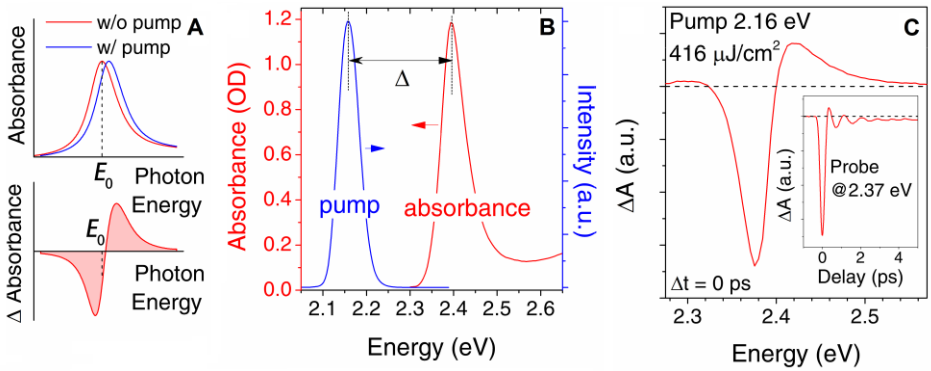

Figure 4.10 | Optical Stark effect in PEPI. (A) The corresponding linear absorption and TA spectral signatures of. (B) The energy separation Δ = 0.24 eV between the excitonic absorption peak E_0 of PEPI (red) and the excitation pump $\hbar\omega$ (blue). (C) TA spectrum of PEPI following linearly polarized pump-probe at Δt = 0 ps. Inset: ultrafast kinetics of OSE showing a fast process comparable to the pulse duration.

4.3.3 Spin-selectivity of OSE

Having established the optical selection rule of OSE (Section 4.1.3), we proceed with our study to incorporate the spin degree of freedom into the picture. From eq. (4.18), it can be inferred that the strength of OSE is an increasing function of Rabi energy $\hbar\Omega_R$. As $\hbar\Omega_R$ parameterizes the optical coupling strength of photon and a state, it is also proportional to the optical selection rules (*i.e.* $\hbar\Omega_R = 0$ for forbidden transition). The implication is that OSE should follow similar selection rules as the optical transition. From the Floquet picture,

it can also be interpreted as states repulsion of the Floquet quasi-state and the equilibrium state to occur only when both states have the same m_J. This gives rise to the spin-selective OSE, whose strength depends on $\hbar\Omega_R$ [eq. (4.18)].

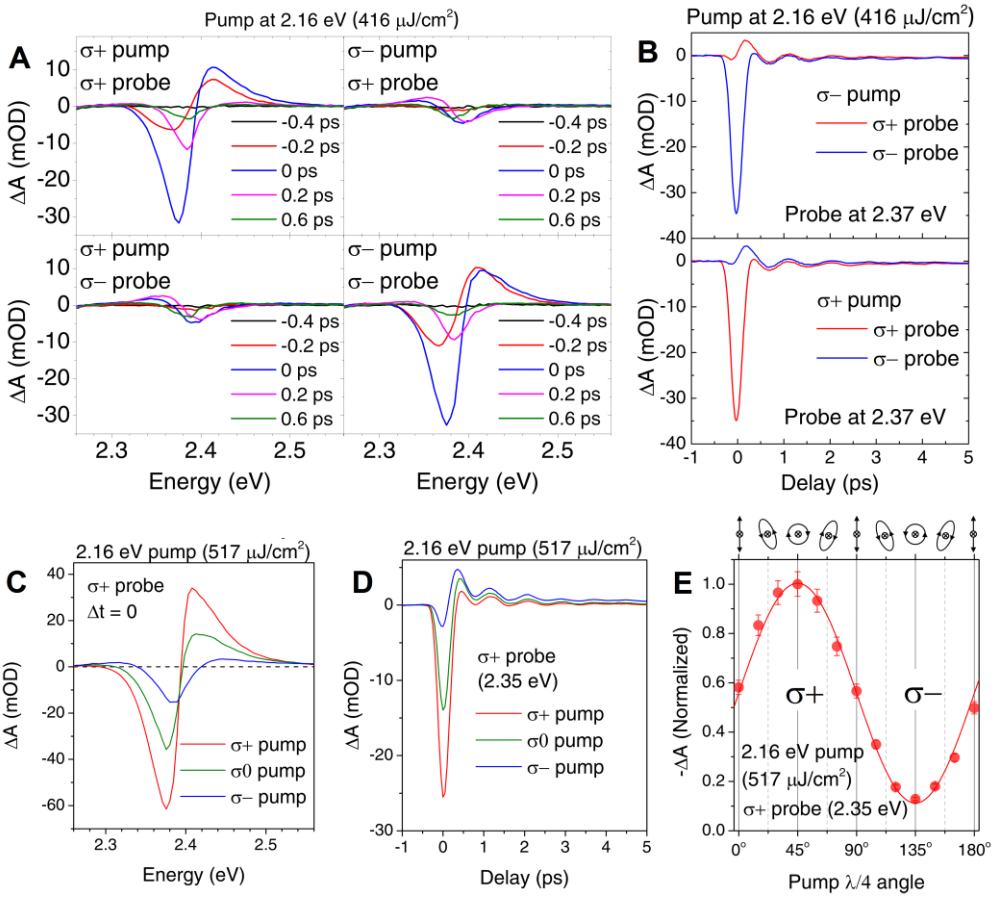

Figure 4.11 | Spin-selective OSE in PEPI thin film. (A) Co- and counter-circularly polarized WLTA spectra at various Δ*t*. (B) The kinetics at the negative ΔA peak (2.37 eV). The experiments were performed by using 2.16 eV pump with a fluence of 416 μJ/cm^2. (C) Pump ellipticity (517 μJ/cm^2) dependent OSE spectra at Δt = 0 ps and (D) their kinetics at 2.35 eV, with σ^+ (red), linearly *s*-polarized (σ0, green) and σ^- (blue) pump polarization and σ^+ probe polarization. (E) Maximum –ΔA signal of σ^+ probe as a function of pump ellipticity, fitted with eq. (4.23).

To evaluate the hypothesis, WLTA studies were performed on PEPI thin films, with polarization controls to selectively induce specific exciton spin state. The experiment was done by using 575 nm (~2.16 eV) pump, which did not linearly excite the sample. **Figure 4.11**A shows the co- and counter-circular pump-probe TA spectra. The corresponding kinetic traces of the probe at the

negative ΔA peak (~2.37 eV) are given in **Figure 4.11**B. The figures show a large photoinduced signal (*i.e.*, ΔA arising from OSE and state-filling) when both pump and probe beams are co-circular. Meanwhile, the signal is greatly reduced for the counter-circular case. The large ΔA signal present only for co-circular case indicates OSE with a specific spin orientation, which validates our hypothesis of the OSE spin-selectivity in PEPI thin film. The small oscillating ΔA signal arises from small exciton population due to two-photon excitation which interacts strongly with coherent phonons (Section 4.2.3).

The spin-selectivity of this OSE process can be further controlled through the ellipticity of pump polarization. In our experiment, it was achieved through varying the fast-axis orientation of the quarter-wave plate (λ/4) in the pump beam and recording the OSE signal as a function of its angle. The TA spectra at the specific pump polarizations: σ^+, linearly *s*-polarized (σ^S) and σ^-, with σ^+ probe are shown in in **Figure 4.11**C, with their respective kinetics shown in in **Figure 4.11**D. Here, the OSE detected by σ^+ probe is expected to only depend on the σ^+ component of the pump. Hence, when the pump polarization is linear, *i.e.*, equal contributions from both σ^+ and σ^- components, the $-\Delta A$ signal is halved. This is evident from the experiment result.

To further validate the hypothesis, we performed OSE measurements at arbitrary pump ellipticity. We expected that that σ^+ probe depends only on the σ^+ component of the pump. Without the loss of generality, given the initial polarization (before λ/4) to be linearly s-polarized ($\theta = 0$), the polarization state $|\psi\rangle$ after passing through the λ/4 at angle θ with respect to the fast axis, can be described by:

$$|\psi\rangle = \cos\theta \begin{pmatrix}1\\0\end{pmatrix} + e^{-\frac{i\pi}{2}} \sin\theta \begin{pmatrix}0\\1\end{pmatrix}, \tag{4.19}$$

where $(1\ 0)^T$ and $(0\ 1)^T$ basis are the Cartesian component projections to the fast and the slow axis of the λ/4, respectively. Here, the component projected to the slow axis is phase-delayed by π/2 (quarter-wave). In this Cartesian basis, the pure left circular $|\sigma^+\rangle$ and right circular $|\sigma^-\rangle$ polarization states can be expressed as:

$$|\sigma^+\rangle = \frac{1}{\sqrt{2}}\left[\binom{1}{0} - e^{\frac{i\pi}{2}}\binom{0}{1}\right], \tag{4.20}$$

$$|\sigma^-\rangle = \frac{1}{\sqrt{2}}\left[\binom{1}{0} + e^{\frac{i\pi}{2}}\binom{0}{1}\right]. \tag{4.21}$$

Based on the relation, the polarization state $|\psi\rangle$ can be expressed in the circular polarization basis:

$$\begin{aligned} |\psi\rangle &= a|\sigma^+\rangle + b|\sigma^-\rangle \\ &= \frac{1}{\sqrt{2}}(\cos\theta + \sin\theta)|\sigma^+\rangle + \frac{1}{\sqrt{2}}(\cos\theta - \sin\theta)|\sigma^-\rangle \end{aligned} \tag{4.22}$$

Where a and b are the complex coefficient of $|\sigma^+\rangle$ and $|\sigma^-\rangle$ components, respectively. The σ^+ component contribution in the polarization state is therefore given by:

$$|a|^2 = \frac{1}{2}(\cos\theta + \sin\theta)^2 = \frac{1}{2}(1 + \sin 2\theta). \tag{4.23}$$

Eq. (4.23) is then used to fit the OSE maximum –ΔA signal (at 2.35 eV σ^+ probe, Δt = 0 ps) as a function of the pump λ/4 angle. The result is shown in **Figure 4.11**E. A non-zero offset is added to the fitting, due to the two-photon absorption, which was discussed previously. The excellent agreement between eq. (4.23) and experimental data hence validate our hypothesis.

4.3.4 Estimation of the energy shift

From the OSE TA spectra, we can estimate the energy shift of exciton spin-states achieved by the OSE. Given the absorption peak function $A(\omega)$ with peak position at ω_0, the transient change of absorption $\Delta A(\omega)$ due to blue-shift of exciton energy $\Delta\omega_0$ can be written as:

$$\Delta A(\omega) = A(\omega - \Delta\omega_0) - A(\omega) = -\frac{dA(\omega)}{d\omega_0}\Delta\omega_0. \tag{4.24}$$

To determine the energy blue shift from $\Delta A(\omega)$, we defined the spectral weight transfer (SWT), which correspond to the total integral of absorption change $\Delta A(\omega)$ across the spectrum from 0 up to the absorption peak ω_0:

$$\text{SWT} \equiv \int_0^{\omega_0} \Delta A(\omega)\, d\omega \tag{4.25}$$

The SWT can be calculated numerically from our experimental data, where $\Delta A(\omega)$ correspond to the OSE TA spectrum. By substituting eq. (4.24) to eq. (4.25), the SWT can also be simplified into:

$$\text{SWT} = -\Delta\omega_0 \int_0^{\omega_0} \frac{dA(\omega)}{d\omega} d\omega = -\Delta\omega_0[A(\omega_0) - A(0)]. \tag{4.26}$$

Since the absorption at zero energy $A(0)$ = 0, the energy shift $\Delta\omega_0$ can be estimated from the SWT by:

$$\Delta E = -\hbar \frac{\text{SWT}}{A(\omega_0)} = -\frac{\hbar}{A(\omega_0)} \int_0^{\omega_0} \Delta A(\omega) d\omega. \tag{4.27}$$

Here, $\hbar\omega_0 = 2.395$ eV is the peak position of the absorption spectrum, with $A(\omega_0) = 1.186$ OD, as shown in **Figure 4.10**B. As the OSE signal vanishes for energy below 2.25 eV, we set the integral range to be 2.25 eV ≤ $\hbar\omega$ ≤ 2.40 eV.

The power dependent study for OSE is shown in **Figure 4.12**, where the ~2.16 eV pump fluence was varied from 208 μJ/cm^2 to 1.66 mJ/cm^2. The co- and counter- circular polarization are shown in **Figure 4.12**A. The spectral signatures for both polarizations increase with increasing pump fluence. Here, we attribute the -ΔA peak (2.39 eV) in the counter-circular TA spectrum (dashed blue traces) to arise from the exciton state-filling. This assignment is consistent with the excitonic peak in the linear absorption spectrum and TA spectrum obtained from above bandgap excitation (3.1 eV pump, see Section 4.2.1). This

exciton bleaching signal exhibits fluence-dependent quadratic behavior consistent with two-photon excitation process, as shown in **Figure 4.12**C.

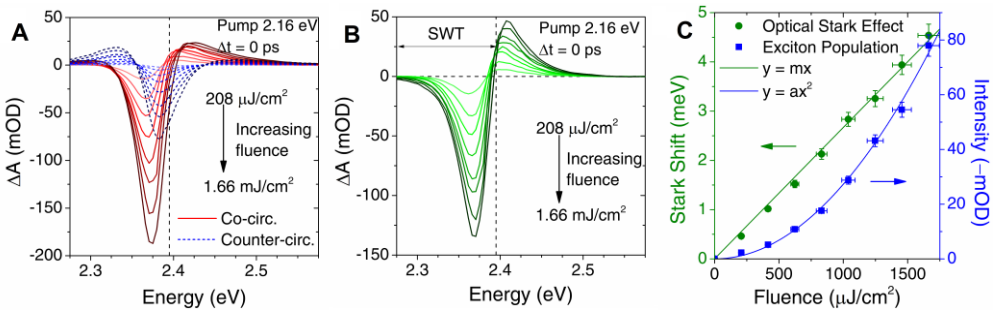

Figure 4.12 | Power dependent OSE study in PEPI thin films. (A) TA spectra for co- (red-solid) and counter-circular (blue-dashed) polarization at Δt = 0 ps. (B) Difference between the co- and counter- circular TA spectra at the same pump fluence at Δt = 0 ps. The vertical dashed line indicates the position of the exciton absorption peak. (C) Estimated Stark shift (green circle, left axis) and two photoexcited exciton population (blue square, right axis) as a function of pump fluence. The former and the latter exhibits linear and quadratic relation, respectively.

To elucidate the OSE contribution and eliminate the excitonic contribution from the signal, we subtract the co-circular TA signal from the counter-circular TA signal at the same pump fluence. The result is presented in **Figure 4.12**B. Based on eq. (4.27), we estimate the energy shift ΔE from OSE using the spectral weight transfer (SWT) of the subtracted signal. **Figure 4.12**C shows the linear dependence of the estimated Stark shift with increasing pump fluence, which yields excellent agreement with the theoretical predictions [eq. (4.18)]. Based on the result in **Figure 4.12**C, a large ΔE up to 4.5 ± 0.2 meV at room temperature can be achieved with a pump fluence of 1.66 mJ/cm^2 without any external magnetic field or photonic cavity. Such splitting of exciton spin-state is equivalent to applying B-field of 70 T, given the *g*-factor of 1.08 [32]. Such huge B-field is hardly achievable in any laboratory with present technology. At a given fluence of 1.66 mJ/cm^2, Δ = 0.24 eV and ΔE = 4.5 ± 0.2 meV, the corresponding Rabi energy can be calculated by eq. (4.18), which yields $\hbar\Omega_R = 66 \pm 3$ meV. The transition dipole moment of PEPI thin film can be estimated from the Rabi energy via the following equation:

$$|p_{12}| = \frac{\hbar\Omega_R}{F} = \frac{\hbar\Omega_R}{\sqrt{2I/n\epsilon_0 c}}. \quad (4.28)$$

Here, F is the electric field by light; I = fluence/duration is the pump intensity; n = 2.1 ± 0.1 is PEPI refractive index [9,33]; ϵ_0 is the vacuum permittivity; and c is the speed of light in vacuum. Given the pump-probe pulse correlation of ~290 fs [**Figure 4.10**C (inset)], we can estimate $F = 143 \pm 4$ MV/m due to pump fluence of 1.66 mJ/cm^2. The transition dipole moment is therefore determined to be $|p_{12}| = (7.4 \pm 0.3) \times 10^{-29}$ C m = 22.4 ± 0.8 Debye. From the transition dipole moment, we can also determine other fundamental properties such as the spontaneous emission rate τ_R^{-1} and exciton reduced mass μ^*, which is related to $|p_{12}|$ by following equations [34]:

$$\tau_R^{-1} = \frac{n^3\omega_0^3|p_{12}|^2}{3\epsilon_0\pi\hbar c^3}, \quad (4.29)$$

$$\mu^* = \frac{3e^2\hbar f}{2\omega_0|p_{12}|^2} \quad (4.30)$$

Here, $f = 0.5$ is the oscillator strength of PEPI [9]. From eq. (4.29), we obtained lifetime of $\tau_R = 98 \pm 5$ ps, which is in excellent agreement with our TA assignment (see Section 4.2.2) and the previous report in literature [24]. This consistency thereby validates the accuracy of our measurements. Meanwhile, the electron effective mass is determined to be $\mu^* = (0.11 \pm 0.01)m_0$. These results are comparable with previous report of exciton reduced mass of $0.09m_0$ [9], which further affirms our results.

4.3.5 Tunability of OSE

We proceed to investigate the tunability of the Rabi energy in 2D lead halide perovskite. This was achieved by varying the halide anions or the organic cations of the system, hence changing the dielectric contrast between the alternating organic and inorganic layers. Herein, we compare PEPI with 2 other types of 2D lead halide perovskites, which are $(C_6H_5C_2H_4NH_3)_2PbBr_4$ (hereafter called as PEPB) and $(C_6H_4FC_2H_4NH_3)_2PbI_4$ (hereafter called as FPEPI). The substitution of the iodine to bromine is known to reduce the dielectric constant

ϵ of the $[PbX_6]^{4-}$ (X = halide) octahedral inorganic layer from ~6.1 to ~4.8 [4,6,9], hence reducing the contrast between the organic phenyl-ethyl-ammonium layer (ϵ ~3.3) [9] and the inorganic layer. Meanwhile, fluorination of the phenyl-ethyl-ammonium cation is known to substitute the para-hydrogen atom with fluorine (*i.e.* $C_6H_5C_2H_4NH_3^+$ to $C_6H_4FC_2H_4NH_3^+$). This fluorination will decrease the dielectric constant of the organic layer due to due to the increase in free volume fraction and large electronegativity of C-F bond [35], hence increases the dielectric contrast.

The measurement result is shown in **Figure 4.13**A and B. The experiment and calculation of Rabi energy were performed by using similar procedures as in PEPI. The Stark shift and Rabi energy follow a linear and square root dependence with respect to the excitation fluence, which is in accordance with our theoretical understanding. Here, substitution of the halide from I to Br reduces the Rabi energy from 66 ± 3 meV to 47 ± 5 meV. Meanwhile, the fluorination of organic component enhances the Rabi energy up to 78 ± 4 meV. It is noteworthy to mention that our results clearly demonstrated the tunability of the Rabi energy (hence the light-matter coupling strength) via facile substitution or modification of the halides and organic cations components.

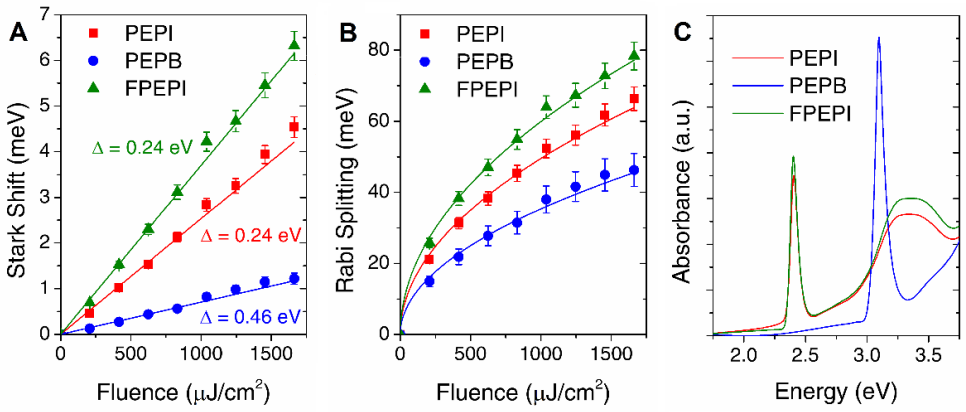

Figure 4.13 | Comparison of OSE in 3 different 2D perovskites. (A) The Stark shift ΔE and (B) the Rabi energy $\hbar\Omega_R$ as function of pump fluence, together with (D) the absorption spectrum of PEPI (red), PEPB (blue) and FPEPI (green).

The facile tunability in this system is indeed a desirable property for integration with technology. From this result, we can also conclude that tuning the Rabi energy in 2D perovskite system is not as trivial as merely modulating

the exciton oscillator strength of the material. It is known that the oscillator strength is proportional to the area under the absorption curve [34]. Given the oscillator strength f of PEPI to be 0.5 [9], the f-values for PEPB and FPEPI were estimated to be ~0.99 and ~0.54, respectively. The accuracy of these f-values is affirmed by comparing the exciton reduced mass [eq. (4.30)] obtained from $\hbar\Omega_R$ and f with reports literature. Here, we obtained $\mu^* = (0.17 \pm 0.02)m_0$, which is consistent with report of $0.18m_0$ from literature [4].

While the oscillator strength is proportional to Rabi-energy, other contributions such as the effective mass and bandgap also play crucial roles [eq. (4.30)]. Our observations suggest that the more deterministic criterion is the dielectric contrast between the barrier and the well layer. **Figure 4.14** shows a plot of normalized Rabi-energy to the square-root of fluence ($\hbar\Omega_R/\sqrt{I}$, hence fluence independent) for various solution-processed 2D perovskite systems as function of oscillator strength and the dielectric contrast. We demonstrated that while $\hbar\Omega_R/\sqrt{I}$ does not exhibit any clear trend with the oscillator strength, a direct increasing correspondence is observed with the dielectric contrast. This later parameter would therefore provide a clearer criterion for the straight-forward tuning of the coupling strength in 2D perovskite. Further theoretical studies are needed to establish the quantitative relationship between the Rabi-energy and the dielectric contrast.

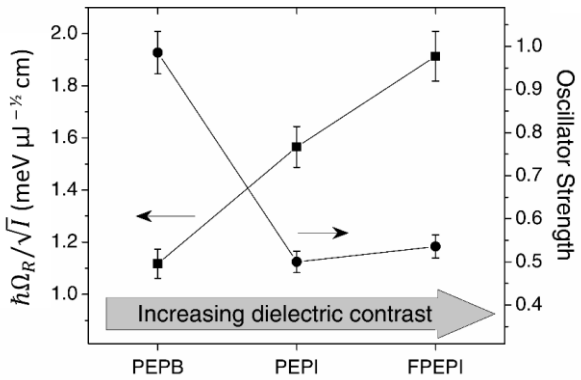

Figure 4.14 | Correlation between the Rabi-energy and the oscillator strength or dielectric contrast. Measurement of Rabi-energy via OSE on various lead-based 2D perovskite systems, *i.e.* PEPB, PEPI, and FPEPI. There is a clear increasing relation between $\hbar\Omega_R/\sqrt{I}$ with the dielectric contrast. Meanwhile, no clear correlation is observed between with the oscillator strength and $\hbar\Omega_R/\sqrt{I}$.

4.3.6 Comparison with conventional semiconductor system

Lastly, to evaluate the robustness of this system and to benchmark our results against the state-of-the-art reported in the literature, we performed a comparison of the obtained Rabi energy on several conventional III-V and II-VI inorganic semiconductor nanostructures, [*i.e.* MQW or quantum dot (QD) system]. The comparison result is summarized in **Table 4.1**.

Table 4.1 | Comparison of OSE and Rabi energy in various semiconductors. The information of laser system and intensity/power used to obtain the results are included. CW refers to continuous wave.

Material	Pump Intensity (Pulse width)	T (K)	Δ (meV)	ΔE (meV)	$\hbar\Omega_R$† (meV)
PEPB thin film	5.5 GW/cm^2 (~600 fs)	300	460	1.2	47
PEPI thin film	5.5 GW/cm^2 (~290 fs)	300	240	4.5	66
FPEPI thin film	5.5 GW/cm^2 (~290 fs)	300	240	6.3	78
Mn:CdTe QD (10-20 nm) [36]	Not stated (CW)	5	0	0.25	0.25
GaAs/AlGaAs MQW (9.26/9.28 nm) [37]	8 MW/cm^2 (~6 ps)	70	18	0.1	1.9
GaAs/AlGaAs MQW (10/10 nm) [38]	~10 GW/cm^2 (~150 fs)	15	29	~1.4*	9.1
GaAs/AlGaAs MQW (10/2.5 nm) [38]	~10 GW/cm^2 (~150 fs)	15	19	~3.5*	12
Interface QD (50 nm) in GaAs/AlAs [39]	0.2 μW (~2 ps)	12	3	0.47	1.75

†The value is estimated from eq. (4.18), if not directly mentioned.

*Estimated energy shift from the figure(s) in ref. [38].

From this comparison table, the significance and novelty of the 2D lead halide perovskite system are apparent from the large Rabi energy as compared to other inorganic semiconductor systems. For instance, the Rabi energy achieved in PEPI is ~5 times larger than what is achieved by conventional GaAs/AlGaAs MQW photoinduced under similar pump intensity [38]. Another major advantage of 2D lead halide perovskites over the inorganic semiconductor

nanostructures is its room temperature applications. Conventional inorganic semiconductors are limited to cryogenic temperature operations for clear resolution of the spin-states [36-44]. Apart from the inorganic system, organic systems (*e.g.* J-aggregates) also offers strong Rabi energy [45], yet are limited by low carrier mobility, which hinders possibility for electronics integration, and lack of SOC, which hinders optical-spin manipulation for opto-spintronic applications. In such case, the hybrid of organic and inorganic 2D lead halide perovskite system displays its robustness over the pure organic and inorganic system, whilst offering facile tunability of the light-matter coupling strength.

4.3.7 Section Summary

In summary, we reported the study of spin-selective optical Stark effect (OSE) in 2D lead halide perovskite system. The novel key results presented in this section can be summarized into the following points:

1. Demonstration of room temperature spin-selective OSE in PEPI thin film. This OSE process is well explained by Jaynes-Cumming model.
2. Estimation of the energy shift by OSE in PEPI thin films. The exciton energy shift achieved by PEPI is equivalent with spin-state splitting by Zeeman effect due to a ~70 T magnetic field.
3. Demonstration of tunability of the Rabi energy by facile substitution of the organic or halide component. We discover that while oscillator strength does not directly correlate with Rabi energy, the dielectric contrast of the organic and inorganic layers does.
4. Estimation of the Rabi energy in several 2D lead halide perovskite materials: PEPI, PEPB, and FPEPI. We demonstrated the robustness of 2D lead halide perovskites over the purely organic and inorganic semiconductor system for room temperature opto-spintronic applications.

4.4 Conclusion

In conclusion, through the study of optical-carrier-spin dynamics in 2D lead halide perovskites presented in this chapter, the prospect of 2D lead halide OIHP for opto-spintronic applications has been demonstrated and evaluated. In particular, strong light-matter interaction in 2D lead halide OIHP combined

with the coupling with the spin degree of freedom offers exciting new prospects for realizing various novel technology such as opto-spin-logic devices [36,39,42-44] and spin-Floquet topological phases [30] for ultrafast optical implementations of quantum information applications [41]. Herein, the 2D organic-inorganic halide perovskites family shows its robustness over the conventional organic and inorganic semiconductor systems for novel opto-spintronics technological applications. While the fundamental understanding of the physics has been established through this study, further studies, especially for devices architectures and integration with other systems are warranted.

4.5 Bibliography

1. Tsai, H., et al., *High-efficiency two-dimensional Ruddlesden–Popper perovskite solar cells.* Nature, 2016. **536**(7616): p. 312-316.
2. Vassilakopoulou, A., D. Papadatos, and I. Koutselas, *Room temperature light emitting diode based on 2D hybrid organic-inorganic low dimensional perovskite semiconductor.* Applied Materials Today, 2016. **5**: p. 128-133.
3. Yuan, M., et al., *Perovskite energy funnels for efficient light-emitting diodes.* Nature Nanotechnology, 2016. **11**: p. 872–877.
4. Kenichiro, T., et al., *Electronic and Excitonic Structures of Inorganic-Organic Perovskite-Type Quantum-Well Crystal* $(C_4H_9NH_3)_2PbBr_4$. Japanese Journal of Applied Physics, 2005. **44**(8R): p. 5923.
5. Even, J., et al., *Electronic model for self-assembled hybrid organic/perovskite semiconductors: Reverse band edge electronic states ordering and spin-orbit coupling.* Physical Review B, 2012. **86**(20): p. 205301.
6. Ishihara, T., J. Takahashi, and T. Goto, *Optical properties due to electronic transitions in two-dimensional semiconductors* $(C_nH_{2n+1}NH_3)_2PbI_4$. Physical Review B, 1990. **42**(17): p. 11099-11107.
7. Brehier, A., et al., *Strong exciton-photon coupling in a microcavity containing layered perovskite semiconductors.* Applied Physics Letters, 2006. **89**(17): p. 171110.

8. Lanty, G., et al., *Strong exciton-photon coupling at room temperature in microcavities containing two-dimensional layered perovskite compounds.* New Journal of Physics, 2008. **10**(6): p. 065007.
9. Hong, X., T. Ishihara, and A.V. Nurmikko, *Dielectric confinement effect on excitons in PbI_4-based layered semiconductors.* Physical Review B, 1992. **45**(12): p. 6961-6964.
10. Mitzi, D.B., K. Chondroudis, and C.R. Kagan, *Organic-inorganic electronics.* IBM J. Res. Dev., 2001. **45**(1): p. 29-45.
11. Gauthron, K., et al., *Optical spectroscopy of two-dimensional layered $(C_6H_5C_2H_4\text{-}NH_3)_2\text{-}PbI_4$ perovskite.* Optics Express, 2010. **18**(6): p. 5912-5919.
12. Umebayashi, T., et al., *Electronic structures of lead iodide based low-dimensional crystals.* Physical Review B, 2003. **67**(15): p. 155405.
13. Fujita, T., et al., *Tunable polariton absorption of distributed feedback microcavities at room temperature.* Physical Review B, 1998. **57**(19): p. 12428-12434.
14. Hirasawa, M., et al., *Magnetoreflection of the lowest exciton in a layered perovskite-type compound $(C_{10}H_{21}NH_3)_2PbI_4$.* Solid State Communications, 1993. **86**(8): p. 479-483.
15. Ishihara, T., et al., *Dielectric confinement effect for exciton and biexciton states in PbI4-based two-dimensional semiconductor structures.* Surface Science, 1992. **267**(1): p. 323-326.
16. Kenichiro, T. and K. Takashi, *Bandgap and exciton binding energies in lead-iodide-based natural quantum-well crystals.* Science and Technology of Advanced Materials, 2003. **4**(6): p. 599.
17. Tanaka, K., et al., *Two-dimensional Wannier excitons in a layered-perovskite-type crystal (C6H13NH3)2PbI4.* Solid State Communications, 2002. **122**(5): p. 249-252.
18. Kagan, C.R., D.B. Mitzi, and C.D. Dimitrakopoulos, *Organic-Inorganic Hybrid Materials as Semiconducting Channels in Thin-Film Field-Effect Transistors.* Science, 1999. **286**(5441): p. 945-947.
19. Mitzi, D.B., C.D. Dimitrakopoulos, and L.L. Kosbar, *Structurally Tailored Organic−Inorganic Perovskites: Optical Properties and Solution-*

Processed Channel Materials for Thin-Film Transistors. Chemistry of Materials, 2001. **13**(10): p. 3728-3740.

20. Mitzi, D.B., et al., *Hybrid Field-Effect Transistor Based on a Low-Temperature Melt-Processed Channel Layer.* Advanced Materials, 2002. **14**(23): p. 1772-1776.
21. Mitzi, D.B., M.T. Prikas, and K. Chondroudis, *Thin Film Deposition of Organic−Inorganic Hybrid Materials Using a Single Source Thermal Ablation Technique.* Chemistry of Materials, 1999. **11**(3): p. 542-544.
22. Amand, T. and X. Marie, *Exciton Spin Dynamics in Semiconductor Quantum Wells*, in *Spin Physics in Semiconductors*, M.I. Dyakonov, Editor. 2008, Springer Berlin Heidelberg: Berlin, Heidelberg. p. 55-89.
23. Giovanni, D., et al., *Highly Spin-Polarized Carrier Dynamics and Ultralarge Photoinduced Magnetization in $CH_3NH_3PbI_3$ Perovskite Thin Films.* Nano Letters, 2015. **15**(3): p. 1553-1558.
24. Chong, W.K., et al., *Dominant factors limiting the optical gain in layered two-dimensional halide perovskite thin films.* Physical Chemistry Chemical Physics, 2016. **18**(21): p. 14701-14708.
25. Lim, S.S., et al., *Modulating carrier dynamics through perovskite film engineering.* Physical Chemistry Chemical Physics, 2016.
26. Sum, T.C., et al., *Spectral Features and Charge Dynamics of Lead Halide Perovskites: Origins and Interpretations.* Accounts of Chemical Research, 2016. **49**(2): p. 294-302.
27. Xing, G., et al., *Low-Temperature Solution-Processed Wavelength-Tunable Perovskites for Lasing.* Nature Materials, 2014. **13**(5): p. 476-480.
28. Uemoto, M. and H. Ajiki, *Large and well-defined Rabi splitting in a semiconductor nanogap cavity.* Optics Express, 2014. **22**(19): p. 22470-22478.
29. Khitrova, G., et al., *Vacuum Rabi splitting in semiconductors.* Nature Physics, 2006. **2**(2): p. 81-90.
30. Sie, E.J., et al., *Valley-selective optical Stark effect in monolayer WS_2.* Nature Materials, 2015. **14**(3): p. 290-294.
31. Autler, S.H. and C.H. Townes, *Stark Effect in Rapidly Varying Fields.* Physical Review, 1955. **100**(2): p. 703-722.

32. Xu, C.-q., et al., *Magneto-optical effects of excitons in $(C_{10}H_{21}NH_3)_2PbI_4$ under high magnetic fields up to 40 T.* Solid State Communications, 1991. **79**(3): p. 249-253.
33. Zhang, S., et al., *Preparations and Characterizations of Luminescent Two-Dimensional Organic-inorganic Perovskite Semiconductors.* Materials, 2010. **3**(5): p. 3385.
34. Hilborn, R.C., *Einstein coefficients, cross sections, f values, dipole moments, and all that.* American Journal of Physics, 1982. **50**(11): p. 982-986.
35. Simpson, J.O. and A.K. St.Clair, *Fundamental insight on developing low dielectric constant polyimides.* Thin Solid Films, 1997. **308–309**: p. 480-485.
36. Le Gall, C., et al., *Optical Stark Effect and Dressed Exciton States in a Mn-Doped CdTe Quantum Dot.* Physical Review Letters, 2011. **107**(5): p. 057401.
37. Von Lehmen, A., et al., *Optical Stark effect on excitons in GaAs quantum wells.* Optics Letters, 1986. **11**(10): p. 609-611.
38. Mysyrowicz, A., et al., *"Dressed Excitons" in a Multiple-Quantum-Well Structure: Evidence for an Optical Stark Effect with Femtosecond Response Time.* Physical Review Letters, 1986. **56**(25): p. 2748-2751.
39. Unold, T., et al., *Optical Stark Effect in a Quantum Dot: Ultrafast Control of Single Exciton Polarizations.* Physical Review Letters, 2004. **92**(15): p. 157401.
40. Bose, R., et al., *Large optical Stark shifts in semiconductor quantum dots coupled to photonic crystal cavities.* Applied Physics Letters, 2011. **98**(12): p. 121109.
41. Joffre, M., et al., *Dynamics of the Optical Stark Effect in Semiconductors*. Journal of Modern Optics, 1988. **35**(12): p. 1951-1964.
42. Reiter, D.E., V.M. Axt, and T. Kuhn, *Optical signals of spin switching using the optical Stark effect in a Mn-doped quantum dot.* Physical Review B, 2013. **87**(11): p. 115430.
43. Amo, A., et al., *Exciton-polariton spin switches.* Nature Photonics, 2010. **4**(6): p. 361-366.
44. Žutić, I., J. Fabian, and S. Das Sarma, *Spintronics: Fundamentals and Applications.* Review of Modern Physics, 2004. **76**(2): p. 323-410.

45. Vasa, P., et al., *Optical Stark Effects in J-Aggregate-Metal Hybrid Nanostructures Exhibiting a Strong Exciton-Surface-Plasmon-Polariton Interaction.* Physical Review Letters, 2015. **114**(3): p. 036802.

CHAPTER 5:

OPTICAL-SPIN DYNAMICS IN MULTI DIMENSIONAL RUDDLESDEN-POPPER ORGANIC-INORGANIC HYBRID LEAD HALIDE PEROVSKITES

This chapter presents the results of the optical studies directed to uncover the fundamental understanding of ultrafast transient photophysics in Ruddlesden-Popper phase lead iodide perovskite systems. Our sample showed a mixed of multiple dimensional phases in one thin film. The first half of this chapter focused on understanding the nature and relaxation dynamics of photoexcited species in these perovskites. It was discovered that excitons were the primary species for phase up to n = 5. The energy funneling rates from one phase (n) to another were also estimated. The second half of this chapter focused on understanding the spin relaxation dynamics of excitons in multidimensional Ruddlesden-Popper phase perovskites. The observed exciton optical-spin dynamics could be modeled by the interplay of direct and indirect exciton spin relaxation pathways. The relaxation rate of each pathway was extracted and found to be counterintuitive to the current understanding in the conventional inorganic semiconductor.

5.1 Linear properties

Recently, researchers have focused on multi-dimensional perovskite system in a bid to realize commercialization of perovskites based optoelectronic devices. While the 3D archetype perovskites have shown marvelous optoelectronics properties, it is also notorious for its instability under ambient air conditions. In contrast, the 2D perovskites with bulky organic cations (*e.g.* $C_6H_5C_2H_4NH_3^+$ in 2D as compared to $CH_3NH_3^+$ in 3D) show higher resistance to moisture degradation. However, it is a strongly excitonic system, which hinders charge extraction for light-harvesting applications. To address these drawbacks, the *Ruddlesden-Popper* (RP) phase perovskites with dimensionality in between of the 2D and 3D are now being explored [1-3]. A recent study has reported an air-stable solar cell (as compared to the MAPI-based cell), with relatively high photoconversion efficiency (PCE) up to 12.5%, made from $(C_4H_9NH_3)_2(CH_3NH_3)_2Pb_3I_{10}$ (n = 3 phase) and $(C_4H_9NH_3)_2(CH_3NH_3)_3Pb_4I_{13}$ (n = 4 phase) RP perovskites [4]. Superior photoluminescence quantum yield (PLQY) of RP perovskite thin films in comparison to both pure 2D and 3D perovskites has also been [5]. In this section, we present the structural and linear optical properties of our solution-processed RP perovskite thin films. These linear properties have important implications for the nonlinear dynamics, which are the interest of this study. Herein, we focus on lead iodide based RP perovskites with phase (n = 1 to 4) as the representative material system.

5.1.1 Structural properties

The uniqueness of RP phase perovskites as compared to their purely 2D and 3D counterparts are their mixed dimensionality. Similar to the 2D system, RP perovskites form multi-quantum-well (MQW) system, however with tunable spatial confinement in z-direction depending on the phase n. The index n denotes the number of connected inorganic-$[PbI_6]^{4-}$ octahedron-layers in the z-direction, where n = 1 refers to pure 2D perovskites and $n = \infty$ refers to pure 3D perovskites. RP perovskite structures for n = 1 to 3 are illustrated in **Figure 4.1**. In our system, the bulk and small organic cations used are $C_6H_5C_2H_4NH_3^+$ and $CH_3NH_3^+$, which are located in between the inorganic slabs and the $[PbI_6]^{4-}$

octahedrons, respectively. The generic formula for our lead iodide RP perovskites with phase *n* is given by $(C_6H_5C_2H_4NH_3)_2(CH_3NH_3)_{n-1}Pb_nI_{3n+1}$.

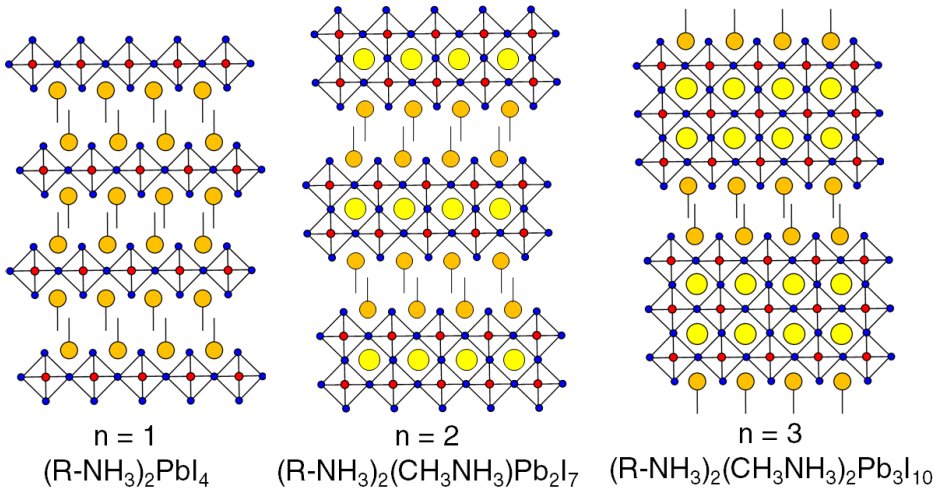

Figure 5.1 | RP perovskites crystal structure. The structures of RP lead iodide perovskites with phase *n* = 1 to 3. The $R\text{-}NH_3^+$ (big circle with tail) and $CH_3NH_3^+$ (big circle) are the bulky and small organic cations, respectively. The generic formula for RP perovskites with phase *n* is given by $(R\text{-}NH_3)_2(CH_3NH_3)_{n-1}Pb_nI_{3n+1}$.

The XRD spectra for *n* = 1 to 4 and *n* = ∞ (3D MAPI) are shown in **Figure 5.2**A. The special cases of *n* = ∞ (MAPI) and *n* = 1 (PEPI) have been discussed in detail in Chapter 3 and 4, respectively. The characteristic plane spacing for the pure 2D and 3D systems are d_{020} and d_{110}, which correspond to the characteristic interlayer spacing and $[PbI_6]^{4-}$ octahedron size, respectively [6,7]. The d_{020} plane spacing for *n* = 1 is illustrated in **Figure 5.2**B. For the case of *n* > 1, both of these characteristic planes will be present, as illustrated in **Figure 5.2**C for phase *n* = 3. For our case, the RP perovskite thin films were prepared by hot-casting of stoichiometric precursor solution for particular phase *n* on quartz substrates (Chapter 2). Hot-casting technique has been demonstrated to produce RP perovskite thin films with better crystallinity [4].

Regardless of the specific stoichiometric ratio which has been designated for particular sample *n*, multiple phases were observed from one thin film sample. It is evident from the XRD spectra in **Figure 5.2**A, wherein each of our *n* = 2, 3 and 4 thin films, the multiple d_{020} peaks which correspond to other phases were observed. The limitation to isolate a single *n*-phase perovskite from

solution processed system have also been reported in the literature [7,8]. An improvement from our current sample fabrication techniques is therefore required, but this is out of the scope of our current study.

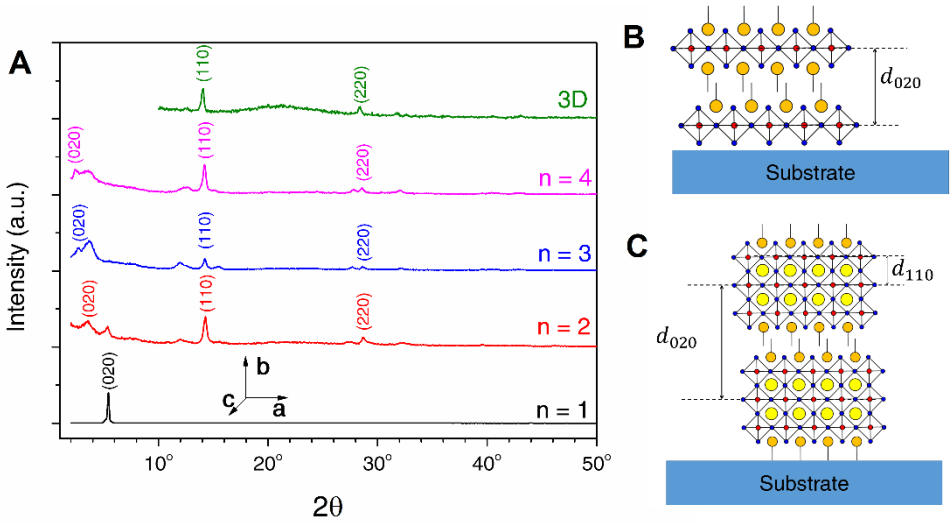

Figure 5.2 | Crystal structures of multi-dimensional RP perovskites. (A) XRD spectra for RP perovskites for phase n = 1 to 4. Illustration for XRD planes for (B) n = 1 and (C) n = 3 phases, showing d_{002} and d_{110} plane spacing.

From the XRD spectra, the plane spacing for various phases can be estimated. For $n = 2, 3, 4$ and ∞, the (110) plane at similar $2\theta = 14.2°$ is observed. Given $2d \sin\theta = \lambda$ with λ = 1.548 Å, this angle corresponds to d_{110} = 6.3 Å which refers to size of $[PbI_6]^{4-}$ octahedron. Furthermore, decreasing 2θ of the (020) diffraction plane was observed with increasing n, which corresponds to increasing interlayer spacing d_{020}. The 2θ and corresponding d_{020} for each n is tabulated in **Table 5.1**. Each increase of n will increase the d_{020} by 7 ± 2 Å, which corresponds to the thickness of a single $[PbI_6]^{4-}$ octahedron layer. The relatively large uncertainty of ± 2 Å is due to experimental inaccuracy at small angle measurement.

Table 5.1 | XRD result for d_{020} plane in RP perovskite thin film. The XRD angle 2θ and its corresponding plane spacing d for each phase n are tabulated.

n	2θ	d_{020} (Å)
1	5.4°	16.1
2	3.6°	24.1

3	2.8°	31.0
4	2.4°	36.2

5.1.2 Linear optical properties

We elucidated the linear optical properties of our solution-processed RP perovskite thin films by using absorption and photoluminescence (PL) spectroscopy. The absorption coefficient and PL spectra for n = 1 to 4 and 3D are shown in **Figure 5.3**. For n = 1, absorption and PL peaks around 520 nm (~2.4 eV) were observed, which correspond to the first excitonic peak in PEPI (Chapter 4). Whereas for n = 2, 3 and 4 samples, multiple absorption peaks were observed for each film, regardless of being made from the same stoichiometric precursor solution. This observation indicates multi n-phases were formed in our single thin film sample, which was also consistent with the observation from the XRD spectra. To differentiate the actual RP phases (n) present in the film, here onwards we will use $\bar{n}$ ('average' n) to refer to the particular film with specific stoichiometry ratio of the precursor solution. For example, in this new terminology, our film made with n = 2 phase stoichiometric ratio will be referred as $\bar{n}$ = 2. In this $\bar{n}$ = 2 film, multiple n = 1 to 4 phases co-exist.

Based on the absorption peak positions, we assigned the corresponding lowest excitonic energy for each of the n-phase. The assignments for n = 1 to 5 phases are summarized in **Table 5.2**. The result is consistent with other reports in the literature [5-7,9]. In our samples, for n > 5, the absorption peaks were too indistinct to be assigned to a particular n-phase.

Table 5.2 | Exciton peak for each of the *n*-phase of RP perovskite thin films. The exciton energies are presented in wavelength (nm) and energy (eV) units.

n	λ_{abs} (nm)	E_0 (eV)
1	516	2.40
2	566	2.19
3	610	2.03
4	645	1.92
5	670	1.85

Noted that the absorption still forms distinct peaks up to n = 3, as opposed to absorption edge in the 3D system. It implies that up to this phase, the RP perovskites are still predominantly excitonic, as compared to free carriers in 3D. As n increases, the peak behavior becomes weaker (less distinct), which signifies the decrease of exciton oscillator strength. The reason behind is the drop of dielectric and spatial confinement in out-of-plane [d_{020}] direction due to the increased thickness of the inorganic layer. Weaker confinement results in the decrease of the exciton energy, as observed in our experiments.

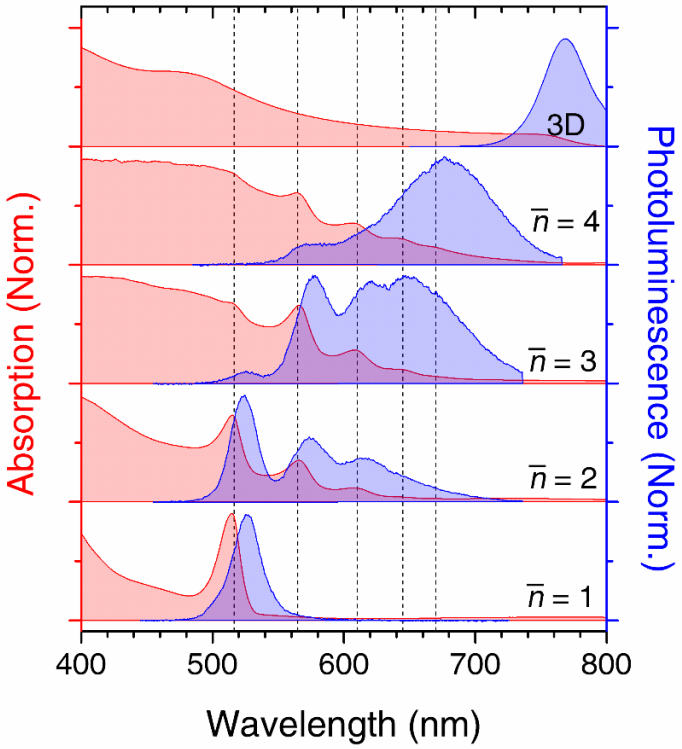

Figure 5.3 | Linear optical properties of RP perovskite thin films. The normalized absorption (red) and integrated PL (blue) spectra of our RP thin films for $\bar{n}$ = 1 to 4 and 3D perovskites. The PL spectra were photoexcited by 400 nm (19 μJ/cm^2) pump.

Meanwhile, for the integrated PL spectra of our RP thin films, multiple peak emissions (except for $\bar{n}$ = 1 sample) were observed. Each of the PL peak corresponds to each of the n-phase present in the films. Relatively large Stokes' shift in the order of few tens of meV (~ 10 nm) were also visually observed for all the visually distinct phases (n = 1 to 3). It implies strong exciton-phonon interaction not only in pure 2D system (as discussed in Chapter 4), but also across multidimensional phases in this material class system. For increasing $\bar{n}$

(especially for $\bar{n}$ = 3 and 4), broad yet relatively strong emission at lower energy (~680 nm) were observed, regardless of the absence of any distinct absorption around the region. This emission may originate from either trap states, bound exciton or efficient energy funneling towards $n \geq 5$ phases with lower energy gap [5]. These $n \geq 5$ phases might also present in our thin films but with much lower density. The assignment of the origin will be elaborated in the next section.

5.1.3 Section summary

In summary, we investigated the structural and linear optical characterization of our solution processed RP perovskites. The key results of this section can be summarized into the following points:

1. Our perovskite thin films form $(C_6H_5C_2H_4NH_3)_2(CH_3NH_3)_{n-1}Pb_nI_{3n+1}$ structure with the phase *n* corresponds to the number of interconnected $[PbI_6]^{4-}$ octahedron layers (*i.e. the* thickness of inorganic layers).
2. Our thin film fabricated for a particular stoichiometric ratio $\bar{n}$ (> 1) contains multiple phases RP perovskites, regardless of its precursor solution.
3. Determination of lowest exciton energy for each phase *n* = 1 to 5. The bandgap (exciton energy) is observed to decrease with increasing *n*.
4. The weakening of excitonic behavior with increasing *n*, due to the weakening of dielectric and spatial confinement of exciton in the out-of-plane direction.

5.2 Transient photoexcited dynamics

Having characterized the linear optical properties of RP perovskites, we proceeded to study the transient photoexcited dynamics. While the ultimate goal is to explicate the optical-spin dynamics, the understanding of transient photoexcited dynamics will help in our interpretation of the observed optical-spin behaviors. In this section, we seek to first establish the fundamental understanding of the existing transient behavior and relaxation mechanisms for various phases and their interaction in RP perovskite thin films. For this purpose, we utilized the white-light transient absorption spectroscopy (WLTA) and the time-resolved photoluminescence spectroscopy (TRPL) as our main characterization techniques.

5.2.1 Transient spectral features

The transient spectral behavior, explicated by WLTA technique of our RP perovskite thin films with $\bar{n}$ = 1 to 4, are shown in **Figure 5.4**A-D. For $\bar{n}$ > 1 sample, multiple overlapping peaks were observed. As mentioned, they originate from multiple *n* phases that are present in the same film. The position of these peaks are consistent with our assignment of the lowest exciton energy for each phase based on our linear absorption spectroscopy (**Table 5.2**). As $\bar{n}$ increases, the amplitude of signature PB peak for lower *n* phase decreases and is eventually buried by strong broad photoinduced absorption (PA) bands induced, most likely by higher *n* (> 3). Such inter-mixing of signals complicates the analysis of transient dynamics for each individual RP phase.

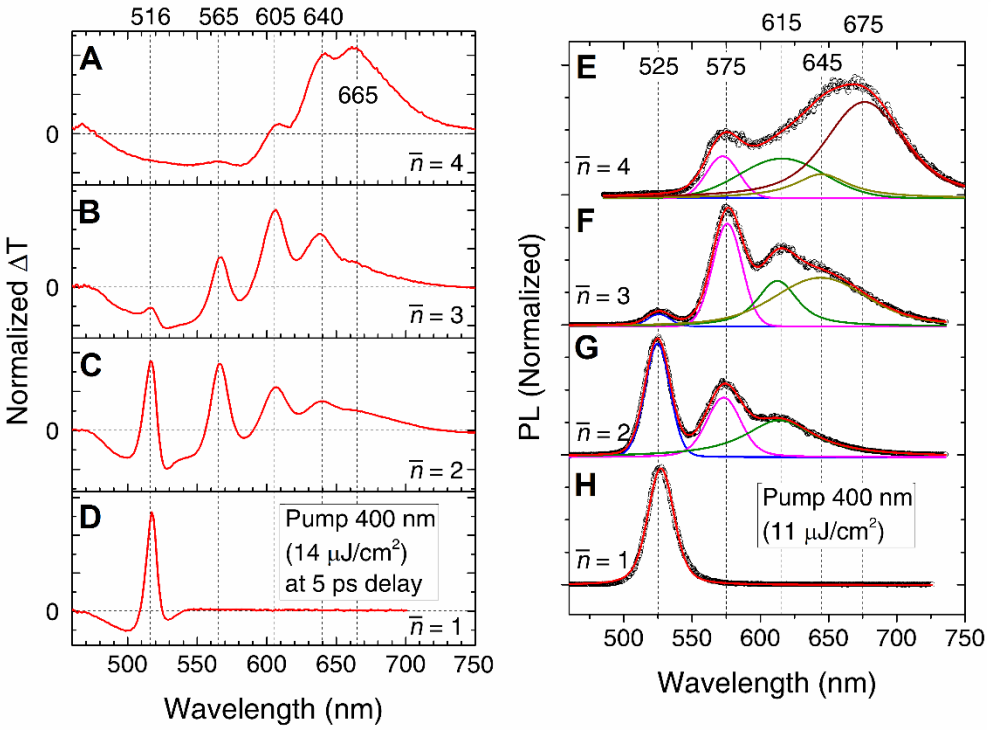

Figure 5.4 | WLTA and TRPL spectra of RP perovskite thin films. (A-D) TA spectra of our RP perovskite thin films with $\bar{n}$ = 1 to 4, photoexcited by 400 nm pump (14 μJ/cm^2) at 5 ps probe delay. PB peaks up to *n* = 5 can be distinguished. (E-H) The first 40 ps-integrated TRPL spectra of our RP perovskite thin films with $\bar{n}$ = 1 to 4, photoexcited by 400 nm pump (5.7 μJ/cm^2). These emission spectra is well-fitted by multiple Voigt peaks, each corresponds to *n* = 1 to 5 RP phases.

To untangle these intermixing of signals, our first approach is focused on identifying the properties of each phase *n* for each of our thin film. To gain further insights, we performed time-resolved photoluminescence (TRPL) studies on our RP perovskite thin films. While this technique is limited only to monitor the population of the radiative states, it is beneficial for us to discern the intricate dynamics of various processes by limiting the information we obtain.

The PL spectra integrated over the first 40 ps, photoexcited by 400 nm pump (~11 μJ/cm^2) are shown in **Figure 5.4**E-H. Here, we deconvolved the spectra with multi-Voigt profiles, to get the contribution of each phase. The Voigt profile is a convolution of Lorentzian (homogeneous) and Gaussian (inhomogeneous) profiles of line shape broadening. It forms a peak function which can mathematically be described as:

$$V(\sigma,\gamma,\omega) = \int_{-\infty}^{\infty} G(\omega,\sigma)L(\omega-\omega',\gamma)d\omega' = A\frac{2\ln 2}{\pi^{3/2}}\left(\frac{\gamma}{\sigma^2}\right)\int_{-\infty}^{\infty}\frac{e^{-x^2}dx}{\left(\frac{\gamma}{\sigma}\right)^2\ln 2+\left(2\sqrt{\ln 2}\left(\frac{\omega-\omega_0}{\sigma}\right)-x\right)^2}. \quad (5.1)$$

Here, $G(\omega,\sigma)$ and $L(\omega,\gamma)$ is the Gaussian and Lorentzian function, respectively; *A* is a constant; ω_0 is the peak position; σ and γ is the linewidth from inhomogeneous and homogeneous broadening, respectively. The line shape of a Voigt profile becomes purely Lorentzian when $\sigma \to 0$ and purely Gaussian when $\gamma \to 0$. One parameter which characterized the "degree of disorder" that causes the broadening is the ratio γ/σ (*i.e.* ratio γ/σ = 0 indicates a pure inhomogeneous broadening). The contribution from inhomogeneous broadening (Gaussian profile) to supposedly Lorentzian profile in the emission of excitonic 2D perovskite system is expected, and has been previously reported [10,11]. Such inhomogeneous broadening may originate from the disorder of the crystal lattices in our thin films.

From **Figure 5.4**B, it is clear that the spectra for $\bar{n}$ > 1 films show several peak features with center wavelengths correspond well to the absorption peaks of each RP perovskite phases. As $\bar{n}$ increases, the contribution to the emission

spectrum shifts from lower to higher *n*. For instance, contribution from *n* = 1 phase became less significant in $\bar{n}$ = 3 sample (**Figure 5.4**F), which totally diminished in $\bar{n}$ = 4 sample (**Figure 5.4**E). These observations are also consistent with our TA result (**Figure 5.4**A-D). Further insight was gained from the analysis of the γ/σ ratio. The γ/σ ratio for each *n* as function of our sample stoichiometric ratio ($\bar{n}$) is shown in **Figure 5.5**. A clear decreasing trend of γ/σ ratio as function of increasing $\bar{n}$ can be observed. This indicates the increase of disorders in lower *n* phase with increasing of CH_3NH_3I:$C_6H_5C_2H_4NH_3I$ stoichiometric ratio in the precursor solutions. This increase of disorder, in addition to its lower density, might diminish the contribution of low *n* phase in high $\bar{n}$ samples in the PL and TA spectra.

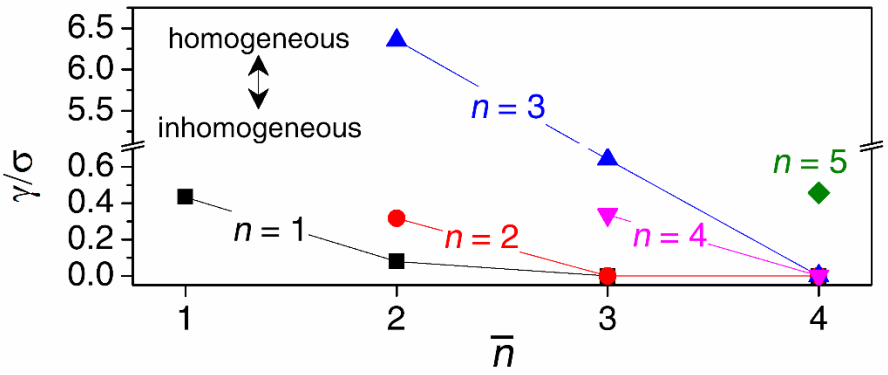

Figure 5.5 | Analysis of γ/σ ratio in RP perovskite thin films. The γ/σ ratio of the Voigt profile for each phase *n* as function of sample stoichiometric ratio $\bar{n}$. The increase (decrease) in the γ/σ ratio indicates the homogeneous (inhomogeneous) contribution to the peak broadening profile.

The increase of disorder in lower *n* might be relevant with our aim of assigning the transient spectral features. Referring back to **Figure 4.1**A-D, significant increase of broad PA band at high energy side ($\lambda \leq 600$ nm) was observed in our samples with increasing $\bar{n}$ from 1 to 4. The amplitude of PA band in our $\bar{n}$ = 4 RP thin film has significant proportion as compared to the amplitude of the PB peak (~50%). This proportion is much significant as compared to the pure 2D ($\bar{n}$ = 1, PEPI, only ~20%, Chapter 4); and even compared to the 3D perovskite system ($\bar{n} = \infty$, MAPI, also only ~20%, Chapter 3). It implies that this broad PA band is likely not to arise from the characteristic change of dimensionality. Other possibilities include PA band from charge

transfer states between the *n* phases in the film; or from the disorders in lower *n* phases in our thin films. These disorders are expected not only to suppress the state bleaching characteristic of each *n* phase but also create "traps" or "defect" states observable as PA band by our WLTA spectroscopy measurement. This hypothesis will be further verified later.

Having understood the nature of our sample, we proceeded to explicate the photophysics behind these intermixed RP phases. The fluence dependent time-integrated PL spectra for each of the film are shown in **Figure 5.6**A. Even within the low experimental range of the fluence, saturation effect of the total integrated PL intensity is observed. Meanwhile, there is also no obvious spectral change observed with increasing fluence across all samples. This negative result shows that there is no optical gain (*i.e.* amplified spontaneous emission) or any other fluence dependent spectral weight transfer process present in our material system. Bearing in mind its superior PL quantum yield [5], realizing an optical gain in RP perovskite system will be a significant achievement for efficient laser applications. However, it is currently out of the scope of the study.

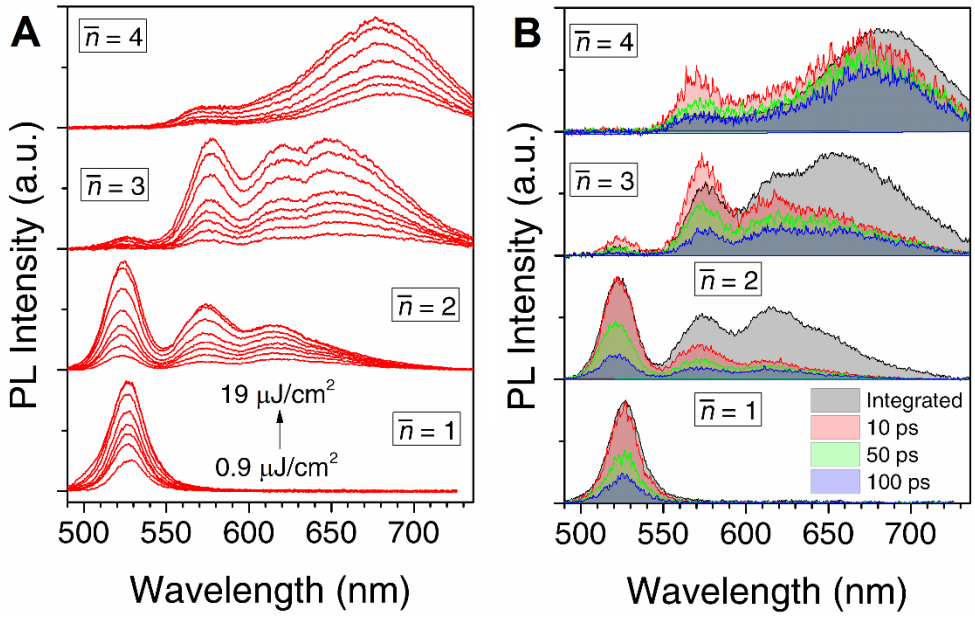

Figure 5.6 | PL spectra of RP perovskite thin films. (A) Fluence dependent time-integrated PL spectra. The samples were photoexcited by 400 nm pump. (B) Comparison between the time-sliced PL spectra at 10 ps (red), 50 ps (green), 100 ps (blue) and the time-integrated spectra (gray). The samples were photoexcited by 400 nm (1.9 μJ/cm^2) pump.

The comparison between the time-sliced and time-integrated PL obtained by TRPL spectroscopy is shown in **Figure 5.6**B. While for $\bar{n}$ = 1 phase, there is no observable difference between the time-sliced and time integrated PL spectra, differences were seen for $\bar{n}$ > 1 system. As compared to the time-sliced spectra, the red side (longer wavelength) of the time-integrated spectra are enhanced, especially around the lowest observable *n*. This phenomenon has also been reported in Ref. [5]. Solely based on this observation, ref. [5] attributed it to a carrier funneling process from low-*n* to high-*n* phases in such intermixed thin films. However, this is not necessarily the case, as this result is insufficient to neither prove nor disprove the assignment. The reason behind might be simply due to lengthening of the relaxation lifetime by reduction of confinement. This matter will in investigated in more detail in the next section. Given the time dependent PL function of $I(t) = I_0 e^{-t/\tau}$, the integrated PL intensity ($I_{PL}^{\text{Int.}}$) is expected not to be only proportional to the initial peak intensity (I_{PL0}) of the emission but also the lifetime (τ) of the system [eq. (5.2)]:

$$I_{PL}^{\text{Int.}} = I_{PL0} \int_0^\infty e^{-t/\tau} dt = I_0 \tau. \tag{5.2}$$

This is consistent with the fact that the carrier/exciton lifetime in lead halide perovskite system increases with decreasing confinement (*i.e.* $\tau_{2D} \ll \tau_{3D}$) [5-7,9,12-14]. Hence, it results in stronger integrated PL emission for higher *n*, regardless of their lower time-sliced initial intensity.

Another valuable insight was the nature of this radiative recombination pathways for each of the RP phase, *i.e.* whether it is a free carrier (bimolecular) or excitonic (monomolecular) recombination. The rate of radiative emission of the system is given by:

$$I_{PL}(t) = -\frac{dn_{\text{rad}}}{dt} \propto n^{\gamma} \tag{5.3}$$

From each of their respective nature, we expected γ = 1 for monomolecular (excitonic) emission and γ = 2 for bimolecular (free carrier) emission. Meanwhile, γ slightly less than these ideal values corresponds to non-radiative trap contribution [15,16]. The PL peak intensity (at t = 0) is therefore related to the initial photoexcitation density n_0 by:

$$I_{PL}(t=0) = I_{PL0} = An_0^{\gamma}$$
$$\log(I_{PL0}) = \gamma \log(n_0) + \log A \qquad (5.4)$$

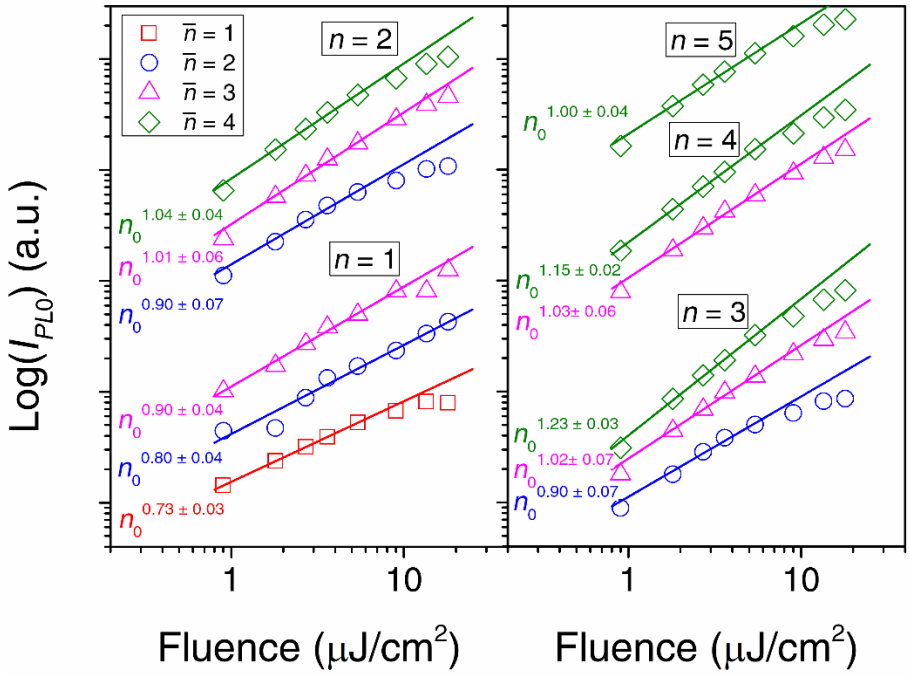

Figure 5.7 | Log-log plot of fluence versus I_{PL0} of RP perovskite thin films. The result for every phase *n* each in samples is presented. The thin film sample for $\bar{n}$ = 1, 2, 3 and 4 are shown as red square, blue circle, magenta triangle and green diamond, respectively. The γ value for each peak is also shown. The plot are y-offset for clarity. Only first 5 data were used for fitting to avoid saturation effect.

It is hence straightforward from eq. (5.4) to derive the radiative relaxation order γ from the gradient in the log-log plot of the initial photoexcitation density (n_0) which is proportional to the excitation fluence and the PL peak intensity (I_{PL0}). The experimental result for each phase *n* for each of our sample $\bar{n}$ is shown in **Figure 5.7**. The result shows that up to *n* = 5, the value of γ is close to 1, which reveals that the radiative recombination pathway in our RP sample mainly

excitonic in nature. In contrast, value of $\gamma \sim 2$ is observed for the case of $n = \infty$ (MAPI), where the radiative emission is mainly bimolecular [17,18]. This trend holds true especially below 10 μJ/cm^2. At higher fluence, the sub-linear deviation from the fitted line comes from the effect of saturation of the absorption.

Further analysis of the result shows that for a particular n, the γ tend to increase from $\gamma < 1$ approaching value of 1, with increasing $\bar{n}$. For instance, γ for $n = 1$ increases from 0.73 ± 0.03 to 0.90 ± 0.04 when $\bar{n}$ increases from 1 to 3. Surprisingly, for contrast it has also been shown previously (**Figure 5.5**) that the disorders also increase with increasing $\bar{n}$. This peculiar behavior implies that the disorder of low n phase in high $\bar{n}$ sample does not act as non-radiative recombination trapping pathway. Instead, the disorders act as a spatial localization center for exciton to radiatively recombine. Such localization will increase spatial overlap of electron and hole's wavefunction, and hence improve the radiative recombination rate. This increase of radiative recombination due to exciton localization has also been reported in other perovskite system, where light emission with higher efficiency is observed in system with much smaller grain size [19,20]. The exciton localization from the disorder might also be the reason of high PLQY reported in these RP perovskite thin films with intermixed phases [5]. Note that for $n > 1$ the values of γ have already approached 1, which also indicates minimum non-radiative trapping contribution in high n phase.

Having understood the excitonic nature of our RP thin films emission, the study proceeded to investigate the transient spectral signature of the RP thin films obtained from WLTA. While $\bar{n} = 2$ to 4 samples differ in their distribution of multiple n-phases population and degree of disorder, they share similar transient spectral (excitonic) behavior. In this case, we will focus on $\bar{n} = 3$ sample as the representative system for our assignment of the origin. TA spectra at 0.5 ps and 5 ps probe delay of $\bar{n} = 3$ sample photoexcited by 400 nm pump (14 μJ/cm^2) are shown in **Figure 5.8**. There are several major differences between the spectra at the early and later time delays. Specifically, at early probe delay (0.5 ps, **Figure 5.8**A) 4 dominant bleaching peaks at λ correspond to $n = 1$ to 4 are observed. Within this timescale, a broad PA band at $\lambda > 650$ nm is also initially observed. However, at the later time (5 ps, **Figure 5.8**B), the initial

n = 1 PB peak has then sunken into a broad PA band at λ < 550 nm. Meanwhile, the amplitudes of the n = 2 to 4 PB peaks have also evolved, *i.e.* weaker n = 2 peak, relatively constant n = 3 peak and stronger n = 4 peak. At the same time, the broad PA band at λ > 650 nm has also changed to a broad PB band. These changes/switching of TA signals in a particular spectral region can be observed as early as at the 1 ps probe delay, which indicates the sub-ps nature of the dynamics.

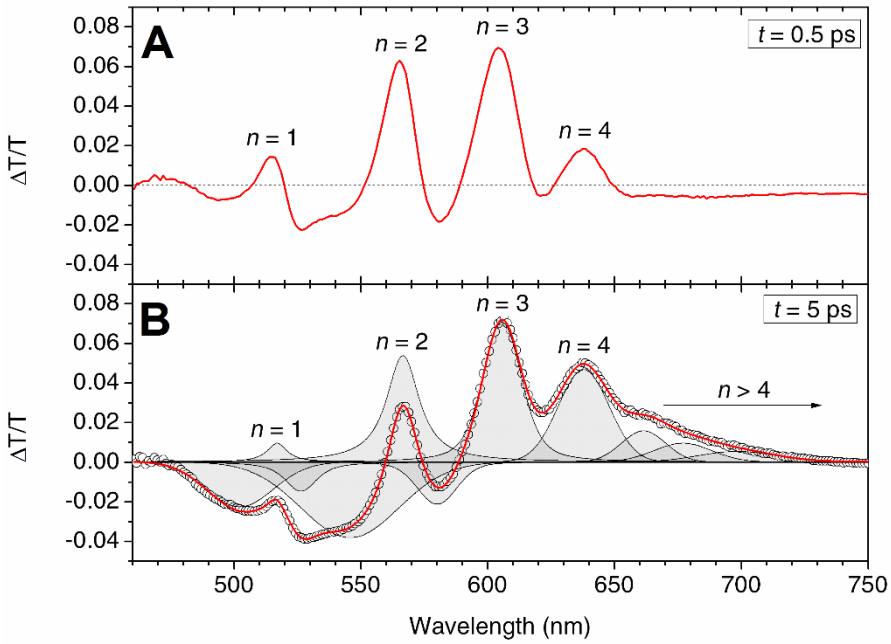

Figure 5.8 | WLTA spectra of $\bar{n}$ = 3 RP perovskite thin film. The WLTA spectra taken at (A) 0.5 ps and (B) 5 ps probe delay were photoexcited by 400 nm pump (14 μJ/cm^2). The 5 ps TA spectrum were fitted with 11 Voigt profiles.

The reason behind such observation is that there are multiple competing processes involving similar spectral region occurring in the system. In order to switch the sign of the TA signal at a particular spectral region, these multiple processes do not only possess different amplitudes of TA spectral signatures, but also different temporal kinetics. In particular, within the short timescale of the TA signal sign switching (< 1 ps), these processes most probably originate from different rise-times. Differences in rise-times, signs, and amplitudes allow one process with the fast rise to initially dominate the spectra at early times, however then engulfed by another process of stronger amplitude but with the slower rise. To deconvolve such complex features, the transient spectrum at 5

ps was then fitted with multi-Voigt profiles (**Figure 5.8**B). The fitting reveals that even at 5 ps, the n = 1 to 4 PB peaks still contributes to the signal. Especially for n = 1, while the exciton population in this phase contributes a positive TA signal, three other stronger PA peaks sharing similar spectral regions overwhelm this small PB peak, resulting in an overall negative $\Delta T/T$ signal. The fitting also reveals the rise of a broad PB band at $\lambda > 650$ originates from multiple $n > 5$ PB peaks with a slower rise.

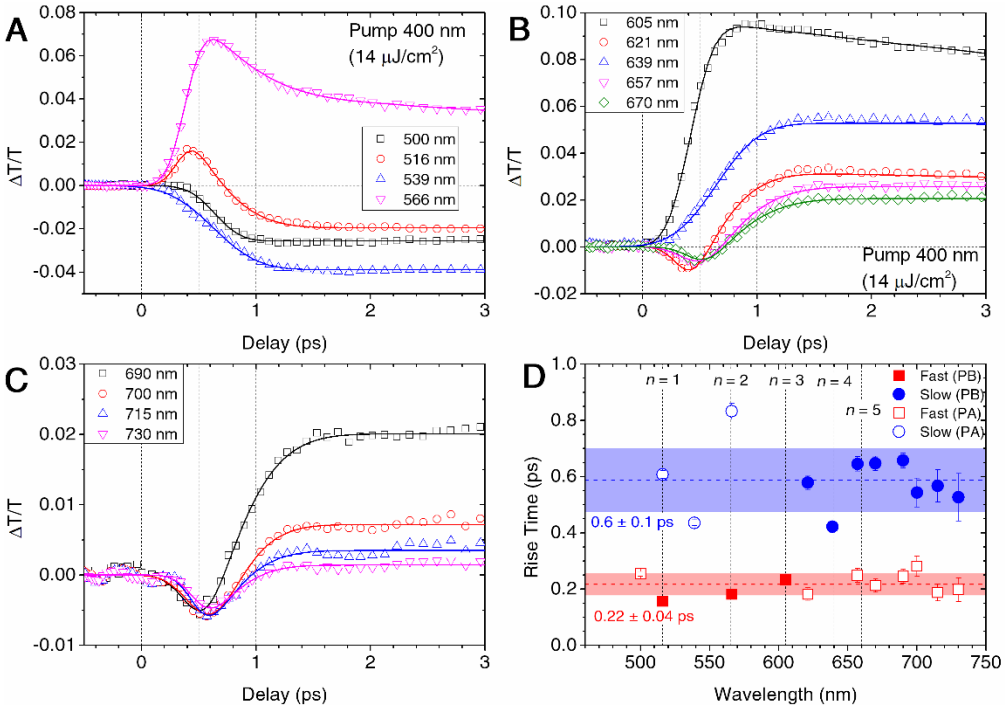

Figure 5.9 | Comparison of early TA kinetics in $\bar{n}$ = 3 RP perovskites. (A-C) The early (3 ps) TA kinetics of $\bar{n}$ = 3 perovskite thin films photoexcited with 400 nm (14 μJ/cm^2) pump at various probe wavelengths. The kinetics were fitted by eq. (5.5). Dashed lines are eye-guides. (D) The compilation of fitted rise time of the competing process. Filled and hollow symbol represents PB and PA signals, respectively. Red square and blue circle represents fast and slow rising process, respectively.

In order to elucidate the origin of these processes, we performed further quantitative analysis on the early time kinetics of the TA signal at various spectral region. Based on the hypothesis of two competing processes with different rise time, we constructed a function to fit the early temporal kinetics (3 ps time window) of the TA signal:

$$\frac{\Delta T}{T}(t) = \frac{1}{2}\sum_{i=1}^{2} A_i \left[1 + \mathrm{erf}\left(\frac{t}{r_i}\right)\right] e^{-t/\tau_i}. \qquad (5.5)$$

Here, the A_i is the amplitude of each dynamics component; r_i is the rise time of the signal, and $\tau_i >> 3$ ps is the lifetime of the signals. The fitted kinetics result is presented in **Figure 5.9**A-C. For most of the spectral regions, the kinetics are well-fitted by using eq. (5.5), which verifies the validity of our hypothesis of the 2 competing processes sharing the similar spectral region.

The fitted rise-times are compiled and presented in **Figure 5.9**D. The result shows that the rise-times are distributed into 2 groups of fast rise (r_1 = 0.22 ± 0.04 ps) and slow rise (r_2 = 0.6 ± 0.1 ps) processes. We attributed the fast and the slow rise to originate from the lower dimensional phases ($n \leq 3$) and higher dimensional phases ($n \geq 4$), respectively. Here, the discussion will be focused on the PB signal, which signifies the population of a particular state. The fast-rising PB signals in n = 1 to 3 phases indicate the immediate formation of excitons after photoexcitation, which is expected for a system with strong binding energy. Meanwhile, for $n \geq 4$, the slow rising PB signal implies a slow state filling process which is likely to originate from hot carrier thermalization towards the band edge, before forming the exciton. This result is also consistent with our previous observation of weaker excitonic interaction for $n \geq 4$ phases, which also might be the reason for relatively efficient charge extraction in n = 4 based RP phase perovskites [4]. Further analysis is required in order to quantify this excitonic interaction. Nonetheless, it is currently beyond the scope of this study.

Note that this analysis of slow/fast rising processes on the TA signal can also be used to discern the origin of the observed PA bands. The fast-rise of the PA band at $\lambda > 650$ nm region implies that this PA band arises from $n \leq 3$ RP phases. This PA band might originate from the high degree of disorder of low n phase in the sample. At the same time, the slow rise of the PA band at 510 nm $< \lambda <$ 550 nm implies that the band arises from $n \geq 4$ phases. The fitting also reveals the PA peak at ~500 nm (**Figure 5.8**B) has a fast rise time, which implies its origin from $n \leq 3$ phases. This peak might be similar to PA1 peak in the pure 2D system (PEPI, Chapter 4), yet with enhanced amplitudes.

5.2.2 Relaxation kinetics

Having established their transient spectral features, we proceed to study the relaxation kinetics our multiphase RP perovskite thin films. This section is focused on answering 2 main problems: (i) how does the dimensionality of RP phases affect the relaxation mechanisms; and (ii) as claimed in Ref. [5], does energy/charge funneling happen in RP perovskite thin film, how fast is the process. To avoid the complication of intermixing multiple competing processes captured by WLTA, TRPL spectroscopy will be used as the main experimental characterization technique in this section. TRPL will limit the time-resolved information obtained only to the population of the radiative states, which will simplify our analysis. Herein, we performed kinetic analysis in the spectral region for each phase *n*.

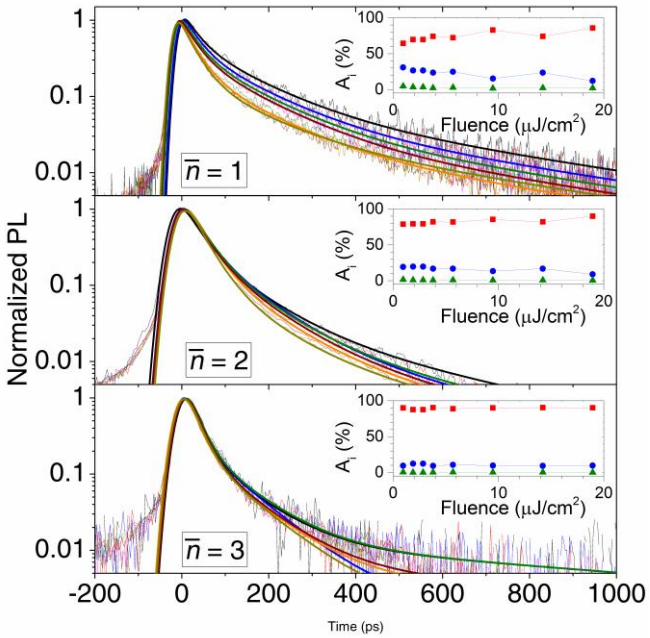

Figure 5.10 | PL Kinetics of RP perovskite thin films at ~525 nm (*n* = 1). The fluence dependent PL kinetics on $\bar{n}$ = 1 to 3 samples were global-fitted over the pump fluence of 0.9 to 19 μJ/cm^2 (400 nm) by using a tri-exponential decay function with lifetimes as shared parameters. Inset: the contribution of each of the lifetime component, shown in red square (A_1), blue circle (A_2) and green triangle (A_3).

The PL kinetics for $\bar{n}$ = 1 to 3 samples at *n* = 1 spectral region (~525 nm), photoexcited by 400 nm pump at room temperature is presented in **Figure 5.10**.

The kinetics is global-fitted across our pump fluence of 0.9 to 19 μJ/cm^2 by using tri-exponential decay function with the three lifetimes as the shared parameters. The third (long-lived) component might come from exciton trapping process. Note that the comparison of lifetime of a phase *n* across samples is a clear-cut indicator whether the energy/carrier funneling happens in the system. If energy/carrier funneling occurs, the exciton lifetime of a particular phase *n* is expected to be quenched with increasing $\bar{n}$, due to the additional phase (*n* + 1) present in the sample. This extra phase acts as exciton quencher. The efficiency (η) of this process is defined as $\eta = 1 - \tau'/\tau$, where τ and τ' are the quenched and unquenched lifetimes, respectively. The fitted lifetimes for $\bar{n}$ = 1 to 3 samples are summarized in the table **Table 5.3**.

Table 5.3 | Fitted lifetimes of the PL kinetics of *n* = 1 phase. The lifetimes were obtained from global fitting of tri-exponential decay across our excitation fluence.

$\bar{n}$	τ_1 (ps)	τ_2 (ps)	τ_3 (ps)
1	33 ± 1	122 ± 3	510 ± 20
2	35 ± 1	99 ± 3	370 ± 30
3	24 ± 1	92 ± 3	1000 ± 100

Based on the magnitude of the lifetimes, we attributed the first lifetime to originate from localized excitons (LX); while the second lifetime to the free exciton (FX) lifetime. This FX lifetime is which is consistent with what has been reported in the literature [13,21]. A small contribution (< 2%) from the third lifetime is attributed to exciton trapping/de-trapping process. A much shorter lifetime from LX as compared to FX is expected due to exciton localization. Localization by grain boundaries, isolated nano-domains or disorders will spatially confine the exciton and hence increase the probability of recombination [19,20]. The population of LX may come from either direct pump excitation or transfer from FX. The insets in **Figure 5.10** show the contribution of each fitted lifetime component. In $\bar{n}$ = 1 sample, the first lifetime component (A_1) is observed to increase with excitation fluence, and saturates around 10 μJ/cm^2 at ~80%. Similar behavior is also observed in $\bar{n}$ = 2 sample,

yet with gentler increase and higher saturation at ~85%. Meanwhile in $\bar{n}$ = 3 sample, a constant A_1 is observed at ~90%. In the meantime, A_2 and A_3 show complementary behavior. This "increase and saturate" trend of A_1 originates from the population transfer from FX to LX with increasing fluence. Increase of localization sites (*i.e.* disorder) with increasing $\bar{n}$ will increase the contribution from directly photoexcited LX, which then diminish the contribution from FX-LX transfer to the PL signal. Consequently, it diminishes the "increase and saturate" behavior, as observed for $\bar{n}$ = 2 and 3. Also need to be taken into notice that in this low fluence excitation range, exciton-exciton annihilation process is expected not to play a major role. Furthermore, exciton-exciton annihilation process is also expected to occur at much a faster lifetime of ≤ 10 ps (Chapter 4).

From the second lifetime (*i.e.* FX lifetime), we observed a pronounced lifetime quenching from $\bar{n}$ = 1 sample to $\bar{n}$ = 2 sample. This FX lifetime quenching is a direct proof of the funneling effect occuring in our RP perovskite thin films. Here, either energy or carrier funneling to other phases acts as extra pathways for *n* = 1 excitons, which increase the depletion rate and hence reduce the lifetime. From FX lifetime quenching (from ~120 ps to ~100 ps), the funneling rate is estimated to be ~1.7×10^{-3} ps^{-1}, with efficiency η = ~17%.

Note that while PL lifetime quenching of the *n* = 1 phase straightforwardly proves funneling effect in RP perovskite thin film, it is unable to clearly distinguish between whether charges or energy are transferred from one phase to another. Meanwhile, the band alignment between phases in RP perovskites are known to be type-II for *n* = 1 to 3, approaching quasi-type I with increasing *n* [5,6]. One of the established methods to confidently distinguish between energy and charge transfer is to study the donor-acceptor distance dependence [*i.e.* $\propto r^{-6}$ for Forster resonance energy transfer (FRET), and $\propto \exp(-r)$ for Dexter electron transfer, where r is the donor-acceptor distance]. In our system however, different *n* phases in the sample are spatially unresolved, which then limit our capability to study the distance dependence of this transfer. Improvements in sample fabrication technique are therefore required to be able to control the domain size of each phase inside the sample.

Nonetheless, our analysis suggested that the funneling effect involved is most likely to be an energy transfer process. The main indicator is the band alignment between different phases in this system, as illustrated in **Figure 5.11**. In either case of quasi-type I or type II configuration, band bending at the phase *n* and *n* + 1 junction will create spatial traps (with expected depth up to few hundreds of meV) for the carriers at both sides of the interface. These carrier traps will hinder the inter-phase transfer of either electron or both electron and hole, depending on the type of their band alignment. Moreover, for the case of RP perovskite thin films with strong exciton binding energy and small Bohr radius of few unit cells [22], spatial trapping of electron/hole will strongly inhibit exciton transfer. Conversely, these traps are not an obstacle for energy transfer process. Moreover, the requirement of spectral overlap between the donor emission and acceptor absorption for energy transfer is also fulfilled in these RP perovskites (**Figure 5.3**). Based on this analysis, we believe that these funneling is mainly an energy transfer process. Also, note that this confinement is expected to decrease with a smaller difference in bandgap between phases (*i.e.* between two high *n* RP phases).

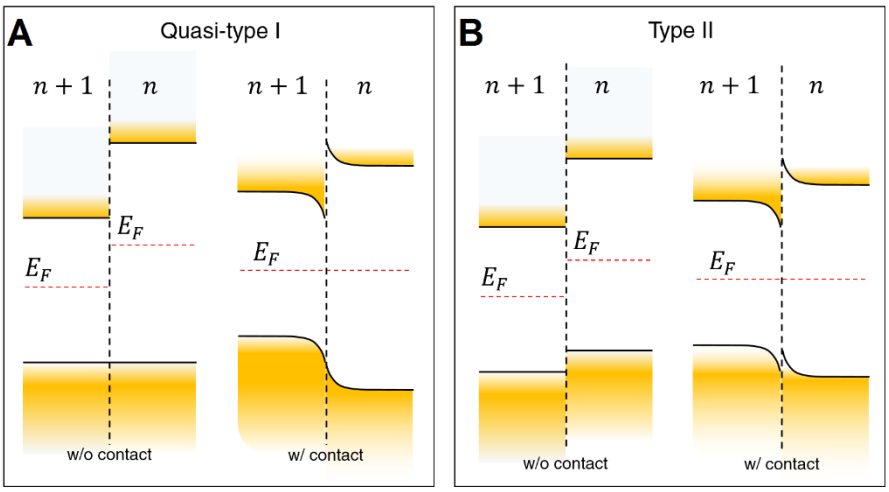

Figure 5.11 | Illustration of inter-phase band alignment in RP perovskites. The band edge alignment between *n* and *n* + 1 RP perovskites phases in (A) quasi-type I and (B) type-II configurations. For both cases, the band bending creates carrier traps. The Fermi level is assumed to be at the center of the gap.

Back to the effect of dimensionality on the exciton dynamics, similar lifetime analysis was also performed on n = 2 phase. The PL kinetics for $\bar{n}$ = 2 to 4 samples spectral region (~575 nm), photoexcited by 400 nm pump at room temperature is presented in **Figure 5.12**. Here, 3 shared lifetimes were used to fit PL emission. The resulting lifetimes obtained are summarized in **Table 5.4**. The first (τ_1, shortest) lifetime component of ~30 ps is attributed to the LX.

Table 5.4 | Fitted lifetimes of the PL kinetics of n = 2 phase. The lifetimes were obtained from global fitting of tri-exponential decay across our excitation fluence.

$\bar{n}$	τ_1 (ps)	τ_2 (ps)	τ_3 (ps)
2	34 ± 1	190 ± 2	1090 ± 20
3	27 ± 1	127 ± 3	550 ± 30
4	28 ± 1	165 ± 3	1180 ± 40

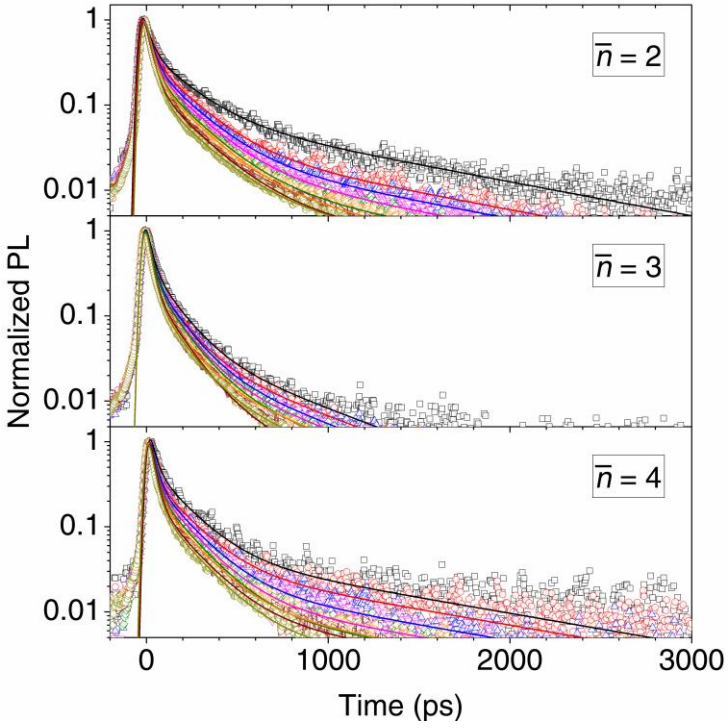

Figure 5.12 | PL Kinetics of RP perovskite thin films at ~575 nm (n = 2). The fluence dependent PL kinetics on $\bar{n}$ = 2 to 4 samples were global-fitted across pump fluence of 0.9 to 19 μJ/cm^2 (400 nm) by using tri-exponential decay function with the lifetimes as their shared parameters.

The second lifetime (τ_2, intermediate) at ~190 ps ($\bar{n} = 2$) is attributed to the FX. Here, quenching of these FX lifetimes is also observed across $\bar{n}$ = 2 to $\bar{n}$ = 3 sample (*i.e.* from ~190 ps to ~127 ps), which signifies the funneling effect from *n* = 2 to *n* = 3 phase. In this case, the funneling rate is estimated to be ~2.6 × 10^{-3} ps^{-1} (η = ~33%). This quenching is greatly reduced on $\bar{n}$ = 4 sample, which might be due to increasing isolated exciton localization sites of *n* = 2 phase in the form of isolated nano-domains. This might result in a decrease of *n* = 2 and 3 phase interfaces areas, which then diminishes the funneling effect. The observed third lifetime (τ_3) is assigned to the exciton trapping/de-trapping.

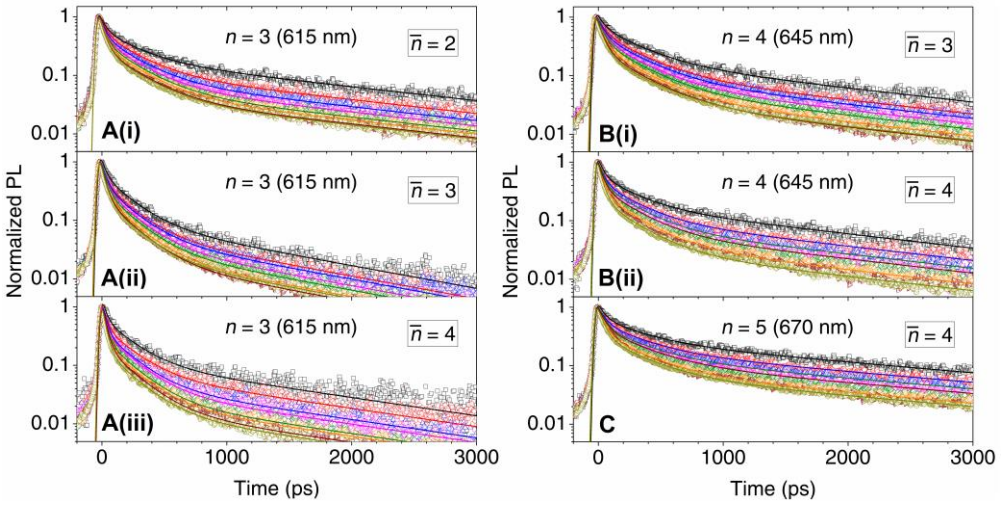

Figure 5.13 | PL Kinetics of RP perovskite thin films for *n* = 3 to 5. The fluence dependent PL kinetics on $\bar{n}$ = 2 to 4 samples of the (A) *n* = 3, (B) *n* = 4 and (C) *n* = 5 phases were global-fitted across pump fluence of 0.9 to 19 μJ/cm^2 (400 nm) by using tri-exponential decay function with the lifetimes as their shared parameters.

A similar analysis was also carried out for *n* = 3 and 4. The fitted lifetimes of the PL kinetics are summarized in **Table 5.5**. Similar quenching of FX lifetime (τ_2) were observed in *n* = 3 phase, which signifies funneling from *n* = 3 to 4 phase. The funneling rate is estimated to be ~1.3 × 10^{-3} ps^{-1}, with efficiency of η = ~24%, for $\bar{n}$ = 2 to $\bar{n}$ = 3 sample. For *n* = 4 phase, inefficient quenching is observed with rate of ~5.6 × 10^{-4} ps^{-1} and efficiency of ~14% is observed. Meanwhile, the funneling process in *n* = 5 phase cannot be analyzed due to the lack of quencher in the samples used for current study.

Table 5.5 | Fitted lifetimes of the PL kinetics of n = 3 to 5 phases. The lifetimes were obtained from global fitting the tri-exponential decay across our excitation fluence.

n	$\bar{n}$	τ_1 (ps)	τ_2 (ps)	τ_3 (ps)
3	2	42 ± 1	252 ± 3	1840 ± 30
	3	35 ± 1	191 ± 2	1120 ± 20
	4	30 ± 1	196 ± 3	1390 ± 30
4	3	51 ± 1	290 ± 3	1830 ± 10
	4	37 ± 1	249 ± 3	1790 ± 20
5	4	51 ± 1	311 ± 4	2380 ± 20

In order to perform a comparative study on the effect of dimensionality, we compiled the measured/estimated properties of each RP phase *n* obtained from our experiments. The result is presented in **Table 5.6**. While it is not clearly seen in LX, FX shows a trend of increasing lifetime with increasing *n*. This result is anticipated due to the intrinsic reduction of spatial confinement from the crystal structure. This reduction of confinement also results in a decrease of the exciton binding energy and oscillator strength [22]. Meanwhile, the estimated efficiency of the energy funneling process is observed to increase from n = 1 and peaked around n = 2 and 3, before it decreases for n = 4. The trend is tentatively attributed to the interplay of absorption-PL spectral overlap and the respective oscillator strength between RP phases. Increasing the absorption-PL overlap is expected to increase the energy transfer probability. Similarly, increasing oscillator strength is also expected to increase the transfer probability. Our observation of "peak-behavior" might also be the reason behind the reported peak behavior of PL quantum yield of RP thin film samples, with maximum peak around average-*n* (or $\langle n \rangle$, similar to $\bar{n}$) of 3 to 5 [5].

Table 5.6 | Compilation of the estimated properties of each phase in RP perovskite thin films. Here, LX is the localized exciton lifetime; FX is the free exciton lifetime; k_F is the funneling rate from n to n + 1 phase; and η is the funneling efficiency.

n	LX (ps)	FX (ps)	τ_3 (ps)	k_F (ps^{-1})	η (%)
1	31 ± 6	120 ± 10	510 ± 20	1.9×10^{-3}	19 ± 1
2	30 ± 4	190 ± 10	1100 ± 100	2.6×10^{-4}	33 ± 1

3	36 ± 6	250 ± 10	1800 ± 50	1.3×10^{-3}	24 ± 1
4	44 ± 10	290 ± 10	1800 ± 50	5.6×10^{-4}	14 ± 1
5	51 ± 5	310 ± 10	2400 ± 100	-	-

5.2.3 Section summary

In summary, we have investigated the spectral features and relaxation kinetics of photoexcited species in RP perovskite thin films. The key results presented in this section can be summarized into the following points:

1. Increase of inhomogeneous broadening in PL emission of each phase (n) in samples with increasing $\bar{n}$. This increase of inhomogeneous broadening implies increasing of disorder present in the sample.
2. Determination of the monomolecular/excitonic nature of the radiative recombination for RP phase from $n = 1$ up to $n = 5$.
3. Decreasing non-radiative trap contribution of a particular phase n with increasing $\bar{n}$. Together with the fact that the disorder of a particular n increase together with $\bar{n}$, it implies that the disorder behaves as exciton localization sites. Such spatial localization will increase the probability of exciton to undergo radiative recombination.
4. Observation of fast/immediate exciton formation for $n = 1$ to 3 phase in the timescale of ~0.2 ps, while slow exciton formation at the timescale of ~0.6 ps for $n \geq 4$ phase.
5. Assignment of PA bands observed by WLTA at $\lambda < 510$ nm and $\lambda > 650$ nm to originate from $n \leq 3$ phase, while PA band at 510 nm $\leq \lambda \leq$ 650 nm to originate from $n \geq 4$ phase.
6. Assignment and lifetime measurement of three species of excitons in RP perovskite thin films for $n = 1$ to 4: localized excitons (lifetime of 25-50 ps), free excitons (lifetime of 150-300 ps) and exciton trapping/de-trapping (100-2500 ps). These lifetimes increase with increasing n due to the intrinsic decrease of spatial confinement in crystal structures.
7. Estimation of inter-phase funneling rate and efficiency in RP perovskites. The energy transfer efficiency is found to be peaked up to ~33% around $n = 2$ or 3 phase.

8. Tentative assignment of energy transfer process (instead of charge transfer) for the funneling effect between different RP phases. This assignment is derived from band bending analysis at the inter-phase junction.

5.3 Optical spin dynamics

Moving from the transient photoexcited exciton dynamics, we proceed to study the dynamics of optical-spin dynamics in RP perovskite thin films. Understanding how the dimensionality affects the spin relaxation is not only novel and interesting from the perspective of fundamental studies but also allows us to assess the potential of this system for opto-spintronic applications.

5.3.1 Exciton angular momentum states

In order to perform optical-spin studies on the material system, it is important to first know the states on which we are probing. Knowledge of these states, especially on the angular momentum states will help us to design and analyze our experiments. Based on DFT calculation, it has been known that the band structures of lead iodide RP perovskites are similar across different dimensional phases, which resembles the pure 2D and 3D system [23]. The conduction band (CB) of this material class consists primarily of Pb 6p orbital, while the valence band (VB) consists primarily of I 5p and Pb 6s orbitals [7,23].

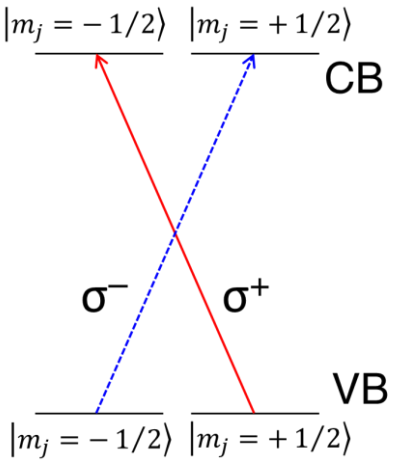

Figure 5.14 | Optical election rule for circular polarization in one-particle picture. Band edge with total angular momentum states $J = 1/2$ and $|m_J = \pm 1/2\rangle$ across dimensionality in RP perovskite system results in similar spin-selective optical excitation by circularly polarized photon.

Another resemblance with the pure 2D and 3D system is its strong spin-orbit coupling (SOC), which strongly reconstructs the band edge of this material [4,7,23]. Hence, we expect similar band-edge characteristic of total angular momentum states $J = 1/2$ and $|m_J = \pm 1/2\rangle$ for both CB and VB, similar to the pure 2D (Chapter 4) and 3D (Chapter 3) perovskite system. From the conservation of angular momentum, such band structures allow photoexcitation of spin polarized carriers/exciton by circularly polarized light with 100% spin polarization (**Figure 5.14**).

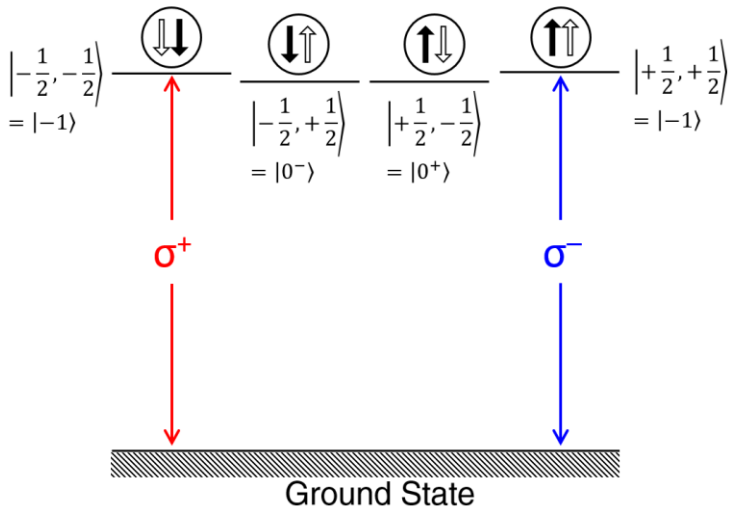

Figure 5.15 | Band-edge exciton angular momentum states in two-particle picture. The electron (solid arrow) and hole (hollow arrow) which constitute the exciton are presented, for straightforward identification of their original angular momentum state m_J. The resultant exciton states are represented in $|m_J^e, m_J^h\rangle$ notation.

Hereafter, a two-particle picture will be used to describe the states of this RP system (in contrast to one particle picture in **Figure 5.14**). This representation is obligatory to properly describe an excitonic system. In two-particle picture, these $J = 1/2$ band edge states are represented by 4 states which are all the possible combinations of electron and hole total angular momentum (*i.e.* m_J^e and m_J^h respectively) to form an exciton. Note that hole angular momentum state (m_J^h) is the inverse of the VB state (*i.e.* $|m_J^h = +1/2\rangle$ holes will populate the $|m_J = -1/2\rangle$ VB states). In $|m_J^e, m_J^h\rangle$ notation, these

four states are: $|+1/2,+1/2\rangle$, $|+1/2,-1/2\rangle$, $|-1/2,+1/2\rangle$, and $|-1/2,-1/2\rangle$. They are illustrated in **Figure 5.15**. The $|+1/2,+1/2\rangle$ (or $|+1\rangle$) and $|-1/2,-1/2\rangle$ (or $|-1\rangle$) states are the optically allowed/active states; while the $|+1/2,-1/2\rangle$ (or $|0^{+}\rangle$) and $|-1/2,+1/2\rangle$ (or $|0^{-}\rangle$) are the optically forbidden/inactive states. Similar selection rule of circularly polarized light is also applied in this representation, where the absorption of $\sigma^{\pm}$ light will populate the $|\pm 1\rangle$ state.

The importance of this representation for our spin dynamics study is the explicit presence of two degenerate optically inactive states (*i.e.* $|+1/2,-1/2\rangle$ and $|-1/2,+1/2\rangle$). While photoexcitation by circularly polarized light will only populate the optically active states, because of spin relaxation, these states might also be populated. In the case of an excitonic system, the bound electron-hole pair is detected as one entity by the probe. Hence, when the excitons move from optically active to inactive states, the exciton will be seen as "missing" by our optical probe. It is marked by the decay of the PB signal of one circular probe polarization, without a concomitant signal rise of the complementary probe polarization. More detail is presented in the subsequent sections. Conversely, in a free carrier system, the population of electron and hole states is detected independently (Chapter 3, section 3.31). Transfer to any band edge state will only transfer the signal weight from one probe polarization to another. This concept gives a fundamental difference between spin dynamics in a free carrier and an excitonic system. It also holds significant importance for our analysis in the later discussion.

5.3.2 Preliminary results

The first question which we would like to address in this section is how the dimensionality affects the photoexcited spin dynamics. To tackle the issue, we performed spin-dependent degenerate transient absorption study with circular polarization control for different phases (n) in our RP perovskite thin films. The samples used for the experiments were chosen to be $\bar{n} = n$. This was to minimize the complication of possible interphase spin-related processes in our signal. The spin dynamics for phase of n = 1 to 4 is shown in **Figure 5.16**. Each phase is probed by their respective resonant wavelength.

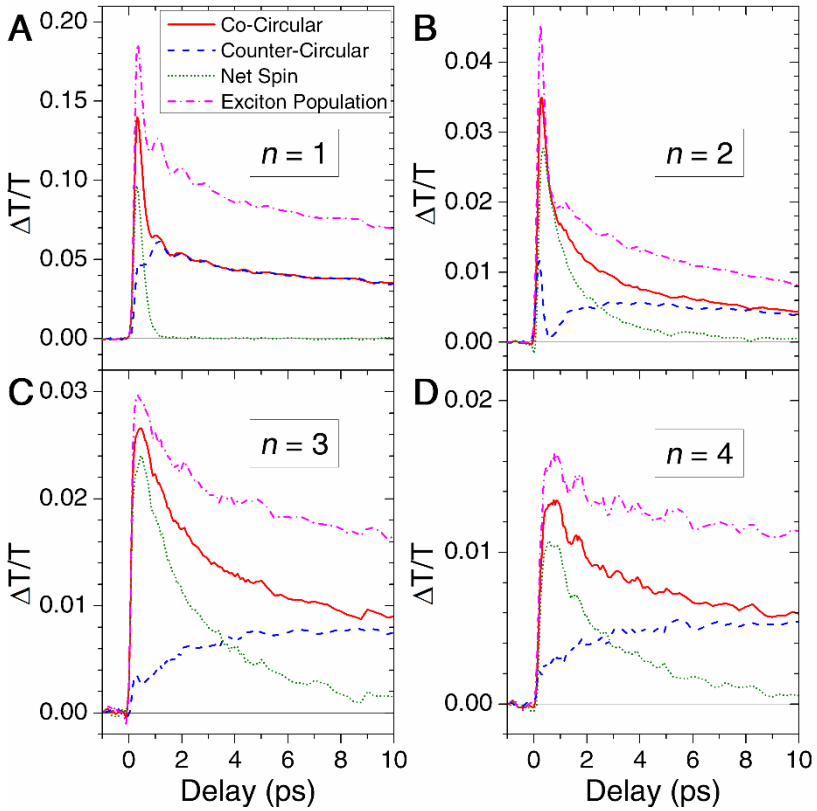

Figure 5.16 | Degenerate spin-dependent kinetics of RP perovskite thin films. (A-D) The kinetics captured by co-circular and counter-circular probe for n = 1 to 4 or RP perovskite thin films are shown in red solid and blue dashed line, respectively. Their difference (*i.e.* net spin) and their total (*i.e.* exciton population) are shown in green dotted and magenta dash-dotted line, respectively.

Similar to our data is presented in Chapter 3 and 4, a different circular component of probe polarization will trace population of different spin states. Without loss of generality, we assumed photoexcitation of spin-polarized exciton by σ^+ pump. Herein, the σ^+ probe will monitor the population of the exciton spin-state which is initially filled by the pump. Hence, a fast-rising PB signal from fast population filling is expected from σ^+ probe. Meanwhile, the σ^- probe will monitor then the population of the complementary exciton spin-state, which is initially empty. As the initial of the photoexcited exciton spin-polarization relaxes, this complementary spin-state is filled. This process will be observed as a simultaneous rise and decay of the σ^- and σ^+ probe signals, respectively. However, if the exciton relaxes to the optically forbidden spin

states, the decay will not be followed by a concomitant rise of the σ^- probe signal. Such process will be discussed in further detail in the next section.

The spin-polarization will eventually reach equilibrium (*i.e.* equal population of both exciton spin-states), which is marked by the merging of these σ^- and σ^+ probe signals. Here, the difference between σ^+ and σ^- probe signals forms a transient exponential decay curve, which represents the net spin polarization dynamics. Meanwhile, their summation signifies the dynamics of the total exciton population.

These described dynamics are indeed observed in **Figure 5.16**(A-D) for all n = 1 to 4. **Figure 5.16**A shows the spin-polarized exciton kinetics of n = 1 RP phase (*i.e.* PEPI) degenerately pumped and probed at its excitonic resonant wavelength of ~515 nm. The detailed transient relaxation kinetics of this system has been discussed in detail in Chapter 4. Similar dynamics reported in Chapter 4 are also observed, *i.e.* sub-ps exciton spin relaxation, ultrafast thermalization, and strong oscillation from the exciton-phonon coupling, which signifies the reproducibility of our result. **Figure 5.16**B shows the spin-polarized exciton kinetics of n = 2 RP phase at its excitonic resonant wavelength of ~570 nm. Similar to n = 1 phase, fast lifetime arising from exciton thermalization is also observed in the early time scale. Such thermalization redistributes the photoexcited exciton population based on Bose-Einstein distribution, which smears out the spectral overlap between the exciton distribution and the relatively narrow optical transition dipole-moment. It is therefore detected as a fast decrease of the PB signal. This process is also commonly observed in excitonic inorganic MQW [24].

Apart from the similar early exciton dynamics, an increase in the spin relaxation lifetime is also observed. **Figure 5.16**C and D shows the spin-polarized exciton kinetics of n = 3 and n = 4 RP phases at their excitonic resonant wavelengths of ~605 nm and ~640 nm, respectively. Here, no obvious fast signal relaxation arising from exciton thermalization is observed for both samples. It is due to weaker oscillator strength and broader optical transition dipole-moment (*i.e.* can be seen in the deconvolution of PL peak – **Figure 5.4**E-H). Further improvement of the spin lifetime with increasing n can also be visually seen.

5.3.3 Exciton spin relaxation pathway

Next, we proceed to first understand the mechanism of the spin relaxation process in an excitonic system. Theoretically, the exciton spin relaxation pathway can be generally categorized into direct and indirect spin relaxation. Direct exciton spin relaxation occurs when the electron and hole undergo simultaneous spin flip due to the electron-hole exchange interaction [24-27]. Meanwhile, indirect exciton spin relaxation occurs due to sequential spin flips of the single particles (either electron or hole), with the spin lifetime limited by the slower single particle spin-flip rate [24,26]. Herein, we attempted to categorize the spin relaxation pathway in RP perovskites phases into these two general categories.

A theoretical explanation for direct exciton spin flip in conventional III-V and II-VI inorganic semiconductor MQW system has been established by Maialle *et al.* [25]. The mechanism behind is attributed to the long-range part of the electron-hole Coulomb exchange interaction, with spin relaxation time inversely proportional to momentum scattering time [25]. Spin-flipping based on this direct pathway will directly transfer the population from $|\pm 1\rangle$ to $|\mp 1\rangle$ states [26]. Assuming an initial excitation by σ^+ pump, the signature of this process is the concomitant rise and decay of the σ^- and σ^+ probe signal, respectively. This process is observed as a decay in the net spin signal [*i.e.* ($\sigma^+ - \sigma^-$)], but not on the total population signal [*i.e.* ($\sigma^+ + \sigma^-$)] – **Figure 5.17**A.

Meanwhile, the indirect or sequential pathway will transfer the population from $|\pm 1\rangle$ to $|0^{\pm}\rangle$ state, and vice versa [26]. Ciuti *et al*. have demonstrated theoretically that the mechanism behind this pathway is dominated by inter-exciton fermion-fermion exchange interaction, during exciton-exciton scattering process [28]. In this case, assuming σ^+ pump, the decay of σ^+ signal will not be followed by the rise of σ^- signal. This process is also reflected in the kinetics of total population signal (**Figure 5.17**B). Experimentally, it is apparent in n = 2 RP phase (**Figure 5.16**B), where the fast decay of co-circular signal is unbalanced with the rise of the counter-circular signal.

Meanwhile, the presence of both direct and direct pathways will result in the observation of two-lifetime components in the net spin signals, with both lifetimes from a combination of single particle lifetime and exciton spin lifetime

[26]. This kinetic can be qualitatively illustrated in **Figure 5.17**. This illustration is also consistent with the result of the theoretical modeling of exciton spin dynamics reported in ref. [25].

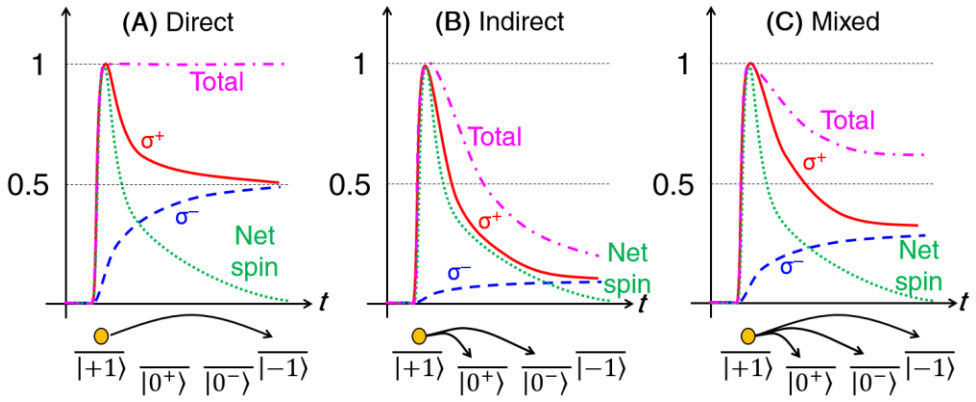

Figure 5.17 | Illustration of exciton spin TA kinetics. Without the loss of generality, the TA kinetics assume σ^+ pump excitation and exciton lifetime much longer than the spin lifetime. The figures show the expected TA probe kinetics for the case of (A) direct, (B) indirect and (C) mixed exciton spin relaxation pathway of the σ^+ (red solid), σ^- (blue dashed), net spin (green dotted) and total population (dashed-dotted).

5.3.4 Exciton spin relaxation model

To quantify the interplay of these pathways in our RP perovskites, we developed a quantitative model on the population dynamics of the spin states. The model is adapted from spin dynamics model in GaAs QW system in ref. [25], but modified for our RP perovskite system. Given the population of $|+1\rangle$, $|0^+\rangle$, $|0^-\rangle$ and $|-1\rangle$ exciton spin states to be N_{+1}, N_{0^+}, N_{0^-} and N_{-1} respectively, the population dynamics can be modelled by the following four coupled differential equations:

$$\frac{dN_{+1}}{dt} = -(W_x + W_e + W_h)N_{+1} + W_h N_{0^+} + W_e N_{0^-} + W_x N_{-1} \quad (5.6)$$

$$\frac{dN_{0^+}}{dt} = +W_h N_{+1} - (W_e + W_h)N_{0^+} + W_e N_{-1} \quad (5.7)$$

$$\frac{dN_{0^-}}{dt} = +W_e N_{+1} - (W_e + W_h)N_{0^-} + W_h N_{-1} \quad (5.8)$$

$$\frac{dN_{-1}}{dt} = +W_x N_{+1} + W_e N_{0^+} + W_h N_{0^-} - (W_x + W_e + W_h)N_{-1}. \quad (5.9)$$

Here, W_x is the direct exciton spin relaxation rate; W_x, W_e and W_h are the exciton, electron and hole recombination rate, respectively. Note that we assumed the spin relaxation rate is much larger than the exciton recombination rate (W_R), hence W_R it is neglected. Another assumption is that the dark exciton will not undergo simultaneous electron and hole flips (*i.e.* $N_{0^+} \leftrightarrow N_{0^-}$) [25]. Without loss of generality, assuming initial σ^+ pump photoexcitation, the initial condition ($t = 0$) of the system is given by:

$$N_{+1} = 1 \tag{5.10}$$

$$N_{0^+} = N_{0^-} = N_{-1} = 0. \tag{5.11}$$

In our case, we are interested in the net spin component (*i.e.* $S \equiv N_{+1} - N_{-1}$). Solving for $S(t)$, we obtain:

$$\begin{aligned} S(t) = \frac{1}{2}\left(1 + \frac{W_x}{\sqrt{W_x^2 + (W_e - W_h^2)}}\right)\exp(-\gamma_1 t) \\ + \frac{1}{2}\left(1 - \frac{W_x}{\sqrt{W_x^2 + (W_e - W_h^2)}}\right)\exp(-\gamma_2 t). \end{aligned} \tag{5.12}$$

Similar with other conventional inorganic semiconductor QW system [24-26], two decay components are observed when both direct and indirect relaxation exciton relaxation pathway co-exist in the RP perovskite system. These two lifetimes are given by:

$$\gamma_1 = W_x + W_e + W_h + \sqrt{W_x^2 + (W_e - W_h)^2} \tag{5.13}$$

$$\gamma_2 = W_x + W_e + W_h - \sqrt{W_x^2 + (W_e - W_h)^2}. \tag{5.14}$$

Based on eq. (5.12) to (5.14), we were able to deconvolve the individual spin relaxation rate of each pathway from our experimental data. Note that based on eq. (5.12), when $W_e = W_h = 0$ (*i.e.* only direct pathway), there will only be a single lifetime component observed. Meanwhile, when $W_x = 0$, there will be two decay lifetimes with equal amplitudes observed.

5.3.5 Effect of dimensionality

The spin lifetime of the n = 1 phase is shown in **Figure 5.18**. Single exponential decay behavior is observed on the transient net spin signal. Based on our previous analysis, the spin relaxation in this n = 1 phase only consists of direct exciton spin flip pathway (*i.e.* $W_e = W_h = 0$), which originate from electron-hole exchange interaction. This assignment is in line with the strong exciton binding energy (~150 meV, Chapter 4) observed in n = 1 phase. The spin relaxation lifetime is also observed to be fluence independent (**Figure 5.18**B), which implies exciton-exciton scattering does not play a role in the spin relaxation process. The average direct spin relaxation rate (W_x) in this n = 1 RP phase is measured to be 4.1 ± 0.1 ps^{-1}, which corresponds to a spin relaxation time of 0.24 ± 0.01 ps.

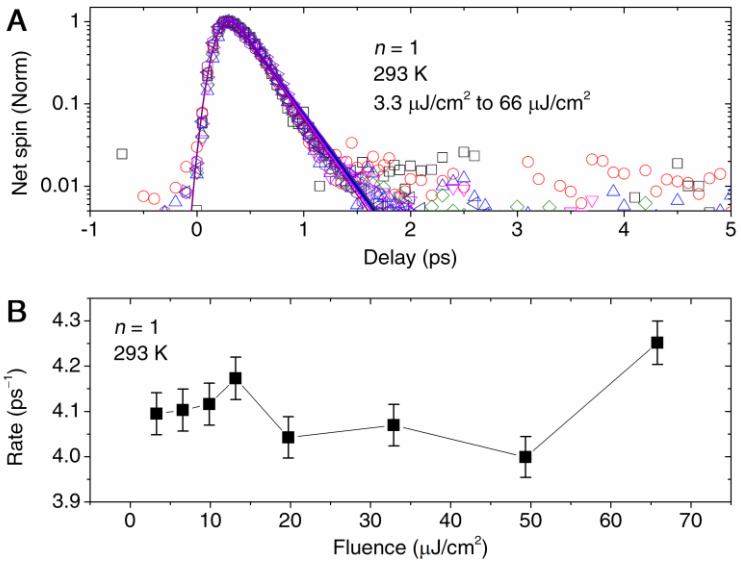

Figure 5.18 | Fluence dependent relaxation time of n = 1 RP perovskite phase. (A) The kinetics fitted with single exponential transient decay function. (B) The spin relaxation rate shows no dependence on fluence. The average W_x for this n = 1 phase is 4.1 ± 0.1 ps^{-1}.

Meanwhile, for $n \geq 2$ phases, an intricate combination of the direct and indirect spin pathway is observed. Based on **Figure 5.16**B-D for n = 2 to 4, a fast decay of the co-circular probe signal is followed by a rise of the counter-circular probe signal, but with a slower rate, which matches the description of mixed pathways of direct and indirect exciton spin-flip (**Figure 5.16**C). Another

evidence of these mixed pathways is the observed two decay lifetime components on the net spin signal. The fluence dependent net spin kinetics for n = 2 to 4 RP phases are fitted by using eq. (5.12). The deconvolved relaxation rates W_x, W_e and W_h are presented in **Figure 5.19**.

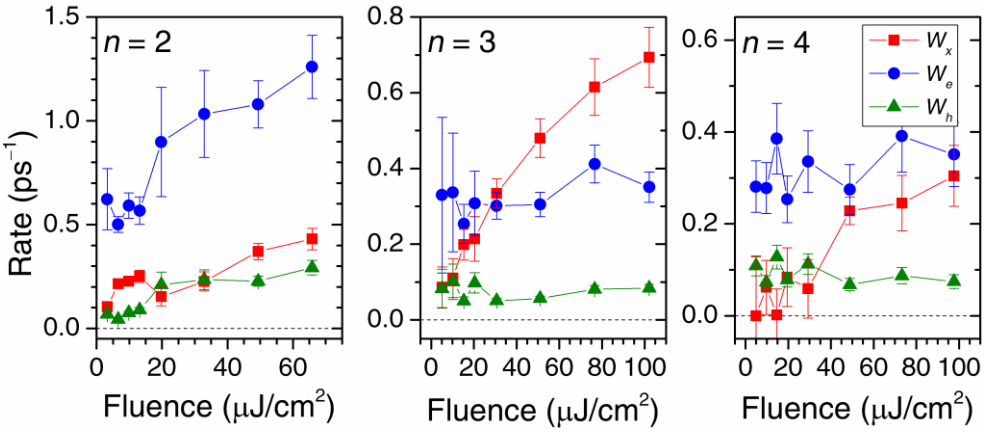

Figure 5.19 | Fluence dependent spin relaxation rate of n = 2 to 4 RP perovskite. The exciton (W_x), electron (W_e) and hole (W_h) spin relaxation rates are shown as red square, blue circle and green triangle, respectively.

Here, we assumed $W_e > W_h$, due to spin-orbital band mixing of the perovskites conduction band (Chapter 3). From the result, for n = 2 phase, the relaxation rates for W_x, W_e and W_h shows an increasing trend with excitation fluence. The dependence of relaxation rates on the excitation density implies that the relaxation mechanisms are related to exciton-exciton scattering process. In this phase, exciton spin (W_x) relaxes at a similar rate as the hole spin (W_h) with values ranging from ~0.1 to ~0.4 ps^{-1}, whereas the electron spin (W_e) relaxes with much faster rate, ranging from ~0.5 to ~1.3 ps^{-1}. Meanwhile, for n = 3 and 4, apart from their lower spin relaxation rates, W_e and W_h are observed to be fluence independent, while W_x maintain similar increasing trend with excitation fluence. They also maintain similar values across n = 3 and 4 samples (W_e = 0.32 ± 0.05 ps^{-1} and W_h = 0.07 ± 0.02 ps^{-1}). Much higher W_x for n = 3 phase as compared to n = 2 and n = 4 phases were also observed. Intriguingly, these relaxation rates shows no clear dependence on the RP dimensionality. While the n = 1 phase is dominated by direct exciton relaxation pathway (W_x), the n = 2 phase shows quite an opposite behavior (*i.e.* dominated by indirect relaxation pathway). Meanwhile, for n = 3 and 4, at low excitation

fluence the indirect relaxation pathways dominate the system, which is then taken over by direct relaxation pathway at high fluence.

Note that such behavior of spin relaxation pathways in RP perovskites is quite perplexing. Theoretically, one would expect either independence or inversely proportionality of direct exciton spin relaxation rate on the excitation fluence. Based on the theoretical modeling by Maialle *et al.* for excitons in III-V and II-VI inorganic semiconductor QW system [25], one would expect an inversely proportional relation between direct exciton spin-flip time and momentum scattering time (*i.e.* slower relaxation rate with more scattering). This relation is still applicable for the case of n = 1 RP phase. While it is independent of exciton density, the direct spin relaxation rate in n = 1 phase is found to decrease to 2.1 ± 0.1 ps^{-1} at 15 K (as compared to 4.1 ± 0.1 ps^{-1} at 293 K). However, it is not applicable for n = 2 to 4 phases, where direct exciton spin-flip rate is enhanced by exciton-exciton scattering. Moreover, based on theoretical modeling also for III-V inorganic semiconductor QW by Ciuti *et al.* [28], exciton-exciton scattering process might enhance the indirect spin flip via inter-exciton carrier-carrier exchange interaction, but not the direct spin-flip process. Meanwhile, our result shows otherwise. It implies that the exciton spin relaxation process in RP system might involve higher order process or follow different mechanisms as compared to typical inorganic semiconductor system. A more theoretical approach is required to unveil the detailed mechanism behind the observation. However, it is out of the scope of the current study.

Regardless of these intricate interplay of multiple spin relaxation pathways, qualitatively the general effect of RP perovskites dimensionality on the spin dynamics can be summarized by the effective spin lifetime. This effective exciton spin lifetime of our RP perovskite thin films as a function of dimensionality is presented in **Figure 5.20**. The samples were photoexcited by 10 μJ/cm^2 pump resonantly at a wavelength matching their respective exciton energies. The effective lifetime is given by $\sum A_i\tau_i/\sum A_i$, where A_i is the amplitude and $\tau_i = 1/\gamma_i$ [eq. (5.13) and (5.14)] is the lifetime component of the decay component. Note that the effective lifetime reported here is by definition the half of the spin lifetime of a single spin-state, as reported in Chapter 3 (*i.e.* similar with the TRFR lifetime; which is the combined rate of spin-states relaxation and filling). Here, a trend of increasing effective spin relaxation time

with increasing n (up to $n = 4$) is observed, which implies that the out-of-plane confinement in this MQW structure has a deteriorating effect on the spin lifetime. However, peculiarly this trend does not generalize up to $n = \infty$ case (*i.e.* MAPI, 3D perovskites). The spin lifetime for 3D perovskites is found to be ~1.8 ps which is slightly shorter than the $n = 3$ phase spin lifetime. It implies that the spin lifetimes possess a peak-behavior, with the maximum peak somewhere in between $n = 3$ and $n = \infty$.

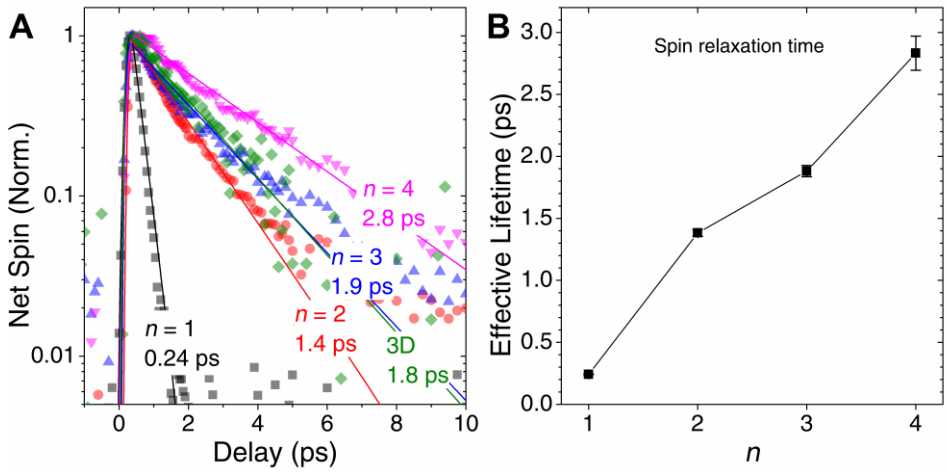

Figure 5.20 | Effective spin lifetime vs dimensionality. (A) The kinetics of spin polarization of RP and 3D perovskite thin films. The samples were photoexcited with 10 μJ/cm^2 pump at their respective resonant wavelengths. The kinetics were fitted with transient single exponential decay function (*i.e.* to represent effective lifetime). (B) The effective spin lifetime seems to increase with increasing n (decreasing confinement).

The cause behind this "spin lifetime vs dimension" peak behavior might not be because of the "excitonic to free carrier" photoexcited species transition. One example would be the $CH_3NH_3PbBr_3$ (MAPB), which is a 3D system with stronger excitonic behavior than MAPI with the estimated binding energy of ≥ 60 meV [29-31]. Having such large binding energy, a significant population of excitons is therefore expected from MAPB, in contrast to significant free carrier population in MAPI. Nonetheless, our result in Chapter 3 shows that both MAPI and MAPB has a similar spin lifetime, regardless of spin-polarized excitons or free carriers. Based on this analysis, we concluded that the increase of spin relaxation is due to a more direct effect of dimensionality on the spin relaxation mechanism. One plausible explanation would be the change of SOC felt by the

excitons due to increase in the well width, which has been previously shown for GaAs QW system [24,25]. Whereas it is consistent with the observation of increasing exciton spin lifetime with *n*, it does not explain the peak behavior or the lower spin lifetime of $n = \infty$ system. The reason behind this observation might be due to the intrinsic behavior of the SOC due to the dimensionality. First-principle calculations are required to verify this correlation, which is currently out of the scope of this study. Nonetheless, while it is yet fully understood, our demonstration of a superior spin lifetime in RP phases as compared to the pure 2D and 3D systems sufficiently exemplifies the facile tunability and untapped potential of OIHP material system.

5.3.6 Section summary

In summary, the optical-spin dynamics in $n = 1$ to 4 phases of lead iodide RP perovskites have been presented and discussed in this section. The novel key results can be summarized into the following points:

1. Modelling of exciton spin relaxation kinetics in RP perovskite system. The exciton system differs from the free carrier system (Chapter 3) due to the presence of dark/optically forbidden exciton states.
2. Deconvolution of the intermixed direct and indirect exciton spin relaxation pathways in RP perovskites. We quantitatively determined the rate for each spin relaxation pathway [*i.e.* excitons' (W_x), electrons' (W_e) and holes' (W_h) spin flip rates] for each of the RP perovskites phases in room temperature. For $n = 1$ phase, W_x dominates the process. For $n = 2$ phase, W_e dominates the process. For $n = 3$ and 4, W_e dominates the process at low excitation fluence, but then overtaken by W_x at higher excitation fluence.
3. Observation of increasing W_x with excitation fluence (*i.e.* exciton-exciton scattering) for $n = 2$ to 4 phases. This is in contrast with the current theoretical understanding of exciton spin relaxation mechanism via electron-hole exchange interaction in III-V semiconductor QW, where W_x is inversely proportional to momentum scattering rate. It implies another mechanism or higher order process might be dominant in RP perovskites.
4. Observation of qualitative trend of increasing effective spin lifetime with increasing *n* in RP perovskite system for $n = 1$ to 4. The trend does not

follow up to $n = \infty$ (3D) case, where the spin lifetime of the 3D perovskite is found to be slightly shorter than $n = 3$ phase. It might be due to the intrinsic behavior of the SOC due to the dimensionality.

5.4 Conclusion

Through the ultrafast optical spectroscopy study in Ruddlesden-Popper (RP) phases of lead halide perovskites presented in this chapter, the fundamental qualitative understanding of optical-carrier-spin dynamics in this system has been laid down. Based on this comprehension, the potential of RP lead halide OIHP for opto-spintronic applications can be demonstrated and evaluated. In particular, RP phases afford plenty of rooms for facile tunability of their optoelectronic properties in between the 2D and 3D perovskites (*e.g.* bandgap, exciton binding energy, oscillator strength, *etc*.). In fact, RP phases might even be more superior as compared to the pure 2D and 3D system. For instance, prior to this study literature has reported a higher luminescence efficiency of RP phases [5], while here we demonstrated superior spin relaxation lifetime of RP phases, as compared to the pure 2D and 3D system. Nonetheless, although the qualitative understanding of the observed spin dynamics in this material system has been established through this study, further quantitative theoretical studies (*i.e.* to further understand the observed dynamics) are still required to realize the full potential of OIHP-based opto-spintronics technology.

5.5 Bibliography

1. Smith, I.C., et al., *A Layered Hybrid Perovskite Solar-Cell Absorber with Enhanced Moisture Stability.* Angewandte Chemie, 2014. **126**(42): p. 11414-11417.
2. Boix, P.P., et al., *Perovskite Solar Cells: Beyond Methylammonium Lead Iodide.* The Journal of Physical Chemistry Letters, 2015. **6**(5): p. 898-907.
3. Yao, K., et al., *Multilayered Perovskite Materials Based on Polymeric-Ammonium Cations for Stable Large-Area Solar Cell.* Chemistry of Materials, 2016. **28**(9): p. 3131-3138.
4. Tsai, H., et al., *High-efficiency two-dimensional Ruddlesden–Popper perovskite solar cells.* Nature, 2016. **536**(7616): p. 312-316.

5. Yuan, M., et al., *Perovskite energy funnels for efficient light-emitting diodes.* Nature Nanotechnology, 2016. **11**: p. 872–877.
6. Cao, D.H., et al., *2D Homologous Perovskites as Light-Absorbing Materials for Solar Cell Applications.* Journal of the American Chemical Society, 2015. **137**(24): p. 7843-7850.
7. Stoumpos, C.C., et al., *Ruddlesden–Popper Hybrid Lead Iodide Perovskite 2D Homologous Semiconductors.* Chemistry of Materials, 2016. **28**(8): p. 2852-2867.
8. Papavassiliou, G.C., *Three- and low-dimensional inorganic semiconductors.* Progress in Solid State Chemistry, 1997. **25**(3): p. 125-270.
9. Milot, R.L., et al., *Charge-Carrier Dynamics in 2D Hybrid Metal–Halide Perovskites.* Nano Letters, 2016. **16**(11): p. 7001-7007.
10. Gauthron, K., et al., *Optical spectroscopy of two-dimensional layered $(C_6H_5C_2H_4\text{-}NH_3)_2\text{-}PbI_4$ perovskite.* Optics Express, 2010. **18**(6): p. 5912-5919.
11. Lanty, G., et al., *Room-Temperature Optical Tunability and Inhomogeneous Broadening in 2D-Layered Organic-Inorganic Perovskite Pseudobinary Alloys.* The Journal of Physical Chemistry Letters, 2014. **5**(22): p. 3958-3963.
12. Quan, L.N., et al., *Ligand-Stabilized Reduced-Dimensionality Perovskites.* Journal of the American Chemical Society, 2016. **138**(8): p. 2649-2655.
13. Chong, W.K., et al., *Dominant factors limiting the optical gain in layered two-dimensional halide perovskite thin films.* Physical Chemistry Chemical Physics, 2016. **18**(21): p. 14701-14708.
14. Xing, G., et al., *Long-Range Balanced Electron- and Hole-Transport Lengths in Organic-Inorganic $CH_3NH_3PbI_3$.* Science, 2013. **342**(6156): p. 344-347.
15. Wang, Y., et al., *Trap-limited charge recombination in intrinsic perovskite film and meso-superstructured perovskite solar cells and the passivation effect of the hole-transport material on trap states.* Physical Chemistry Chemical Physics, 2015. **17**(44): p. 29501-29506.
16. He, H., et al., *Exciton localization in solution-processed organolead trihalide perovskites.* Nature Communications, 2016. **7**: p. 10896.

17. Cadelano, M., et al., *Photoexcitations and Emission Processes in Organometal Trihalide Perovskites*. Perovskite Materials - Synthesis, Characterisation, Properties, and Applications. 2016.
18. Saba, M., et al., *Correlated electron-hole plasma in organometal perovskites.* Nature Communications, 2014. **5**.
19. Xing, G., et al., *Low-Temperature Solution-Processed Wavelength-Tunable Perovskites for Lasing.* Nature Materials, 2014. **13**(5): p. 476-480.
20. Cho, H., et al., *Overcoming the electroluminescence efficiency limitations of perovskite light-emitting diodes.* Science, 2015. **350**(6265): p. 1222-1225.
21. Giovanni, D., et al., *Tunable room-temperature spin-selective optical Stark effect in solution-processed layered halide perovskites.* Science Advances, 2016. **2**(6): p. 1600477.
22. Hong, X., T. Ishihara, and A.V. Nurmikko, *Dielectric confinement effect on excitons in PbI_4-based layered semiconductors.* Physical Review B, 1992. **45**(12): p. 6961-6964.
23. Grote, C., B. Ehrlich, and R.F. Berger, *Tuning the near-gap electronic structure of tin-halide and lead-halide perovskites via changes in atomic layering.* Physical Review B, 2014. **90**(20): p. 205202.
24. Amand, T. and X. Marie, *Exciton Spin Dynamics in Semiconductor Quantum Wells*, in *Spin Physics in Semiconductors*, M.I. Dyakonov, Editor. 2008, Springer Berlin Heidelberg: Berlin, Heidelberg. p. 55-89.
25. Maialle, M.Z., E.A. de Andrada e Silva, and L.J. Sham, *Exciton spin dynamics in quantum wells.* Physical Review B, 1993. **47**(23): p. 15776-15788.
26. Sham, L.J., *Spin relaxation in semiconductor quantum wells.* Journal of Physics: Condensed Matter, 1993. **5**(33A): p. A51.
27. Runge, E., *Excitons in Semiconductor Nanostructures*, in *Solid State Physics*, E. Henry and S. Frans, Editors. 2003, Academic Press. p. 149-305.
28. Ciuti, C., et al., *Role of the exchange of carriers in elastic exciton-exciton scattering in quantum wells.* Physical Review B, 1998. **58**(12): p. 7926-7933.
29. Sestu, N., et al., *Absorption F-Sum Rule for the Exciton Binding Energy in Methylammonium Lead Halide Perovskites.* The Journal of Physical Chemistry Letters, 2015. **6**(22): p. 4566-4572.

30. Zheng, K., et al., *Exciton Binding Energy and the Nature of Emissive States in Organometal Halide Perovskites.* The Journal of Physical Chemistry Letters, 2015. **6**(15): p. 2969-2975.
31. Tanaka, K., et al., *Comparative Study on the Excitons in Lead-Halide-Based Perovskite-Type Crystals $CH_3NH_3PbBr_3$ $CH_3NH_3PbI_3$.* Solid State Communications, 2003. **127**(9–10): p. 619-623.

CHAPTER 6:

SUMMARY, CONCLUSION AND FUTURE WORK

This chapter presents the summary and conclusion of the works which have been reported in this thesis. The implications and scientific outlook of this optical-spin dynamics study in lead halide perovskites are elaborated in the broader context of the research field. Several outstanding questions on the spin dynamics in lead halide perovskites which have not been answered yet through this study are discussed in detail. Possible future studies required to answer the outstanding questions are also proposed.

6.1 Summary of the study

We have explored the potential of a class of material system, known as *organic-inorganic hybrid perovskites* (OIHP), for novel *opto-spintronic* technology applications. As implied by its name, opto-spintronics means devices whose functionality utilizes electrons' spins and their interaction with light. Realization of this 'currently theoretical' technology would give rise to faster and more efficient devices, which might revolutionize the industry. The first crucial step towards its realization is the choice of a material system with excellent properties which can sustain such technology.

Based on this motivation, OIHP comes into the picture. In addition to its recently reported excellent optoelectronics properties, strong *spin-orbit coupling* (SOC) has been the main rationale behind the choice of material system. Strong SOC in OIHP originating from heavy lead ion creates an excellent system for optical manipulation of the material's spin degree of freedom since the orbital component of the electrons' wavefunction (which interacts with light) is strongly coupled with the spin component. The focus of this study is therefore to explore this untapped potential of OIHP, via the pursuit of fundamental understanding of its transient optical-spin dynamics.

Herein, we performed material synthesis and optical studies on the solution-processed multidimensional organic-inorganic hybrid lead halide perovskite system. Our study spans across 2D perovskites (interconnected $[PbI_6]^{4-}$ octahedrons only in *xy*-plane, forming multi-quantum-well system), the perovskites with dimensionality in between 2D and 3D (*Ruddlesden-Popper* perovskites phase) and the 3D perovskites (interconnected $[PbI_6]^{4-}$ octahedrons in all *xyz*-direction). Since the band-edge of lead halide perovskites consists of $|m_J = \pm 1/2\rangle$ angular momentum state, we showed that the photoexcitation of spin-polarized carriers or excitons is possible across the dimensionality in lead halide OIHP. By using transient absorption spectroscopy technique, we were able to monitor the temporal evolution of the photoexcited spin polarization and deduce the dominant relaxation mechanism in the system.

In the 3D system (*i.e.* $CH_3NH_3PbI_3$), which is dominated by free carriers, we deduced *Elliot-Yafet* mechanism to be responsible for the carrier spin relaxation, but with weak spin-phonon coupling. We also discovered a large

Faraday rotation (FR), up to 10°/μm in 3D perovskites [1]. Conversely, in the 2D system [*i.e.* $(C_6H_5C_2H_4NH_3)_2PbI_4$], which is strongly excitonic, we observed simultaneous exciton spin relaxation via *electron-hole exchange interaction*. Such strong excitonic behavior results in spin-selective *Optical Stark Effect* (OSE), *i.e.* spin selective blue shift of exciton energy due to strong coupling with light. This interaction is parameterized by *Rabi energy*, which in the case of 2D perovskites in room temperature is a few times larger than in conventional inorganic semiconductors in cryogenic temperature. Moreover, we discovered that the Rabi energy can be straightforwardly tuned by changing the dielectric contrast between the organic and inorganic components [2].

In the meantime, for the Ruddlesden-popper phase perovskite system [*i.e.* $(C_6H_5C_2H_4NH_3)_2(CH_3NH_3)_{n-1}PbI_{3n+1}$], we determined that up to $n = 5$, excitons are still the dominant photoexcited species in the material. The exciton spin relaxation in this phase is characterized by an intricate interplay between direct and indirect/sequential spin relaxation. From the analysis, we observed that the relaxation rate behavior in this system does not follow the current theoretical understanding of the spin-flip mechanism for an exciton in a conventional III-V semiconductor quantum well, which implies another mechanism or higher order process might be dominant. Nevertheless, we were able to qualitatively assign an increasing effective spin lifetime trend with increasing n for $n = 1$ to 4. The trend does not follow up to the 3D case, which might be due to the intrinsic behavior of the SOC due to the dimensionality.

6.2 Outstanding questions

To some extent, our results have laid down the fundamental understanding of the transient optical-spin properties and demonstrated the robustness of OIHP material system. Nevertheless, there are still some relevant questions left unanswered within the scope of this work. Herein we proposed few questions, which if answered would further strengthen our comprehension on the system.

a. Is it possible to tune the spin-orbit coupling strength in perovskite system?
Strong spin-orbit coupling in lead halide perovskites acts both beneficially by allowing optical spin manipulation, and adversely by enhancing spin

relaxation process. Ability to tune the spin-orbit coupling will enable us to compromise between these two effects for the optimization of its spin properties. Our results demonstrated that this spin-orbit coupling in lead halide perovskite system mainly originates from the Pb^{2+} cation. Doping/substituting of the Pb^{2+} cation might allow us to modify the spin-orbit coupling strength inside the material.

b. *How will the spin properties change when we move from polycrystalline film to single crystal perovskites?*

Our results demonstrated that spin relaxation of carriers in 3D lead halide perovskite thin films originated mainly from scattering events with other carriers, defects, impurities and grain boundaries, via Elliot-Yafet mechanism. Meanwhile, our results also show that scattering with phonons conserves the spin. While phonon scattering is an intrinsic property of the material (cannot be improved), defects and grain boundaries can be eliminated by using better sample fabrication techniques. Our result hence implies that the spin lifetime is expected to be enhanced in better samples. In our current study, we used polycrystalline thin film samples where these spin-scattering centers were abundant. However, for the case of single crystal samples, the defects and trap states are dramatically reduced as compared to thin film samples [3]. Hence it is interesting to study how the spin dynamics differ in single crystals.

c. *What is the fundamental mechanism behind the exciton spin-flip process in Ruddlesden-Popper perovskites?*

As reported in Chapter 5, we observed a peculiar behavior of the exciton spin relaxation rates in Ruddlesden-Popper perovskites. In the developed theoretical model for the inorganic quantum well system, the direct exciton spin relaxation occurs via electron-hole exchange interaction with rate inversely proportional to momentum scattering rate [4-6]. Meanwhile, the indirect/sequential exciton spin relaxation occurs via inter-exciton fermion-fermion exchange interaction with a rate proportional to exciton-exciton scattering rate [7]. However, in Ruddlesden-Popper perovskite system (for n = 2 to 4), we observed the contrary: direct (indirect) exciton spin

relaxation rate was proportional (independent) to exciton-exciton scattering rate. This observation suggests that other mechanism or higher order process, which has yet to be understood, dominates in Ruddlesden-Popper perovskite system. Therefore, a new theoretical framework is required to explain the fundamental mechanism behind the observed phenomena.

d. How does the spin-orbit coupling strength change with dimensionality in Ruddlesden-Popper perovskites?

As reported in Chapter 5, another peculiar phenomenon observed in Ruddlesden-Popper perovskites is the effective spin lifetime as a function of dimensionality. We observed a general trend of initially increasing spin lifetime with increasing n (decreasing confinement) up to $n = 4$. However, this trend does not globally apply across all n. We found that the spin lifetime of the bulk system (3D, $n = \infty$) is shorter than $n > 3$ phase. We hypothesized that this phenomenon might originate from the spin-orbit coupling strength experienced by the excitons, which are changing in an intricate manner with the dimensionality. This hypothesis can be proven theoretically by first-principle calculation. If it is proven correct, dimensionality might become an additional platform (apart from doping) for tuning the spin-orbit coupling strength in lead halide perovskite system.

6.3 Proposed future works

Herein, we propose some future works which in our opinion might help to either solve the unanswered questions left by this study or explore the prospect and expand the capability of this material system for opto-spintronic applications.

6.3.1 Perovskite single crystals

As has been mentioned, our results indicate that the spin relaxation time can be further improved by using a material system with low defects and impurities. Single crystal might be one possible avenue to achieve it. It has been established that dramatically lower defects and traps density in the single crystal as compared to the polycrystalline film results in the extended carrier diffusion

length and lifetime [3]. Similar dramatic improvement on the spin lifetime and diffusion length are also expected to occur in high-quality single crystal samples.

Nevertheless, up to now, there are several challenges in performing spin measurement in perovskites single crystals. The main challenge comes from the thickness of the single crystal sample. Up to now, the thickness of single crystal perovskite samples fabricated is in mm size, which is too thick to be penetrated by optical probe. While measurement in reflection geometry (in contrast to transmission) can still be performed, such measurement will only allow us to probe the surface properties of the sample. In the meantime, for our current typical single crystal samples, such low defect regions are located in the crystal bulk, while the surface properties closely resemble the polycrystalline thin film samples [8,9]. Such limitation prevents us to probe the spin dynamics in defect-free perovskite system. Another attempt is to utilize two-photon excitation process which has greater penetration range [9]. However, such transition with Δm_J = 0 or ± 2 selection rule prevent us to optically excite spin polarized carrier/excitons in perovskites' $|m_J = \pm 1/2\rangle$ band edge states.

Under such circumstances, the only possibility is to improve our current sample fabrication techniques of single crystal system. An approach which can be taken is to either improve the surface properties of the single crystal or fabrication of high quality thin single crystal sample. Having high-quality thin single crystal sample will allow us to optically probe interesting spin phenomena in low defect system.

6.3.2 Magnetic doping in perovskites

In our current study, the magnetization in the samples is induced only by circularly polarized light, without any intrinsically built-in magnetization. This intrinsic magnetization can be introduced into the system by facile doping with ferromagnetic cations (*e.g.* Mn^{2+}, Co^{2+}, *etc.*). Such spontaneous magnetization has prospective applications in non-volatile storing devices. Therefore, it will be interesting to study the interaction between the built-in magnetization of these dopants with the photoinduced magnetization induced by our pump beam.

Just recently, Nafradi *et al.* have reported optical switching of magnetism in Mn-doped perovskite $CH_3NH_3PbI_3$ [10]. In their report, they discovered

ferromagnetic order in perovskite sample with 10% doping concentration, light illumination melts the ferromagnetic order of the Mn dopant. They assigned it to the rapid melting of the local magnetic order by photoexcited electron through the Ruderman–Kittel–Kasuya–Yosida interactions without heating up the spin system. The melting of the magnetic order then allows one to simply reorient the ferromagnetic direction by using an external magnetic field. Although in their work the magnetic order can only be sustained at very low temperature (T_C = 25 K), similar systems could also be done by incorporating another ferromagnetic dopant with much higher Curie temperature. Meanwhile, they also proposed a memory-storage device based on this discovery, as shown in **Figure 6.1**.

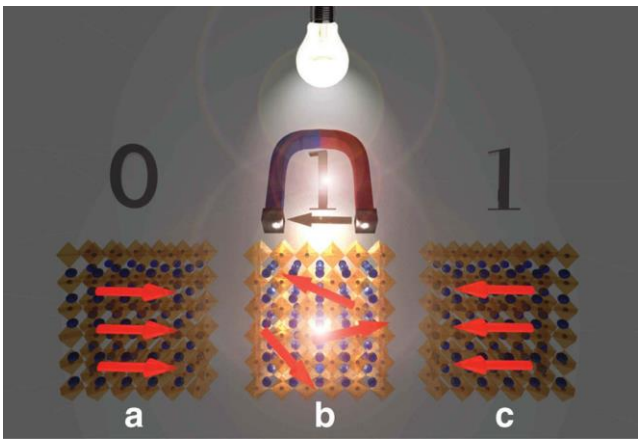

Figure 6.1 | Magnetism switching in Mn-doped perovskites. The ferromagnetic order of the system can be melted by light illumination and rearranged by external magnetic field. This can hold applications for storage devices. The figure is adapted from ref. [10].

The result from ref. [10] has demonstrated not only the possibility of integration of magnetic dopants into lead halide perovskite system but also interaction between the magnetic moment of these dopants with photoexcited carriers. It supports our hypothesis that these magnetic dopants can also interact with photoexcited spin-polarized carriers. If the hypothesis is correct, the current work can be further expanded, *i.e.* magnetic switching not by external magnetic field, but only by illumination of circularly polarized light. Such concept of magnetism switching solely by circularly polarized light has been investigated in numerous complex magnetic heterostructures, involving

relatively complicated switching mechanism [11]. If such phenomenon can be realized in solution processed 3D perovskites, it would allow cheaper and more versatile integration into electronic devices.

Apart from all-optical magnetic switching, another possible direction of expansion is to investigate the multiferroic behavior in these lead halide perovskites. While indeed in some of 2D lead halide perovskite system co-existence of ferroelectric and ferromagnetic properties has been reported [12,13], the coupling between these two ferroic properties has not been demonstrated. Moreover, the Curie temperature for these co-existing ferroic phases to occur is pretty low (< 5 K), which hinders practical applications. Meanwhile, it has been believed that lead halide perovskite system also possesses an intrinsic ferroelectric characteristic [14-18]. By facile magnetic cation doping, the ferromagnetic characteristic can also be introduced into the system. It is interesting therefore to investigate the coexistence and coupling between these two ferroic properties in such solution-processed system. Such approach might allow us to achieve room temperature multiferroic system.

6.3.3 Theory on the spin dynamics in Ruddlesden-Popper perovskites

Lastly, another possible further study is the theoretical investigation of the spin dynamics in Ruddlesden-Popper perovskites phases. Herein, we proposed a first-principle calculation via *Density Functional Theory* (DFT) to systematically investigate the effect of dimensionality on the spin-orbit coupling (SOC) strength. In OIHP system, the SOC strength could be parameterized from how much its conduction band splits due to SOC. By using DFT, it can simply be done by comparing the calculated band structure with and without SOC. Such study could confirm our hypothesis on the intricate relation between the intrinsic structural confinement from the crystal and the spin-orbit coupling experienced by photoexcited carrier/exciton. If our hypothesis is correct, dimensionality can be an additional avenue for tuning the spin properties in perovskite system.

6.4 Implication, conclusion, and outlook

To conclude, this study has focused on the gain of fundamental comprehension of the photoexcited transient spin dynamics in RP perovskites. It has implications not only to fulfill scientific curiosity but also to assess the suitability of OIHP system for opto-spintronic applications. Apart from its solution processability (low production cost), chemical flexibility for facile tuning of its excellent optoelectronics properties is a highly desired quality possessed by this system.

Our result has shown that lead halide OIHP material system possesses the essential prerequisites for opto-spintronic technology, which is the capability for optical manipulation of its spin degree of freedom. Multi-dimensionality of this system affords an additional platform for broad range tunability of its properties. This includes the facile tunability of not only its optical properties (*e.g.* bandgap, exciton binding energy, oscillator strength, *etc.*) but also its spin properties (*e.g.* spin relaxation mechanism, spin relaxation time, *etc.*), revealed by our transient studies. While it has not reached the stage of integration into actual devices, through this study we have laid down the basic foundation of the system, from which we can either proceed to dig deeper into its more fundamental exotic physics, or to design and optimize novel opto-spintronic devices [11,19-22]. For instance, from our result, short spin lifetime and huge FR and OSE in this system might be suitable for optical spin-switch or spin-injector devices.

Herein, we foresee a great prospect of OIHP material system. Another recently published study has also demonstrated a possibility for magnetic ion doping into the lead halide perovskite system [10], which further expands the tunability and capability of OIHP. We call for further studies to solve problems which have not been answered by this thesis. Full comprehension on the fundamental properties will enable us to realize the full potential of OIHP material system.

6.5 Bibliography

1. Giovanni, D., et al., *Highly Spin-Polarized Carrier Dynamics and Ultralarge Photoinduced Magnetization in $CH_3NH_3PbI_3$ Perovskite Thin Films.* Nano Letters, 2015. **15**(3): p. 1553-1558.
2. Giovanni, D., et al., *Tunable room-temperature spin-selective optical Stark effect in solution-processed layered halide perovskites.* Science Advances, 2016. **2**(6): p. 1600477.
3. Dong, Q., et al., *Electron-hole diffusion lengths > 175 μm in solution-grown $CH_3NH_3PbI_3$ single crystals.* Science, 2015. **347**(6225): p. 967-970.
4. Maialle, M.Z., E.A. de Andrada e Silva, and L.J. Sham, *Exciton spin dynamics in quantum wells.* Physical Review B, 1993. **47**(23): p. 15776-15788.
5. Sham, L.J., *Spin relaxation in semiconductor quantum wells.* Journal of Physics: Condensed Matter, 1993. **5**(33A): p. A51.
6. Amand, T. and X. Marie, *Exciton Spin Dynamics in Semiconductor Quantum Wells*, in *Spin Physics in Semiconductors*, M.I. Dyakonov, Editor. 2008, Springer Berlin Heidelberg: Berlin, Heidelberg. p. 55-89.
7. Ciuti, C., et al., *Role of the exchange of carriers in elastic exciton-exciton scattering in quantum wells.* Physical Review B, 1998. **58**(12): p. 7926-7933.
8. Grancini, G., et al., *CH3NH3PbI3 perovskite single crystals: surface photophysics and their interaction with the environment.* Chemical Science, 2015. **6**(12): p. 7305-7310.
9. Wu, B., et al., *Discerning the Surface and Bulk Recombination Kinetics of Organic-Inorganic Halide Perovskite Single Crystals.* Advanced Energy Materials, 2016. **6**(14): p. 1600551-n/a.
10. Náfrádi, B., et al., *Optically switched magnetism in photovoltaic perovskite CH3NH3(Mn:Pb)I3.* Nature Communications, 2016. **7**: p. 13406.
11. Kimel, A.V., *All-optical switching: Three rules of design.* Nature Materials, 2014. **13**(3): p. 225-226.

12. Polyakov, A.O., et al., *Coexisting Ferromagnetic and Ferroelectric Order in a CuCl4-based Organic-Inorganic Hybrid.* Chemistry of Materials, 2012. **24**(1): p. 133-139.
13. Zhang, Y., et al., *The First Organic-Inorganic Hybrid Luminescent Multiferroic: (Pyrrolidinium)MnBr3.* Advanced Materials, 2015. **27**(26): p. 3942-3946.
14. Kim, M., et al., *Switchable S = 1/2 and J = 1/2 Rashba bands in ferroelectric halide perovskites.* Proceedings of the National Academy of Sciences, 2014. **111**(19): p. 6900-6904.
15. Stroppa, A., et al., *Tunable ferroelectric polarization and its interplay with spin-orbit coupling in tin iodide perovskites.* Nature Communications, 2014. **5**.
16. Ghosh, S., D. Di Sante, and A. Stroppa, *Strain Tuning of Ferroelectric Polarization in Hybrid Organic-Inorganic Perovskite Compounds.* The Journal of Physical Chemistry Letters, 2015. **6**(22): p. 4553-4559.
17. Fan, Z., et al., *Ferroelectricity of CH3NH3PbI3 Perovskite.* The Journal of Physical Chemistry Letters, 2015. **6**(7): p. 1155-1161.
18. Kutes, Y., et al., *Direct Observation of Ferroelectric Domains in Solution-Processed CH3NH3PbI3 Perovskite Thin Films.* The Journal of Physical Chemistry Letters, 2014. **5**(19): p. 3335-3339.
19. Awschalom, D.D. and M.E. Flatte, *Challenges for semiconductor spintronics.* Nature Physics, 2007. **3**(3): p. 153-159.
20. Bader, S.D. and S.S.P. Parkin, *Spintronics.* Annual Review of Condensed Matter Physics, 2010. **1**(1): p. 71-88.
21. Osamu, W., *Femtosecond all-optical devices for ultrafast communication and signal processing.* New Journal of Physics, 2004. **6**(1): p. 183.
22. Kepenekian, M., et al., *Rashba and Dresselhaus Effects in Hybrid Organic-Inorganic Perovskites: From Basics to Devices.* ACS Nano, 2015.

APPENDIX

A. Jones Calculus

Jones calculus is a representation of the light polarization in matrix notation, discovered by R. C. Jones in 1941. The coordinate used as the basis is the Cartesian coordinate, where $\hat{x} \times \hat{y} = \hat{z}$. The light is assumed to propagate in +z-direction. The electric field of EM wave can be expressed in following notation:

$$\vec{E}(z,t) = \begin{pmatrix} E_x \\ E_y \end{pmatrix} = e^{i(\omega t - kz + \phi_0)} |\text{Polarization}\rangle$$

where the incident intensity is normalized as $E_0^2 = |E_x|^2 + \left|E_y\right|^2$. Note that the initial phase shift ϕ_0 is unimportant and can be neglected in our derivation.

Polarization	Notation	Figure
Vertical	$\|s\rangle = E_0 \begin{pmatrix} 0 \\ 1 \end{pmatrix}$	-
Horizontal	$\|p\rangle = E_0 \begin{pmatrix} 1 \\ 0 \end{pmatrix}$	-
Left Circular (σ^+)	$\|L\rangle = \frac{E_0}{\sqrt{2}} \begin{pmatrix} 1 \\ -i \end{pmatrix}$	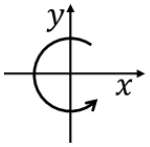
Right Circular (σ^-)	$\|R\rangle = \frac{E_0}{\sqrt{2}} \begin{pmatrix} 1 \\ +i \end{pmatrix}$	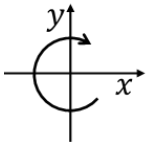
Elliptical	$\|\psi\rangle = ae^{i\phi}\|L\rangle + be^{-i\phi}\|R\rangle$ $A = \|a + b\\|E_0$ $B = \|a - b\\|E_0$ $a^2 + b^2 = 1;\ a, b \in \Re$	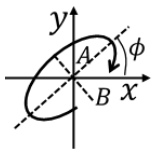

Any linear optical elements, which perform a transformation on light polarization can be presented in matrix notation, known as *Jones matrices*. Herein, we derived the Jones matrices of a linear polarizer, a half-wave-plate, and a quarter-wave-plate, with fast axis oriented at CCW angle θ relative from the light polarization (ϕ):

Linear polarizer		$\begin{pmatrix} \cos^2\theta & \sin\theta\cos\theta \\ \sin\theta\cos\theta & \sin^2\theta \end{pmatrix}$
Half-wave plate ($\lambda/2$)		$\begin{pmatrix} \cos 2\theta & \sin 2\theta \\ \sin 2\theta & -\cos 2\theta \end{pmatrix}$
Quarter-wave plate ($\lambda/4$)	θ	$\frac{1}{\sqrt{2}}\begin{pmatrix} i+\cos 2\theta & \sin 2\theta \\ \sin 2\theta & i-\cos 2\theta \end{pmatrix}$
	$-45°$	$\frac{1}{\sqrt{2}}\begin{pmatrix} i & -1 \\ -1 & i \end{pmatrix}$
	$0°$	$\frac{1}{\sqrt{2}}\begin{pmatrix} i+1 & 0 \\ 0 & i-1 \end{pmatrix}$
	$45°$	$\frac{1}{\sqrt{2}}\begin{pmatrix} i & 1 \\ 1 & i \end{pmatrix}$
	$90°$	$\frac{1}{\sqrt{2}}\begin{pmatrix} i-1 & 0 \\ 0 & i+1 \end{pmatrix}$

In our case, understanding these transformations are essential for our degenerate transient absorption experiment, to distinguish what quantity we are measuring. There are three possible detection modes: (1) without wave-plate, (2) with half-wave-plate and (3) with quarter-wave-plate. Note that the input refers to the probe light polarization after the sample, *i.e.* before the Wollaston prism (WP) and the balanced photodetector (BPD) (**Figure 2.6**); whilst the output refers to the probe light polarization after the optical element. Without any wave-plate reading of BPD ($|E_x|^2 - |E_y|^2$) is given by:

Input	$\boldsymbol{|E_x|^2 - |E_y|^2}$
$\left\|Lin_\phi\right\rangle = E_0\begin{pmatrix}\cos\phi \\ \sin\phi\end{pmatrix}$	$E_0^2\cos 2\phi$
$\|L\rangle = \frac{E_0}{\sqrt{2}}\begin{pmatrix}1 \\ -i\end{pmatrix}$	0
$\|R\rangle = \frac{E_0}{\sqrt{2}}\begin{pmatrix}1 \\ i\end{pmatrix}$	0
$ae^{i\phi}\|L\rangle + be^{-i\phi}\|R\rangle$	$2E_0^2 ab\cos 2\phi$

Meanwhile, inserting the half-wave-plate with fast axis oriented at angle θ between the light polarization and the fast axis before WP and BPD, the reading of BPD ($|E_x|^2 - |E_y|^2$) changes into:

Input	Output	$\|\boldsymbol{E_x}\|^2 - \left\|\boldsymbol{E_y}\right\|^2$
$E_0\begin{pmatrix}\cos\phi\\ \sin\phi\end{pmatrix}$	$E_0\begin{pmatrix}\cos(2\theta-\phi)\\ \sin(2\theta-\phi)\end{pmatrix}$	$E_0^2\cos(2\phi-4\theta)$
$\|L\rangle$	$\frac{E_0}{\sqrt{2}}\begin{pmatrix}e^{-2i\theta}\\ ie^{-2i\theta}\end{pmatrix}$	0
$\|R\rangle$	$\frac{E_0}{\sqrt{2}}\begin{pmatrix}e^{2i\theta}\\ -ie^{2i\theta}\end{pmatrix}$	0
$ae^{i\phi}\|L\rangle + be^{-i\phi}\|R\rangle$	$\frac{E_0}{\sqrt{2}}\begin{pmatrix}ae^{i\phi}e^{-2i\theta}+be^{-i\phi}e^{2i\theta}\\ iae^{i\phi}e^{-2i\theta}-ibe^{-i\phi}e^{i2\theta}\end{pmatrix}$	$2E_0^2ab\cos(2\phi-4\theta)$

On the other hand, inserting quarter-wave-plate (λ/4) oriented at angle 45º in between the light polarization and the fast axis (*i.e.* θ = 45º) will transform the reading of BPD ($|E_x|^2 - \left|E_y\right|^2$) into:

Input	Output	$\|\boldsymbol{E_x}\|^2 - \left\|\boldsymbol{E_y}\right\|^2$
$E_0\begin{pmatrix}\cos\phi\\ \sin\phi\end{pmatrix}$	$\frac{E_0}{\sqrt{2}}\begin{pmatrix}i\cos\phi+\sin\phi\\ \cos\phi+i\sin\phi\end{pmatrix}$	0
$\|L\rangle$	$E_0\begin{pmatrix}0\\ 1\end{pmatrix}$	$-E_0^2$
$\|R\rangle$	$\frac{1+i}{2}E_0\begin{pmatrix}1\\ 0\end{pmatrix}$	$+E_0^2$
$ae^{i\phi}\|L\rangle + be^{-i\phi}\|R\rangle$	$E_0\begin{pmatrix}ibe^{-i\phi}\\ iae^{i\phi}\end{pmatrix}$	$E_0^2(b^2-a^2)$

When pump is introduced, it induces small changes in the values of a, b and ϕ ($a \to a'$, $b \to b'$ and $\phi \to \phi'$). These small transient changes are the pump-induced changes, in which we are interested. Note that the change in E_0 has been included in the changes of a and b (*i.e.* $a'^2 + b'^2 \neq 1$). We assumed that pump-induced change (δQ) is much lesser than the steady-state value (Q):

$$Q' = Q + \delta Q;\ \frac{\delta Q}{Q} \ll 1.$$

Assuming that the BPD is initially balanced when pump is off (*i.e.* ϕ = 45°, BPD reading is zero), without using any wave-plate before WP and BPD, the pump-induced reading of the BPD ($|E_x|^2 - |E_y|^2$) is given by:

Input	$\boldsymbol{\Delta\left(|E_x|^2 - |E_y|^2\right)}$
$E_0'\begin{pmatrix}\cos(\phi')\\ \sin(\phi')\end{pmatrix}$	$-2E_0^2\ \delta\phi$
$a'e^{i\phi'}\|R\rangle + b'e^{-i\phi'}\|L\rangle$	$-4E_0^2 ab\ \delta\phi$

Based on the equation, this detection mode is only sensitive to the pump-induced rotation ($\delta\phi$), which means it can be used to measure pump-induced Faraday rotation (FR). Meanwhile, using an initially balanced half-wave-plate when pump is off (*i.e.* $|\phi - 2\theta| = 45°$), the pump-induced reading of the BPD is given by:

Input	$\boldsymbol{\Delta\left(|E_x|^2 - |E_y|^2\right)}$
$E_0'\begin{pmatrix}\cos(\phi')\\ \sin(\phi')\end{pmatrix}$	$-2E_0^2\ \delta\phi$
$a'e^{i\phi'}\|L\rangle + b'e^{-i\phi'}\|R\rangle$	$-4E_0^2 ab\ \delta\phi$

Similar to the former, this detection mode is also only sensitive to the $\delta\phi$, which can be used to measure pump-induced FR. Herein, the FR is given by:

$$\delta\phi = \frac{|E_x|^2 - |E_y|^2}{4E_0^2 ab} \approx \frac{|E_x|^2 - |E_y|^2}{2E_0^2} = \frac{\Delta I}{2I_0}.$$

Here, we approximated the input beam to be almost linearly polarized (*i.e.* $a = b \approx 1/\sqrt{2}$), which is valid for our experimental setup. Lastly, for detection mode using an initially balanced quarter-wave-plate (λ/4) when pump is off, (*i.e.* θ = 45°, ϕ = 90°, and $a = b = 1/\sqrt{2}$), the pump-induced reading of the BPD is given by:

Input	$\boldsymbol{\Delta\left(\lvert E_x\rvert^2-\lvert E_y\rvert^2\right)}$
$E_0'\begin{pmatrix}\cos\phi'\\ \sin\phi'\end{pmatrix}$	0
$a'e^{i\phi'}\lvert L\rangle + b'e^{-i\phi'}\lvert R\rangle$	$\frac{E_0^2}{\sqrt{2}}(\delta b-\delta a)$

Since this detection mode is also only sensitive to the δa and δb, it can be used to measure pump-induced Faraday ellipticity.

B. Model for transient exciton dynamics in 2D perovskites

In Chapter 4, we reported a phenomenological model to describe the transient exciton dynamics in (PEPI). Herein, we reported the detail of the model. The model's temporal component model is adapted based on transient quad-exponential decay function; while the spectral component is the summation of three Lorentzian functions based on the observed transient excitonic transition. The transient signal at wavelength λ and time *t* is given by:

$$\frac{\Delta T}{T}(\lambda,t)=\sum_{i=1}^{3}L_i(\lambda,t)\sum_{j=1}^{4}\frac{C_{ij}}{2}\left[1+\operatorname{erf}\left(\frac{t}{r}-\frac{r}{2\tau_j}\right)\right]\exp\left(-\frac{t}{\tau_j}\right).$$

The parameter *r* refers to the laser time constant; C_{ij} refers to the coefficient; τ_j refers to the decay lifetime; and $L_i(\lambda,t)$ refers to the Lorentzian peak function at a particular time *t*. The dependence of L_i on time is implicit within its center peak position, which oscillates due to coherent exciton-phonon coupling and red shifts during the thermalization process. The function $L_i(\lambda,t)$ can be mathematically described as:

$$L_i(\lambda,t)=\frac{2A_i}{\pi}\frac{\lambda_{Fi}}{4\left[\lambda-\lambda_{C_i}-\lambda_T(t)+\lambda_O(t)\right]^2+\lambda_{Fi}^2}.$$

Here, A_i is the Lorentzian peak area; λ_{Fi} is the Full Width Half Maximum (FWHM) of the Lorentzian peak; $\lambda_T(t)=\lambda_T^0[1+\operatorname{erf}(t/\tau_i)]/2$ is the peak position shift; $\lambda_0(t)=\lambda_O^0\cos(2\pi f+\phi)\operatorname{erf}(t/r-r/2\tau_O)\exp(-t/\tau_O)$; λ_O^0 is

the oscillation amplitude; f is the oscillation frequency; and τ_0 is the coherence time. The parameter used for the model can be summarized in the table below.

Parameters	**Value**	**Parameters**	**Value**
r	0.123 ps	C_{11}	1.495
τ_1	0.374 ps	C_{21}	3.346
τ_2	13.1 ps	C_{31}	7.052
τ_3	124 ps	$C_{12} = C_{13} = C_{14}$	0.707
A_1	0.299	$C_{22} = C_{23} = C_{24}$	1.394
A_2	0.502	$C_{32} = C_{33} = C_{34}$	0.482
A_3	0.187	λ_T^0	5.365 nm
λ_{F1}	27.1 nm	λ_O^0	0.4 nm
λ_{F2}	10.4 nm	f	1.15 THz
λ_{F3}	11.8 nm	ϕ	0
λ_{C1}	501.3 nm	τ_O	1.20 ps
λ_{C2}	517.9 nm	$\boldsymbol{R^2}$	**0.9734**
λ_{C3}	524.1 nm		

Based on the model, we were able to satisfactorily global-fit the transient data across whole spectral and temporal window of our measurement, with $R^2 = 0.9734$.